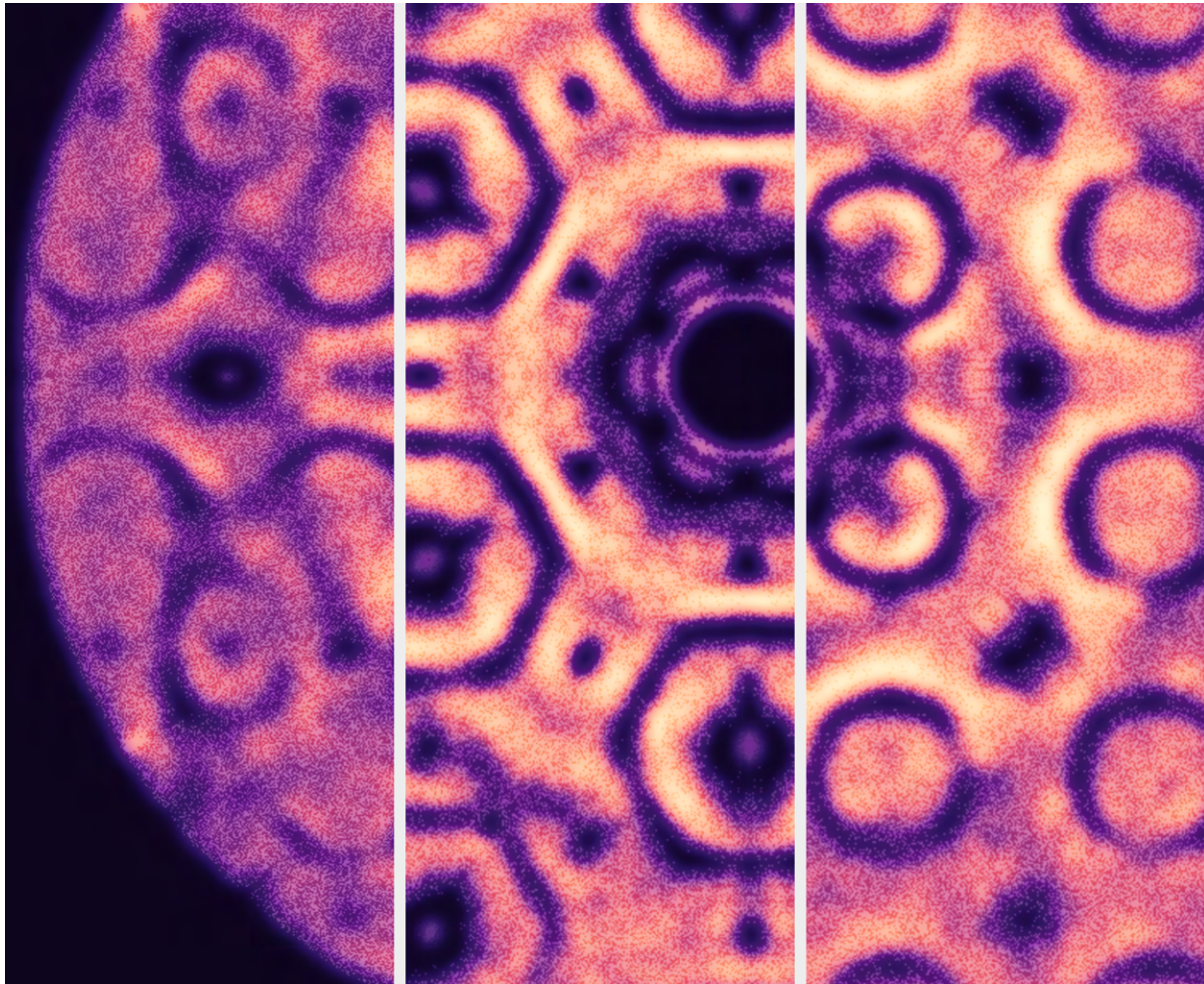


# Refining short-range order parameters from diffuse electron scattering

Romy Poppe



Supervisor **prof. dr. Joke Hadermann**

Thesis submitted in fulfilment of the requirements for the degree of Doctor of Science: Physics  
Faculty of Science — Department of Physics — Antwerp, 2023



University  
of Antwerp





Faculty of Science  
Department of Physics

# Refining short-range order parameters from diffuse electron scattering

Thesis submitted in fulfilment of the requirements for the degree of  
Doctor of Science: Physics  
at the University of Antwerp

**Romy Poppe**

Antwerp, 2023

Supervisor  
prof. dr. Joke Hadermann

## **Jury**

### **Chairman**

prof. dr. Paul Scheunders, University of Antwerp, Belgium

### **Supervisor**

prof. dr. Joke Hadermann, University of Antwerp, Belgium

### **Members**

prof. dr. Milorad Milosevic, University of Antwerp, Belgium

prof. dr. Ute Kolb, Johannes Gutenberg University Mainz, Germany

prof. dr. Arkadiy Simonov, ETH Zürich, Switzerland

## **Contact**

Romy Poppe

University of Antwerp

Faculty of Science

EMAT - Electron Microscopy for Materials Science

Groenenborgerlaan 171, 2020 Antwerpen, België

Romy.Poppe@uantwerpen.be

© 2023 Romy Poppe

All rights reserved.

# Contents

---

<b>1</b>	<b>Introduction</b>	<b>7</b>
1.1	Short-range order . . . . .	8
1.1.1	Occupational, displacive and magnetic disorder . . . . .	8
1.1.2	Short-range order vs. long-range order . . . . .	10
1.1.3	Interpretation of the diffuse scattering . . . . .	12
1.1.4	Three-dimensional difference pair distribution function (3D- $\Delta$ PDF) . . . . .	12
1.2	Electron diffraction . . . . .	14
1.2.1	Elastic and inelastic scattering . . . . .	15
1.2.2	Braggs' law . . . . .	15
1.2.3	X-rays, electrons and neutrons . . . . .	18
1.3	Acquisition of diffuse electron scattering data . . . . .	22
1.3.1	Precession electron diffraction . . . . .	22
1.3.2	Three-dimensional electron diffraction . . . . .	22
1.4	Calculation of the diffuse scattering . . . . .	24
1.5	Refinement of the short-range order . . . . .	25
1.5.1	Monte Carlo refinement . . . . .	26
1.5.2	Reverse Monte Carlo refinement . . . . .	30
1.5.3	Three-dimensional difference pair distribution function refinement . . . . .	31

## CONTENTS

<b>2</b>	<b>One-dimensional diffuse scattering - <math>\text{Li}_{1.2}\text{Ni}_{0.13}\text{Mn}_{0.54}\text{Co}_{0.13}\text{O}_2</math></b>	<b>33</b>
2.1	Introduction . . . . .	34
2.2	Experimental details . . . . .	34
2.2.1	Synthesis . . . . .	34
2.2.2	Data acquisition . . . . .	34
2.2.3	Data processing . . . . .	35
2.3	Description of the disorder . . . . .	35
2.4	Effect of different parameters on the observed diffuse scattering . . . . .	40
2.4.1	Orientation of the grid in the sampleholder . . . . .	40
2.4.2	In-zone electron diffraction . . . . .	42
2.4.3	Background subtraction . . . . .	42
2.4.4	Symmetry averaging . . . . .	44
2.4.5	Different types of twinning . . . . .	45
2.5	Calculated diffuse scattering . . . . .	48
2.6	Refinement of the short-range order . . . . .	51
2.7	Determination of the spinel/layered phase ratio . . . . .	57
2.8	Conclusion . . . . .	62
<b>3</b>	<b>Three-dimensional diffuse scattering - <math>\text{Nb}_{0.84}\text{CoSb}</math></b>	<b>63</b>
3.1	Introduction . . . . .	64
3.2	Experimental details . . . . .	64
3.2.1	Synthesis . . . . .	64
3.2.2	Data acquisition . . . . .	65
3.2.3	Data processing . . . . .	65
3.3	Dynamical refinement of the average crystal structure . . . . .	66
3.4	Effect of different parameters on the observed diffuse scattering . . . . .	70

3.4.1	In-zone electron diffraction . . . . .	70
3.4.2	Background subtraction . . . . .	72
3.4.3	Symmetry averaging . . . . .	73
3.4.4	Convergence of the electron beam . . . . .	74
3.4.5	Detector point spread function . . . . .	75
3.4.6	Crystal mosaicity . . . . .	76
3.4.7	X-ray and electron diffraction . . . . .	78
3.5	Calculated diffuse scattering . . . . .	80
3.5.1	Long-range order model . . . . .	80
3.5.2	Short-range order model . . . . .	81
3.5.3	Calculation of the diffuse scattering . . . . .	83
3.6	Three-dimensional difference pair distribution function . . . . .	90
3.7	Refinement of the short-range order . . . . .	95
3.7.1	Monte Carlo refinement . . . . .	95
3.7.2	Three-dimensional difference pair distribution function refinement	104
3.8	Application of the model to $\text{LiNi}_{0.5}\text{Sn}_{0.3}\text{Co}_{0.2}\text{O}_2$ . . . . .	110
3.8.1	Introduction . . . . .	110
3.8.2	Scanning transmission electron microscopy . . . . .	111
3.8.3	Powder X-ray diffraction . . . . .	113
3.8.4	Three-dimensional electron diffraction . . . . .	114
3.9	Conclusion . . . . .	120
	<b>Conclusions and outlook</b>	<b>123</b>
	Bibliography . . . . .	125
	<b>A Curriculum vitae</b>	<b>145</b>

*CONTENTS*

**B Acknowledgments**

**149**



# Summary

---

Electrons, X-rays and neutrons that pass through a thin crystalline sample will be diffracted. Diffraction patterns of crystalline materials contain Bragg reflections (sharp discrete intensity maxima) and diffuse scattering (a weak continuous background). The Bragg reflections contain information about the average crystal structure (the type of atoms and the average atomic positions), whereas the diffuse scattering contains information about the short-range order (deviations from the average crystal structure that are ordered on a local scale). Because the properties of many materials depend on the short-range order, refining short-range order parameters is essential for understanding and optimizing material properties.

The refinement of short-range order parameters has previously been applied to the diffuse scattering in single-crystal X-ray and single-crystal neutron diffraction data but not yet to the diffuse scattering in single-crystal electron diffraction data. In this thesis, we will verify the possibility to refine short-range order parameters from the diffuse scattering in single-crystal electron diffraction data. Electron diffraction allows to acquire data on submicron-sized crystals, which are too small to be investigated with single-crystal X-ray and single-crystal neutron diffraction.

In Chapter 1, we will explain the effect of short-range order on the diffuse scattering. We will also explain how the three-dimensional difference pair distribution function can be used to determine the origin of the observed diffuse scattering. Finally, we will give an overview of the different methods that can be used to refine short-range order parameters from single-crystal diffuse scattering data.

In Chapter 2, we will refine short-range order parameters from the one-dimensional diffuse scattering in electron diffraction data acquired on the lithium-ion battery cathode material  $\text{Li}_{1.2}\text{Ni}_{0.13}\text{Mn}_{0.54}\text{Co}_{0.13}\text{O}_2$ . The number of stacking faults and the twin percentages will be refined from the diffuse scattering using a Monte Carlo refinement. We will also describe a method to determine the spinel/layered phase ratio from the intensities of the Bragg reflections in electron diffraction data.

In Chapter 3, we will refine short-range order parameters from the three-dimensional diffuse scattering in both single-crystal electron and single-crystal X-ray diffraction data acquired on  $\text{Nb}_{0.84}\text{CoSb}$ . The correlations between neighbouring vacancies and the displacements of Sb and Co atoms will be refined from the diffuse scattering using

## *CONTENTS*

a Monte Carlo refinement and a three-dimensional difference pair distribution function refinement. To determine the accuracy of the refined correlation coefficients, the displacements of Sb and Co atoms refined from the diffuse scattering will be compared with the displacements refined from the Bragg reflections in single-crystal X-ray diffraction data. The effect of different experimental parameters on the spatial resolution of the observed diffuse scattering will also be investigated. Finally, the model of the short-range Nb-vacancy order in  $\text{Nb}_{0.84}\text{CoSb}$  will also be applied to  $\text{LiNi}_{0.5}\text{Sn}_{0.3}\text{Co}_{0.2}\text{O}_2$ .

## Dutch summary

---

Elektronen, X-stralen en neutronen die door een dun kristallijn materiaal worden gestuurd, zullen worden verstrooid. Diffractiepatronen van kristallijne materialen bevatten zowel Bragg reflecties (scherpe discrete intensiteitsmaxima) als diffuse verstrooiing (een zwakke continue achtergrond). De Bragg reflecties bevatten informatie over de gemiddelde kristalstructuur (het type atomen en de gemiddelde atoomposities). De diffuse verstrooiing daarentegen bevat informatie over defecten in het kristalrooster (afwijkingen t.o.v. de gemiddelde kristalstructuur die geordend zijn over korte afstanden). Omdat de eigenschappen van veel materialen afhankelijk zijn van defecten in het kristalrooster, is het belangrijk om het aantal defecten en de ordening van defecten te kunnen kwantificeren.

Parameters zoals het aantal defecten en de ordening van defecten zijn eerder al verfijnd geweest uit de diffuse verstrooiing in röntgendiffractie en neutronendiffractie data, maar nog niet uit de diffuse verstrooiing in elektronendiffractie data. Het doel van deze thesis is daarom om te kijken of deze parameters ook verfijnd kunnen worden uit de diffuse verstrooiing in elektronendiffractie data. Met elektronendiffractie is het mogelijk om kristallen te bestuderen die kleiner zijn dan een micrometer, wat niet mogelijk is met röntgendiffractie en neutronendiffractie.

In Hoofdstuk 1 zullen we bespreken wat de invloed is van de ordening van defecten op de diffuse verstrooiing. Vervolgens zullen we uitleggen hoe de driedimensionale paarverderingsfunctie gebruikt kan worden om te bepalen welk type defecten verantwoordelijk zijn voor de diffuse verstrooiing. Tot slot, zullen we een overzicht geven van verschillende methoden die gebruikt kunnen worden om parameters te verfijnen uit de diffuse verstrooiing.

In Hoofdstuk 2 zullen we parameters verfijnen uit de eendimensionale diffuse verstrooiing in elektronendiffractie data opgenomen op  $\text{Li}_{1.2}\text{Ni}_{0.13}\text{Mn}_{0.54}\text{Co}_{0.13}\text{O}_2$ , een kathodemateriaal dat gebruikt wordt in lithium-ion batterijen. Het aantal stapelfouten en het percentage van de verschillende tweelingen zullen worden verfijnd uit de diffuse verstrooiing door gebruik te maken van een Monte Carlo verfijning. Daarnaast hebben we ook een methode ontwikkeld om de verhouding van de spinel fase en de gelaagde fase te bepalen uit de intensiteit van de Bragg reflecties in elektronendiffractie data.

In Hoofdstuk 3 zullen we parameters verfijnen uit de driedimensionale diffuse

## *CONTENTS*

verstrooiing in elektronendiffractie data en in röntgendiffractie data opgenomen op  $\text{Nb}_{0.84}\text{CoSb}$ . De correlaties tussen naburige vacatures en de atoomposities van Sb en Co zullen worden verfijnd uit de diffuse verstrooiing door gebruik te maken van een Monte Carlo verfijning en een driedimensionale paarverderingsfunctie verfijning. Om de nauwkeurigheid van de verfijnde correlatiecoëfficiënten te bepalen, zullen de atoomposities van Sb en Co verfijnd uit de diffuse verstrooiing vergeleken worden met de atoomposities van Sb en Co verfijnd uit de Bragg reflecties in röntgendiffractie data. Ook zullen we de invloed onderzoeken van verschillende experimentele parameters op de resolutie van de diffuse verstrooiing. Het model van de Nb-vacature ordening in  $\text{Nb}_{0.84}\text{CoSb}$  zal ook worden toegepast op  $\text{LiNi}_{0.5}\text{Sn}_{0.3}\text{Co}_{0.2}\text{O}_2$ .

## List of abbreviations

---

ADT	automated diffraction tomography
CCD	charge-coupled device
cRED	continuous rotation electron diffraction
DFT	discrete Fourier transform
EDT	electron diffraction tomography
FFT	fast Fourier transform
HAADF-STEM	high-angle annular dark-field scanning transmission electron microscopy
HPC	high performance computing
HR-STEM	high-resolution scanning transmission electron microscopy
IEDT	integrated electron diffraction tomography
MicroED	microcrystal electron diffraction
NED	nano electron diffraction
PED	precession electron diffraction
PEDT	precession electron diffraction tomography
RED	rotation electron diffraction
SAED	selected area electron diffraction
TEM	transmission electron microscopy
1D-PDF	one-dimensional pair distribution function
3D- $\Delta$ PDF	three-dimensional difference pair distribution function
3D ED	three-dimensional electron diffraction

## *CONTENTS*

# Chapter 1

## Introduction

---

Diffraction patterns of crystalline materials contain Bragg reflections, arising from the periodicity of the crystalline lattice, and diffuse scattering, arising from the disorder. Any deviation from the average crystal structure gives rise to diffuse scattering. When the deviations from the average structure are ordered on a local scale, they are referred to as short-range order. Because the properties of many materials depend on the short-range order, refining short-range order parameters is essential for understanding and optimizing material properties.

The refinement of short-range order parameters has previously been applied to the diffuse scattering in single-crystal X-ray and single-crystal neutron diffraction data but not yet to the diffuse scattering in single-crystal electron diffraction data. In this thesis, we will verify the possibility to refine short-range order parameters from the diffuse scattering in single-crystal electron diffraction data. Electron diffraction allows to acquire data on submicron-sized crystals, which are too small to be investigated with single-crystal X-ray and single-crystal neutron diffraction.

In this chapter, we will first explain the difference between short-range order and long-range order, and explain how the three-dimensional difference pair distribution function (3D- $\Delta$ PDF) can be used to determine the origin of the observed diffuse scattering. Then, we will discuss the advantages and disadvantages of electron diffraction compared to X-ray and neutron diffraction. Finally, we will give an overview of the different methods that can be used to refine short-range order parameters from single-crystal diffuse scattering data.

## 1.1 Short-range order

### 1.1.1 Occupational, displacive and magnetic disorder

According to the International Union of Crystallography, a crystalline material is defined as a material that exhibits *essentially* a sharp diffraction pattern [1]. The word *essentially* means that most of the intensity of the diffraction is concentrated in relatively sharp Bragg reflections, besides the always present diffuse scattering.

Diffuse scattering (i.e., the weak continuous scattering between the Bragg reflections) has been studied since the earliest days of crystallography [2, 3]. It occurs whenever a crystal contains disorder – that is, when there are any deviations from the average crystal structure [4]. Disorder in crystalline materials can be divided in three categories: occupational disorder, displacive disorder and magnetic disorder [5].

**Occupational disorder:** Also referred to as substitutional or compositional disorder. A site in the unit cell can be occupied by more than one atom type.<sup>1</sup>

**Displacive disorder:** The displacement of atoms from their average positions. For example the relaxation of atoms around vacancies.

**Magnetic disorder:** Disorder in the orientation of the spins of unpaired electrons (i.e., magnetic moments) in magnetic materials.

The collective vibration of atoms about their average positions (phonons) is an example of displacive disorder and can be described by lattice dynamics. The corresponding diffuse scattering is called **thermal diffuse scattering** [4].<sup>2</sup> Because the number of phonons increases with increasing temperature, thermal diffuse scattering can be reduced by cooling the sample [8].

Some examples of disordered materials are listed below. These examples illustrate that in most materials the diffuse scattering is due to both occupational and displacive disorder.

- **KCl<sub>0.5</sub>Br<sub>0.5</sub>** has a disordered rock salt structure. The weak lines of thermal diffuse scattering that connect neighbouring Bragg reflections in the  $hk0$  plane reconstructed from single-crystal X-ray diffraction data (Figure 1.1 (a)) are caused by phonons (displacive disorder). Monte Carlo simulations showed that the formation

---

<sup>1</sup>In 2015, approximately 30% of the more than 800.000 structures in the Cambridge Structural Database contained occupational disorder [6, 7].

<sup>2</sup>Since a temperature of 0 K is impossible to reach, the diffraction patterns of all crystals contain thermal diffuse scattering.



of  $\text{Cl}^-$  - and  $\text{Br}^-$  -rich domains (occupational disorder) and the resulting atomic displacements due to different  $\text{Cl}^-$  and  $\text{Br}^-$  ionic radii (displacive disorder) cause an increase in the width of the thermal diffuse scattering [9].

- $\text{Zr}_{0.82}\text{Y}_{0.18}\text{O}_{1.91}$  is an ion conductor used in solid oxide fuel cells [10], oxygen sensors [11] and oxygen pumps [12]. The oxygen sites are partially occupied by vacancies. The diffuse scattering in the  $hk0$  plane reconstructed from single-crystal X-ray diffraction data (Figure 1.1 (b)) is due to correlations between neighbouring vacancies (occupational disorder) and the relaxation of the Zr, Y and O atoms around these vacancies (displacive disorder) [13].
- $\text{Cu}_{1.95}\text{Se}$  is a thermoelectric material. The  $0kl$  plane reconstructed from single-crystal X-ray diffraction data acquired on  $\text{Cu}_{1.95}\text{Se}$  at 300 K is shown in Figure 1.1 (c). The diffuse streaks indicate that the structure is ordered in two dimensions but disordered in the third dimension. The diffuse streaks are due to one-dimensional stacking disorder: mirrored and non-mirrored layers are shifted along three possible inter-layer vectors (occupational disorder). The very weak three-dimensional diffuse scattering in Figure 1.1 (c) is most likely thermal diffuse scattering caused by phonons (displacive disorder) [14].
- $\text{Fe}_{1.1}\text{Mn}_{0.9}\text{O}_3$  is a frustrated magnet. Figure 1.1 (d) shows the  $hk0$  plane reconstructed from single-crystal neutron diffraction data acquired on  $\text{Fe}_{1.1}\text{Mn}_{0.9}\text{O}_3$  at 7 K. The diffuse scattering close to the central beam is caused by correlations between the magnetic moments of Mn and Fe atoms (magnetic disorder). Nearest-neighbour Mn and Fe atoms have magnetic moments that tend to align in opposite directions (antiferromagnetic correlations), while next-nearest neighbour Mn and Fe atoms have magnetic moments that tend to align in the same direction (ferromagnetic correlations). The weak diffuse scattering further away from the central beam is caused by occupational and/or displacive disorder. The thermal diffuse scattering was removed by the neutron spectrometer [15].

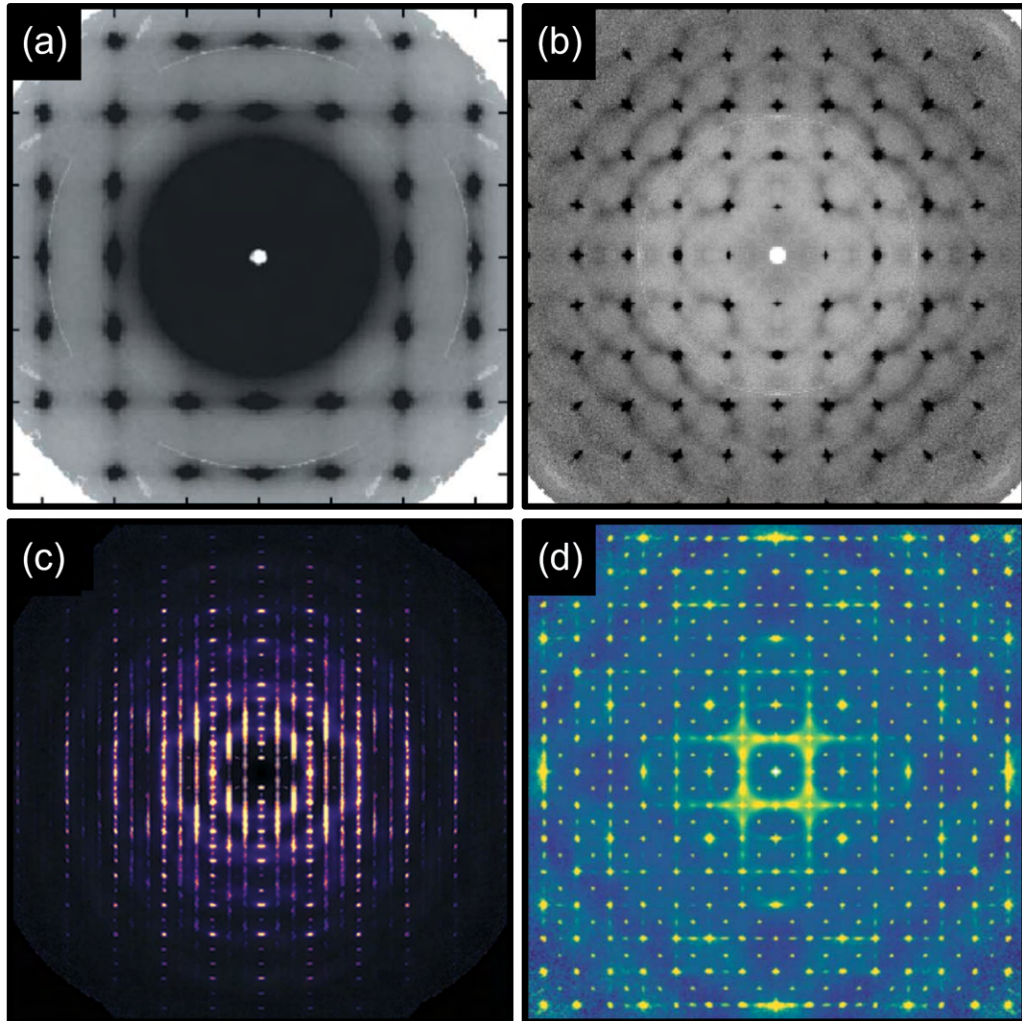


Figure 1.1: Single-crystal diffuse scattering data acquired on a)  $\text{KCl}_{0.5}\text{Br}_{0.5}$  [9], b)  $\text{Zr}_{0.82}\text{Y}_{0.18}\text{O}_{1.91}$  [13], c)  $\text{Cu}_{1.95}\text{Se}$  [14] and d)  $\text{Fe}_{1.1}\text{Mn}_{0.9}\text{O}_3$  [15].

### 1.1.2 Short-range order vs. long-range order

The diffraction pattern of a perfect crystal (i.e., a three-dimensional array of identical unit cells) contains sharp Bragg reflections at integer  $hkl$  values (Figure 1.2 (a)). Real crystals, however, only approximate this ideal. Their diffraction patterns contain both Bragg reflections, arising from the periodicity of the crystalline lattice, and diffuse scattering, arising from the disorder. In general, any deviation from the average crystal structure gives rise to diffuse scattering [4]. When the disorder is completely random, a broad diffuse background will be visible (Figure 1.2 (b)), which is called monotonic diffuse Laue scattering [16]. For materials in which the disorder is correlated, highly structured diffuse scattering can be observed between the Bragg reflections (Figure 1.2 (c)). When

the deviations from the average structure are ordered on a local scale, they are referred to as **local order** or **short-range order**. Examples of technologically important materials with short-range order include alloys [17], shape-memory alloys [18], ferroelectrics [19], superconductors [20, 21], fast ion conductors [22, 23], semiconductors [24] and pharmaceuticals [25, 26] [4]. Deviations from the average structure that are ordered over longer distances are referred to as **long-range order** [27]. Structures that exhibit long-range order are named modulated structures and can be divided in commensurately and incommensurately modulated structures. The diffraction patterns of commensurately modulated structures can be indexed with three  $hkl$  values, which is not the case for incommensurately modulated structures which should be indexed using superspace crystallography [28]. Figure 1.2 (d) shows the diffraction pattern of a commensurately modulated structure. The additional sharp Bragg reflections at non-integer  $hkl$  values are called satellite reflections.

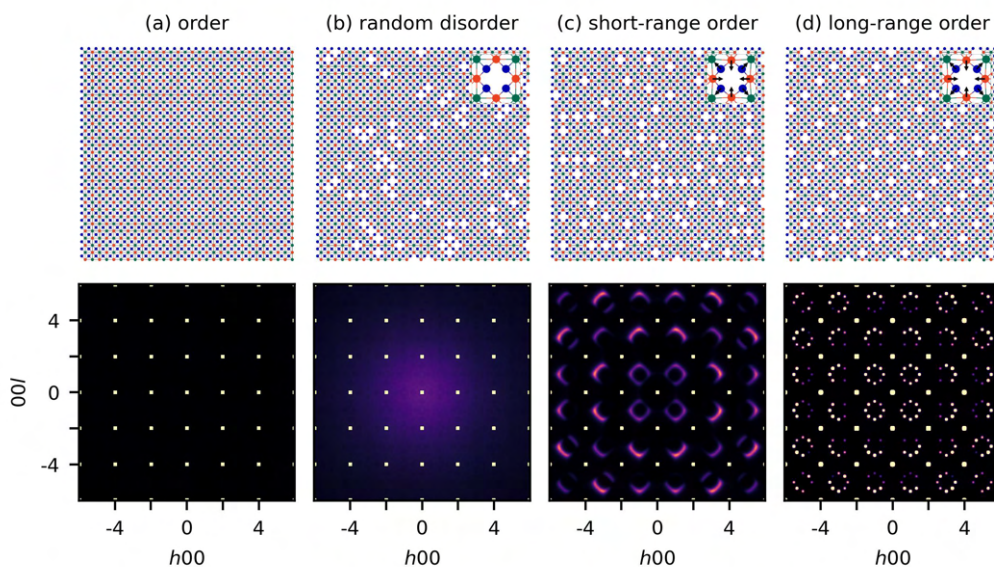


Figure 1.2: Structure models and their corresponding calculated single crystal X-ray diffraction patterns. (a) The calculated  $h0l$  plane of a perfectly ordered NbCoSb crystal without vacancies shows sharp Bragg reflections at integer  $hkl$  values. (b) Nb<sub>0.84</sub>CoSb structure with a random vacancy distribution and without displacements of Sb and Co atoms. The random vacancy distribution gives rise to monotonic diffuse Laue scattering. (c) Nb<sub>0.84</sub>CoSb structure with correlations between nearest and next-nearest neighbour vacancies. Displacements of Sb and Co atoms are indicated by arrows. The short-range Nb-vacancy order in (c) results in highly structured diffuse scattering between the Bragg reflections, whereas the long-range Nb-vacancy order in (d) results in sharp satellite reflections. Structure models were calculated in *DISCUS*. Single-crystal X-ray diffraction patterns were calculated in *DISCUS* and *Scatty*.

### 1.1.3 Interpretation of the diffuse scattering

The intensities and positions of the Bragg reflections contain information about the average crystal structure, whereas the intensity distribution of the diffuse scattering contains information about the short-range order (i.e., the deviations from the average crystal structure that are ordered on a local scale). Diffuse scattering can occur in one, two, or in three dimensions. A crystal that is ordered along two dimensions but disordered along the third dimension will show one-dimensional diffuse streaks. A common example are stacking faults, where two-dimensional periodic layers are shifted relative to each other. When the crystal is ordered along one dimension but disordered along the other two dimensions, then the diffuse scattering will be in the form of two-dimensional diffuse planes. Finally, three-dimensional diffuse clouds indicate disorder along all three dimensions [4].

In the 1940s, analytical models were developed to describe the observed diffuse scattering (see [29, 30, 31, 32, 33, 34] for some examples) [4]. These first analytical models were restricted to one-dimensional disorder problems. In 1950, Cowley and Warren extended the theory to two- and three-dimensional disorder problems [27, 35, 16] by using short-range order parameters  $\alpha_{mn}^{uvw}$  [4]:

$$\alpha_{mn}^{uvw} = 1 - \frac{P_{mn}^{uvw}}{\text{occ}}. \quad (1.1)$$

$\alpha_{mn}^{uvw}$  are referred to as ‘Warren-Cowley short-range order parameters’.  $P_{mn}^{uvw}$  is the probability that sites  $m$  and  $n$  are occupied by the same atom type,  $uvw$  is the interatomic vector and  $\text{occ}$  is the occupancy [36, 37].

### 1.1.4 Three-dimensional difference pair distribution function (3D- $\Delta$ PDF)

The 3D- $\Delta$ PDF is the Fourier transform of the three-dimensional diffuse scattering in single-crystal diffraction data [38]. For  $\text{Zr}_{0.82}\text{Y}_{0.18}\text{O}_{1.91}$ ,  $\text{Cu}_{1.95}\text{Se}$  and  $\text{Fe}_{1.1}\text{Mn}_{0.9}\text{O}_3$ , the 3D- $\Delta$ PDF was used to determine the origin of the observed diffuse scattering as it provides information about correlations between neighbouring atoms that are not represented by the average structure. Figure 1.3 shows an example of the  $x0z$  plane of the 3D- $\Delta$ PDF calculated from the three-dimensional diffuse scattering in single-crystal X-ray diffraction data after subtraction of the Bragg reflections. Positive 3D- $\Delta$ PDF values are displayed in red and negative 3D- $\Delta$ PDF values in blue. Positive/negative 3D- $\Delta$ PDF values mean that the probability of finding scattering densities separated by the corresponding interatomic vector is higher/lower in the real structure than in the average structure [39]. Because X-rays are scattered by the electron cloud, the scattering densities in the X-ray 3D- $\Delta$ PDF are electron densities. Neutrons, on the other hand, are scattered by both the atomic nuclei and the spin of the unpaired electrons, and in the latter case the scattering densities are magnetization densities [15]. Only recently,

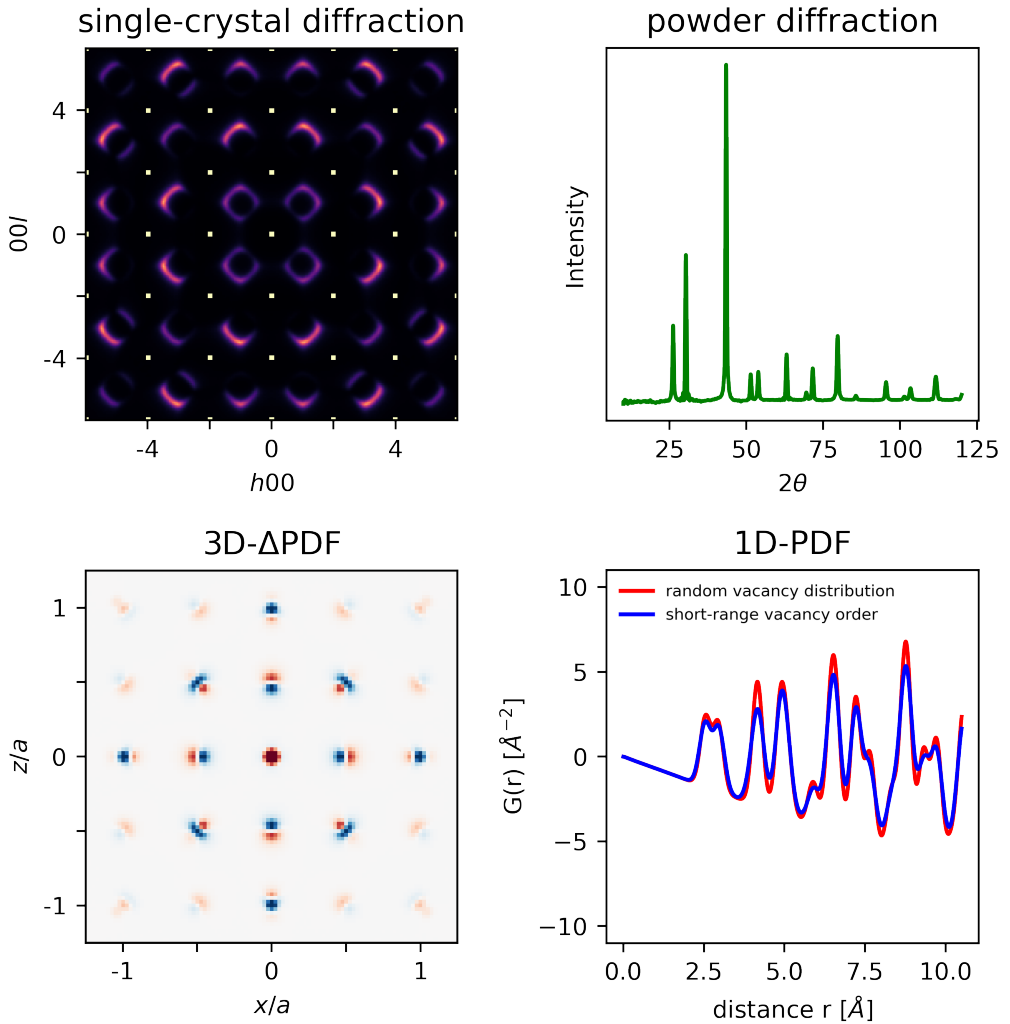


Figure 1.3: Single-crystal and powder X-ray diffraction data calculated for a  $\text{Nb}_{0.84}\text{CoSb}$  crystal with short-range order. The diffuse scattering is due to correlations between nearest and next-nearest neighbour vacancies and relaxations of Co and Sb atoms around these vacancies. The 3D- $\Delta$ PDF is the Fourier transform of the single-crystal diffuse scattering while the one-dimensional pair distribution function (1D-PDF) is the Fourier transform of the intensities in the powder diffraction pattern. Both the 3D- $\Delta$ PDF and the 1D-PDF provide information about correlations between neighbouring atoms. The 1D-PDF was calculated for a  $\text{Nb}_{0.84}\text{CoSb}$  crystal with a random vacancy distribution and no displacements of Co and Sb atoms (red) and for a  $\text{Nb}_{0.84}\text{CoSb}$  crystal with short-range Nb-vacancy order and with displacements of Co and Sb atoms (blue). Single-crystal and powder X-ray diffraction data were calculated in *DISCUS*. The 1D-PDF was calculated in *DISCUS* and the 3D- $\Delta$ PDF was calculated in *MANTID*.

## CHAPTER 1. INTRODUCTION

Schmidt and co-workers showed that the 3D- $\Delta$ PDF can also be reconstructed from the diffuse scattering in single-crystal electron diffraction data [40]. Electrons are scattered by the atomic nucleus and the electron cloud, and the scattering densities in the electron 3D- $\Delta$ PDF are thus atomic charge densities.

In this thesis, we will focus on the diffuse scattering in single-crystal electron diffraction data and the corresponding 3D- $\Delta$ PDF. Single-crystal electron diffraction allows the study of submicron-sized crystals which are too small to be investigated with single-crystal X-ray and single-crystal neutron diffraction. Alternative methods that are frequently used to analyse the diffuse scattering in submicron-sized crystals are powder X-ray diffraction and powder electron diffraction. Powder diffraction data are acquired on powder samples (instead of single crystals) and show concentric rings. The X-ray powder diffraction pattern in Figure 1.3 shows the intensity of these rings projected onto one dimension in function of the scattering angle  $2\theta$ . The 1D-PDF in Figure 1.3 is the Fourier transform of the intensities in the powder diffraction pattern (both Bragg and diffuse scattering) [41]. Because Bragg and diffuse scattering cannot be separated, the 1D-PDF contains information about correlations between all neighbouring atoms (unlike the 3D- $\Delta$ PDF, which only contains information about correlations that are not represented by the average structure). The peaks in the 1D-PDF correspond to the interatomic distances between all pairs of atoms within the crystal. The main limitation of powder PDF analysis is peak overlap. Peaks that correspond to interatomic vectors of similar length but different spatial directions will overlap due to the one-dimensional nature of the powder PDF [39]. This is not the case for the single-crystal 3D- $\Delta$ PDF, where correlations between atoms separated by interatomic vectors of similar length but different spatial directions can easily be distinguished [39]. When a powder sample consists of multiple phases, then the signals of all these phases will overlap, making the analysis of the 1D-PDF even more difficult [42]. Because the 3D- $\Delta$ PDF is the Fourier transform of the diffuse scattering data from one single crystal, its analysis cannot be hampered by the overlap of multiple phases.

### 1.2 Electron diffraction

In a transmission electron microscope (TEM), electrons are directed to a thin sample. The electrons that hit the sample are called the incident beam. Electrons coming through the sample are separated into those that suffer no angular deviation (the direct beam) and those scattered by the sample through measurable angles (the scattered beams). The direct beam is responsible for the bright intensity in the centre of a diffraction pattern and the scattered beams account for the spots that appear around the direct beam [8].

### 1.2.1 Elastic and inelastic scattering

Electrons going through a thin sample are either scattered or transmitted and either lose energy (inelastic scattering) or don't lose energy (elastic scattering). The Bragg reflections in electron diffraction patterns are caused by **elastically scattered electrons**. Because electrons have an electric charge, they are scattered by both the positively charged atomic nucleus and the negatively charged electron cloud. Electrons scattered by the electron cloud have angular deviations of only a few degrees, while those scattered close to the atomic nucleus are scattered through much larger angles, up to  $180^\circ$ . Scattering through angles  $\theta > 90^\circ$  is called backscattering and the probability for backscattering to occur increases with increasing sample thickness. For thin samples, scattering is most likely to occur in the forward direction and most scattered electrons have scattering angles  $< 5^\circ$ . Because **inelastically scattered electrons** lose energy, they have a higher wavelength than the incident electrons. Electrons in the incident beam may lose energy due to the ejection of electrons, the emission of X-rays or by the generation of phonons or plasmons. Incident beam electrons that lose energy due to the creation of phonons are responsible for the thermal diffuse scattering in electron diffraction patterns. The mean free path for phonon scattering (the average distance that an electron travels between two phonon scattering events) at room temperature varies from a couple of nm for Au up to about 350 nm for Al [8].

### 1.2.2 Braggs' law

The average structure of a crystalline material can be described by a three-dimensional lattice. Each point in the crystal lattice can be described by a lattice vector  $\mathbf{r}$ , which can be written as a linear combination of the unit cell vectors  $\mathbf{a}$ ,  $\mathbf{b}$  and  $\mathbf{c}$ :

$$\mathbf{r} = x\mathbf{a} + y\mathbf{b} + z\mathbf{c}. \quad (1.2)$$

The reciprocal lattice is the Fourier transform of the crystal lattice in real space, which is constructed by the reciprocal unit cell vectors  $\mathbf{a}^*$ ,  $\mathbf{b}^*$  and  $\mathbf{c}^*$  [43]:

$$\mathbf{a}^* = \frac{\mathbf{b} \times \mathbf{c}}{V}, \mathbf{b}^* = \frac{\mathbf{c} \times \mathbf{a}}{V}, \mathbf{c}^* = \frac{\mathbf{a} \times \mathbf{b}}{V}, \quad (1.3)$$

With  $V$  the volume of the unit cell.

A set of parallel and equally spaced lattice planes with interplanar distance  $d$  can be described by the Miller indices  $(hkl)$ . Figure 1.4 shows an incident plane wave with a fixed wavelength  $\lambda$  that is elastically scattered from a set of lattice planes  $(hkl)$  through an angle  $\theta$  (the scattering angle). Each point on the set of lattice planes  $(hkl)$  will act as a source of spherical waves and these spherical waves will interfere. When the spherical waves are in phase, then the amplitude will be increased by many orders of magnitude, which is called constructive interference. Braggs' law states that the spherical waves are

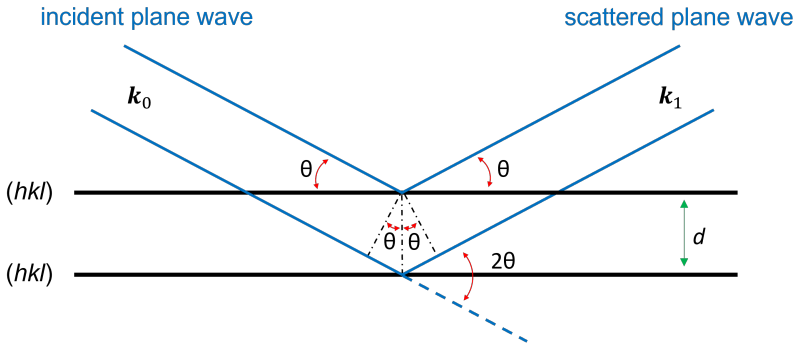


Figure 1.4: Geometrical illustration of the Bragg's law. An incident plane wave with wave vector  $\mathbf{k}_0$  is elastically scattered from a set of lattice planes  $(hkl)$ . The path difference between the upper and lower ray is equal to  $2d \sin(\theta)$ , with  $\theta$  the scattering angle and  $d$  the interplanar distance. There is no path difference between rays scattered on the same lattice plane. Constructive interference will occur when the path difference is equal to  $n\lambda$ , with  $\lambda$  the wavelength. Figure inspired from [43].

in phase when the path difference,  $2d \sin(\theta)$  (see Figure 1.4), is an integer number  $n$  of the wavelength  $\lambda$  [43, 8]:

$$2d \sin(\theta) = n\lambda. \quad (1.4)$$

The resulting waves are plane waves, scattered in different directions, and have the same wavelength  $\lambda$  as the incident plane wave. The distance  $d$  between the lattice planes can thus be calculated from the wavelength  $\lambda$  (which depends on the acceleration voltage) and the scattering angle  $\theta$  [8].

For a perfect crystal, constructive interference will only occur at specific points in reciprocal space. Consequently, the reciprocal lattice will be a three-dimensional array of points. Each reciprocal lattice point  $hkl$  corresponds to waves scattered from a set of lattice planes  $(hkl)$  and can be described by a reciprocal lattice vector  $\mathbf{Q}$ , which can be written as a linear combination of the reciprocal unit cell vectors  $\mathbf{a}^*$ ,  $\mathbf{b}^*$  and  $\mathbf{c}^*$  [43, 8]:

$$\mathbf{Q} = 2\pi(h\mathbf{a}^* + k\mathbf{b}^* + l\mathbf{c}^*). \quad (1.5)$$

The starting point of  $\mathbf{Q}$  is the origin of the reciprocal lattice and its end is the reciprocal lattice point  $hkl$ . The direction of  $\mathbf{Q}$  is perpendicular to the lattice planes  $(hkl)$  and its length is inversely proportional to the distance  $d$  between the lattice planes  $(hkl)$  [43, 8]:

$$|\mathbf{Q}| = \frac{2\pi}{d}. \quad (1.6)$$

The Ewald sphere is a visual representation of the reciprocal lattice points that satisfy the Bragg's law (Figure 1.5). When an incident wave with wave vector  $\mathbf{k}_0$  is elastically scattered from a set of lattice planes  $(hkl)$ , then the length of the wave vector of the



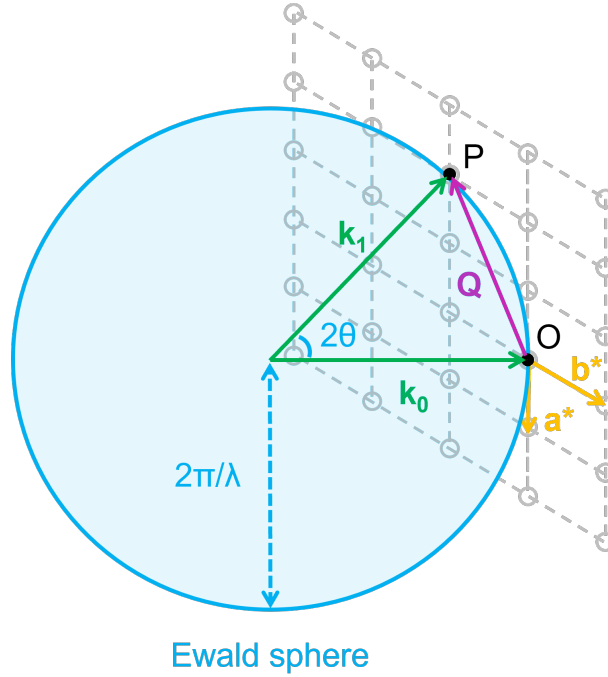


Figure 1.5: The Ewald sphere intersecting a two-dimensional array of reciprocal lattice points. The wave vectors of the incoming ( $\mathbf{k}_0$ ) and the scattered ( $\mathbf{k}_1$ ) waves have their origin in the centre of the Ewald sphere. The origin (O) of the reciprocal lattice is located on the surface of the Ewald sphere at the end of  $\mathbf{k}_0$ . Reciprocal lattice points that intersect with the surface of the Ewald sphere [e.g., point P ( $\bar{2}\bar{1}$ )] satisfy the Bragg's law.  $\mathbf{Q} = -2\mathbf{a}^* - \mathbf{b}^*$  is the reciprocal lattice vector of point P. Figure inspired from [7].

scattered wave  $\mathbf{k}_1$  will be identical to the length of the wave vector of the incident wave  $\mathbf{k}_0$  [43]:

$$|\mathbf{k}_1| = |\mathbf{k}_0| = \frac{2\pi}{\lambda}. \quad (1.7)$$

When the starting point of  $\mathbf{k}_1$  is translated to the starting point of  $\mathbf{k}_0$ , then the angle between  $\mathbf{k}_0$  and  $\mathbf{k}_1$  is  $2\theta$  (Figure 1.4 and Figure 1.5). If the end of  $\mathbf{k}_0$  is defined as the origin of the reciprocal lattice, then constructive interference will only occur when the end of  $\mathbf{k}_1$  coincides with a point in the reciprocal lattice. All possible orientations of  $\mathbf{k}_1$  delineate a sphere in three dimensions, which is called the Ewald sphere. The Ewald sphere is a sphere of radius  $|\mathbf{k}_0| = |\mathbf{k}_1| = 2\pi/\lambda$  and its centre is the starting point of  $\mathbf{k}_0$  and  $\mathbf{k}_1$ . The Ewald sphere passes through the origin of the reciprocal lattice and reciprocal lattice points  $hkl$  that intersect the surface of the Ewald sphere satisfy Bragg's law [43].

From Figure 1.5, it is clear that:

$$\mathbf{k}_1 = \mathbf{k}_0 + \mathbf{Q}, \quad (1.8)$$

## CHAPTER 1. INTRODUCTION

which is the Bragg's law in vector form. The Bragg's law in Equation 1.4 can also be derived from Figure 1.5 [43]:

$$|\mathbf{k}_1| \sin(\theta) = |\mathbf{k}_0| \sin(\theta) = \frac{|\mathbf{Q}|}{2} \Rightarrow 2d \sin(\theta) = \lambda. \quad (1.9)$$

A diffraction pattern is thus the intersection of the Ewald sphere with the reciprocal lattice of the examined material. The reciprocal lattice points that coincide with the surface of the Ewald sphere are called Bragg reflections. In a diffraction experiment the crystal is rotated, which corresponds to a rotation of the reciprocal lattice around its origin [43].

The smaller the wavelength of the incident radiation, the larger the radius of the Ewald sphere. Since the wavelength of high-energy incident electrons is small ( $\lambda = 0.01969 \text{ \AA}$  at 300 kV), the radius of the Ewald sphere ( $\sim 319 \text{ \AA}^{-1}$ ) is large compared to the distance between the reciprocal lattice points (order of  $\text{\AA}^{-1}$ ). Therefore, the Ewald sphere can be approximated as a flat plane perpendicular to the incident beam and an electron diffraction pattern can be approximated as a two-dimensional section through the three-dimensional reciprocal lattice. The sample examined in a transmission electron microscope is very thin, causing the reciprocal lattice points to be elongated (also called relrods or reciprocal lattice rods). Also reciprocal lattice points that do not perfectly satisfy Bragg's law will thus be intersected by the Ewald sphere [8].

The positions of the scattered beams are determined by the unit cell parameters while the intensity of the scattered beams is determined by the atom types and atomic coordinates. [8]

### 1.2.3 X-rays, electrons and neutrons

The scattered intensity  $I(\mathbf{Q})$  is obtained by multiplying the structure factor  $F(\mathbf{Q})$  by its complex conjugate [43, 8]:

$$I(\mathbf{Q}) = F(\mathbf{Q})F^*(\mathbf{Q}), \quad (1.10)$$

with  $\mathbf{Q}$  a reciprocal lattice vector (Equation 1.5). The structure factor  $F(\mathbf{Q})$  is the amplitude of the scattered wave and is defined as [43, 8]:

$$F(\mathbf{Q}) = \sum_{j=1}^N f_j(\mathbf{Q}) \exp(i\mathbf{Q} \cdot \mathbf{r}_j), \quad (1.11)$$

with  $N$  the number of atoms in the crystal,  $\mathbf{r}_j = x_j\mathbf{a} + y_j\mathbf{b} + z_j\mathbf{c}$  the direct lattice vector of atom  $j$  with atomic coordinates  $x_j$   $y_j$   $z_j$  and  $f_j(\mathbf{Q})$  the atomic form factor of atom  $j$ . The phase factor  $\exp(2\pi i\mathbf{Q} \cdot \mathbf{r}_j)$  takes account of the phase difference between waves scattered from atoms on different but parallel lattice planes with the same Miller indices  $(hkl)$  [43, 8].

Diffraction from crystals can only be observed when the wavelength  $\lambda$  of the radiation is of the same order of magnitude as the shortest interatomic distances, which is the case for X-rays, electrons and neutrons [43]. Most structures in crystallographic databases have been determined from single-crystal and powder X-ray diffraction [44, 45, 46, 6, 47]. For instance, 84.5 % of the structures in the Inorganic Crystal Structure Database have been determined from X-ray diffraction, 14.8 % from neutron diffraction and 0.7 % from electron diffraction. The main differences between X-rays, electrons and neutrons are compared in Table 1.1.

Table 1.1: Comparison of X-ray, electron and neutron diffraction.  $Z$  is the atomic number [43].

	X-rays	electrons	neutrons
Scattering by	electron cloud	atomic nuclei and electron cloud	atomic nuclei and electron spin
Atomic form factor, $f(\mathbf{Q})$	$f$ is dependent of $\mathbf{Q}$ and $f(\mathbf{Q}) \propto Z$	$f$ is dependent of $\mathbf{Q}$ and $f(\mathbf{Q}) \propto Z^{\frac{1}{3}}$	$f$ is independent of $\mathbf{Q}$ (for nuclear scattering)
Wavelength range, $\lambda$	0.5–2.5 Å	0.019–0.025 Å	~ 1 Å
Crystal size	1-500 $\mu\text{m}$	10 nm-1 $\mu\text{m}$	>1 mm
Source	diffractometer or synchrotron	transmission electron microscope	neutron source
Theory of diffraction	kinematical	dynamical	kinematical

For neutrons, the atomic form factors  $f_j(\mathbf{Q})$  are replaced by the coherent neutron scattering lengths, which are independent of  $\mathbf{Q}$ . For X-rays and electrons, the atomic form factors  $f_j(\mathbf{Q})$  can be calculated by [43]:

$$f(\mathbf{Q}) = \sum_{i=1}^4 \left[ a_i \exp \left( -b_i \left( \frac{|\mathbf{Q}|}{4\pi} \right)^2 \right) \right] + c, \quad (1.12)$$

The coefficients  $a_1, a_2, a_3, a_4, b_1, b_2, b_3, b_4$  and  $c$  (X-rays and electrons) and the scattering lengths (neutrons) of the different elements are tabulated in the International Tables of Crystallography Volume C [48].

The atomic form factor  $f_j(\mathbf{Q})$  is a measure of the amplitude of a wave elastically scattered from an isolated atom [8]. Figure 1.6 (a) shows a comparison between the X-ray and electron atomic form factors and the coherent neutron scattering length of oxygen as functions of  $d^* = \frac{|\mathbf{Q}|}{2\pi} = 2\frac{\sin(\theta)}{\lambda}$ . The X-ray and electron atomic form factors of lithium, oxygen and cobalt are shown in Figure 1.6 (b-c). For X-rays and electrons,  $f(\mathbf{Q})$  decreases with increasing scattering angle  $\theta$ , while  $f(\mathbf{Q})$  increases with increasing atomic number  $Z$  [8].

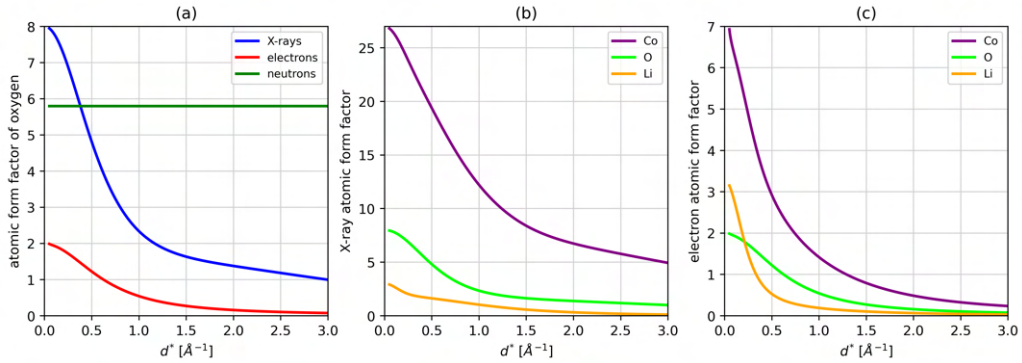


Figure 1.6: (a) Electron and X-ray atomic form factors of oxygen and the coherent neutron scattering length of oxygen as functions of  $d^* = \frac{|\mathbf{Q}|}{2\pi} = 2\frac{\sin(\theta)}{\lambda}$ . (b) X-ray and (c) electron atomic form factors of lithium, oxygen and cobalt.

**X-rays** interact with both the electron cloud and the atomic nuclei, however, because the interaction is inversely proportional to the mass of the particle and a proton is  $\sim 2000\times$  heavier than an electron, the interaction with the atomic nuclei is negligible and it is allowed to say that X-rays are only scattered by the electron cloud [49]. Heavy atoms have more electrons than light atoms, which means that heavy atoms scatter X-rays stronger than light atoms. Figure 1.6 (b) shows that the X-ray atomic form factor is proportional to the atomic number  $Z$  and decreases exponentially towards a constant with increasing  $d^*$ . At  $d^* = 0$ , the X-ray atomic form factor is the sum of  $a_1, a_2, a_3, a_4$  and  $c$ , which is equal to the total number of electrons in atom  $j$  (or the atomic number  $Z$ ) [43]. Single-crystal X-ray diffraction data can be acquired at a synchrotron or using an in-house diffractometer. Synchrotron sources require crystals larger than  $\sim 1 \mu\text{m}$ , while in-house X-ray diffraction experiments require crystals larger than  $\sim 10 \mu\text{m}$  [49].

Because **electrons** have an electric charge, they interact with both the positively charged atomic nuclei and the negatively charged electron cloud, which both contribute to the electrostatic potential  $\phi(\mathbf{r})$  of the atoms in the crystal [43, 8]:

$$\nabla^2 \phi(\mathbf{r}) = -4\pi(\rho_n(\mathbf{r}) - \rho_e(\mathbf{r})), \quad (1.13)$$

where  $\rho_n(\mathbf{r})$  is the charge density of the atomic nucleus and  $\rho_e(\mathbf{r})$  is the charge density of the electron cloud [36]. Because the electron atomic form factor is proportional to  $Z^{1/3}$  [43] (whereas the X-ray atomic form factor is proportional to  $Z$ ), it is easier to detect light atoms nearby heavy atoms for electrons than for X-rays. This is illustrated in Figure 1.6 (b-c) where the difference between the atomic form factors of light atoms (lithium and oxygen) and heavy atoms (cobalt) is smaller for electrons than for X-rays.

The main advantage of electron diffraction is that electrons are scattered more strongly than X-rays and neutrons. Electron diffraction can thus be used to acquire data on submicron-sized crystals, which are too small to be investigated with single-crystal X-ray and single-crystal neutron diffraction [42]. The kinematical theory of diffraction assumes that a scattered wave is not scattered again before it leaves the crystal. This assumption is reasonable for X-rays and neutrons, but not for electrons. Due to the strong interaction of electrons with the atoms in the crystal, electrons can be scattered multiple times while going through the crystal. When multiple scattering (or dynamical scattering) occurs, the intensities are no longer directly related to the structure factor (Equation 1.10). On average, multiple scattering increases the intensity of weaker Bragg reflections, whereas strong Bragg reflections become less intense [50]. The intensities of symmetry-related reflections are also expected to be different due to multiple scattering [51]. The theory taking into account multiple scattering is referred to as the dynamical theory of diffraction [36, 43]. Typical values of the mean free path (the average distance that an electron travels between two scattering events) are of the order of tens of nanometres and the single-scattering approximation is thus only valid for very thin crystals. As the probability for multiple scattering to occur increases with increasing sample thickness, it is important to acquire electron diffraction data on small crystals. Multiple scattering will also be more likely in crystals with a higher density, crystals with heavy elements and highly ordered crystals. Since higher-energy electrons are less likely to be scattered by the sample than lower-energy electrons, higher acceleration voltages will result in less electron scattering and will thus also reduce the amount of multiple scattering [8].

**Neutrons** are scattered by both the atomic nuclei and the spins of the unpaired electrons (magnetic moments). Because the atomic nucleus is much smaller than the wavelength  $\lambda$  of the neutrons, the neutron scattering length is independent of the reciprocal lattice vector  $\mathbf{Q}$  (Figure 1.6 (a)). Unlike X-ray or electron diffraction, there is no relationship between the magnitude of the neutron scattering length and the atomic number  $Z$ . The neutron scattering length is also different for different isotopes of the same element [43]. This makes neutron diffraction very helpful in calculating site occupancies for materials with neighbouring elements in the Periodic Table and for determining the positions of very light atoms such as hydrogen and lithium [52]. Because neutrons interact with the spins of the unpaired electrons, single-crystal neutron diffraction can also be used to study local magnetic correlations in materials such as spin liquids, spin glasses and frustrated magnets [53]. The disadvantage is that neutron diffraction requires single crystals larger than 1 mm [43].

## 1.3 Acquisition of diffuse electron scattering data

### 1.3.1 Precession electron diffraction

Precession electron diffraction (PED) is a method that is often used to record the intensities of the Bragg reflections with reduced multiple scattering [54]. In PED, the electron beam is tilted away from the optical axis of the TEM by a certain angle (the precession angle, typically  $1-3^\circ$ ) and rotated on the surface of a cone with the vertex fixed on the sample plane. The resulting PED pattern is obtained by integrating the intensities in the acquired off-axis electron diffraction patterns. When the crystal is oriented along a zone-axis, and the electron beam is tilted away from this zone-axis, the total number of possible paths will be reduced, and consequently also the amount of multiple scattering.

### 1.3.2 Three-dimensional electron diffraction

The atomic structure of crystalline materials can be determined from both single-crystal and powder diffraction experiments, using X-rays, neutrons or electrons. For a long time, electron diffraction was considered unsuitable for structure solution and refinement because the intensities in in-zone electron diffraction patterns are influenced by strong multiple scattering. The development of three-dimensional electron diffraction (3D ED) in 2007 [55, 56] allowed the acquisition of electron diffraction data with less multiple scattering compared to in-zone electron diffraction patterns. Since 2009, the number of structures determined by electron diffraction has grown rapidly (Figure 1.7) [47, 51]. The increasing attention on 3D ED is confirmed by the fact that it has been considered one of the main scientific breakthroughs of the year 2018 [57].

Crystals large enough for single-crystal X-ray diffraction experiments often need to be grown by adapted synthesis methods, which could potentially alter the local order [59]. The main advantage of 3D ED is that it allows to determine the crystal structure of materials for which no crystals large enough for single-crystal X-ray diffraction are available [42].

In 3D ED, two-dimensional electron diffraction patterns are acquired while the crystal is tilted around the goniometer axis of the TEM stage (Figure 1.8). The angular range is limited by the presence of the objective lens pole pieces, and depends on the sample holder. The tomography holder used in this thesis, for example, has a tilt range of  $\pm 80^\circ$ . The acquired electron diffraction patterns are used to reconstruct the three-dimensional reciprocal lattice from which the unit cell parameters can be determined. The positions and intensities of the reciprocal lattice points can be used for structure solution and refinement [42].

The term 3D ED was introduced in 2019 by Gemmi and co-workers [42] and is

### 1.3. ACQUISITION OF DIFFUSE ELECTRON SCATTERING DATA

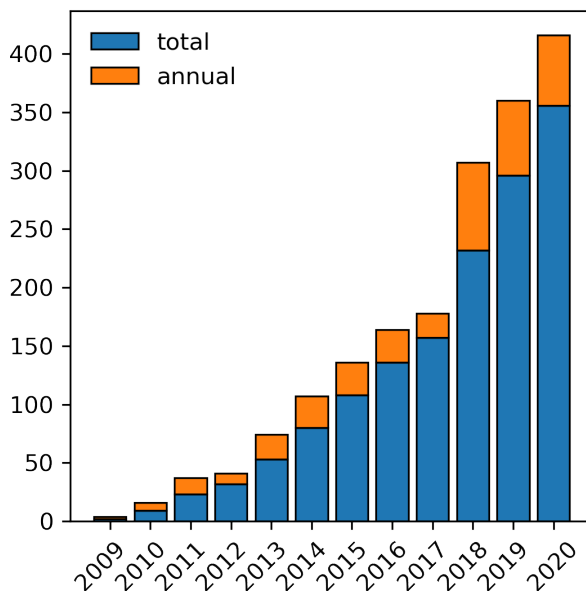


Figure 1.7: Total and annual number of structures solved by 3D ED. Figure made from data provided in the Supplementary Information of [58].

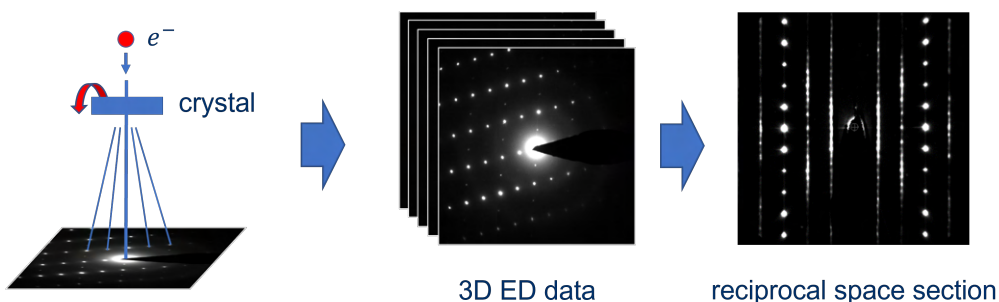


Figure 1.8: Schematics of the principle of 3D ED.

used as a unifying term for the data acquisition methods automated diffraction tomography (ADT [55, 56]), electron diffraction tomography (EDT [60]), rotation electron diffraction (RED [61, 62]), precession electron diffraction tomography (PEDT [63, 64]), microcrystal electron diffraction (MicroED [65]), integrated electron diffraction tomography (IEDT [66]) and continuous rotation electron diffraction (cRED [67, 68]) [49]. In ADT, EDT and RED the crystal is tilted with fixed angular steps and each step an electron diffraction pattern is acquired. In PEDT the electron diffraction patterns are acquired in precession mode while in MicroED, IEDT and cRED the electron diffraction patterns are collected while continuously rotating the crystal at a constant speed (analogous to X-ray and neutron diffraction [51]).

## CHAPTER 1. INTRODUCTION

The crystals analysed in 3D ED are usually smaller than 1  $\mu\text{m}$  and may move out from the illuminated area due to the mechanical instability of the goniometer, especially at high tilt angles. To guarantee that the crystal stays entirely illuminated during the whole data collection, the crystal position can be checked every few degrees and, if necessary, the crystal can be moved to stay in the beam [42]. This procedure can also be automated by compensating the sample drift through an equivalent shift of the electron beam, which is called crystal tracking [55].

When refining the average structure from single-crystal X-ray diffraction data using a standard least-squares refinement, it is assumed that the intensities of the Bragg reflections are proportional to the square of the absolute value of the structure factor (Equation 1.10). Because electrons are scattered multiple times while going through the crystal, this assumption is not valid for 3D ED data. A least-squares refinement in which the intensities are calculated using the dynamical theory of diffraction was developed by Palatinus and co-workers [69, 70, 71] and is implemented in *JANA2020* [72]. The dynamical refinement in *JANA2020* requires 3D ED data collected with precession (PEDT), continuous rotation (MicroED, IEDT or cRED) or stepwise 3D ED data acquired with a tilt step  $\leq 0.1^\circ$  (ADT, EDT, RED) [51], and processed using the program *PETS2* [73].

### 1.4 Calculation of the diffuse scattering

In the kinematic approximation, the intensity of the diffuse scattering and the Bragg reflections is proportional to the square of the absolute value of the structure factor (Equation 1.10). This equation is also used to calculate the diffuse scattering from a model crystal with short-range order. The structure factor  $F(\mathbf{Q})$  in Equation 1.11 then needs to be calculated for each reciprocal lattice point  $hkl$  within the plane or volume of interest. The structure factor can be calculated explicitly from the atomic coordinates  $x_j$   $y_j$   $z_j$  and the atomic form factors  $f_j(\mathbf{Q})$  of the atoms in the model crystal. This method is called the **discrete Fourier transform** (DFT). An alternative approach for the calculation of the structure factor is to use a **fast Fourier transform** (FFT) algorithm [74, 75], which accelerates the calculation of the diffuse scattering by two or three orders of magnitude. The FFT algorithm requires sampling atomic positions on an equally spaced grid and is exact for systems in which the disorder is occupational, magnetic, or in which atomic displacements are drawn from a discrete set of values. For systems in which the atomic displacements can take a continuous range of values, the FFT can only be applied to a specified order of approximation [53].

Because the simulation of a model crystal with short-range order is computationally very demanding, the model crystal usually contains far fewer unit cells ( $10^4$ ) than the real crystal ( $10^{23}$ ), which introduces high-frequency noise in the calculated diffuse scattering. High-frequency noise occurs because the calculated diffuse scattering is



## 1.5. REFINEMENT OF THE SHORT-RANGE ORDER

dominated by many essentially uncorrelated atom pairs that are large distances apart [53]. One approach to reduce this high-frequency noise, is to divide the model crystal into a set of smaller overlapping regions, called **lots**, and to average the diffuse scattering from these lots [76, 77]. If each lot has a size of  $n_{lot} \times n_{lot} \times n_{lot}$  unit cells, then  $n_{lot}$  should be larger than the correlation length of the longest correlations, but smaller than or equal to  $n_{crystal}/2$ , to avoid contributions from periodic images of the crystal [53]. The lots should be randomly distributed within the crystal, and the number of lots should be chosen so that each atom is included at least once [78]. This approach is effective at reducing high-frequency noise but has the disadvantage that the diffuse scattering is artificially blurred. An alternative approach to reduce the high-frequency noise, is to use **Lanczos resampling** [79, 80]. Lanczos resampling has the advantage that the calculated diffuse scattering is less blurry than the diffuse scattering calculated using the lots approach. Another method that is frequently used to reduce noise in the calculated diffuse scattering, is to average the diffuse scattering intensities from many individual crystals [37].

Many different programs exist that allow diffuse scattering calculations. The programs used in this thesis are *DISCUS* [77] and *Scatty* [53]. Both programs allow the user to choose between the DFT and the FFT approach for the calculation of the diffuse scattering. *Scatty* uses Lanczos resampling to reduce the high-frequency noise while *DISCUS* uses lots in the DFT approach and Lanczos resampling in the FFT approach.

For the calculation of the structure factor in *DISCUS* with the DFT method, the finite size of the model crystal gives rise to additional, unwanted intensities in the calculated diffraction pattern. To avoid these finite size effects, the number of grid points (*pixels*) along a certain direction in reciprocal space should be chosen according to [37]:

$$pixels = m \cdot length \cdot n_{crystal} + 1. \quad (1.14)$$

With  $m \in \mathbb{N}_0$ , *length* the length of the reciprocal space segment and  $n_{crystal}$  the number of unit cells along the corresponding direction in real space.

### 1.5 Refinement of the short-range order

Structure solution and refinement are used to solve and refine the average structure of crystalline materials from the intensities of the Bragg reflections. Parameters that are most commonly refined are the average atomic positions, site occupancies and atomic displacement parameters (atomic displacement parameters take into account the collective vibration of atoms about their average positions). However, for many materials, the local structure differs significantly from the average structure. When the deviations from the average structure are ordered on a local scale, they are referred to as local order or short-range order. Materials with short-range order have diffraction patterns that contain both Bragg reflections and diffuse scattering. Because the properties

## CHAPTER 1. INTRODUCTION

of many materials depend on the short-range order, refining short-range order parameters is essential for understanding and optimizing material properties.

In most studies on the diffuse scattering in single-crystal electron diffraction data, the diffuse scattering in experimental data is qualitatively compared with the diffuse scattering in calculated data [81, 82, 83, 84, 85, 86, 87, 88]. The development of 3D ED in 2007 [55, 56] allowed the acquisition of three-dimensional electron diffuse scattering data with less multiple scattering compared to in-zone electron diffraction patterns. A quantitative analysis of the diffuse scattering in 3D ED data has only been reported by Krysiak and co-authors in the case of one-dimensional diffuse scattering [89, 90]. The authors employed a fitting procedure to a series of simulated data to determine the number of stacking faults in two zeolites.

Unlike the refinement of the average crystal structure, there is no general approach to refine short-range order parameters from single-crystal diffuse scattering data. Over the last decades, three approaches have been developed: the Monte Carlo refinement, the Reverse Monte Carlo refinement and the 3D- $\Delta$ PDF refinement, which will be explained below.

In this thesis, we used a Monte Carlo refinement to refine the short-range order parameters in  $\text{Li}_{1.2}\text{Ni}_{0.13}\text{Mn}_{0.54}\text{Co}_{0.13}\text{O}_2$  (Chapter 2). The short-range order parameters in  $\text{Nb}_{0.84}\text{CoSb}$  were refined using both a Monte Carlo refinement and a 3D- $\Delta$ PDF refinement (Chapter 3).

### 1.5.1 Monte Carlo refinement

The Monte Carlo method is based on the Metropolis algorithm [91] and requires the construction of a model crystal with short-range order. Information on the type of short-range order can be obtained from the diffuse scattering itself (one-, two- or three-dimensional), the interpretation of the features in the 3D- $\Delta$ PDF, the average structure refinement (refined occupancies, displacements and atomic displacement parameters), high-resolution scanning transmission electron microscopy (HR-STEM) images and other prior knowledge.

Monte Carlo simulations are used to create a model of the short-range order. The total energy of the crystal is expressed as a function of short-range order parameters such as the interactions between neighbouring atoms or the displacement of atoms from their average positions. During the Monte Carlo simulation, the desired short-range order parameters are obtained by minimizing the total energy of the crystal. Each refinement cycle, the short-range order parameters are adjusted, and the model crystal is recalculated. The diffuse scattering is calculated and compared with the observed diffuse scattering. This process is repeated until the best agreement between calculated and

## 1.5. REFINEMENT OF THE SHORT-RANGE ORDER

observed diffuse scattering intensities is obtained [92, 4].

The Monte Carlo method allows the accurate refinement of short-range order parameters from the intensity distribution of the diffuse scattering in single-crystal diffraction data (see [93, 25, 4, 94] for some examples). The disadvantage, however, is that Monte Carlo refinements are computationally very slow since each refinement cycle requires the full construction of the disordered structure and the calculation of the corresponding diffuse scattering.

The short-range order parameters can be adjusted by using a least-squares refinement algorithm [95] or a differential evolutionary refinement algorithm [78]. Both algorithms are implemented in *DISCUS*.

### 1.5.1.1 Least-squares refinement

One approach to obtain the short-range order parameters that best describe the experimentally observed diffuse scattering intensity is to use a least-squares algorithm [95].

Each refinement cycle, the short-range order parameters are adjusted and the model crystal is recalculated. This process is repeated for a certain number of refinement cycles until the goodness-of-fit parameter  $\chi^2$  converges to its minimum [95].

$$\chi^2 = \sum_{i=1}^N \frac{[I_{\text{obs}}(\mathbf{Q}_i) - I_{\text{calc}}(\mathbf{Q}_i)]^2}{I_{\text{obs}}(\mathbf{Q}_i)} \quad (1.15)$$

The sum is over all measured reciprocal lattice points  $\mathbf{Q}_i$ ,  $I_{\text{obs}}$  and  $I_{\text{calc}}$  are the experimental and calculated diffuse scattering intensities.

Each refinement cycle, the short-range order parameters  $\mathbf{p} = (p_1, p_2, p_3, \dots, p_j, \dots, p_n)$  are adjusted by a small amount  $\Delta p_j$  [95]:

$$\Delta p_j = \sum_{k=1}^n A_{jk}^{-1} B_k \quad (1.16)$$

With  $n$  the number of short-range order parameters. The least-squares matrix  $\mathbf{A}$  and the vector  $\mathbf{B}$  contain the partial derivatives of  $\Delta I = I_{\text{obs}}(\mathbf{Q}_i) - I_{\text{calc}}(\mathbf{Q}_i)$  with respect to each of the short-range order parameters  $p_j$  [95].

$$A_{jk} = \sum_{i=1}^N \frac{1}{I_{\text{obs}}(\mathbf{Q}_i)} \frac{\partial \Delta I}{\partial p_j} \frac{\partial \Delta I}{\partial p_k} \quad (1.17)$$

$$B_k = - \sum_{i=1}^N \frac{1}{I_{\text{obs}}(\mathbf{Q}_i)} \Delta I_{\text{trial}} \frac{\partial \Delta I}{\partial p_k} \quad (1.18)$$

## CHAPTER 1. INTRODUCTION

The model crystal is calculated for two sets of short-range order parameters  $\mathbf{p}^+ = (p_1, p_2, p_3, \dots, p_j + \delta_j, \dots, p_n)$  and  $\mathbf{p}^- = (p_1, p_2, p_3, \dots, p_j - \delta_j, \dots, p_n)$ .

The corresponding diffuse scattering is calculated and numerical estimates of the partial derivatives  $\partial\Delta I/\partial p_j$  are calculated as [95]:

$$\frac{\partial\Delta I}{\partial p_j} = \sum_{i=1}^N \frac{\Delta I_{p^+} - \Delta I_{p^-}}{2\delta_j} \quad (1.19)$$

The least-squares refinement has been successfully applied for the refinement of short-range order parameters in [95, 93, 96, 97]. However, when the initial short-range order parameters are not sufficiently close to the global minimum, the refinement may converge to a local minimum. To overcome this problem, several sets of initial short-range order parameters should be tested [78]. An alternative approach is to use a differential evolutionary algorithm, as will be discussed in the next section.

### 1.5.1.2 Differential evolutionary refinement

For the refinements in this thesis, the differential evolutionary algorithm [98] in *DISCUS* was used to find the short-range order parameters that best describe the experimentally observed diffuse scattering. The advantage is that the probability to get stuck in a local minimum is lower than for a least-squares refinement. The disadvantage is that a differential evolutionary refinement is slower than a least-squares refinement [37].

The differential evolutionary algorithm mimics the changes in a plant or animal population similar to the Darwinian principle of natural evolution. The algorithm starts with a group of  $M$  members (parents). Each member represents a set of  $N$  short-range order parameters. Next, the algorithm creates a new group of  $M$  members (children) by adjusting the short-range order parameters of their parents. The parents and the children with the lowest R-values (Equation 1.20) survive and will be the parents of the new generation (survival of the fittest). This procedure is repeated for a number of refinement cycles (generations) until the R-value converges to its minimum [37].

$$R_w = \sqrt{\frac{\sum_i w_i [I_{\text{obs}}(\mathbf{Q}_i) - I_{\text{calc}}(\mathbf{Q}_i)]^2}{\sum_i w_i [I_{\text{obs}}(\mathbf{Q}_i)]^2}} \quad (1.20)$$

The sum is over all measured reciprocal lattice points  $\mathbf{Q}_i$ ,  $I_{\text{obs}}$  and  $I_{\text{calc}}$  are the observed and calculated diffuse scattering intensities. The weights  $w_i$  assign an appropriate statistical weight to each data point  $i$ . A schematic diagram of the differential evolutionary algorithm for  $M = 3$  and  $N = 2$  is shown in Figure 1.9.

The process by which new children are generated is illustrated in Figure 1.10 for

### 1.5. REFINEMENT OF THE SHORT-RANGE ORDER

$N = 2$ . For each parent P, the algorithm starts by choosing three random members I, II and III. The difference vector  $\mathbf{v}$  between the members I and II is multiplied by a scale factor  $f$  and added to member III. The resulting point in parameter space is called the donor D. By random choice, short-range order parameters are taken either from the donor D or from the parent P. To ensure that the parent P is not replicated, one parameter is always taken from the donor D. The probability by which the other short-range order parameters are taken from the donor D is called the cross-over probability. If both parameters are taken from the donor D, the child is the donor D itself. If the parameter  $p_1$  is taken from the donor D and the parameter  $p_2$  taken from the parent P, the child will be the position labelled (D,P). Alternatively, if the parameter  $p_1$  is taken from the parent P and the parameter  $p_2$  is taken from the donor D, the child will be the position labelled (P,D). To prevent convergence into a local minimum instead of the global minimum, the number of children should be chosen equal to the number of parents  $M$ , and both should be chosen at least 10 times the number of refined short-range order parameters [37]. The optimal values for the cross-over probability and the scale factor were determined by [99] and are respectively 0.9 and 0.81.

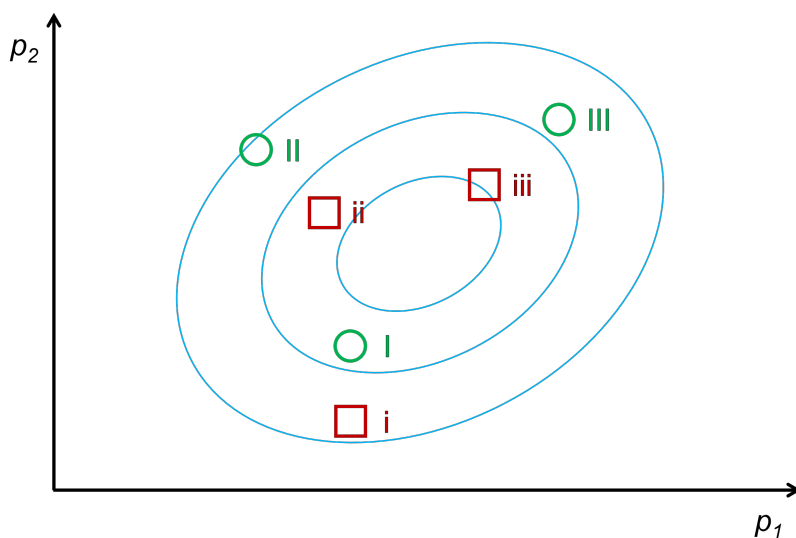


Figure 1.9: Schematic diagram of the differential evolutionary algorithm in two-dimensional parameter space. The parents I, II, and III generate the children i, ii, and iii by modification of the short-range order parameters  $p_1$  and  $p_2$ . The children ii and iii and the parent I have the lowest R values and will thus be the parents of the new generation. The lines of equal R values are shown in blue [37].

The differential evolutionary algorithm in *DISCUS* has been successfully applied for the refinement of short-range order parameters from powder X-ray diffraction data [100, 101, 102, 103, 104, 105, 106]. The possibility to apply the differential evolutionary algorithm on the diffuse scattering in single-crystal X-ray diffraction data has been

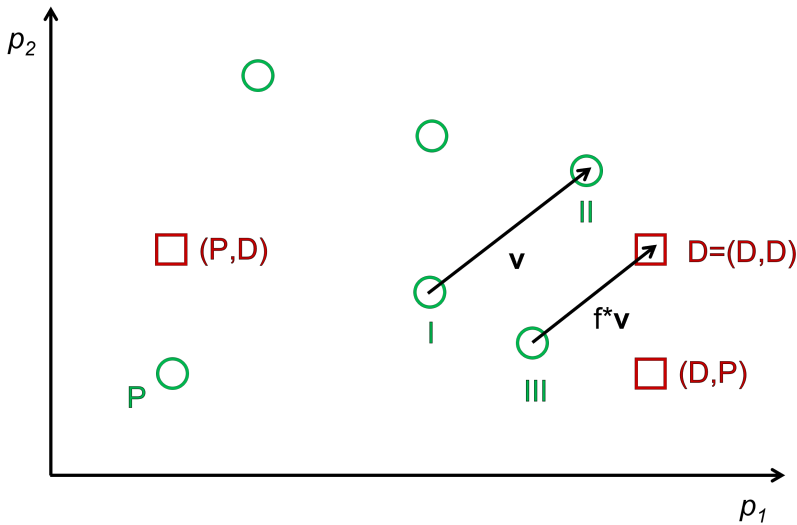


Figure 1.10: Schematic diagram of the differential evolutionary algorithm in two-dimensional parameter space. The members of the current generation are shown as circles. The possible children of the parent P are shown as squares.

demonstrated by Weber and Bürgi [78]. Seven short-range order parameters were refined: three pair interaction energies  $J_a$ ,  $J_b$  and  $J_c$ , three spring force constants  $k_a$ ,  $k_b$  and  $k_c$  and one displacement  $d$  from the average position. The refinement resulted in a good visual agreement between observed and calculated diffuse scattering intensities and in a relatively low value of  $R = 0.148(3)$ . However, due to the relatively large number of parameters, the refinement took 29 days for 220 generations with ten processors running in parallel. The differential evolutionary algorithm used in this thesis is a modified version of the original algorithm used by Weber and Bürgi.

### 1.5.2 Reverse Monte Carlo refinement

The Reverse Monte Carlo method was developed by McGreevy and Pusztai in 1988 [107]. The Reverse Monte Carlo method can be used when the origin of the diffuse scattering is unknown since it does not require to build a model of the short-range order. One can for example start from the average crystal structure. Each Reverse Monte Carlo step, the occupancy or displacement of a randomly selected atom is changed by some random amount. After each Reverse Monte Carlo step, the diffuse scattering is calculated and compared with the experimentally observed diffuse scattering [92, 4]. Every move which improves the fit to the data is accepted. The moves which worsen the fit are accepted with a probability  $P = \exp(-\Delta\chi^2/2)$ . The refinement is repeated until the goodness-of-fit parameter  $\chi^2$  (Equation 1.21) converges to its minimum (i.e., until the best agreement

## 1.5. REFINEMENT OF THE SHORT-RANGE ORDER

between calculated and observed diffuse scattering intensities is obtained) [92, 37, 4].

$$\chi^2 = \sum_{i=1}^N \frac{[I_{\text{obs}}(\mathbf{Q}_i) - I_{\text{calc}}(\mathbf{Q}_i)]^2}{\sigma^2} \quad (1.21)$$

The sum is over all measured data points  $\mathbf{Q}_i$ ,  $I_{\text{obs}}$  stands for the experimentally observed intensity and  $I_{\text{calc}}$  for the calculated intensity. The parameter  $\sigma$  controls the fraction of ‘bad’ moves that are accepted. A successful Reverse Monte Carlo refinement requires careful selection of constraints to end up with a chemically and physically sensible structure model [37].

Reverse Monte Carlo refinements are much faster than direct Monte Carlo refinements. The disadvantage, however, is that Reverse Monte Carlo refinements do not allow the refinement of short-range order parameters [92, 4]. The atomic positions and occupancies are randomly adjusted, and possible correlations should be calculated after the refinement (see [108, 109, 110, 111, 112, 113, 114, 115, 116, 117] for examples on single-crystal diffuse scattering).

Programs that allow Reverse Monte Carlo refinements from single-crystal diffuse scattering data are *DISCUS* and *rmc-discord* [117]. Both programs allow to calculate correlations for occupational, displacive and magnetic disorder from the refined model [37, 117].

### 1.5.3 Three-dimensional difference pair distribution function refinement

A different approach to refine short-range order parameters from single-crystal diffuse scattering data is the 3D- $\Delta$ PDF refinement, which is implemented in the program *Yell* [118].

The intensity of the diffuse scattering in *Yell* is calculated as the sum of signals from all atomic pairs in the crystal:

$$I(\mathbf{Q})_{\text{diff}} = \sum_{uvw} \sum_{mn} \left( p_{mn}^{uvw} \exp(-\mathbf{Q}^T \boldsymbol{\beta}_{mn}^{uvw} \mathbf{Q}) \exp[i\mathbf{Q} \cdot (\mathbf{r}_{mn}^{uvw} + \mathbf{u}_{mn}^{uvw})] \right. \\ \left. - c_m c_n \exp[-\mathbf{Q}^T (\boldsymbol{\beta}_m + \boldsymbol{\beta}_n) \mathbf{Q}] \exp[i\mathbf{Q} \cdot \mathbf{r}_{mn}^{uvw}] \right) f_m^*(\mathbf{Q}) f_n(\mathbf{Q}), \quad (1.22)$$

with  $\mathbf{r}_{mn}^{uvw}$  the vector between the average positions of atoms  $m$  and  $n$  that are  $(u, v, w)$  unit cells apart,  $c_m$  and  $c_n$  the average occupancies,  $\boldsymbol{\beta}_m$  and  $\boldsymbol{\beta}_n$  the matrices of the average atomic displacement parameters, and  $f_m(\mathbf{Q})$  and  $f_n(\mathbf{Q})$  the atomic form factors [39, 118].

*Yell* allows to refine three types of short-range order parameters: substitutional correlations  $p_{mn}^{uvw}$ , size-effect parameters  $\mathbf{u}_{mn}^{uvw}$  and atomic displacement correlations  $\boldsymbol{\beta}_{mn}^{uvw}$ . Substitutional correlations  $p_{mn}^{uvw}$  describe the probability of finding the atoms  $m$

## CHAPTER 1. INTRODUCTION

and  $n$  separated by the vector  $\mathbf{r}_{mn}^{uvw}$ . Size-effect parameters  $\mathbf{u}_{mn}^{uvw}$  quantify the difference between the real and the average interatomic vector between atoms  $m$  and  $n$ . Atomic displacement correlations  $\beta_{mn}^{uvw}$  describe correlations between the atomic displacement parameters [39, 118].

*Yell* provides the choice of two algorithms for calculating the diffuse scattering intensities from a disorder model [118]. One option is to use Equation 1.22, which is precise but very slow. As an alternative, *Yell* allows to calculate the three-dimensional diffuse scattering from the 3D- $\Delta$ PDF via a FFT algorithm.

The short-range order parameters are refined by using a least-squares refinement. Each refinement cycle, the short-range order parameters are adjusted and the R-value in Equation 1.20 [37] is calculated. This process is repeated until the R-value converges to its minimum. The short-range order parameters are refined against the three-dimensional diffuse scattering, and not against the 3D- $\Delta$ PDF, because experimental artefacts (e.g., due to saturated reflections) are more easily detected if refinements are done against the diffuse scattering [39].

3D- $\Delta$ PDF refinements are much faster than Monte Carlo and reverse Monte Carlo refinements since they do not require the construction of a model crystal. The disadvantage, however, is that 3D- $\Delta$ PDF refinements may result in non-physical structure models [119]. *Yell* is designed to be used on desktop computers and refinements can be performed within minutes or hours (in contrast, Monte Carlo refinements may take a few days or weeks) [118]. The refinement time is roughly proportional to  $N_{\text{pix}}N_{\text{pairs}}N_{\text{params}}$ , where  $N_{\text{pix}}$  is the number of pixels in the experimental diffuse scattering data,  $N_{\text{pairs}}$  is the number of interatomic pairs and  $N_{\text{params}}$  is the number of refined short-range order parameters. The number of interatomic pairs is proportional to the square of the number of atoms per chemical unit, which may grow quickly with the number of atoms in the unit cell [118]. 3D- $\Delta$ PDF refinements have been successfully applied on the diffuse scattering in single-crystal X-ray diffraction data [120, 121, 122, 123, 124, 125].



## One-dimensional diffuse scattering - $\text{Li}_{1.2}\text{Ni}_{0.13}\text{Mn}_{0.54}\text{Co}_{0.13}\text{O}_2$

---

*The results of this chapter were published in:*

- Poppe, R., Vandemeulebroucke, D., Neder, R. B., & Hadermann, J. (2022). Quantitative analysis of diffuse electron scattering in the lithium-ion battery cathode material  $\text{Li}_{1.2}\text{Ni}_{0.13}\text{Mn}_{0.54}\text{Co}_{0.13}\text{O}_2$ . *IUCrJ*, 9(5), 695-704.
- Quintelier, M., Perkisas, T., Poppe, R., Batuk, M., Hendrickx, M., & Hadermann, J. (2021). Determination of Spinel Content in Cycled  $\text{Li}_{1.2}\text{Ni}_{0.13}\text{Mn}_{0.54}\text{Co}_{0.13}\text{O}_2$  Using Three-Dimensional Electron Diffraction and Precession Electron Diffraction. *Symmetry*, 13(11), 1989.

The goal of this thesis is to verify the possibility to refine short-range order parameters from the diffuse scattering in single-crystal electron diffraction data. In this chapter, the approach will be demonstrated on  $\text{Li}_{1.2}\text{Ni}_{0.13}\text{Mn}_{0.54}\text{Co}_{0.13}\text{O}_2$ , which is a cathode material for lithium-ion batteries. Electron diffraction data acquired on  $\text{Li}_{1.2}\text{Ni}_{0.13}\text{Mn}_{0.54}\text{Co}_{0.13}\text{O}_2$  show one-dimensional diffuse streaks. The number of stacking faults and the twin percentages will be refined from the intensity profile of the diffuse streaks using a Monte Carlo refinement in *DISCUS*.

The effect of background subtraction, symmetry averaging and multiple scattering on the intensity profile of the diffuse streaks in three-dimensional electron diffraction (3D ED) data will also be discussed.

The commercialization of lithium-ion batteries with  $\text{Li}_{1.2}\text{Ni}_{0.13}\text{Mn}_{0.54}\text{Co}_{0.13}\text{O}_2$  as a cathode material is still hampered by a significant capacity and voltage decay on cycling. The capacity and voltage decay is mainly due to the transformation of the layered structure to a spinel structure. In this chapter, we will also describe a method to determine the spinel/layered phase ratio from the intensities of the Bragg reflections in 3D ED data.

## 2.1 Introduction

Li-rich Mn-rich layered oxides ( $Li_{1+x}M_{1-x}O_2$ , with  $M = Ni, Mn, Co$ ) are promising cathode materials for lithium-ion batteries due to their high specific capacity of more than  $250 \text{ mAh g}^{-1}$ . However, their commercialization is still hampered by a significant capacity and voltage decay on cycling [126, 127, 128, 129]. Where the contributions of transition metal ion migration and spinel domain formation to the capacity and voltage decay have been extensively studied [130, 131, 132, 133, 134], the contribution of the number of stacking faults has so far only been investigated in [135]. In lithium-ion battery cathode materials, stacking faults are formed during crystal growth but the number of stacking faults may change when recharging the battery. The authors of [135] refined the average number of stacking faults in  $Li_2MnO_3$  from the diffuse scattering in powder X-ray diffraction data using the program *FAULTS* [136] and found that the voltage decay is smaller for crystals with a larger number of stacking faults. However, further research is required to determine a possible correlation between the number of stacking faults and the voltage decay on cycling.

An alternative approach to determine a possible correlation between the number of stacking faults and the voltage decay on cycling would be to quantify the change in the number of stacking faults upon charging and discharging. This could be done by charging and discharging the powder sample in an electrochemical cell filled with a liquid electrolyte inside a transmission electron microscope, and by acquiring several 3D ED data sets at different stages during cycling [137]. The number of stacking faults could then later be refined from the intensity profile of the one-dimensional diffuse streaks in the reciprocal space sections reconstructed from these 3D ED data.

The first step towards this goal, however, is to accurately refine the number of stacking faults, which will be the scope of this chapter.

## 2.2 Experimental details

### 2.2.1 Synthesis

The  $Li_{1.2}Ni_{0.13}Mn_{0.54}Co_{0.13}O_2$  powder was prepared by a carbonate co-precipitation method followed by calcination. The details of the synthesis were published in [138].

### 2.2.2 Data acquisition

Samples were prepared by dispersing the powder in ethanol. A few droplets of the suspension were deposited on a copper grid covered with an amorphous carbon film.

## 2.3. DESCRIPTION OF THE DISORDER

In-zone selected area electron diffraction (SAED) patterns were acquired with an FEI Tecnai G2 electron microscope operated at 200 kV using an FEI Eagle 2k charge-coupled device (CCD) (2048 x 2048 pixels with 16-bit dynamic range). In-zone precession electron diffraction (PED) patterns were acquired with a precession angle of  $1^\circ$  using a DigiSTAR precession device from NanoMEGAS.

High-angle annular dark-field scanning transmission electron microscopy (HAADF-STEM) images and 3D ED data were acquired with an aberration-corrected cubed FEI Titan 80-300 electron microscope operated at 300 kV using a GATAN US1000XP CCD (4096 x 4096 pixels with 16-bit dynamic range). For the acquisition of the 3D ED data, the crystal was illuminated in SAED mode with an exposure time of 1 s per frame. Electron diffraction patterns were acquired with a Fischione tomography holder (tilt range of  $\pm 80^\circ$ ), in a stepwise manner (step size of  $0.2^\circ$ ), using an in-house developed script. Energy filtered 3D ED data were acquired with a Quantum 966 Gatan Image Filter, with a slit width of 10 eV. The crystals were entirely illuminated during the whole data collection.

### 2.2.3 Data processing

The *PETS2* software was used to process the 3D ED data. The reciprocal lattice of all 3D ED data was indexed with a monoclinic  $C2/m$  unit cell with cell parameters  $a = 4.9360(2)$  Å,  $b = 8.5479(3)$  Å,  $c = 5.0172(2)$  Å,  $\alpha = \gamma = 90^\circ$  and  $\beta = 109.017(3)^\circ$  [138]. No inversion symmetry was applied to the three-dimensional reciprocal lattice. The reciprocal space sections were reconstructed with a pixel size of  $0.007$  Å<sup>-1</sup> and a slab thickness of  $0.014$  Å<sup>-1</sup>. The background of the 3D ED data as well as the SAED patterns was subtracted using *PETS2*.

## 2.3 Description of the disorder

The crystal structure of  $\text{Li}_{1.2}\text{Ni}_{0.13}\text{Mn}_{0.54}\text{Co}_{0.13}\text{O}_2$  consists of alternating layers of oxygen atoms, layers of lithium atoms, and layers that contain both transition metal atoms and lithium atoms [see Figure 2.1 (a)]. The monoclinic  $C2/m$  unit cell [139, 140, 141] is indicated in black. The honeycomb ordering of the lithium-rich positions in the transition metal layers – also called honeycomb layers [142, 143, 144] – is shown in Figure 2.1 (b).

Figure 2.2 shows two HAADF-STEM images of  $\text{Li}_{1.2}\text{Ni}_{0.13}\text{Mn}_{0.54}\text{Co}_{0.13}\text{O}_2$ . The honeycomb ordering of the lithium-rich positions in the transition metal layers manifests itself as pairs of 0.14 nm separated bright dots with less bright dots in between. As the intensity of the atom columns in the HAADF-STEM images is proportional to the atomic number of the element ( $I \sim Z^2$ ), the bright dots correspond to atom columns of

CHAPTER 2. ONE-DIMENSIONAL DIFFUSE SCATTERING -  
 $\text{Li}_{1.2}\text{Ni}_{0.13}\text{Mn}_{0.54}\text{Co}_{0.13}\text{O}_2$

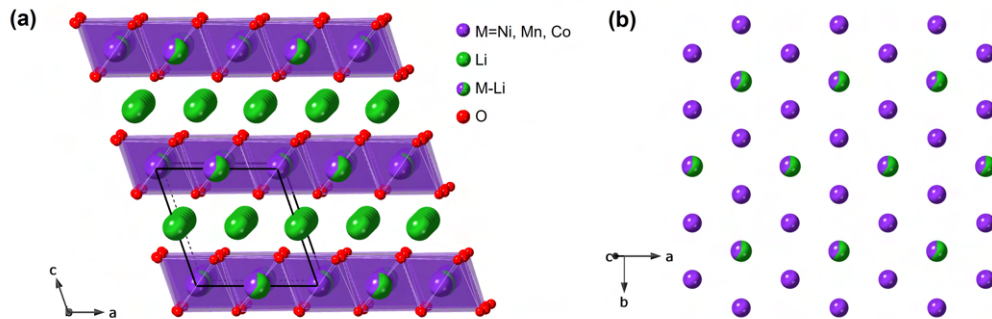


Figure 2.1: (a) Crystal structure of layered  $\text{Li}_{1.2}\text{Ni}_{0.13}\text{Mn}_{0.54}\text{Co}_{0.13}\text{O}_2$  seen along the [010] direction of the monoclinic  $C2/m$  unit cell (indicated in black). Purple octahedra represent  $\text{MO}_6$  octahedra, with  $M = \text{Ni}, \text{Mn}, \text{Co}$ . (b) Honeycomb ordering of the lithium-rich positions in the transition metal layers. Green, purple and red spheres represent lithium atoms, transition metal atoms, and oxygen atoms, respectively.

transition metal atoms, whereas the less bright dots correspond to atom columns that contain both lithium atoms and transition metal atoms. The atom columns that contain lithium atoms and oxygen atoms are too weak to be observed [138].

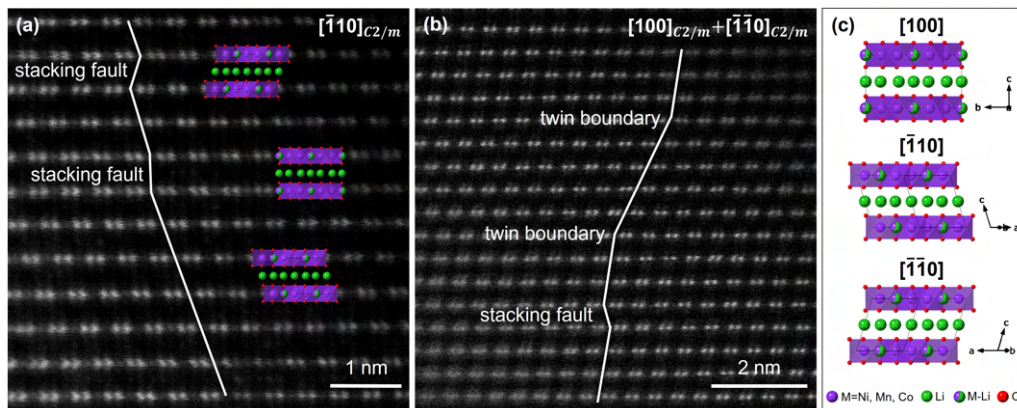


Figure 2.2: (a-b) HAADF-STEM images of  $\text{Li}_{1.2}\text{Ni}_{0.13}\text{Mn}_{0.54}\text{Co}_{0.13}\text{O}_2$ . The bright dots correspond to atom columns of transition metal atoms, whereas the less bright dots correspond to atom columns that contain both lithium atoms and transition metal atoms. The lines in (a) and (b) show the lateral displacements of the honeycomb layers. At the scale of a few unit cell repetitions, stacking faults and twin boundaries can be observed. (c) The two stacking faults indicated in (a) are equivalent to the  $C2/m$  unit cell seen along the [100] and  $[\bar{1}\bar{1}0]$  directions. Green, purple and red spheres represent lithium atoms, transition metal atoms, and oxygen atoms, respectively.

Figure 2.2(a) shows the HAADF-STEM image of a  $\text{Li}_{1.2}\text{Ni}_{0.13}\text{Mn}_{0.54}\text{Co}_{0.13}\text{O}_2$

### 2.3. DESCRIPTION OF THE DISORDER

crystal seen along the  $[\bar{1}10]$  direction of the monoclinic  $C2/m$  unit cell. In a crystal without stacking faults, all lithium-rich positions would lie in rows parallel to the  $c$  axis of the monoclinic  $C2/m$  unit cell. However, in reality, stacking faults occur due to lateral displacements of the honeycomb layers. If the stacking direction of adjacent layers is the same over several unit cells, but not over the whole crystal, then these adjacent layers will form twin domains. The difference between stacking faults and twin domains is clarified in the HAADF-STEM image in Figure 2.2 (b) in which the twin boundaries are indicated. In the following, we thus make a distinction between twin domains as groups of adjacent layers with the same stacking direction; and stacking faults as single layers with a different stacking direction.

The twin domains indicated in Figure 2.2 (b) are rotation twins with 3-fold twin axis  $[103]$  (the  $[103]$  direction in real space corresponds to the  $c^*$  direction in reciprocal space) [145]. The twin matrices for a rotation of respectively  $120^\circ$  and  $240^\circ$  around  $[103]$  are:

$$\begin{aligned} \mathbf{U}_{120^\circ} &= \begin{pmatrix} -1/2 & 3/2 & 1/2 \\ -1/2 & -1/2 & 1/6 \\ 0 & 0 & 1 \end{pmatrix}, \\ \mathbf{U}_{240^\circ} &= \begin{pmatrix} -1/2 & -3/2 & 1/2 \\ 1/2 & -1/2 & -1/6 \\ 0 & 0 & 1 \end{pmatrix}. \end{aligned} \quad (2.1)$$

Application of both twin matrices on the  $[100]$  zone axis results in the  $[\bar{1}10]$  and  $[\bar{1}\bar{1}0]$  zone axes. Figure 2.2 (c) illustrates that the two stacking faults indicated in Figure 2.2 (a) are equivalent to the  $C2/m$  unit cell seen along the  $[100]$  and  $[\bar{1}\bar{1}0]$  directions.

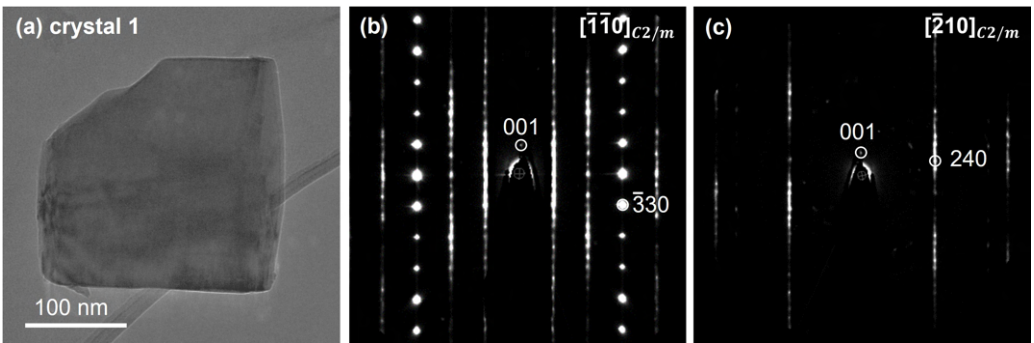


Figure 2.3: (a)  $\text{Li}_{1.2}\text{Ni}_{0.13}\text{Mn}_{0.54}\text{Co}_{0.13}\text{O}_2$  crystal. (b-c)  $[\bar{1}\bar{1}0]$  and  $[\bar{2}10]$  reciprocal space sections reconstructed from a 3D ED series acquired on the crystal in (a).

Figure 2.3 (a) shows an image of a single  $\text{Li}_{1.2}\text{Ni}_{0.13}\text{Mn}_{0.54}\text{Co}_{0.13}\text{O}_2$  crystal on which 3D ED data have been acquired (this crystal will further on be denoted as crystal 1). The reconstructed  $[\bar{1}\bar{1}0]$  and  $[\bar{2}10]$  reciprocal space sections are shown in Figure 2.3 (b-c). The diffuse streaks along the  $c^*$  direction are due to stacking faults

*CHAPTER 2. ONE-DIMENSIONAL DIFFUSE SCATTERING -  
LI<sub>1.2</sub>NI<sub>0.13</sub>MN<sub>0.54</sub>CO<sub>0.13</sub>O<sub>2</sub>*

whereas the intensity maxima along the diffuse streaks are due to rotation twins with 3-fold twin axis [103]. Figure 2.4 shows the effect of 3-fold rotation twinning on the [001], [010], [100], [ $\bar{1}10$ ] and [ $\bar{1}\bar{1}0$ ] reciprocal space sections. Rotation twinning with 3-fold twin axis [103] will cause overlap of the reflections in the [ $\bar{1}\bar{1}0$ ], [ $\bar{1}10$ ] and [100] reciprocal space sections.

### 2.3. DESCRIPTION OF THE DISORDER

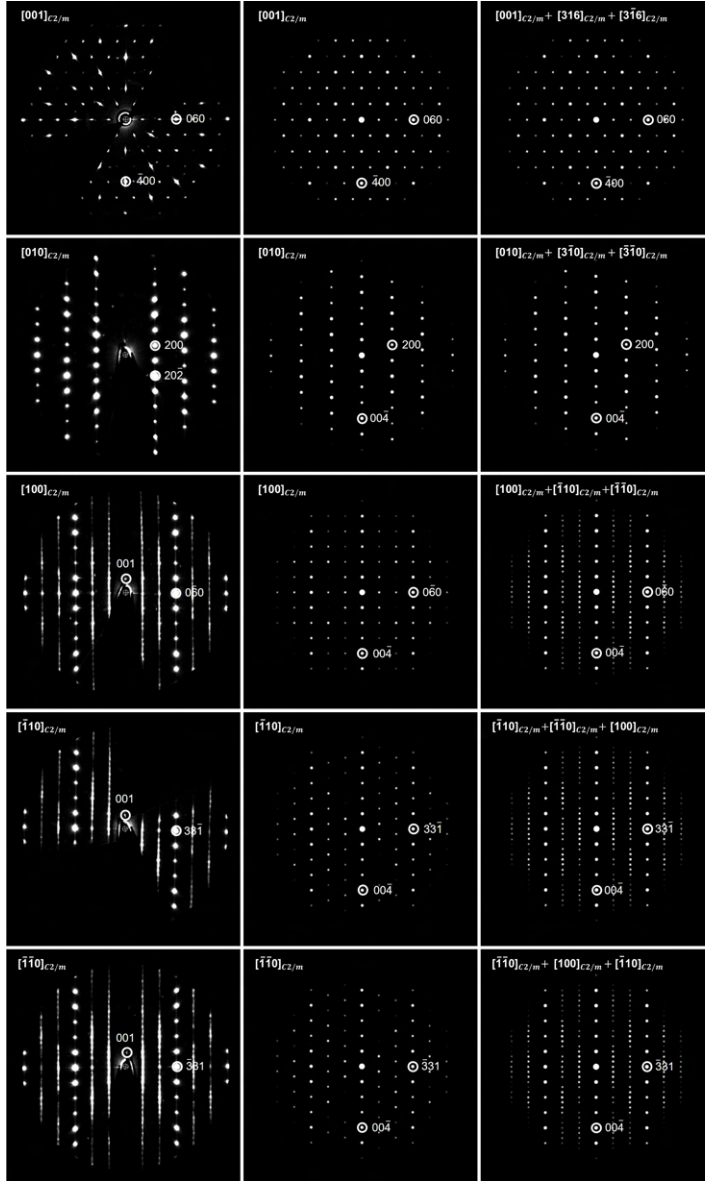


Figure 2.4: Column 1:  $[001]$ ,  $[010]$ ,  $[100]$ ,  $[\bar{1}\bar{1}0]$  and  $[\bar{1}\bar{1}\bar{0}]$  reciprocal space sections reconstructed from a 3D ED series acquired on  $\text{Li}_{1.2}\text{Ni}_{0.13}\text{Mn}_{0.54}\text{Co}_{0.13}\text{O}_2$  [crystal 1]. Column 2: calculated electron diffraction patterns for a crystal without twinning. Column 3: calculated electron diffraction patterns for a crystal with rotation twinning with 3-fold twin axis  $[103]$ . The intensity maxima along the diffuse streaks in column 1 are thus due to overlap of the reflections in the  $[\bar{1}\bar{1}\bar{0}]$ ,  $[\bar{1}\bar{1}0]$  and  $[100]$  reciprocal space sections. The electron diffraction patterns in column 2-3 were calculated in *SingleCrystal*.

## 2.4 Effect of different parameters on the observed diffuse scattering

### 2.4.1 Orientation of the grid in the sampleholder

To see if the orientation of the crystal in the sample holder affects the intensity profile of the diffuse streaks in the reciprocal space sections, three 3D ED series were acquired on the same crystal (denoted hereafter as crystal 2), with the same settings (beam size, intensity, exposure time), but with a different orientation of the grid in the sample holder.

Figure 2.5 (a-c) and Figure 2.5 (e-g) show respectively the  $[2\bar{1}0]$  and the  $[\bar{1}\bar{1}0]$  reciprocal space section reconstructed from series 1, 2 and 3. For series 2, the grid was rotated  $45^\circ$  clockwise compared with series 1. For series 3, the grid was rotated  $90^\circ$  clockwise compared with series 1. The intensity profiles of the diffuse streaks indicated in Figure 2.5 (a-c) and Figure 2.5 (e-g) are shown in respectively Figure 2.5 (d) and Figure 2.5 (h). When comparing the green, pink and blue curves, it becomes clear that the intensity profile of the diffuse streaks is different for series 1, 2 and 3. Since all three 3D ED series were acquired with exactly the same settings, this implies that the orientation of the crystal in the sample holder affects the intensity profile of the diffuse streaks.

From the dynamical theory of diffraction, we know that the reflection intensities depend on the orientation and thickness of the crystal [70]. Since we acquired data on a rod-shaped crystal, the crystal thickness may change during the collection of the 3D ED series, depending on the rotation axis. The rotation axes corresponding to series 1, 2 and 3 are indicated in Figure 2.5 (i). For series 1 the crystal thickness is larger at high tilt angles than at low tilt angles ( $\pm 340$  nm vs.  $\pm 175$  nm). For series 3 the crystal thickness stays approximately the same during the whole tilt series ( $\pm 175$  nm). Consequently, the amount of multiple scattering will be larger for series 1 than for series 2 and 3, which might explain the differences in the intensity profile of the diffuse streaks of series 1, 2 and 3.

The reciprocal space sections in Figure 2.3, Figure 2.4 and Figure 2.5 were reconstructed without frame scaling (frame intensity scale equal to 1 for all frames) because the frame scales calculated by *PETS2* are less reliable for low-symmetry crystal systems. To calculate the frame scales, *PETS2* matches the intensities of symmetry equivalent reflections. The presence of rotation twins with 3-fold twin axis  $[103]$  reduces the Laue class from  $2/m$  to  $-1$ . For Laue class  $-1$ , the only symmetry equivalent reflections are on the same frames or on the immediately neighbouring frames, making the frame scaling less reliable.



## 2.4. EFFECT OF DIFFERENT PARAMETERS ON THE OBSERVED DIFFUSE SCATTERING

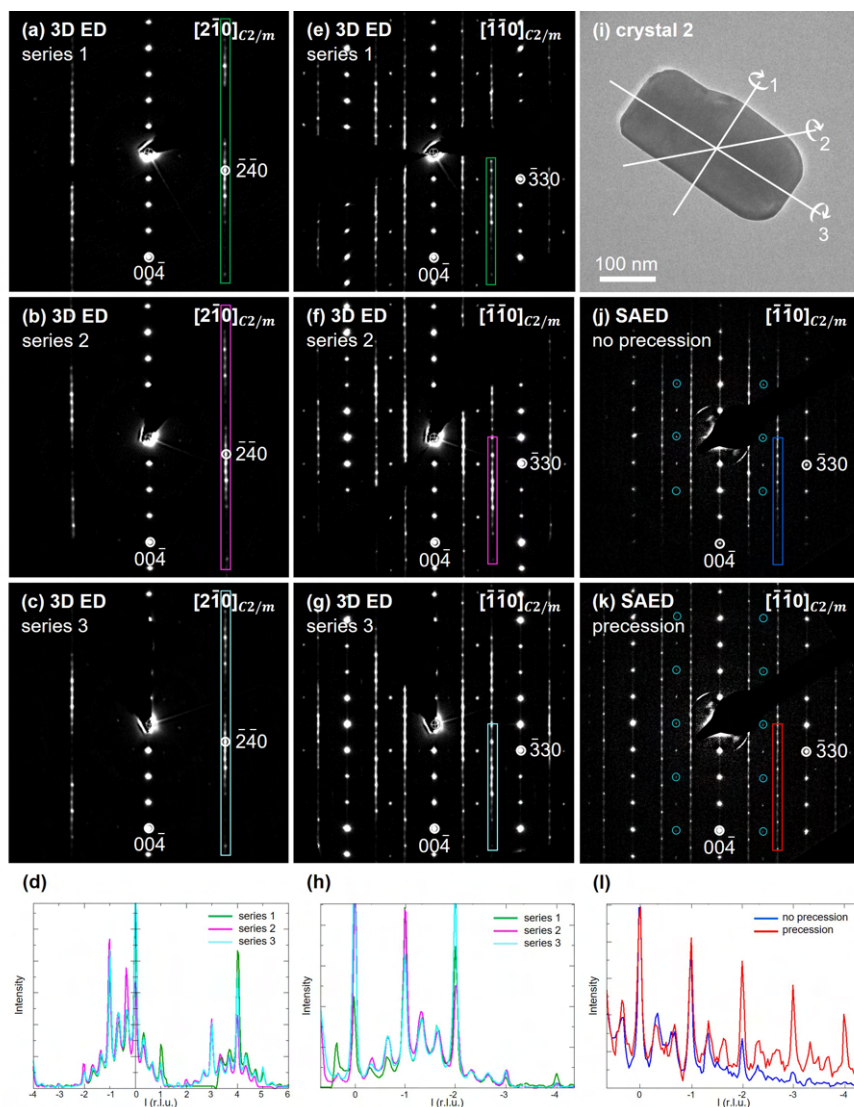


Figure 2.5: **(a-c, e-g)**  $[2\bar{1}0]$  and  $[\bar{1}\bar{1}0]$  reciprocal space sections reconstructed from three 3D ED series acquired on the same crystal, but with the grid rotated over  $45^\circ$  (series 2) and  $90^\circ$  (series 3) clockwise compared with series 1. **(d, h)** The intensity profiles of the diffuse streaks indicated in (a-c) and in (e-g). **(i)**  $\text{Li}_{1.2}\text{Ni}_{0.13}\text{Mn}_{0.54}\text{Co}_{0.13}\text{O}_2$  crystal on which all 3D ED series and SAED patterns have been acquired. The rotation axes corresponding to series 1, 2 and 3 are indicated. **(j)**  $[\bar{1}\bar{1}0]$  SAED pattern, which corresponds to the same orientation as the reciprocal space sections in (e-g). **(k)** The same in-zone SAED pattern but acquired with a precession angle of  $1^\circ$ . The reflections circled in blue in (j-k) are due to multiple scattering. **(l)** The intensity profile of the diffuse streaks indicated in (j-k).

### 2.4.2 In-zone electron diffraction

3D ED allows the acquisition of three-dimensional electron diffuse scattering data with less multiple scattering compared to in-zone SAED patterns. To compare the difference between reciprocal space sections reconstructed from 3D ED data and in-zone SAED patterns, the 3D ED data and in-zone SAED patterns in Figure 2.5 were acquired on the same crystal. Figure 2.5 (j) shows the  $[\bar{1}\bar{1}0]$  SAED pattern, which corresponds to the same orientation as the reciprocal space sections in Figure 2.5 (e-g). Figure 2.5 (k) shows the same SAED pattern but acquired with a precession angle of  $1^\circ$ . The intensity profile of the diffuse streaks indicated in Figure 2.5 (j-k) is shown in Figure 2.5 (l).

The increase in intensity between  $l = -1$  and  $l = -2$  in the intensity profile of the diffuse streaks in the reciprocal space sections reconstructed from 3D ED [Figure 2.5 (h)] is not visible in the intensity profile of the diffuse streak in the SAED pattern [Figure 2.5 (l)]. Because reciprocal space sections are reconstructed from a set of off-zone electron diffraction patterns, they exhibit less multiple scattering compared to in-zone SAED patterns. The intensity distribution of the diffuse streaks in the in-zone PED pattern is very similar to the one in in-zone SAED pattern (Figure 2.5 (j-k)). The main difference is that the higher-order Bragg reflections have higher intensities in the in-zone PED pattern than in the in-zone SAED pattern. Comparing the in-zone PED pattern with the reciprocal space sections reconstructed from 3D ED data acquired on the same crystal shows that several reflections in the PED pattern are solely due to multiple scattering (reflections indicated by the blue circles). Bragg reflections are distinct points, whereas diffuse scattering is continuously distributed in reciprocal space. An in-zone PED pattern is obtained by integrating the intensities within a volume in reciprocal space (determined by the precession angle). Higher precession angles will thus decrease the spatial resolution of the observed diffuse scattering.

### 2.4.3 Background subtraction

For the 3D ED data in Figure 2.5, the background of the individual frames has been subtracted in *PETS2* before the reconstruction of the reciprocal space sections. The background of the in-zone SAED pattern and in-zone PED pattern in Figure 2.5 has also been subtracted in *PETS2*.

The background in electron diffraction data is due to inelastic scattering of the incoming electrons (thermal diffuse scattering), electrons scattered by the amorphous carbon film, and sensor intrinsic background noise of the CCD. Thermal diffuse scattering can be subtracted using an energy filter. Figure 2.6 shows the  $[100]$  reciprocal space section reconstructed from 3D ED data acquired with and without energy filter on the same crystal (crystal 2). The energy filter blocks inelastically scattered electrons with an energy loss of more than 10 eV. Except for using an energy filter, the

## 2.4. EFFECT OF DIFFERENT PARAMETERS ON THE OBSERVED DIFFUSE SCATTERING

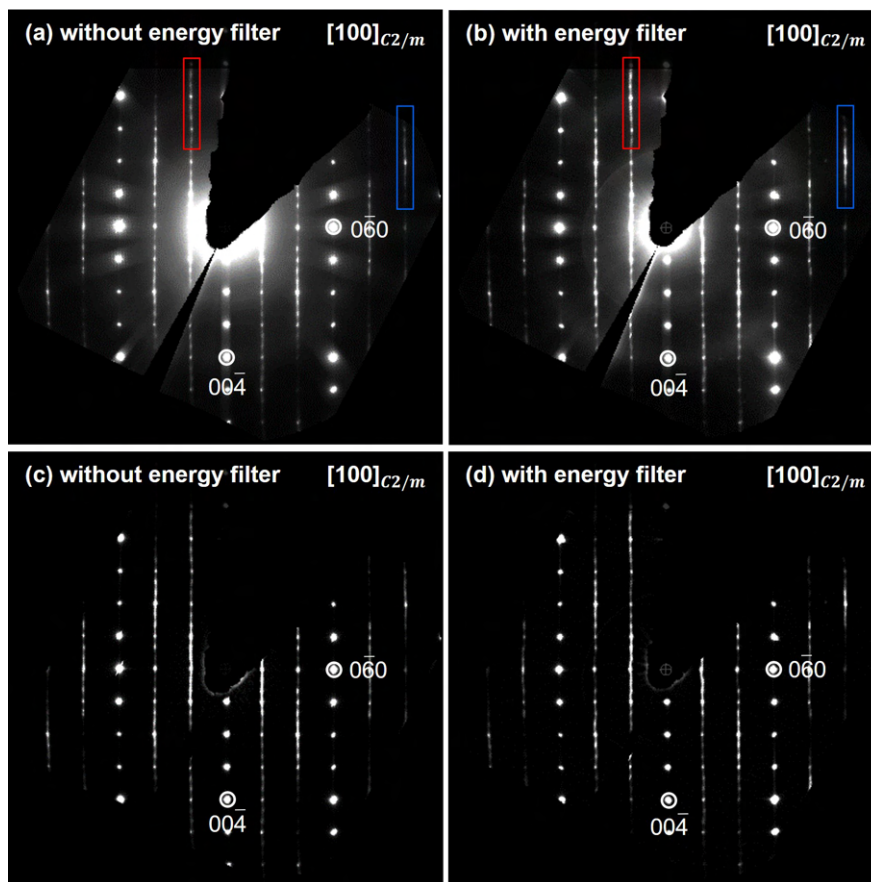


Figure 2.6: Comparison of the  $[100]$  reciprocal space section reconstructed from 3D ED data acquired with and without energy filter, before and after background subtraction in *PETS2*. Data acquired on  $\text{Li}_{1.2}\text{Ni}_{0.13}\text{Mn}_{0.54}\text{Co}_{0.13}\text{O}_2$  [crystal 2].

experimental settings were identical for both 3D ED data sets. The  $[100]$  reciprocal space section reconstructed from 3D ED data acquired without energy filter shows strong diffuse intensity bands (Figure 2.6 (a)). The diffuse intensity bands are weaker in the  $[100]$  reciprocal space section reconstructed from 3D ED data acquired with energy filter but can still be observed (Figure 2.6 (b)). An energy filter with a slit width of 10 eV reduces the thermal diffuse scattering but does not entirely remove it. The  $[100]$  reciprocal space sections after background subtraction in *PETS2* are shown in Figure 2.6 (c-d). After background subtraction in *PETS2*, the  $[100]$  reciprocal space section looks similar for the energy-filtered and non-energy filtered data. The experimental background and the thermal diffuse scattering are subtracted, while the elastic diffuse scattering remains. Subtracting the background of the individual frames in *PETS2* before the reconstruction of the three-dimensional reciprocal lattice is thus the best method to obtain diffuse scattering data that can be used for quantitative analysis.

Another way to estimate the background would be to repeat the 3D ED data acquisition under the same conditions but without the crystal illuminated by the electron beam. In the case of one-dimensional or two-dimensional diffuse scattering, the background intensity could also be estimated from the intensities of the surrounding voxels. However, both methods do not subtract the thermal diffuse scattering, and would thus require energy-filtered 3D ED data.

Another difference between Figure 2.6(a) and Figure 2.6(b) are intensity differences in the intensity profile of the diffuse streaks. The diffuse streaks indicated in blue and red are more intense for the data acquired with energy filter. However, because of the asymmetry in the intensities in Figure 2.6(b), these intensity differences are more likely due to small deviations in the orientations of the individual frames than due to the use of the energy filter. The orientations of the individual frames could not be optimized in *PETS2* due to the diffuse streaks. Several effects (the limited accuracy of the goniometer of the TEM stage, the inaccuracy of the orientation matrix or small unpredictable movements of the crystal under the electron beam) may cause the orientation of a frame as calculated from the orientation matrix to be inaccurate [71].

#### 2.4.4 Symmetry averaging

The volume percentages of the three different twins are not identical. The Laue class of the average crystal structure ( $2/m$ ) can thus not be applied to the diffuse scattering. The highest symmetry that can be applied to the diffuse scattering is inversion symmetry (Laue class  $-I$ ). Figure 2.7 shows the  $[\bar{1}\bar{1}0]$  and  $[\bar{2}10]$  reciprocal space sections in Figure 2.3, before and after applying inversion symmetry. Applying inversion symmetry does not allow to fill the missing wedge in the three-dimensional reciprocal lattice. Because full reciprocal space coverage is required for the calculation of the three-dimensional difference pair distribution function (3D- $\Delta$ PDF), the 3D- $\Delta$ PDF could not be reconstructed. A solution could be to increase the data completeness by combining data sets from several crystals, or combining several data sets from the same crystal acquired with a different orientation of the grid in the sample holder.

## 2.4. EFFECT OF DIFFERENT PARAMETERS ON THE OBSERVED DIFFUSE SCATTERING

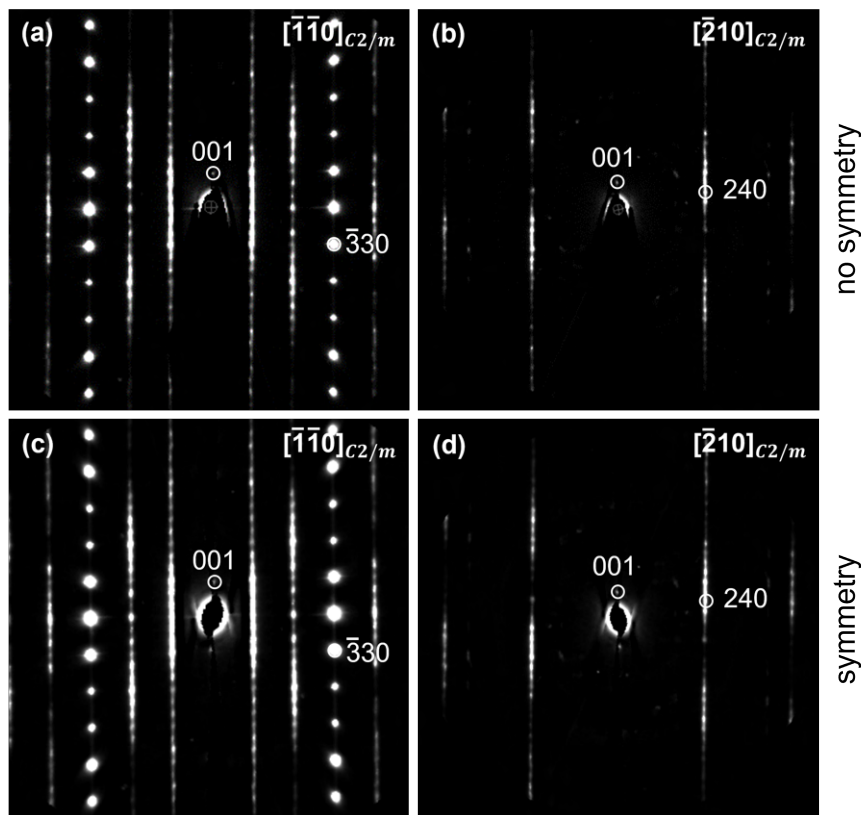


Figure 2.7: Comparison of the  $[\bar{1}\bar{1}0]$  and  $[\bar{2}10]$  reciprocal space sections reconstructed from 3D ED data, before and after applying inversion symmetry. Data acquired on  $\text{Li}_{1.2}\text{Ni}_{0.13}\text{Mn}_{0.54}\text{Co}_{0.13}\text{O}_2$  [crystal 1].

### 2.4.5 Different types of twinning

The reflections between the diffuse streaks in the  $[\bar{1}\bar{1}0]$  reciprocal space sections of crystal 2 in Figure 2.5 (e-g) are not present in the  $[\bar{1}\bar{1}0]$  reciprocal space section of crystal 1 in Figure 2.3. At first glance, these additional reflections could be due to the presence of the spinel phase [146]. However, careful inspection of the 3D reciprocal lattice shows that they are due to rotation twins with 4-fold twin axis  $[323]$  (a rotation about  $90^\circ$  around  $[323]$  in the monoclinic unit cell with space group  $C2/m$  corresponds to a rotation about  $90^\circ$  around  $[010]$  in the parent cubic unit cell with space group  $Fm\bar{3}m$ ). These rotation twins are domains with a different orientation of the lithium and transition metal layers [145, 126, 147]. Figure 2.8 gives an overview of the zones that will overlap with the  $[001]$ ,  $[010]$ ,  $[100]$ ,  $[\bar{1}10]$  and  $[\bar{1}\bar{1}0]$  zones as a result of both rotation twinning with 3-fold twin axis  $[103]$  and rotation twinning with 4-fold twin axis  $[323]$ . The reflections between the diffuse streaks in the  $[\bar{1}\bar{1}0]$  reciprocal space sections in Figure 2.5 (e-g) are thus due to overlap of the  $[\bar{1}\bar{1}0]$  zone axis with the  $[\bar{3}\bar{1}\bar{6}]$ ,  $[\bar{3}1\bar{6}]$  and  $[00\bar{1}]$  zone axes.

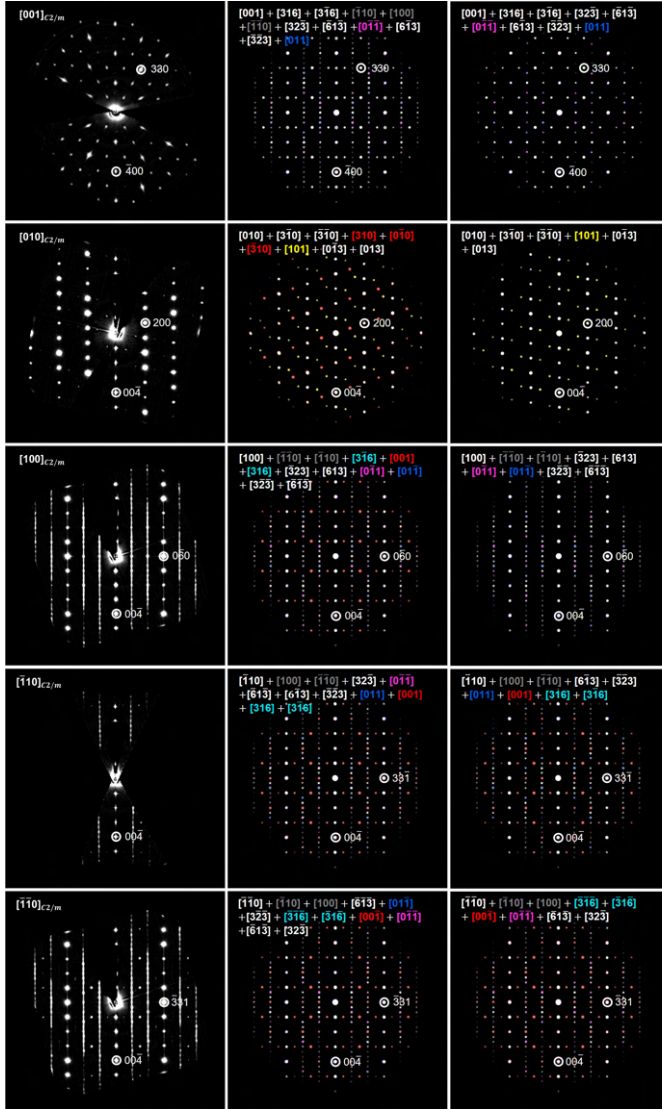


Figure 2.8: Column 1:  $[001]$ ,  $[010]$ ,  $[100]$ ,  $[\bar{1}10]$  and  $[\bar{1}\bar{1}0]$  reciprocal space sections reconstructed from 3D ED data acquired on  $Li_{1.2}Ni_{0.13}Mn_{0.54}Co_{0.13}O_2$  [crystal 2, series 3 in Figure 2.5]. Column 2: calculated electron diffraction patterns for a crystal with 3 rotation twins with 3-fold twin axis  $[103]$  and 4 rotation twins with 4-fold twin axis  $[323]$ . Column 3: calculated electron diffraction patterns for a crystal with 3 rotation twins with 3-fold twin axis  $[103]$  and 3 rotation twins with 4-fold twin axis  $[323]$ . The weak reflections in the reciprocal space sections in column 1 are thus due to the presence of 2 additional twins with a different orientation of the lithium and transition metal layers. The weak reflections in the  $[001]$  reciprocal space section are too weak to be observed. The electron diffraction patterns in columns 2-3 were calculated in *SingleCrystal*.

## 2.4. EFFECT OF DIFFERENT PARAMETERS ON THE OBSERVED DIFFUSE SCATTERING

The twin matrices for a rotation of respectively  $90^\circ$ ,  $180^\circ$  and  $270^\circ$  around  $[323]$  are:

$$\begin{aligned}
 \mathbf{V}_{90^\circ} &= \begin{pmatrix} 1/2 & 3/2 & -1/2 \\ -1/6 & 1/2 & 1/2 \\ 1 & 0 & 0 \end{pmatrix}, \\
 \mathbf{V}_{180^\circ} &= \begin{pmatrix} -1/2 & 3/2 & 1/2 \\ 1/3 & 0 & 1/3 \\ 1/2 & 3/2 & -1/2 \end{pmatrix}, \\
 \mathbf{V}_{270^\circ} &= \begin{pmatrix} 0 & 0 & 1 \\ 1/2 & 1/2 & -1/6 \\ -1/2 & 3/2 & 1/2 \end{pmatrix}.
 \end{aligned} \tag{2.2}$$

Application of these three twin matrices on the  $[\bar{1}\bar{1}0]$  zone axis, results in the  $[\bar{6}\bar{1}\bar{3}]$ ,  $[\bar{3}\bar{1}\bar{6}]$  and  $[0\bar{1}\bar{1}]$  zone axes. Rotation twinning with 3-fold twin axis  $[103]$  causes additional overlap of the  $[\bar{6}\bar{1}\bar{3}]$  zone axis with the  $[01\bar{1}]$  and  $[3\bar{2}\bar{3}]$  zone axes; of the  $[\bar{3}\bar{1}\bar{6}]$  zone axis with the  $[\bar{3}\bar{1}\bar{6}]$  and  $[00\bar{1}]$  zone axes; and of the  $[0\bar{1}\bar{1}]$  zone axis with the  $[\bar{6}\bar{1}\bar{3}]$  and  $[32\bar{3}]$  zone axes. Consequently, the  $[\bar{1}\bar{1}0]$  zone will overlap with 11 other zones ( $[\bar{1}\bar{1}0]$ ,  $[100]$ ,  $[\bar{6}\bar{1}\bar{3}]$ ,  $[01\bar{1}]$ ,  $[3\bar{2}\bar{3}]$ ,  $[\bar{3}\bar{1}\bar{6}]$ ,  $[\bar{3}\bar{1}\bar{6}]$ ,  $[00\bar{1}]$ ,  $[0\bar{1}\bar{1}]$ ,  $[\bar{6}\bar{1}\bar{3}]$  and  $[32\bar{3}]$ ).

Comparison of the reflections in the reciprocal space sections in Figure 2.8 (column 1) with the calculated electron diffraction patterns for a crystal with 3 rotation twins with 4-fold twin axis  $[323]$  (column 3), shows that only 3 of the 4 rotation twins with 4-fold twin axis  $[323]$  are present in crystal 2. Since some of the reflections in the  $[0\bar{1}\bar{1}]$  and the  $[00\bar{1}]$  zone do overlap with the diffuse streaks in the  $[\bar{1}\bar{1}0]$  zone, rotation twins with 4-fold twin axis  $[323]$  affect the intensity profile of the diffuse streaks.

Inspection of the reciprocal space sections reconstructed from 3D ED series acquired on 20 different  $\text{Li}_{1.2}\text{Ni}_{0.13}\text{Mn}_{0.54}\text{Co}_{0.13}\text{O}_2$  crystals, shows that all crystals have rotation twins with 3-fold twin axis  $[103]$ , while only 7 of the 20 crystals have rotation

twins with 4-fold twin axis  $[323]$  (domains with a different orientation of the lithium and transition metal layers). Reflection splitting in the  $[010]$  reciprocal space section (Figure 2.9) is due to reflection twins with mirror plane  $(001)$  [148, 149]. Reflection twins were present in 5 of the 20 investigated crystals. Since both rotation twins with 4-fold twin axis  $[323]$  and reflection twins with mirror plane  $(001)$  affect the intensity profile of the diffuse streaks, the refinement will be applied on crystal 1, which only has rotation twins with 3-fold twin axis  $[103]$ .

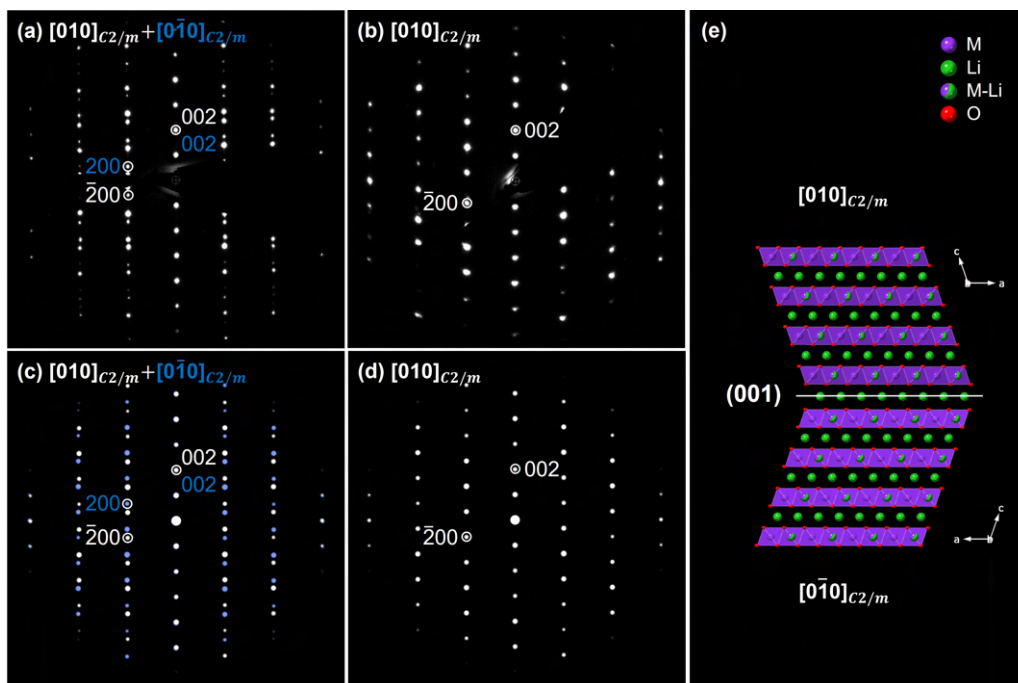


Figure 2.9: (a-b) Reconstructed  $[010]$  reciprocal space section of a crystal (a) with and (b) without reflection twins, indexed with the  $C2/m$  unit cell of  $Li_{1.2}Ni_{0.13}Mn_{0.54}Co_{0.13}O_2$ . (c-d) Calculated electron diffraction patterns for a crystal (c) with and (d) without reflection twins. (e) Two reflection twins with mirror plane  $(001)$  seen along the  $[010]$  direction. The electron diffraction patterns in (c-d) were calculated in *SingleCrystal*. Green, purple and red spheres represent lithium atoms, transition metal atoms, and oxygen atoms, respectively.

## 2.5 Calculated diffuse scattering

The *DISCUS* software package was used to build a model of the stacking faults and rotation twins with 3-fold twin axis  $[103]$  and to calculate the diffuse scattering.

To simulate a  $Li_{1.2}Ni_{0.13}Mn_{0.54}Co_{0.13}O_2$  crystal with stacking faults, a stack of



## 2.5. CALCULATED DIFFUSE SCATTERING

several layers was created [150]. Each layer is a slab of the  $C2/m$  crystal structure with a thickness of one  $C2/m$  unit cell along the  $c$  direction. As the lithium-rich positions in subsequent honeycomb layers can shift relative to each other by  $\mathbf{c}$ ,  $1/3 \mathbf{b} + \mathbf{c}$ , or  $1/2 \mathbf{a} + 1/6 \mathbf{b} + \mathbf{c}$ , the translation vectors  $M_{ij}$  between two adjacent layers  $i$  and  $j$  were defined by

$$\mathbf{M} = \begin{pmatrix} (0, 0, 1) & (1/2, 1/6, 1) & (0, 1/3, 1) \\ (0, 1/3, 1) & (0, 0, 1) & (1/2, 1/6, 1) \\ (1/2, 1/6, 1) & (0, 1/3, 1) & (0, 0, 1) \end{pmatrix}. \quad (2.3)$$

For instance, the translation vector  $M_{23} = (1/2, 1/6, 1)$  on the second row and the third column means that a layer of type 3 is shifted by  $1/2 \mathbf{a} + 1/6 \mathbf{b} + \mathbf{c}$  relative to the previous layer when that layer is of type 2. In our model, all layer types are identical but undergo a different translation, so each layer type gets a different numbering. As stacking faults (single layers with a different translation vector) may occur in each twin domain (a group of adjacent layers with the same translation vector), the transition probability matrices for the  $[100]$ ,  $[\bar{1}10]$  and  $[\bar{1}\bar{1}0]$  twin domain were defined by

$$\begin{aligned} \mathbf{A}_{[100]} &= \begin{pmatrix} 1-s & s/2 & s/2 \\ s/2 & 1-s & s/2 \\ s/2 & s/2 & 1-s \end{pmatrix}, \\ \mathbf{A}_{[\bar{1}10]} &= \begin{pmatrix} s/2 & s/2 & 1-s \\ 1-s & s/2 & s/2 \\ s/2 & 1-s & s/2 \end{pmatrix}, \\ \mathbf{A}_{[\bar{1}\bar{1}0]} &= \begin{pmatrix} s/2 & 1-s & s/2 \\ s/2 & s/2 & 1-s \\ 1-s & s/2 & s/2 \end{pmatrix}. \end{aligned} \quad (2.4)$$

with  $A_{ij}$  the probabilities for one of the translation vectors  $M_{ij}$  to be chosen and  $s$  the stacking fault probability ( $0 \leq s \leq 1$ ), which was considered identical for the  $[100]$ ,  $[\bar{1}10]$  and  $[\bar{1}\bar{1}0]$  twin. The layers of the  $[\bar{1}10]$  and  $[\bar{1}\bar{1}0]$  twin domains were rotated by respectively  $120^\circ$  and  $240^\circ$  around  $[103]$ . In the following, the percentage of the  $[100]$ ,  $[\bar{1}10]$  and  $[\bar{1}\bar{1}0]$  twin in the crystal will be denoted by  $p_{[100]}$ ,  $p_{[\bar{1}10]}$  and  $p_{[\bar{1}\bar{1}0]}$ .

Figure 2.10(b) shows the  $[100]$  reciprocal space section calculated for a crystal with a stacking fault probability of 60% and twin percentages of  $p_{[100]} = 50\%$  and  $p_{[\bar{1}10]} = p_{[\bar{1}\bar{1}0]} = 25\%$ . Diffuse streaks are visible for  $k \neq 3n$  with  $n \in \mathbb{N}$ . The width of the Bragg reflections and the diffuse streaks is inversely proportional to the number of unit cells in one layer. The  $[100]$  section was calculated for a crystal that consists of 4000 layers of 100 unit cells. The intensities were averaged over 400 calculations to create a smooth intensity distribution.

Figure 2.11(a) shows the intensity profile of the  $04l$  diffuse streak for increasing stacking fault probability. When the stacking fault probability increases from 0% to 60%, the discrete intensity maxima at integer  $l$  values merge together. From a stacking fault probability of 80% onward, intensity peaks with maxima at half-integer  $l$  values

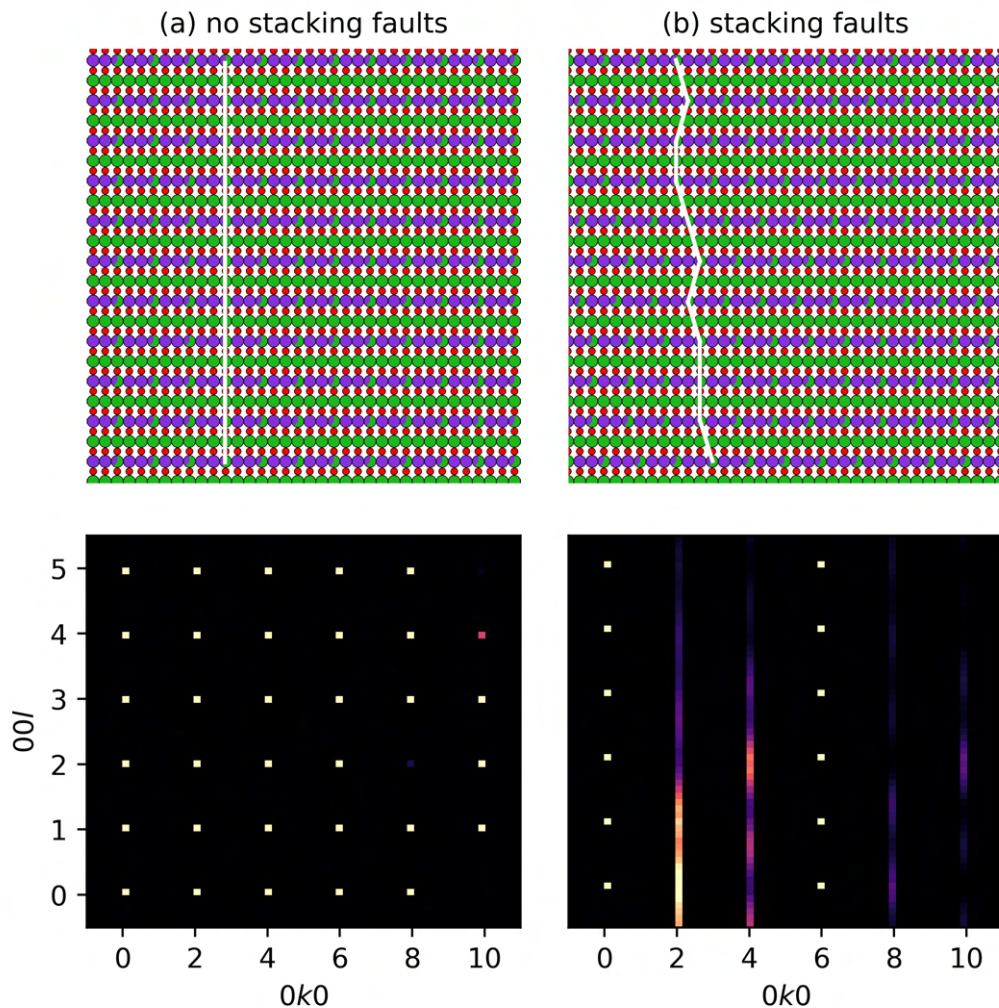


Figure 2.10: (a) The  $[100]$  reciprocal space section calculated for (a) a crystal without stacking faults, (b) a crystal with a stacking fault probability of 60% and twin percentages of  $p_{[100]} = 50\%$  and  $p_{[\bar{1}10]} = p_{[\bar{1}\bar{1}0]} = 25\%$ .

appear. The reason is that for a stacking fault probability of 100%, only two possible shifts can occur, which results again in a more periodic stacking of the layers. The intensity profiles in Figure 2.11 (a) were calculated for a crystal that consists of only one twin, whereas the intensity profiles in Figure 2.11 (b) were calculated for a crystal that consists of all  $[100]$ ,  $[\bar{1}10]$  and  $[\bar{1}\bar{1}0]$  twin domains. Rotation twinning with 3-fold twin axis  $[103]$  causes additional intensity maxima along the diffuse streaks at  $l = n + 1/3$  and/or  $l = n + 2/3$ . The intensity profiles in Figure 2.11 (b) were calculated for  $p_{[100]} = 50\%$  and  $p_{[\bar{1}10]} = p_{[\bar{1}\bar{1}0]} = 25\%$ .

To illustrate the effect of different percentages of the  $[100]$ ,  $[\bar{1}10]$  and  $[\bar{1}\bar{1}0]$  twin

## 2.6. REFINEMENT OF THE SHORT-RANGE ORDER

domains on the intensity profile of the 04*l* diffuse streak, the intensity profiles in Figure 2.11 (c) were calculated for different values of  $p_{[100]}$ ,  $p_{[\bar{1}10]}$  and  $p_{[\bar{1}\bar{1}0]}$  (black curve:  $p_{[100]} = 50\%$ ,  $p_{[\bar{1}10]} = p_{[\bar{1}\bar{1}0]} = 25\%$ ; red curve:  $p_{[\bar{1}\bar{1}0]} = 50\%$ ,  $p_{[\bar{1}10]} = p_{[100]} = 25\%$ ; green curve:  $p_{[\bar{1}10]} = 50\%$ ,  $p_{[\bar{1}\bar{1}0]} = p_{[100]} = 25\%$ ). The intensity profile of the diffuse streaks in Figure 2.11 were calculated for a crystal that consists of 4000 layers of 64 unit cells. The intensities were averaged over 1000 calculations to create a smooth intensity distribution.

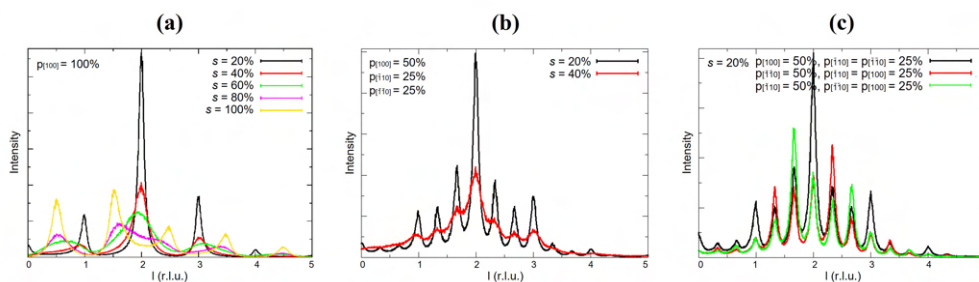


Figure 2.11: The intensity profile of the 04*l* diffuse streak (a) for a crystal that consists of only one twin ( $p_{[100]} = 100\%$ ) and for a stacking fault probability of respectively 20%, 40%, 60%, 80% and 100%; (b) for a crystal that consist of all [100],  $[\bar{1}10]$  and  $[\bar{1}\bar{1}0]$  twin domains ( $p_{[100]} = 50\%$  and  $p_{[\bar{1}10]} = p_{[\bar{1}\bar{1}0]} = 25\%$ ) and for a stacking fault probability of respectively 20% and 40%; (c) for different percentages of the [100],  $[\bar{1}10]$  and  $[\bar{1}\bar{1}0]$  twin domains. With  $s$  the stacking fault probability and  $p_{[100]}$  and  $p_{[\bar{1}10]}$  the percentages of the [100] and the  $[\bar{1}10]$  twin in the crystal.

## 2.6 Refinement of the short-range order

To refine the stacking fault probability and the percentage of the different twins in the crystal, the model of the  $\text{Li}_{1.2}\text{Ni}_{0.13}\text{Mn}_{0.54}\text{Co}_{0.13}\text{O}_2$  crystal with stacking faults and twin domains was implemented in a differential evolutionary algorithm in *DISCUS*. The number of parents and the number of children were both chosen to be 28 which is the number of cores in one node on the Leibniz cluster, and which is approximately ten times the number of refined parameters. To speed up the calculation, the 28 children were calculated in parallel. The Monte Carlo refinement (<https://doi.org/10.5281/zenodo.8212664>) took three days of wall-clock time for 50 generations, using 28 cores in parallel. The refinement algorithm was first tested on diffuse scattering data calculated from simulated structures with known short-range order parameters, to check that the short-range order parameters converge towards the correct values.

As discussed in the previous section, the intensity distribution of the diffuse streaks depends on both the stacking fault probability  $s$  and the percentage of the [100],

$[\bar{1}\bar{1}0]$  and  $[\bar{1}\bar{1}0]$  twin in the crystal denoted by  $p_{[100]}$ ,  $p_{[\bar{1}10]}$  and  $p_{[\bar{1}\bar{1}0]}$ . Since  $p_{[\bar{1}\bar{1}0]} = 1 - p_{[100]} - p_{[\bar{1}10]}$ , it was sufficient to refine  $s$ ,  $p_{[100]}$  and  $p_{[\bar{1}10]}$ .

Refining the atomic coordinates and occupancies from our 3D ED data in *Jana2020* was not successful; probably because of the combination of stacking faults, rotation twins with 3-fold twin axis  $[103]$  and multiple scattering. Therefore, we used the atomic coordinates, atomic displacement parameters, and cell parameters of  $Li_{1.2}Ni_{0.15}Mn_{0.55}Co_{0.1}O_2$  determined by powder neutron diffraction [151] [ICSD 237940]. Since the Ni/Mn/Co ratio in  $Li_{1.2}Ni_{0.15}Mn_{0.55}Co_{0.1}O_2$  is only slightly different from the Ni/Mn/Co ratio in  $Li_{1.2}Ni_{0.13}Mn_{0.54}Co_{0.13}O_2$ , the effect on the atomic coordinates and atomic displacement parameters will be negligible. To decrease the refinement time, we used the integer occupancies in Table 2.1 (the position with most lithium was considered as fully occupied by lithium, the other position was considered as fully occupied by manganese) instead of the occupancies determined by [151]. This simplification of the model has a negligible effect on the intensity profile (Figure 2.12). The refinement algorithm calculates the diffuse scattering from a crystal that consists of 2000 layers of one unit cell<sup>1</sup>. To create a smooth intensity distribution, the algorithm averages the intensity profile over 100 calculations.

The refinement was applied on the intensity profile of the diffuse streaks indicated in the  $[\bar{1}\bar{1}0]$  and  $[\bar{2}10]$  reciprocal space sections in Figure 2.3 (b-c) [details in Figure 2.13 (a-b)]. A custom Matlab script was used to extract the intensity profile of the diffuse streaks and convert it to input for *DISCUS*. Figure 2.14 and Figure 2.15 show the evolution of the R value and the short-range order parameters for the first 50 generations. The refined short-range order parameters and the R value at generation 50 are listed in Table 2.2.

The electron diffraction patterns in Figure 2.13 (c-d) were calculated for the refined short-range order parameters, for a crystal that consists of 2000 layers of 100 unit cells. The agreement between the experimental and the calculated intensity profile is better for the diffuse streak indicated in the  $[\bar{2}10]$  section than for the diffuse streak indicated in the  $[\bar{1}\bar{1}0]$  section [Figure 2.13 (e-f)]. Since *DISCUS* calculates the intensity profiles according to the standard formula for kinematic scattering, the intensity differences between the experimental and the calculated intensity profile are probably due to multiple scattering. Multiple scattering increases the intensity of weaker Bragg reflections, whereas strong Bragg reflections become less intense [50]. The  $\bar{2}20$  reflection for example, is much stronger in the experimental than in the calculated  $[\bar{1}\bar{1}0]$  section [peak at  $l = 0$  in Figure 2.13 (e)]. Figure 2.13 (g-h) shows two electron diffraction patterns that were used to reconstruct the  $[\bar{1}\bar{1}0]$  and  $[\bar{2}10]$  sections in Figure 2.13 (a-b). In the electron diffraction pattern in Figure 2.13 (g), more reflections are simultaneously excited than in the electron diffraction pattern in Figure 2.13 (h), which might explain

<sup>1</sup>When using integer occupancies, the number of unit cells in one layer has no influence on the intensity profile.

## 2.6. REFINEMENT OF THE SHORT-RANGE ORDER

Table 2.1: Column 2-4: Atomic coordinates, atomic displacement parameters and occupancies of the  $C2/m$  unit cell of  $\text{Li}_{1.2}\text{Ni}_{0.15}\text{Mn}_{0.55}\text{Co}_{0.1}\text{O}_2$  determined by powder neutron diffraction [151] and used for the simulation of the model in *DISCUS*. Column 5: Occupancies used for the Monte Carlo refinement. The use of integer occupancies implies that the transition metal atoms in the Li-rich positions are replaced by Li, and that all Ni ( $Z=28$ ) and Co ( $Z=27$ ) atoms are replaced by Mn ( $Z=25$ ). With  $M = \text{Ni}, \text{Mn}, \text{Co}$ .

Atom type	x, y, z	$U_{iso}(\text{\AA}^2)$	Occupancies	Integer occ.
Li	0, 0, 0.5	0.0117(2)	0.9957(11)	1
M	0, 0, 0.5	0.0117(2)	0.0043(11)	0
Li	0, 0.6551, 0.5	0.0125(4)	0.9900(6)	1
M	0, 0.6551, 0.5	0.0125(4)	0.0100(6)	0
Li	0, 0.5, 0	0.0029(2)	0.364(1)	1
M	0, 0.5, 0	0.0029(2)	0.636(1)	0
Li	0, 0.1660, 0	0.0076(4)	0.128(1)	0
M	0, 0.1660, 0	0.0076(4)	0.872(1)	1
O	0.2226, 0, 0.2232	0.0049(4)	1	1
O	0.2539, 0.3223, 0.2256	0.0056(8)	1	1

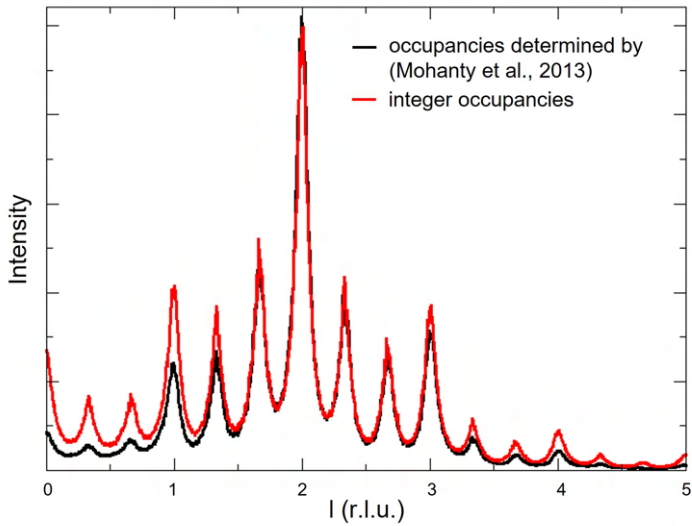


Figure 2.12: Intensity profile of the  $04l$  diffuse streak simulated with 1) integer occupancies 2) the occupancies determined by powder neutron diffraction [151]. Both profiles were calculated for a crystal with a stacking fault probability of 20% and twin percentages of  $p_{[100]} = 50\%$  and  $p_{[\bar{1}10]} = p_{[\bar{1}\bar{1}0]} = 25\%$ .

why multiple scattering effects are larger for the  $\bar{2}20$  reflection than for the  $\bar{2}44$  reflection.

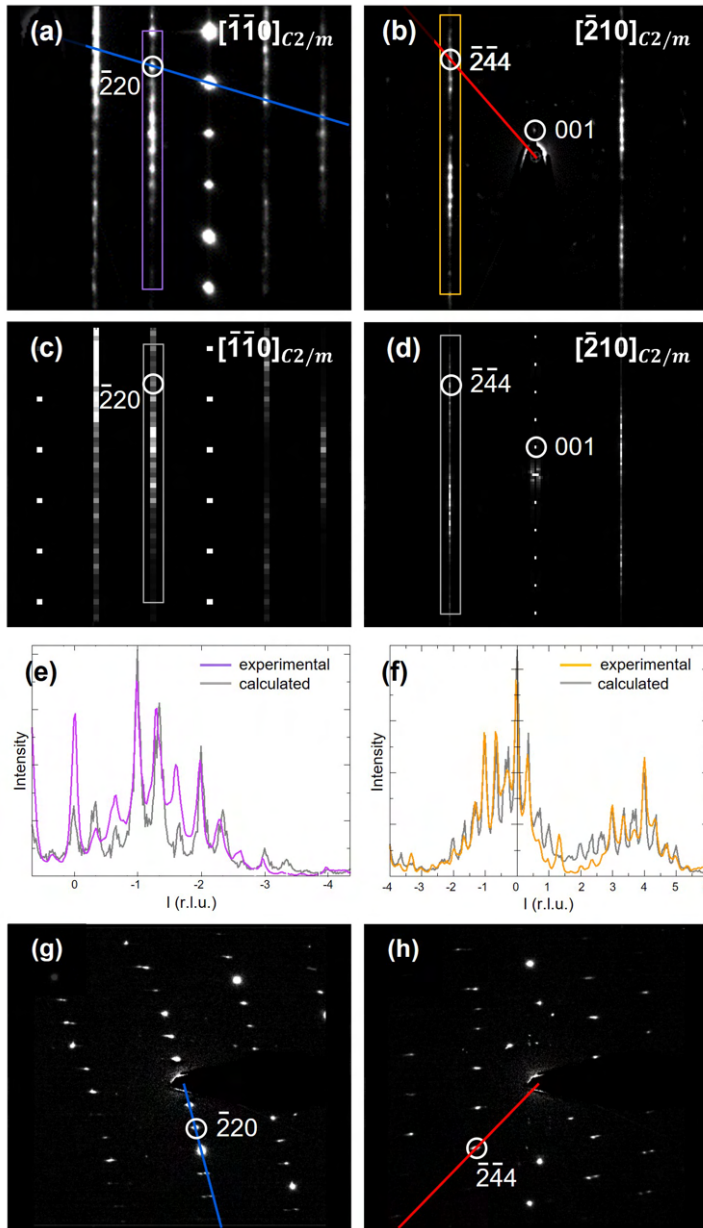


Figure 2.13: **(a-b)**  $[\bar{1}\bar{1}0]$  and  $[\bar{2}10]$  reciprocal space sections of crystal 1. **(c-d)** Electron diffraction patterns calculated for the refined short-range order parameters at generation 50. **(e-f)** The intensity profile of the diffuse streaks indicated in (a-b) together with the intensity profiles calculated for the refined short-range order parameters at generation 50. **(g-h)** Two electron diffraction patterns that were used to reconstruct the  $[\bar{1}\bar{1}0]$  and  $[\bar{2}10]$  sections in (a-b). The blue and red lines indicated in (g-h) correspond to the blue and red lines indicated in (a-b).

## 2.6. REFINEMENT OF THE SHORT-RANGE ORDER

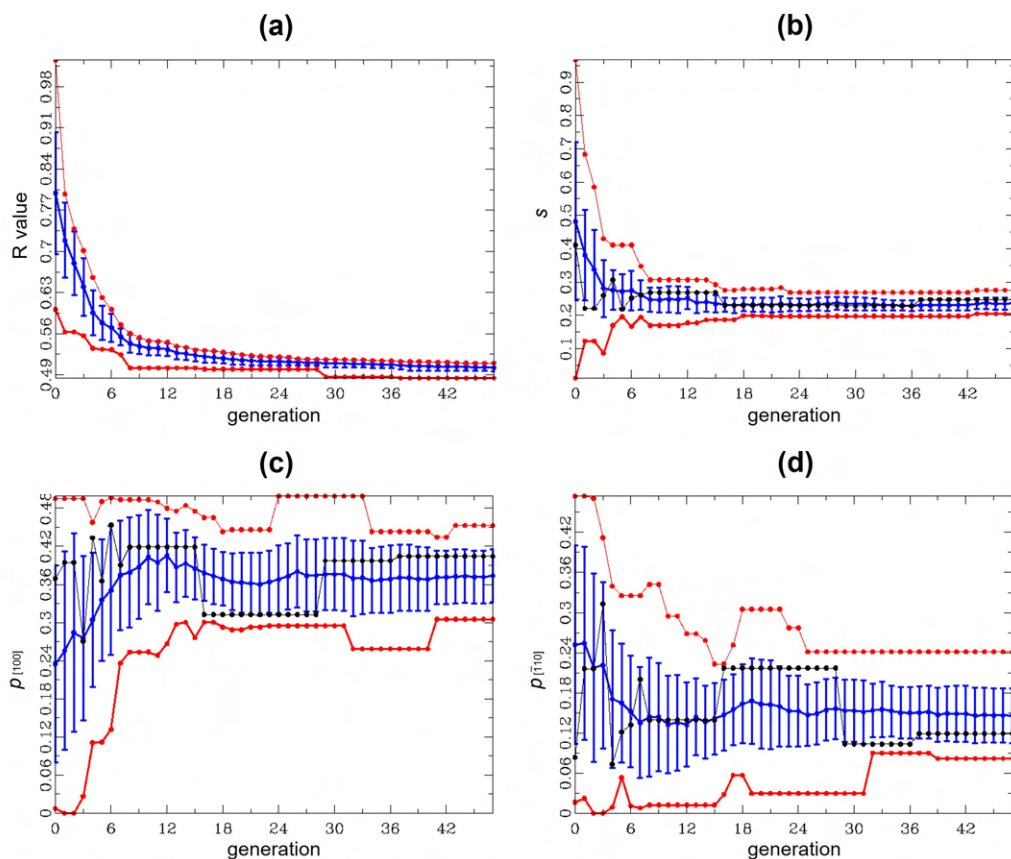


Figure 2.14: Refinement applied on the intensity profile of the diffuse streak indicated in the  $[\bar{1}\bar{1}0]$  reciprocal space section in Figure 2.13 (a). Evolution of (a) the R value, (b) the stacking fault probability  $s$ , (c) the percentage of the [100] twin  $p_{[100]}$  and (d) the percentage of the  $[\bar{1}10]$  twin  $p_{[\bar{1}10]}$  as a function of the generation number. The figure shows the average (blue), smallest and highest (red) value at each generation. The value with the lowest R value at each generation is shown in black.

As mentioned before, no frame scaling was applied during the reconstruction of the reciprocal space sections in Figure 2.13 (a-b). Frame scaling corrects for variations in the crystal thickness and/or variations in the illuminated volume. Even though the whole crystal was illuminated during the collection of the 3D ED data, variations in the crystal thickness might affect the intensities and consequently also the experimental intensity profile of the diffuse streaks.

It should also be noted that resolution effects were not considered in the Monte Carlo refinement. In Section 3.4, we will show that the spatial resolution of the observed diffuse scattering depends on various effects including the convergence of the electron beam, the detector point spread function and the crystal mosaicity. To account for

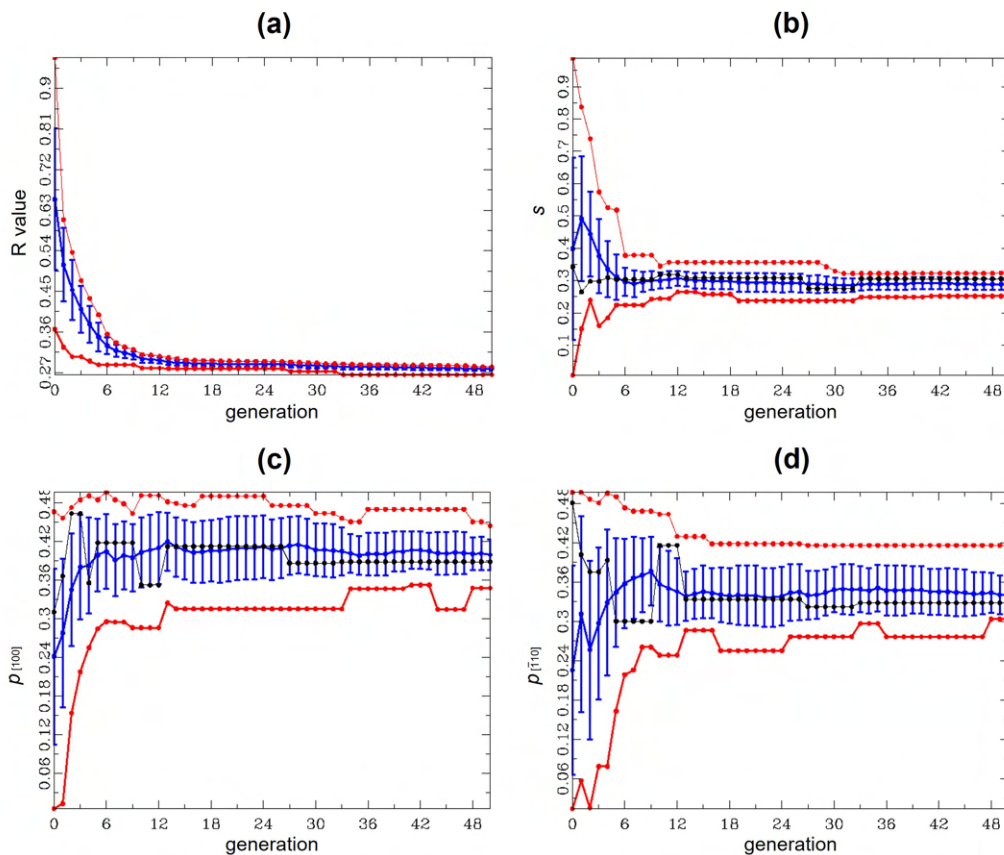


Figure 2.15: Refinement applied on the intensity profile of the diffuse streak indicated in the  $[\bar{2}10]$  reciprocal space section in Figure 2.13 (b). Evolution of (a) the R value, (b) the stacking fault probability  $s$ , (c) the percentage of the  $[100]$  twin  $p_{[100]}$  and (d) the percentage of the  $[\bar{1}10]$  twin  $p_{[\bar{1}10]}$  as a function of the generation number. The figure shows the average (blue), smallest and highest (red) value at each generation. The value with the lowest R value at each generation is shown in black.

resolution effects, the intensity of each pixel in the calculated intensity profile should be convoluted with a Gaussian function. The intensity maxima in the experimental intensity profile in Figure 2.13 are thus less sharp than in the calculated intensity profile. Figure 2.11 (a) shows that the intensity maxima are sharper at lower stacking fault probabilities. The refined stacking fault probability in Table 2.2 is thus probably overestimated.

Small intensity differences between the experimental and the calculated intensity profile of the diffuse streaks can also be due to deviations in the atomic coordinates and occupancies. The atomic coordinates were refined using powder neutron diffraction data [151]. However, stacking faults (peak broadening) and twinning (peak overlap) were not taken into account. The actual atomic coordinates and occupancies might thus be



## 2.7. DETERMINATION OF THE SPINEL/LAYERED PHASE RATIO

Table 2.2: Refined short-range order parameters and R value at generation 50 for the intensity profile of the diffuse streaks indicated in the  $[\bar{1}\bar{1}0]$  and  $[\bar{2}10]$  reciprocal space sections of crystal 1. With  $s$  the stacking fault probability and  $p_{[100]}$  and  $p_{[\bar{1}10]}$  the percentages of the  $[100]$  and the  $[\bar{1}10]$  twin in the crystal.

parameter	refined value $[\bar{1}\bar{1}0]$	refined value $[\bar{2}10]$
$s$	0.24(2)	0.29(2)
$p_{[100]}$	0.37(5)	0.40(3)
$p_{[\bar{1}10]}$	0.15(5)	0.34(3)
R value	50.3(7)	27.8(5)

different from the ones in [151] which will affect the calculated intensity profile of the diffuse streaks.

Krysiak and co-workers, who previously reported a quantitative analysis of diffuse scattering in single-crystal electron diffraction data on two zeolites, assigned the small intensity differences between their experimental and calculated patterns to inelastic scattering and an insufficiently sensitive detector [89, 90]. Because zeolites mainly consist of light elements [O ( $Z=8$ ) and Si ( $Z=14$ )] and because their 3D ED data were acquired on thinner crystals (100 nm), the intensities in the 3D ED data of Krysiak and co-workers were probably less influenced by multiple scattering.

## 2.7 Determination of the spinel/layered phase ratio

The commercialization of lithium-ion batteries with Li-rich Mn-rich layered oxides ( $\text{Li}_{1+x}\text{M}_{1-x}\text{O}_2$ , with  $\text{M} = \text{Ni}, \text{Mn}, \text{Co}$ ) as cathode materials is still hampered by a significant capacity and voltage decay on cycling [126, 127, 128, 129]. The capacity and voltage decay are mainly due to transition metal ion migration and spinel domain formation [130, 131, 132, 133, 134].  $\text{Li}_{1.2}\text{Ni}_{0.13}\text{Mn}_{0.54}\text{Co}_{0.13}\text{O}_2$  has a layered structure with space group  $C2/m$  [138] (Figure 2.16(a)). During charging and discharging of the battery, the layered structure transforms to a spinel structure with space group  $Fd\bar{3}m$  [152] (Figure 2.16(b)).

Figure 2.17 shows a HAADF-STEM image acquired on  $\text{Li}_{1.2}\text{Ni}_{0.13}\text{Mn}_{0.54}\text{Co}_{0.13}\text{O}_2$ . The spinel structure can be observed at the crystal surface. An in situ synchrotron powder X-ray diffraction study suggested that the transformation from the layered structure to the spinel structure also occurs in the bulk of the crystals [134].

The advantage of 3D ED is that it allows to determine the crystal structure of submicron-sized crystals. 3D ED data were acquired on  $\text{Li}_{1.2}\text{Ni}_{0.13}\text{Mn}_{0.54}\text{Co}_{0.13}\text{O}_2$  with

CHAPTER 2. ONE-DIMENSIONAL DIFFUSE SCATTERING -  
 $\text{Li}_{1.2}\text{Ni}_{0.13}\text{Mn}_{0.54}\text{Co}_{0.13}\text{O}_2$

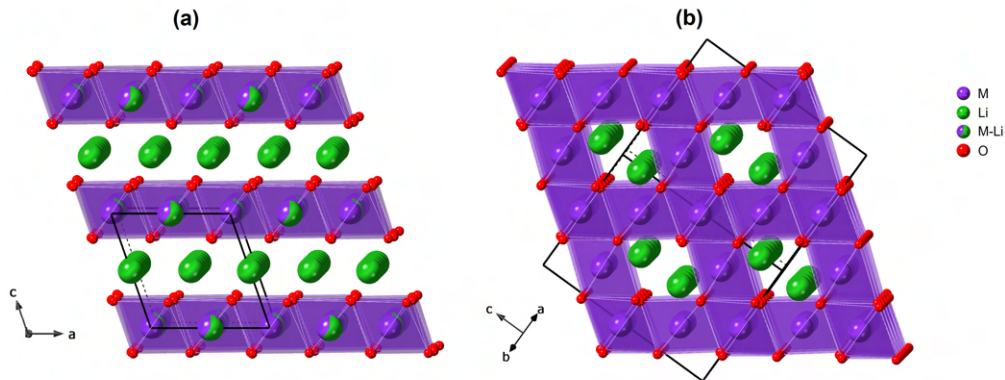


Figure 2.16: During charging and discharging of the battery, the crystal structure of  $\text{Li}_{1.2}\text{Ni}_{0.13}\text{Mn}_{0.54}\text{Co}_{0.13}\text{O}_2$  transforms from the layered structure in (a) to the spinel structure in (b). The monoclinic  $C2/m$  unit cell in (a) and the cubic  $Fd\bar{3}m$  unit cell in (b) are indicated in black. Purple octahedra represent  $\text{MO}_6$  octahedra, with  $M = \text{Ni}, \text{Mn}, \text{Co}$ . Green, purple and red spheres represent lithium atoms, transition metal atoms, and oxygen atoms, respectively.

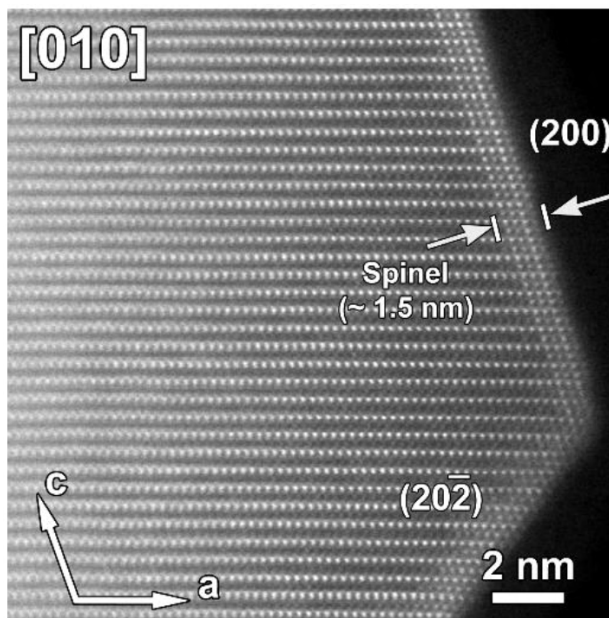


Figure 2.17: HAADF-STEM image acquired on  $\text{Li}_{1.2}\text{Ni}_{0.13}\text{Mn}_{0.54}\text{Co}_{0.13}\text{O}_2$  along the  $[010]$  direction of the  $C2/m$  unit cell.

a low electron dose since irradiating the sample with an intense electron beam might induce the formation of the spinel structure [153, 154, 155]. Refining the volume ratio between the layered structure and the spinel structure from our 3D ED data by using

## 2.7. DETERMINATION OF THE SPINEL/LAYERED PHASE RATIO

a least squares refinement in *Jana2020* was not successful; probably because of the combination of stacking faults, rotation twins with 3-fold twin axis [103] and multiple scattering.

As a solution, we developed an alternative method to determine the volume ratio between different phases from the intensities of the reflections in 3D ED data. The method is based on the fact that the intensity ratio between a reflection that is only caused by the spinel structure and a reflection that is caused by both the spinel structure and the layered structure corresponds to a unique volume ratio between the layered structure and the spinel structure.

To validate the method, in-zone electron diffraction patterns of spherical core-shell particles were calculated in *DISCUS*. Core-shell particles with a layered core [151] [ICSD 237940] and a spinel shell [152] [ICSD 40485] were simulated for different layered/spinel volume ratios. No stacking faults or twins were included in the model. To build a core-shell particle in *DISCUS*, the cell parameters of both structures need to be identical. This was achieved by transforming the  $C2/m$  unit cell and the  $Fd\bar{3}m$  unit cell to a common supercell with cell parameters  $a = b = 9.8707 \text{ \AA}$ ,  $c = 14.2301 \text{ \AA}$ ,  $\alpha = \beta = 90^\circ$  and  $\gamma = 120^\circ$ . The transformation matrices are:

$$\mathbf{P}_{C2/m \rightarrow \text{supercell}} = \begin{pmatrix} 1 & 1 & 1 \\ -1 & 1 & 0 \\ 0 & 0 & 3 \end{pmatrix}, \mathbf{P}_{Fd\bar{3}m \rightarrow \text{supercell}} = \begin{pmatrix} 0.5 & 0.5 & -1 \\ 0.5 & -1 & -1 \\ -1 & 0.5 & -1 \end{pmatrix}. \quad (2.5)$$

Figure 2.18 shows the cross-section of a spherical core-shell particle with  $10 \times 10 \times 10$  supercell unit cells and a spinel/layered volume ratio of 50:50. Figure 2.19 shows the [100] and  $[\bar{1}10]$  electron diffraction patterns calculated in *DISCUS* for a spinel content of 5, 20 and 50%. The 033 reflection is only caused by the spinel structure, whereas the 066 reflection is caused by both the spinel structure and the layered structure. The intensity ratio of both reflections allows thus to determine volume ratio between the layered structure and the spinel structure. Figure 2.20 shows the relationship between the intensity ratio of both reflections and the percentage of spinel in the crystal.

To determine the percentage of spinel in the crystal ( $x$ ), the 3D ED data acquired on  $\text{Li}_{1.2}\text{Ni}_{0.13}\text{Mn}_{0.54}\text{Co}_{0.13}\text{O}_2$  were processed using *PETS2*. The three-dimensional reciprocal lattice was indexed with a supercell with cell parameters  $a = b = 9.8707 \text{ \AA}$ ,  $c = 14.2301 \text{ \AA}$ ,  $\alpha = \beta = 90^\circ$  and  $\gamma = 120^\circ$ . The intensities of the Bragg reflections determined by *PETS2* ( $I(\mathbf{Q})$ ) were then used to calculate the percentage of spinel in the crystal ( $x$ ):

$$I(\mathbf{Q}) = |xF_{\text{spinel}}(\mathbf{Q}) + (1-x)F_{\text{layered}}(\mathbf{Q})|^2, \quad (2.6)$$

with  $\mathbf{Q}$  a reciprocal lattice vector (Equation 1.5),  $F_{\text{spinel}}(\mathbf{Q})$  the structure factor of the spinel phase and  $F_{\text{layered}}(\mathbf{Q})$  the structure factor of the layered phase. The percentage of spinel in the crystal ( $x$ ) was calculated from the intensity ratio of all possible reflection pairs (with one reflection only caused by the spinel structure and one reflection caused

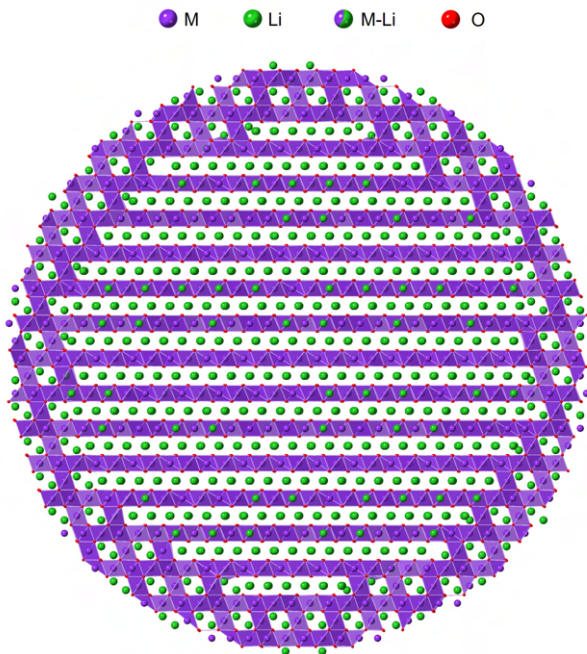


Figure 2.18: Cross-section of a spherical core-shell  $Li_{1.2}Ni_{0.13}Mn_{0.54}Co_{0.13}O_2$  particle used for calculating electron diffraction patterns in *DISCUS*. The particle has a size of  $10 \times 10 \times 10$  supercell unit cells with a layered core and a spinel shell. The spinel/layered ratio used for the simulation of this particle is 50:50. Purple octahedra represent  $MO_6$  octahedra, with  $M = Ni, Mn, Co$ . Green, purple and red spheres represent lithium atoms, transition metal atoms, and oxygen atoms, respectively.

by both the spinel structure and the layered structure).

The method was applied to determine the spinel/layered phase ratio in a submicron sized  $Li_{1.2}Ni_{0.13}Mn_{0.54}Co_{0.13}O_2$  crystal that was cycled 150 times. After 150 charge-discharge cycles, 4% of the  $Li_{1.2}Ni_{0.13}Mn_{0.54}Co_{0.13}O_2$  crystal was transformed from the layered structure to the spinel structure. The spinel/layered phase ratio in a submicron sized  $Li_{1.2}Ni_{0.13}Mn_{0.54}Co_{0.13}O_2$  crystal that was 100 times cycled has previously been determined using in situ synchrotron powder X-ray diffraction [134]. The authors found that after 100 charge-discharge cycles, 5 % of the  $Li_{1.2}Ni_{0.13}Mn_{0.54}Co_{0.13}O_2$  crystal was transformed from the layered structure to the spinel structure, which is close to the spinel/layered phase ratio of 4% determined using 3D ED.

The proposed method could also be applied to determine the phase ratio in other multi-phase materials, as long as some reflections belong to only one of the two phases.

## 2.7. DETERMINATION OF THE SPINEL/LAYERED PHASE RATIO

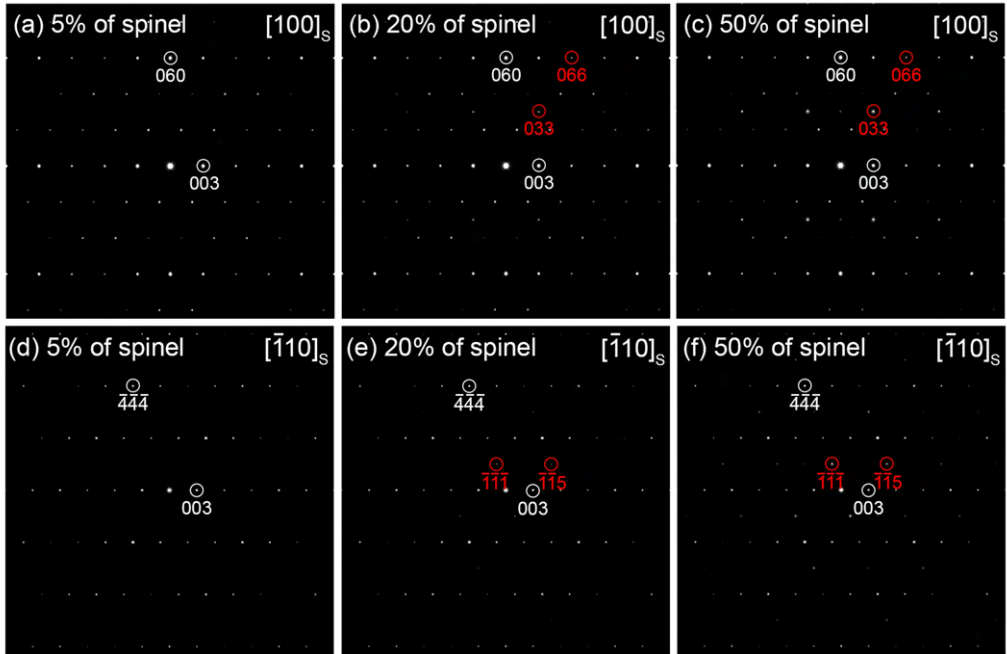


Figure 2.19:  $[100]$  and  $[\bar{1}10]$  electron diffraction patterns calculated for, respectively, 5%, 20% and 50% of spinel, for a spherical crystal with  $10 \times 10 \times 10$  supercell unit cells.

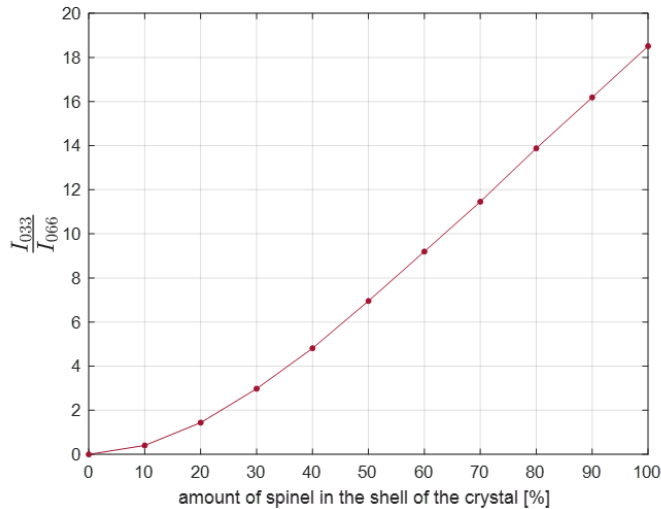


Figure 2.20: The intensity ratio of the 033 reflection and the 066 reflection depends on the volume ratio between the layered structure and the spinel structure. The 033 reflection is only caused by the spinel structure, whereas the 066 reflection is caused by both the spinel structure and the layered structure.

## 2.8 Conclusion

In this chapter, we showed that short-range order parameters can be refined from the one-dimensional diffuse scattering in 3D ED data. As 3D ED requires much smaller crystal sizes than single-crystal X-ray diffraction, this opens up the possibility to refine short-range order parameters in materials for which no crystals large enough for single-crystal X-ray diffraction are available.

Lithium-ion battery cathode materials consist of submicron-sized crystals, which are too small to be investigated with single-crystal X-ray diffraction. Three types of twins may occur in  $\text{Li}_{1.2}\text{Ni}_{0.13}\text{Mn}_{0.54}\text{Co}_{0.13}\text{O}_2$ : rotation twins with 3-fold twin axis [103], rotation twins with 4-fold twin axis [323], and reflection twins with mirror plane (001). Inspection of the three-dimensional reciprocal lattice of 20 different  $\text{Li}_{1.2}\text{Ni}_{0.13}\text{Mn}_{0.54}\text{Co}_{0.13}\text{O}_2$  crystals, showed that all crystals had rotation twins with 3-fold twin axis [103], 7 of the 20 crystals had rotation twins with 4-fold twin axis [323], and 5 of the 20 crystals had reflection twins with mirror plane (001).

Short-range order parameters were refined from the one-dimensional diffuse scattering in 3D ED data acquired on a 200 nm sized  $\text{Li}_{1.2}\text{Ni}_{0.13}\text{Mn}_{0.54}\text{Co}_{0.13}\text{O}_2$  crystal that only had rotation twins with 3-fold twin axis [103]. The number of stacking faults and the twin percentages were refined from the diffuse scattering using a Monte Carlo refinement in *DISCUS*. For the diffuse scattering in the  $[\bar{2}10]$  reciprocal space section of the investigated crystal, the best agreement between the observed and calculated intensities was achieved for a stacking fault probability of 29(2) % and twin percentages of  $p_{[100]} = 40(3)$  %,  $p_{[\bar{1}10]} = 34(3)$  % and  $p_{[\bar{1}\bar{1}0]} = 26(6)$  %.

Finally, we described a method to determine the spinel/layered phase ratio from the Bragg reflections in 3D ED data acquired on  $\text{Li}_{1.2}\text{Ni}_{0.13}\text{Mn}_{0.54}\text{Co}_{0.13}\text{O}_2$ . The method was applied to a crystal that was 150 times cycled. After 150 charge-discharge cycles, 4% of the crystal was transformed from the layered structure to the spinel structure, which is close to the spinel/layered phase ratio that has previously been determined using in situ synchrotron powder X-ray diffraction [134].

## Three-dimensional diffuse scattering - $\text{Nb}_{0.84}\text{CoSb}$

---

*The results of this chapter will be published in:*

- (*in preparation*) Poppe, R., & Hadermann, J., Diffuse electron scattering data acquisition for quantitative analysis.
- (*submitted for publication*) Poppe, R., Roth, N., Neder, R. B., Palatinus, L., Iversen, B. B., & Hadermann, J., Refinement of the short-range order parameters from the diffuse scattering in single-crystal electron diffraction data.

In this chapter, we will refine short-range order parameters from the three-dimensional diffuse scattering in both three-dimensional electron diffraction (3D ED) and single-crystal X-ray diffraction data. The defective half-Heusler system  $\text{Nb}_{0.84}\text{CoSb}$  was chosen as a reference material. The correlations between neighbouring vacancies and the displacements of Sb and Co atoms will be refined from the diffuse scattering using a Monte Carlo refinement in *DISCUS* and a three-dimensional difference pair distribution function (3D- $\Delta$ PDF) refinement in *Yell*. To determine the accuracy of the refined correlation coefficients, the displacements of Sb and Co atoms refined from the diffuse scattering will be compared with the displacements refined from the Bragg reflections in single-crystal X-ray diffraction data. The Nb occupancy and the displacements of Sb and Co atoms will also be refined from the Bragg reflections in 3D ED data, and compared with reference values refined from the Bragg reflections in single-crystal X-ray diffraction data.

The effect of different experimental parameters on the spatial resolution of the observed diffuse scattering will also be investigated. Finally, the model of the short-range Nb-vacancy order in  $\text{Nb}_{0.84}\text{CoSb}$  will also be applied to  $\text{LiNi}_{0.5}\text{Sn}_{0.3}\text{Co}_{0.2}\text{O}_2$ .

### 3.1 Introduction

Defective half-Heusler systems  $X_{1-x}YZ$ , such as  $Nb_{1-x}CoSb$ , are used as thermoelectric materials. Their thermoelectric properties depend on the vacancy distribution, which can be adjusted by varying the synthesis temperature or quench rate [156]. The diffuse scattering in  $Nb_{0.84}CoSb$  (Figure 3.1) is due to correlations between neighbouring vacancies and the relaxation of Sb and Co atoms around these vacancies [157, 156].

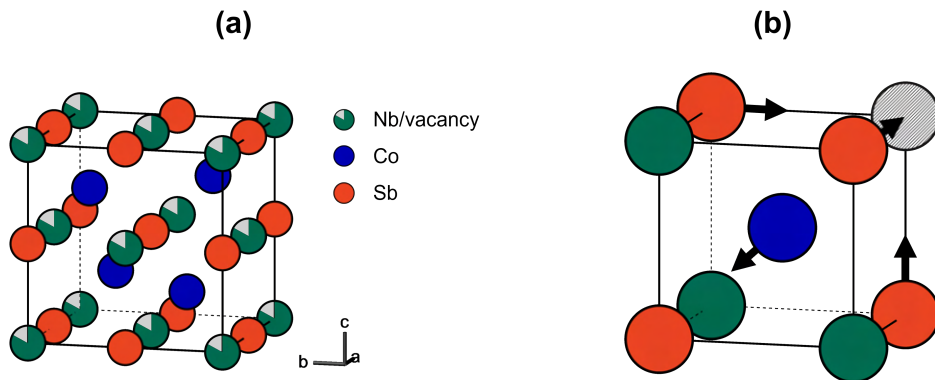


Figure 3.1: (a) Unit cell of the average crystal structure of  $Nb_{0.84}CoSb$ . Nb and Sb atoms form a rock salt structure, whereas Nb and Co atoms form a sphalerite structure. (b) Arrows indicate the local displacements of Sb and Co atoms. Sb atoms move towards neighbouring vacancies, whereas Co atoms move away from neighbouring vacancies. Figure adapted from [156].

## 3.2 Experimental details

### 3.2.1 Synthesis

The samples that were used in this study were previously used by [156] and are referred to as the ‘SC-0.81’ and ‘Q-0.84 #2’ samples. Two different synthesis methods were used to prepare these samples. The ‘SC-0.81’ sample has nominal stoichiometry  $Nb_{0.81}CoSb$  and was slowly cooled (SC) using an induction furnace. The ‘Q-0.84 #2’ sample has nominal stoichiometry  $Nb_{0.84}CoSb$  and was thermally quenched (Q) from the melt. Details of the synthesis can be found in [156] for the slowly cooled sample and in [158] for the thermally quenched sample. The thermally quenched sample  $Nb_{0.84}CoSb$  (Q-0.84 #2) only has short-range Nb-vacancy order, whereas the slowly cooled sample  $Nb_{0.81}CoSb$  (SC-0.81) also has long-range Nb-vacancy order.



### 3.2.2 Data acquisition

Samples for electron diffraction data collection were prepared by dispersing the powder in ethanol. A few droplets of the suspension were deposited on a copper grid covered with an amorphous carbon film. Ultra-thin amorphous carbon grids were used to reduce the experimental background.

In-zone selected area electron diffraction (SAED) patterns were acquired with an FEI Tecnai G2 electron microscope operated at 200 kV using an FEI Eagle 2k charge-coupled device (CCD) (2048 x 2048 pixels with 16-bit dynamic range). In-zone precession electron diffraction (PED) patterns were acquired with a precession angle of  $1^\circ$  using a DigiSTAR precession device from NanoMEGAS.

3D ED data were acquired with an aberration-corrected cubed FEI Titan 80-300 electron microscope operated at 300 kV using a GATAN US1000XP CCD (4096 x 4096 pixels with 16-bit dynamic range). One 3D ED data set was acquired using a Quantum Detectors MerlinEM hybrid pixel detector (512 x 512 pixels with 24-bit dynamic range). The crystal was illuminated in SAED mode with an exposure time of 1 s per frame. Electron diffraction patterns were acquired with a Fischione tomography holder (tilt range of  $\pm 80^\circ$ ), in a stepwise manner, using an in-house developed script. Energy filtered 3D ED data were acquired with a Quantum 966 Gatan Image Filter, with a slit width of 10 eV.

The 3D ED data used for the dynamical refinement were collected with a step size of  $0.1^\circ$  on crystals with a size of 80-200 nm. The crystals were entirely illuminated during the whole data collection. The 3D ED data used for the diffuse scattering analysis were collected with a step size of  $0.1$  or  $0.2^\circ$  on crystals with a size of 200-3000 nm. For the larger crystals, only a thin part of the crystal was illuminated, which was recentred inside the aperture every few degrees.

Details on the acquisition of the single-crystal X-ray diffraction data can be found in [156].

### 3.2.3 Data processing

*PETS2* was used to process the 3D ED data including background subtraction of the individual frames, integration of the Bragg reflection intensities for the dynamical refinement, and applying symmetry with Laue class  $m\bar{3}m$  in the reconstruction of the three-dimensional reciprocal lattice. The three-dimensional reciprocal lattice of all 3D ED data was indexed with a cubic unit cell with cell parameter  $a = 5.89864(3) \text{ \AA}$  and space group  $F\bar{4}3m$  [159].

### 3.3 Dynamical refinement of the average crystal structure

Dynamical refinements of the average crystal structure were performed in *Jana2020*. Because the space group  $F\bar{4}3m$  is non-centrosymmetric, a twinning inversion matrix was defined. Refined parameters include the Nb occupancy, the twin fraction or Flack parameter, a thickness parameter, harmonic displacement parameters of Sb, Nb and Co, and one scale factor per virtual frame. The Nb occupancy was allowed to refine freely, whereas the occupancies of Sb and Co were fixed to 1. The intensities in the dynamical refinement were calculated for a wedge-shaped crystal [70]. The dynamical refinement parameters were set to  $g_{\max} = 2.4 \text{ \AA}^{-1}$ ,  $S_{g_{\max}}(\text{matrix}) = 0.025 \text{ \AA}^{-1}$ ,  $S_{g_{\max}}(\text{refine}) = 0.1$ ,  $R_{S_g}^{\max} = 0.66$ , and  $N_{\text{int}} = 100$ . The meaning of the dynamical refinement parameters can be found in [70, 71].

Since the intensities of the Bragg reflections in 3D ED data depend on the crystal thickness, the dynamical refinement requires the refinement of a thickness parameter. The number of refined parameters in the dynamical refinement from 3D ED is much larger than for the kinematical refinement from single-crystal X-ray diffraction. For the kinematical refinement applied to single-crystal X-ray diffraction data, one scale factor was refined for the whole dataset. For the dynamical refinement applied to 3D ED data, one scale factor was refined for each virtual frame, which is necessary because several factors (changes in the illuminated area of the crystal, slowly growing contamination of the crystal, and varying crystal thickness and thus absorption) influence the overall scale of each frame [71].

The percentage of vacancies on the Nb sites and the average displacements of Sb and Co atoms in the thermally quenched sample (Q-0.84 #2) were refined from the Bragg reflections in 3D ED data using a dynamical refinement, and were compared with reference values refined from the Bragg reflections in single-crystal X-ray diffraction data [156].

3D ED data were acquired on three different crystals, and each data set was processed separately using *PETS2*. Analogous to the refinement of the average structure from the Bragg reflections in single-crystal X-ray diffraction data [156], the dynamical refinement of the average structure was done in two stages. In the first stage (center model), the displacements of Sb and Co atoms were fixed to zero. In the second stage (split model), Sb atoms were off-centered at  $(1/2+\Delta, 1/2, 1/2)$ , Co atoms were off-centered at  $(1/4-\delta, 1/4-\delta, 3/4-\delta)$ , and the displacements of Sb and Co atoms ( $\Delta$  and  $\delta$ ) were allowed to refine freely.

Results of the dynamical refinement for the center model and for the split model are shown in Table 3.1. The standard uncertainties on the Nb occupancy and the average displacements of Sb and Co atoms only consider random errors in the intensities of the Bragg reflections and are thus underestimated. Differences between the refined Nb

### 3.3. DYNAMICAL REFINEMENT OF THE AVERAGE CRYSTAL STRUCTURE

Table 3.1: Average structure refinement for the thermally quenched sample (Q-0.84 #2). The dynamical refinement from the Bragg reflections in 3D ED data acquired on three different crystals is compared with the reference refinement from the Bragg reflections in single-crystal X-ray diffraction data [156].  $d_{\min}$  is the resolution,  $N_{\text{tot}}$  is the total number of reflections used in the refinement,  $N_{\text{all}}$  is the total number of unique reflections used in the refinement,  $N_{\text{obs}}$  the number of observed unique reflections for which  $I_{\text{obs}} > 3\sigma(I_{\text{obs}})$ ,  $N_{\text{outl}}$  the number of reflections excluded from the refinement, and  $N_{\text{par}}$  the number of refined parameters.  $R_1(\text{obs})$  is the conventional R-value of the observed reflections,  $wR_2(\text{all})$  the weighted R-value of all reflections,  $GOF(\text{obs})$  the goodness of fit of the observed reflections, and  $\text{occ}_{\text{Nb}}$  the refined Nb occupancy.

	X-rays	electrons (crystal 1)	electrons (crystal 2)	electrons (crystal 3)
$d_{\min}$ (Å)	0.4	0.5	0.5	0.45
$N_{\text{tot}}$	10474	1258	2323	2308
completeness	100%	98.31%	98.59%	98.89%
<b>Center model</b>				
$N_{\text{obs}}/N_{\text{all}}$	202/202	457/457	684/721	717/853
$N_{\text{outl}}$	0	5	7	5
$N_{\text{par}}$	7	59	52	56
$R_1(\text{obs})$ (%)	2.76	7.84	11.01	6.62
$wR_2(\text{all})$ (%)	6.00	21.04	27.91	17.81
$GOF(\text{obs})$	1.318	9.14	9.64	4.92
$\text{occ}_{\text{Nb}}$	0.831(1)	0.855(24)	0.822(20)	0.798(12)
<b>Split model</b>				
$N_{\text{obs}}/N_{\text{all}}$	292/292	459/459	683/720	718/855
$N_{\text{outl}}$	0	3	8	3
$N_{\text{par}}$	11	64	57	61
$R_1(\text{obs})$ (%)	0.49	7.85	10.82	6.93
$wR_2(\text{all})$ (%)	0.78	20.92	27.59	18.59
$GOF(\text{obs})$	0.58	9.12	9.56	5.15
$\text{occ}_{\text{Nb}}$	0.827(2)	0.863(25)	0.811(20)	0.796(15)
Sb shift (Å)	0.141(1)	0.133(15)	0.183(8)	0.181(11)
Co shift (Å)	0.130(1)	0.184(8)	0.088(165)	0.148(24)

occupancy and the refined Sb and Co displacements for the three crystals can be due to real differences in the Nb occupancy and the Sb and Co displacements between the three crystals or can be due to systematic errors in the calculation of the intensities in the dynamical refinement. Systematic errors are caused by: (i) strong multiple scattering caused by the high atomic numbers of Nb, Sb and Co; (ii) the relatively low data-to-parameter ratio (i.e., the number of observed reflections per refined parameter); (iii) no optimization of the frame orientation angles. The orientations of the frames could not be optimized due to the limited number of reflections on each frame. The limited accuracy of the goniometer of the transmission electron microscopy (TEM) stage or small unpredictable movements of the crystal during the acquisition of the data may cause the orientation of a frame as calculated from the orientation matrix to be inaccurate [70]. It should also be noted that the R-values and the refined parameters slightly depend on the dynamical refinement parameters. For example, changing the value for  $R_{S_g}^{\max} = 0.66$  from 0.66 to 0.8 changed the refined Nb occupancy by 1.9% for crystal 1, by 0.3% for crystal 2, and by 0.1% for crystal 3.

The average Nb occupancy of the three crystals  $\bar{x}$  was calculated using Equation 3.1:

$$\bar{x} = \frac{\sum_{i=1}^3 \frac{x_i}{s_i^2}}{\sum_{i=1}^3 \frac{1}{s_i^2}}, \quad \frac{1}{s_{\bar{x}}^2} = \sum_{i=1}^3 \frac{1}{s_i^2}, \quad (3.1)$$

with  $x_i$  the Nb occupancy of each crystal and  $s_i$  the standard uncertainty on the Nb occupancy. For the split model, the average Nb occupancy refined from the Bragg reflections in 3D ED data (0.813(11)) differs by only 0.014(11) from the Nb occupancy refined from the Bragg reflections in single-crystal X-ray diffraction data (0.827(2)). Refined occupancies are more accurate for highly symmetric unit cells, such as for *Nb<sub>0.84</sub>CoSb*, than for low symmetric unit cells. Palatinus and co-workers previously compared the Fe/Mg occupancy in (Mg<sub>x</sub>Fe<sub>1-x</sub>)<sub>2</sub>Si<sub>2</sub>O<sub>6</sub> refined from the Bragg reflections in 3D ED data with the Fe/Mg occupancy refined from the Bragg reflections in single-crystal X-ray diffraction data, and found a difference in Fe/Mg occupancy of 0.028(8) [70, 160].

For the single-crystal X-ray diffraction data, the R-value improved significantly after refinement of the displacements of Sb and Co atoms [156], while for the 3D ED data, the R-value stayed approximately the same (Table 3.1). The average displacements refined from the Bragg reflections in 3D ED data (0.175(6) Å for Sb, and 0.180(8) Å for Co) were calculated using Equation 3.1 and differ by 0.040(5) Å from the average displacements refined from the Bragg reflections in single-crystal X-ray diffraction data (0.141(1) Å for Sb and 0.130(1) Å for Co). Palatinus and co-workers previously compared the displacements refined from the Bragg reflections in 3D ED data with the displacements refined from the Bragg reflections in single-crystal X-ray diffraction data for three different samples and found a difference in bond length between 0.01 Å and 0.02 Å [70]. The difference in bond length is thus larger for *Nb<sub>0.84</sub>CoSb* than for the samples reported in [70], which could be due to differences in the amount of multiple scattering. The atomic numbers of the elements of the samples in [70] are lower than the

### 3.3. DYNAMICAL REFINEMENT OF THE AVERAGE CRYSTAL STRUCTURE

atomic numbers of Nb, Sb and Co. Because the average mean free path between two scattering events is smaller in samples with elements with higher atomic numbers, the intensities in the 3D ED data acquired on Nb<sub>0.84</sub>CoSb are more influenced by multiple scattering than the intensities in the 3D ED data acquired on the samples in [70].

Figure 3.2 shows the difference Fourier maps ( $F(\text{obs})-F(\text{calc})$ ) in the  $x0.5z$  plane after refinement of the average structure of the thermally quenched sample (Q-0.84 #2) with the center model, both for the single-crystal X-ray diffraction data and the 3D ED data acquired on the three different crystals. The average positions of Sb and Nb atoms

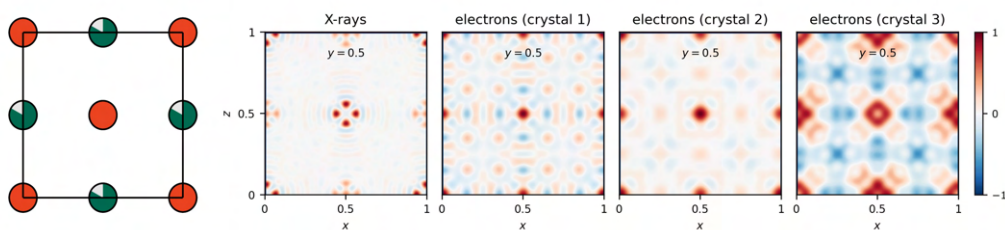


Figure 3.2: Left: The average positions of Sb (orange) and Nb (green) atoms in the  $x0.5z$  plane. Right: Difference Fourier maps in the  $x0.5z$  plane after refinement of the average structure of the thermally quenched sample (Q-0.84 #2) with the center model, both for single-crystal X-ray diffraction data and 3D ED data acquired on three different crystals.

in the  $x0.5z$  plane are shown on the left. The red/blue features in the difference Fourier map represent the residual electron density for X-ray diffraction and the residual atomic charge density for electron diffraction. In the difference Fourier map of the single-crystal X-ray diffraction data, four maxima in the residual electron density can be observed around the average position of the Sb atom, which indicate splitting of the Sb position. Splitting of the Sb position is unclear from the difference Fourier maps of the 3D ED data acquired on crystal 1 and crystal 2 but is clear from the difference Fourier map of the 3D ED data acquired on crystal 3, even though the maxima in the residual atomic charge density are broader than for X-ray diffraction. Differences between the difference Fourier maps of the three crystals are likely due to systematic errors in the calculation of the intensities in the dynamical refinement. This also explains the difference between the average Sb displacement refined from the Bragg reflections in 3D ED and single-crystal X-ray diffraction data.

## 3.4 Effect of different parameters on the observed diffuse scattering

### 3.4.1 In-zone electron diffraction

Figure 3.3 shows the  $h0l$  and  $hhl$  planes reconstructed from 3D ED data, in-zone SAED patterns, and in-zone PED patterns acquired on the same crystal. The diffuse circles in the  $h0l$  plane reconstructed from 3D ED show clear intensity modulations. By contrast, the diffuse circles in the in-zone SAED pattern have almost the same intensity everywhere due to multiple scattering. The intensity distribution of the diffuse scattering in the in-zone PED patterns is very similar to the one in the in-zone SAED patterns. As discussed in Subsection 2.4.2, the higher-order Bragg reflections have higher intensities in in-zone PED patterns than in in-zone SAED patterns. The spatial resolution of the diffuse scattering is also lower in in-zone PED patterns than in in-zone SAED patterns.

3.4. EFFECT OF DIFFERENT PARAMETERS ON THE OBSERVED  
DIFFUSE SCATTERING

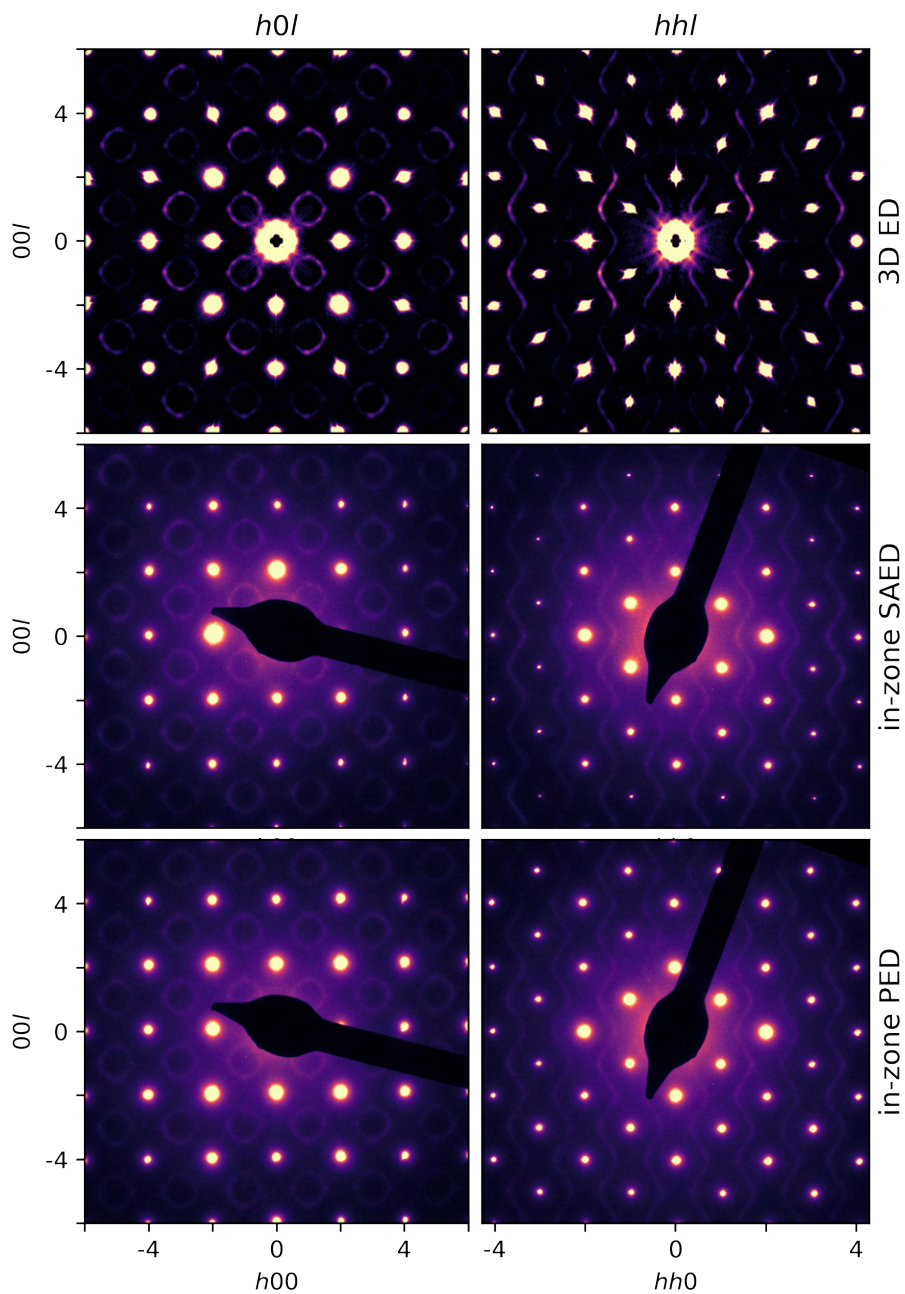


Figure 3.3: Comparison of the  $h0l$  and  $hhl$  planes reconstructed from 3D ED data, in-zone SAED patterns, and in-zone PED patterns acquired on the same crystal. Data acquired on the thermally quenched sample (Q-0.84 #2).

### 3.4.2 Background subtraction

The background of the in-zone SAED patterns and in-zone PED patterns in Figure 3.3 has not been subtracted. For the 3D ED data, the background of the individual frames has been subtracted in *PETS2* before the reconstruction of the *h0l* and *hhl* planes. Figure 3.4 shows the *hhl* plane reconstructed from 3D ED data acquired with and without energy filter on the same crystal. Except for using an energy filter, the experimental settings were identical for both 3D ED data sets. The *hhl* planes after background subtraction in *PETS2* are also shown in Figure 3.4. As discussed in Subsection 2.4.3, an energy filter

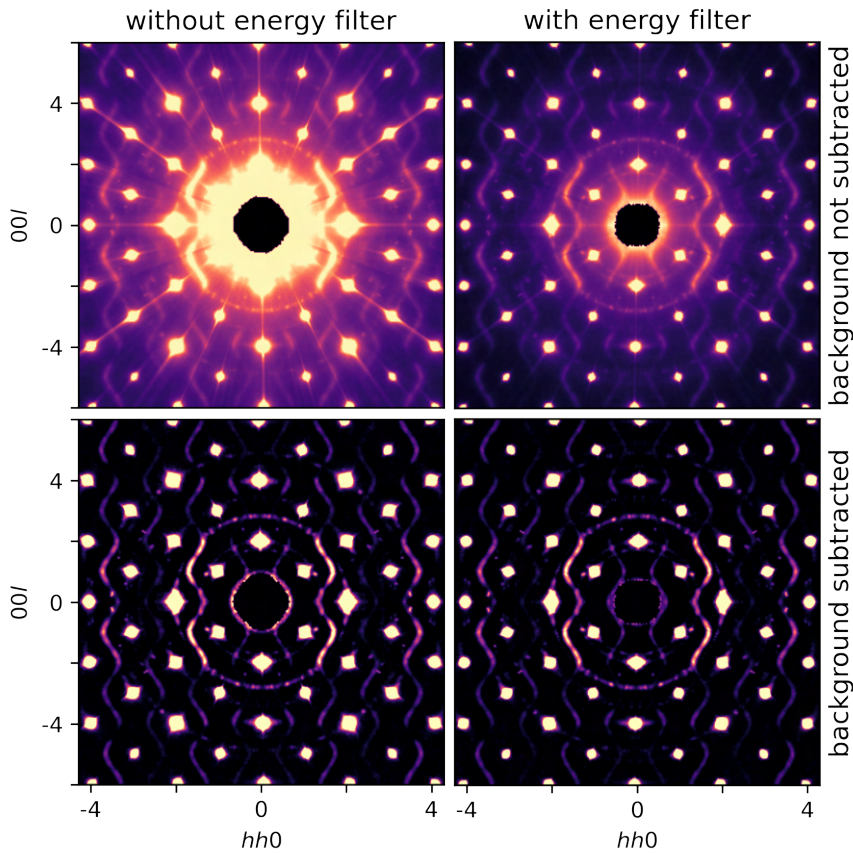


Figure 3.4: Comparison of the *hhl* plane reconstructed from 3D ED data acquired with and without energy filter, before and after background subtraction in *PETS2*. The circle passing through the (220) Bragg reflection is due to neighbouring crystals. Due to symmetry averaging with Laue class  $m\bar{3}m$ , each additional reflection in the *hhl* plane will appear four times. Data acquired on the thermally quenched sample (Q-0.84 #2).

with a slit width of 10 eV reduces the thermal diffuse scattering but does not entirely remove it. Subtracting the background of the individual frames in *PETS2* before the reconstruction of the three-dimensional reciprocal lattice is thus the best method to obtain



### 3.4. EFFECT OF DIFFERENT PARAMETERS ON THE OBSERVED DIFFUSE SCATTERING

diffuse scattering data that can be used for quantitative analysis.

#### 3.4.3 Symmetry averaging

Figure 3.5 shows the  $h0l$  and  $hhl$  planes reconstructed from 3D ED data before and after applying symmetry averaging with Laue class  $m\bar{3}m$ . The  $h0l$  and  $hhl$  planes before applying symmetry averaging have a missing wedge due to the limited tilt range ( $90^\circ$  for the thermally quenched sample (Q-0.84 #2) and  $100^\circ$  for the slowly cooled sample (SC-0.81)). Applying symmetry averaging with Laue class  $m\bar{3}m$  allows to fill the missing wedge in the three-dimensional reciprocal lattice, which is required for the calculation of the 3D- $\Delta$ PDF in Section 3.6.

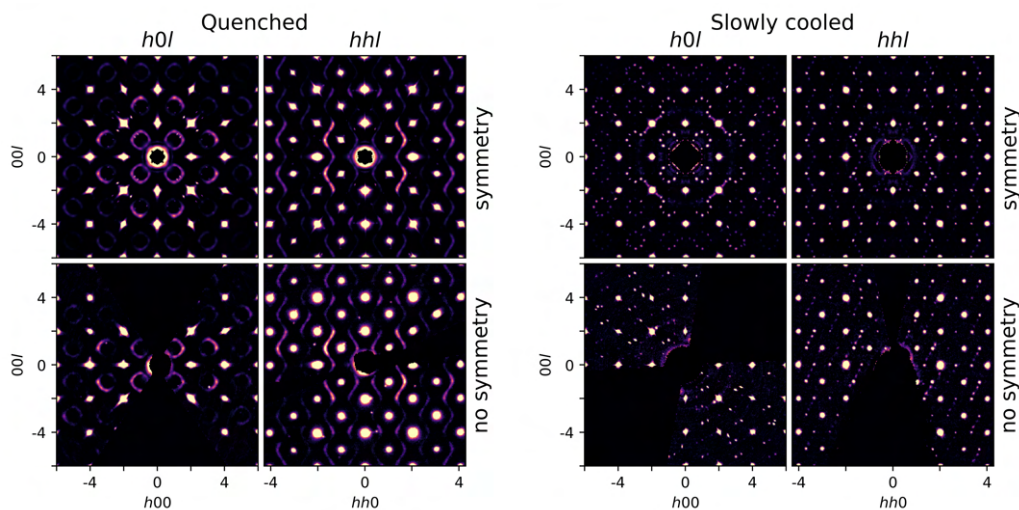


Figure 3.5: Comparison of the  $h0l$  and  $hhl$  planes reconstructed from 3D ED data before and after applying symmetry averaging with Laue class  $m\bar{3}m$ , both for the thermally quenched sample (Q-0.84 #2) and the slowly cooled sample (SC-0.81). The additional reflections between the Bragg reflections are due to neighbouring crystals. Due to symmetry averaging with Laue class  $m\bar{3}m$ , each additional reflection in the  $h0l$  plane will appear eight times, while each additional reflection in the  $hhl$  plane will appear four times.

The 3D ED data for the slowly cooled sample (SC-0.81) were acquired on a 150 nm sized crystal. Crystals with long-range Nb-vacancy order consist of twins with different orientations [161]. Each twin orientation gives rise to one pair of satellite reflections. Because some twin orientations are missing, not all satellite reflections are visible in the  $h0l$  and  $hhl$  planes before symmetry averaging. Symmetry averaging with Laue class  $m\bar{3}m$  will thus introduce additional satellite reflections corresponding to the other twin orientations.

### 3.4.4 Convergence of the electron beam

In 3D ED, the crystal can be illuminated either in SAED mode or in nano electron diffraction (NED) mode [42]. In SAED mode, the incident electron beam is parallel, and the sample area used for collecting diffraction data is determined by the selected area aperture. In NED mode, a small C2 condenser aperture is inserted, and the sample area used for collecting diffraction data is determined by the beam size. The incident electron beam in NED mode is usually slightly convergent. Acquiring 3D ED data in SAED mode will thus improve the spatial resolution of the observed diffuse scattering. Figure 3.6 shows the  $h0l$  and  $hhl$  planes reconstructed from 3D ED data acquired on the same crystal in SAED mode and in NED mode. Due to the slightly convergent electron beam in NED

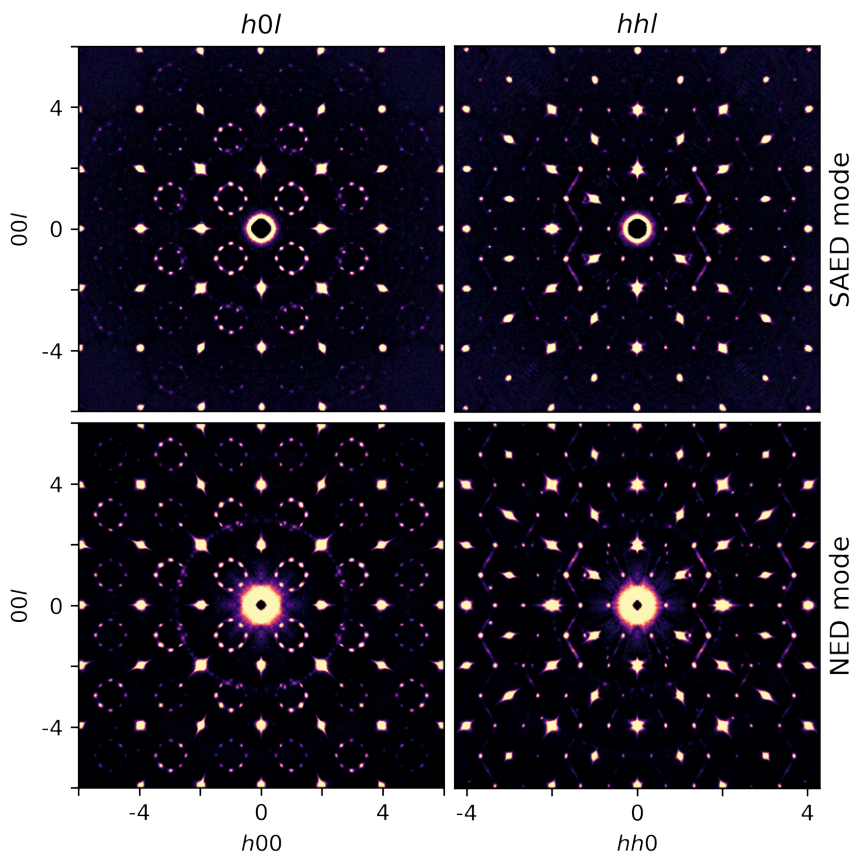


Figure 3.6: Comparison of the  $h0l$  and  $hhl$  planes reconstructed from 3D ED data acquired in SAED and NED mode. Data acquired on the slowly cooled sample (SC-0.81).

mode, the higher-order Bragg reflections have higher intensities for the 3D ED data acquired in NED mode than for the 3D ED data acquired in SAED mode.

### 3.4. EFFECT OF DIFFERENT PARAMETERS ON THE OBSERVED DIFFUSE SCATTERING

#### 3.4.5 Detector point spread function

Important detector performance characteristics for diffuse scattering measurements include a narrow detector point spread function, low sensor intrinsic background noise, and a high dynamic range [4]. Hybrid pixel detectors such as Pilatus [162], XPAD [163] or Medipix [164] are used for the acquisition of high-quality single-crystal X-ray diffuse scattering data at synchrotron sources. The point spread function is essentially one pixel broad, they can be operated under zero intrinsic noise conditions, and the dynamic range is higher than for CCDs [4].

Figure 3.7 shows the  $hhl$  plane reconstructed from 3D ED data acquired with a GATAN US1000XP CCD and a Quantum Detectors MerlinEM hybrid pixel detector on the same crystal. In contrast to X-ray diffraction, the detector point spread function

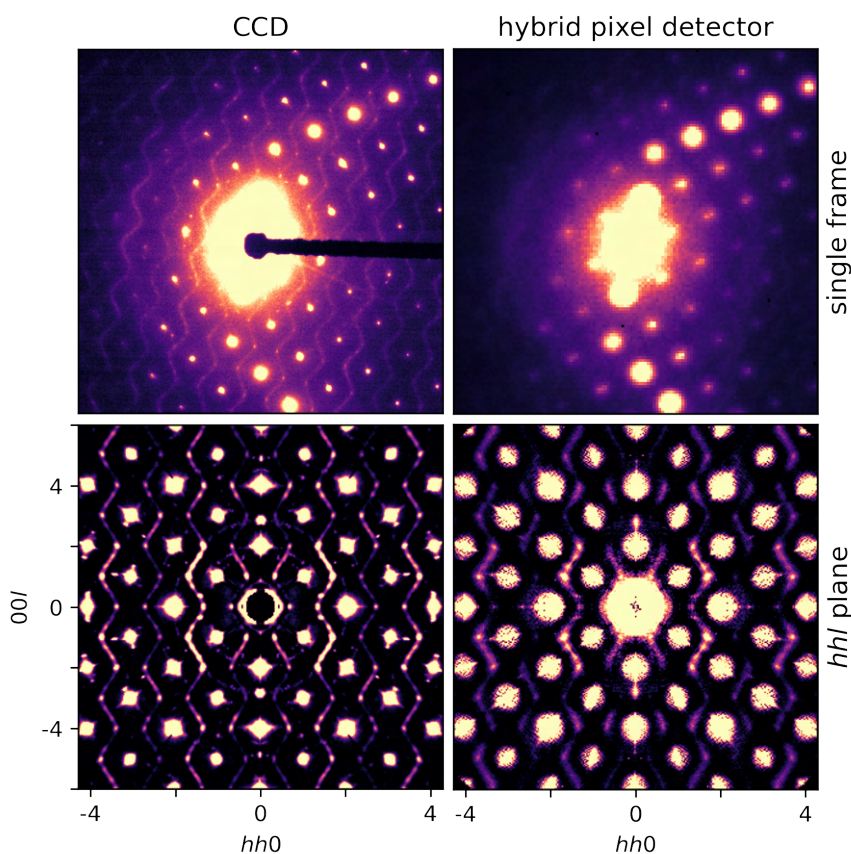


Figure 3.7: Comparison of the  $hhl$  plane reconstructed from 3D ED data acquired with a GATAN US1000XP CCD and a Quantum Detectors MerlinEM hybrid pixel detector on the same crystal. Data acquired on the thermally quenched sample (Q-0.84 #2).

for electron diffraction is much broader for the hybrid pixel detector than for the CCD,

which can be explained by charge sharing [165]. Electrons that fall in on the hybrid pixel detector create a charge cloud in the silicon sensor. Electrostatic repulsion and charge diffusion cause the charge cloud to expand, which explains why electrons are also detected by neighbouring pixels. The spatial resolution of the observed diffuse scattering is thus higher for 3D ED data acquired with a CCD than for 3D ED data acquired with a hybrid pixel detector.

### 3.4.6 Crystal mosaicity

Figure 3.8 shows the  $h0l$  and  $hhl$  planes reconstructed from 3D ED data acquired on five different crystals of the thermally quenched sample (Q-0.84 #2). The angular broadening of the Bragg reflections is larger for crystal 4 than for crystal 5, which is due to differences in the crystal mosaicity. Crystals consist of domains in which the lattice planes are slightly misaligned. The larger the spread of lattice plane orientations, the larger the mosaicity. The spatial resolution of the observed diffuse scattering will be higher for crystals with a lower mosaicity.

Not all crystals of the thermally quenched sample (Q-0.84 #2) have identical diffuse scattering. All crystals have satellite reflections on top of the diffuse scattering, but their sharpness is different. The sharpness of the satellite reflections is related to the correlation length of the local Nb-vacancy order.

It should also be noted that the Bragg reflections close to the central beam were overexposed due to the limited dynamical range of the CCD. When the integral dose loaded on a single pixel exceeds the saturation limit, electrons will spill to neighbouring pixels giving rise to blooming or streaking effects [4].

### 3.4. EFFECT OF DIFFERENT PARAMETERS ON THE OBSERVED DIFFUSE SCATTERING

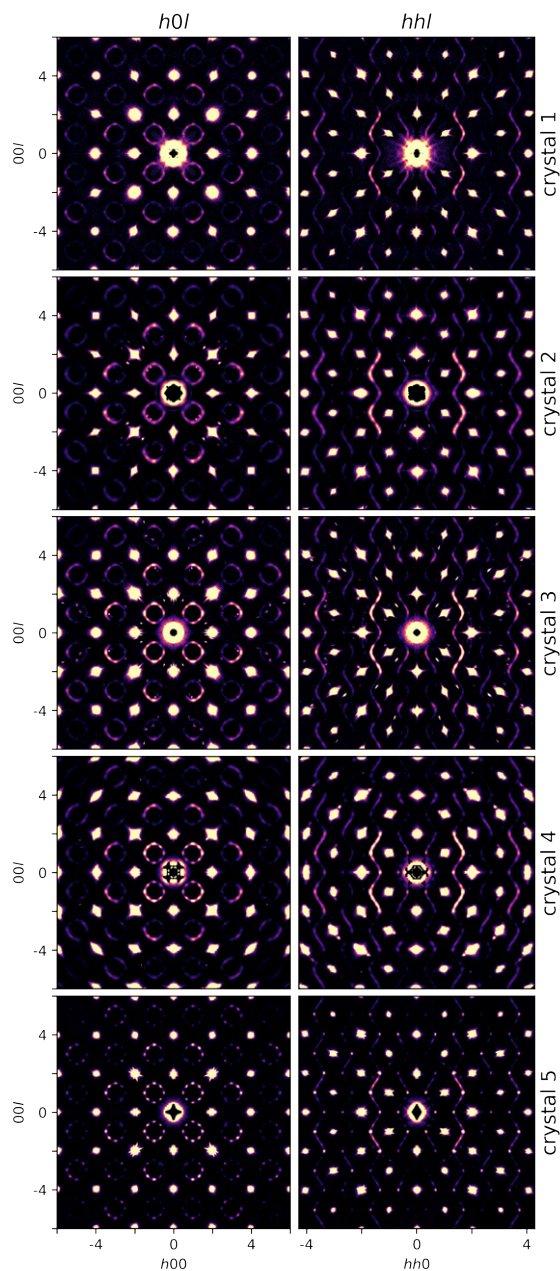


Figure 3.8: Comparison of the  $h0l$  and  $hhl$  planes reconstructed from 3D ED data acquired on five different crystals of the thermally quenched sample (Q-0.84 #2). The additional reflections between the Bragg reflections for crystals 2 and 3 are due to neighbouring crystals. Due to symmetry averaging with Laue class  $m\bar{3}m$ , each additional reflection in the  $h0l$  plane will appear eight times, while each additional reflection in the  $hhl$  plane will appear four times.

### 3.4.7 X-ray and electron diffraction

Figure 3.9 shows the  $hhl$  plane and the planes 1, 2, 3 and 4 voxels above the  $hhl$  plane, reconstructed from single-crystal X-ray and 3D ED data acquired on the slowly cooled sample (SC-0.81). Each plane has a thickness of one voxel. The  $hhl$  plane reconstructed from 3D ED data shows additional satellite reflections compared with the  $hhl$  plane reconstructed from single-crystal X-ray diffraction data (reflections indicated by the white circles). These additional satellite reflections have their maximum intensity in the plane four voxels above the  $hhl$  plane. The Bragg reflections are broader in the 3D ED data than in the single-crystal X-ray diffraction data, which was also observed in [13]. The spatial resolution of the observed diffuse scattering is thus lower for 3D ED than for single-crystal X-ray diffraction. Consequently, the reflections indicated by the white circles in the  $hhl$  plane reconstructed from 3D ED are from slightly above and below the  $hhl$  plane.

To account for resolution effects, the intensity of each pixel in the calculated diffuse scattering data will be convoluted with a Gaussian function. The standard deviation of the Gaussian function will be estimated from the intensity profile of unsaturated Bragg reflections.

### 3.4. EFFECT OF DIFFERENT PARAMETERS ON THE OBSERVED DIFFUSE SCATTERING

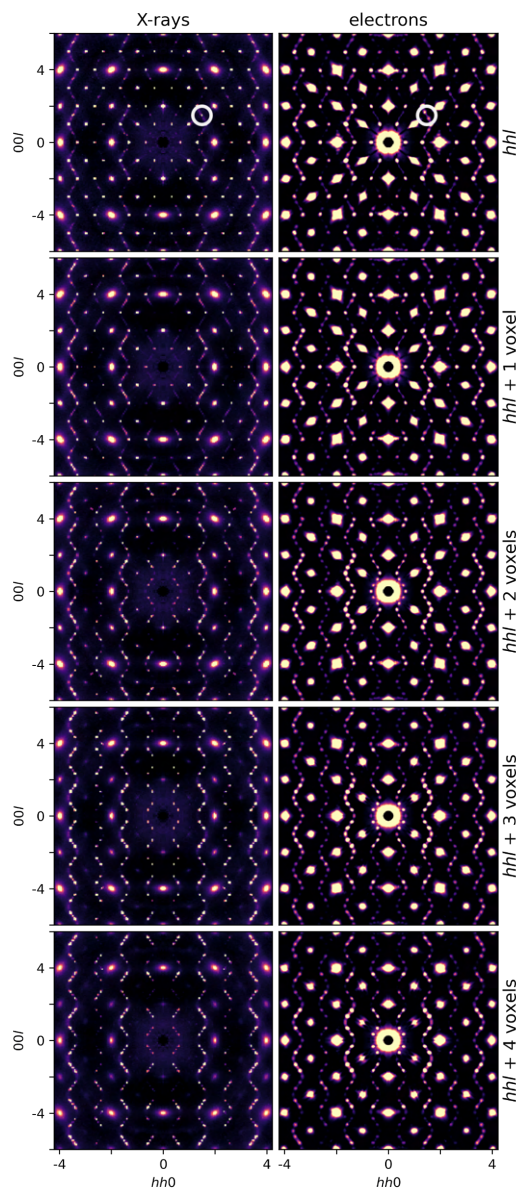


Figure 3.9: Comparison of the  $hhl$  plane and the planes 1, 2, 3 and 4 voxels above the  $hhl$  plane, reconstructed from single-crystal X-ray diffraction and 3D ED data. The  $hhl$  plane reconstructed from 3D ED data shows additional satellite reflections compared with the  $hhl$  plane reconstructed from single-crystal X-ray diffraction data (reflections indicated by the white circles). These additional satellite reflections have their maximum intensity four voxels above the  $hhl$  plane. Data acquired on the slowly cooled sample (SC-0.81).

### 3.5 Calculated diffuse scattering

*DISCUS* was used to build a model of the short-range Nb-vacancy order in the thermally quenched sample  $Nb_{0.84}CoSb$  (Q-0.84 #2) and of the long-range Nb-vacancy order in the slowly cooled sample  $Nb_{0.81}CoSb$  (SC-0.81).

#### 3.5.1 Long-range order model

For the long-range order model, a cell with a size of  $6 \times 6 \times 6$  NbCoSb unit cells (cell parameter  $a = 5.89864(3)$  Å, space group  $F\bar{4}3m$  [159]) was created, and 1/6 of the Nb atoms were replaced by vacancies to form the B1 structure<sup>1</sup> as defined in [157]. Each Sb atom was moved by 0.148 Å towards its neighbouring vacancy, and each Co atom was moved by 0.128 Å away from its neighbouring vacancy (displacements refined from the Bragg reflections in the single-crystal X-ray diffraction data of the slowly cooled sample  $Nb_{0.81}CoSb$  (SC-0.81)) [156]. The Sb atoms were moved along the cubic  $\langle 100 \rangle$  directions, while the Co atoms were moved along the cubic  $\langle 111 \rangle$  directions (Figure 3.1 (b)). The resulting B1 cell (Figure 3.10) has cell parameter  $a = 35.3918(2)$  Å and space group  $PI$ . A structure with a size of  $6 \times 6 \times 6$  B1 cells was created in *DISCUS*.

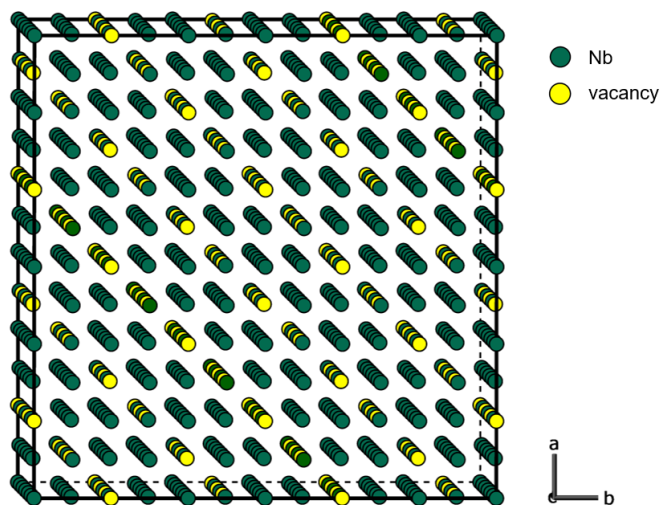


Figure 3.10: B1 structure, as defined in [157], showing the Nb-vacancy ordering in the long-range order model. Sb and Co atoms are omitted for clarity.

<sup>1</sup>In [156], the BD structure was used instead of the B1 structure. The BD structure is a combination of the B1 structure and the A2 structure. The BD, B1 and A2 structures are defined in [157]. Because we noticed that the diffraction patterns calculated from the B1 structure agree better with the experimental diffraction patterns than the ones calculated from the BD structure, we used the B1 structure instead of the BD structure.



### 3.5.2 Short-range order model

Correlation coefficients  $c_{mn}^{uvw}$  between neighbouring vacancies in *DISCUS* are defined as [166, 37]:

$$c_{mn}^{uvw} = \frac{P_{mn}^{uvw} - (\text{occ}_{\text{Nb}})^2}{\text{occ}_{\text{Nb}}(1 - \text{occ}_{\text{Nb}})}, \quad (3.2)$$

with  $P_{mn}^{uvw}$  the probability that sites  $m$  and  $n$  are occupied by the same atom type,  $uvw$  the interatomic vector and  $\text{occ}_{\text{Nb}}$  the Nb occupancy. Negative values of  $c_{mn}^{uvw}$  indicate that sites  $m$  and  $n$  tend to be occupied by different atom types while positive values of  $c_{mn}^{uvw}$  indicate that sites  $m$  and  $n$  tend to be occupied by the same atom type. A correlation value of zero describes a random distribution of the two atom types. The maximum negative value of  $c_{mn}^{uvw}$  for a given occupancy  $\text{occ}_{\text{Nb}}$  is  $-\text{occ}_{\text{Nb}}/(1 - \text{occ}_{\text{Nb}})$  ( $P_{mn}^{uvw} = 0$ ), the maximum positive value is  $+1$  ( $P_{mn}^{uvw} = \text{occ}_{\text{Nb}}$ ).

According to Equation 3.2, the maximum negative value of  $c_{(1/2,1/2,0)}$  is  $\approx -4.78$  ( $P_{mn}^{(1/2,1/2,0)} = 0$ ), with  $P_{mn}^{(1/2,1/2,0)}$  the probability that two nearest neighbouring Nb sites  $m$  and  $n$  are occupied by Nb atoms. However, for  $\text{Nb}_{0.84}\text{CoSb}$  a value of  $P_{mn}^{(1/2,1/2,0)} = 0$  cannot be achieved and the maximum achievable negative value of  $c_{(1/2,1/2,0)}$  is  $\approx -0.20$ .

For the short-range order model, a starting structure with a size of  $25 \times 25 \times 25$  NbCoSb unit cells (cell parameter  $a = 5.89864(3)$  Å, space group  $F\bar{4}3m$  [159]) was created. 1/6 of the Nb atoms were randomly selected and replaced by vacancies. Periodic boundary conditions were imposed to avoid edge effects.

A Monte Carlo simulation in *DISCUS* is used to minimize the energy  $E$  of the crystal until the target correlations between nearest neighbour vacancy pairs ( $c_{(1/2,1/2,0)}$ ) and next-nearest neighbour vacancy pairs ( $c_{(1,0,0)}$ ) are achieved. The energy  $E$  of the crystal is defined as [157]:

$$E = \frac{1}{2} \sum_{i=1}^{N_{\text{vac}}} \left( J_1 \sum_j^{12\text{NN}} S_{ij} + J_2 \sum_{j'}^{6\text{NNN}} S_{ij'} \right), \quad (3.3)$$

with  $N_{\text{vac}}$  the number of vacancies in the crystal. The summation in the first term is over all 12 nearest neighbour (NN) vacancy sites  $j$  of vacancy  $i$ , whereas the summation in the second term is over all six next-nearest neighbour (NNN) vacancy sites  $j'$  of vacancy  $i$ .  $S_{ij} = 1$  if site  $j$  is occupied by a vacancy and  $S_{ij} = 0$  if site  $j$  is occupied by a Nb atom. Similarly,  $S_{ij'} = 1$  if site  $j'$  is occupied by a vacancy and  $S_{ij'} = 0$  if site  $j'$  is occupied by a Nb atom.  $J_1$  is the energy assigned to a nearest neighbour vacancy pair, and  $J_2$  is the energy assigned to a next-nearest neighbour vacancy pair. Nearest and next-nearest neighbour vacancies will avoid each other when  $J_1 > 0$  and  $J_2 > 0$ . During the Monte Carlo simulation, the values of the energies  $J_1$  and  $J_2$  in Equation 3.3 are adjusted and the target correlations  $c_{(1/2,1/2,0)}$  and  $c_{(1,0,0)}$  are calculated. When the target correlations  $c_{(1/2,1/2,0)}$  and  $c_{(1,0,0)}$  are achieved, the energy  $E$  of the crystal will be equal to zero [37].

Each Monte Carlo step, two randomly selected Nb atoms/vacancies are switched positions. When the new configuration has a lower energy  $E$ , then it is always accepted. When the new configuration has a higher energy  $E$ , then it is only accepted when the transition probability  $P$ , given by

$$P = \frac{\exp(-\Delta E/kT)}{1 + \exp(-\Delta E/kT)}, \quad (3.4)$$

is less than a random number  $\eta$ , chosen uniformly in the range [0,1].  $\Delta E$  is the energy difference between the new and the old configuration,  $T$  is the temperature, and  $k$  is Boltzmann's constant. The temperature  $T$  controls the proportion of accepted modifications that lead to a higher energy  $E$ . If  $T = 0$ , only changes that decrease the energy  $E$  will be accepted. The higher the temperature  $T$ , the more moves will be accepted that lead to a higher energy  $E$  [92, 4, 37]. In all Monte Carlo simulations,  $kT$  was chosen equal to 0.001. One Monte Carlo cycle is defined as the number of Monte Carlo steps necessary to visit every crystal site once on average. The number of Monte Carlo cycles was chosen equal to 500 times the number of atoms within the crystal.

A second Monte Carlo simulation in *DISCUS* is used to minimize the energy  $E$  of the crystal until the target distances between a vacancy  $i$  and a neighbouring Sb atom  $k$  ( $\tau_{ik}$ ) and between a vacancy  $i$  and a neighbouring Co atom  $k'$  ( $\tau_{ik'}$ ) are achieved. The energy  $E$  of the crystal is defined by a Lennard-Jones potential energy:

$$E = \frac{1}{2} \sum_{i=1}^{N_{\text{vac}}} \left( \sum_k^{6\text{Sb}} D \left[ \left( \frac{\tau_{ik}}{d_{ik}} \right)^{12} - \left( \frac{\tau_{ik}}{d_{ik}} \right)^6 \right] + \sum_{k'}^{4\text{Co}} D \left[ \left( \frac{\tau_{ik'}}{d_{ik'}} \right)^{12} - \left( \frac{\tau_{ik'}}{d_{ik'}} \right)^6 \right] \right), \quad (3.5)$$

with  $N_{\text{vac}}$  the number of vacancies in the crystal and the potential depth  $D = -100$ . The summation in the first term is over all six neighbouring Sb atoms  $k$  of vacancy  $i$ , whereas the summation in the second term is over all four neighbouring Co atoms  $k'$  of vacancy  $i$ .  $d_{ik}$  is the distance between a vacancy  $i$  and a neighbouring Sb atom  $k$ .  $d_{ik'}$  is the distance between a vacancy  $i$  and a neighbouring Co atom  $k'$ . During the Monte Carlo simulation, the values of the distances  $d_{ik}$  and  $d_{ik'}$  in Equation 3.5 are adjusted. When the target distances  $\tau_{ik}$  and  $\tau_{ik'}$  are achieved, the Lennard-Jones potential energy will achieve its minimum.

Each Monte Carlo step, one Sb atom is moved towards its neighbouring vacancy and one Co atom is moved away from its neighbouring vacancy. When the new configuration has a lower energy  $E$ , then it is always accepted. When the new configuration has a higher energy  $E$ , then it is only accepted when the transition probability  $P$  in Equation 3.4 is less than a random number  $\eta$ , chosen uniformly in the range [0,1] [37]. The number of Monte Carlo cycles was chosen equal to 1000 times the number of atoms within the crystal.

### 3.5.3 Calculation of the diffuse scattering

The intensities in reciprocal space were calculated according to the standard formula for kinematic scattering (Equation 1.10). The structure factor  $F(\mathbf{Q})$  was calculated using the discrete Fourier transform (DFT) (Equation 1.11).

Three-dimensional electron diffraction (3D ED) data were acquired on the thermally quenched sample  $\text{Nb}_{0.84}\text{CoSb}$  (Q-0.84 #2) and the slowly cooled sample  $\text{Nb}_{0.81}\text{CoSb}$  (SC-0.81). Figure 3.11 shows the  $h0l$  plane reconstructed from single-crystal X-ray and single-crystal electron diffraction data acquired on both samples. The  $h0l$  plane

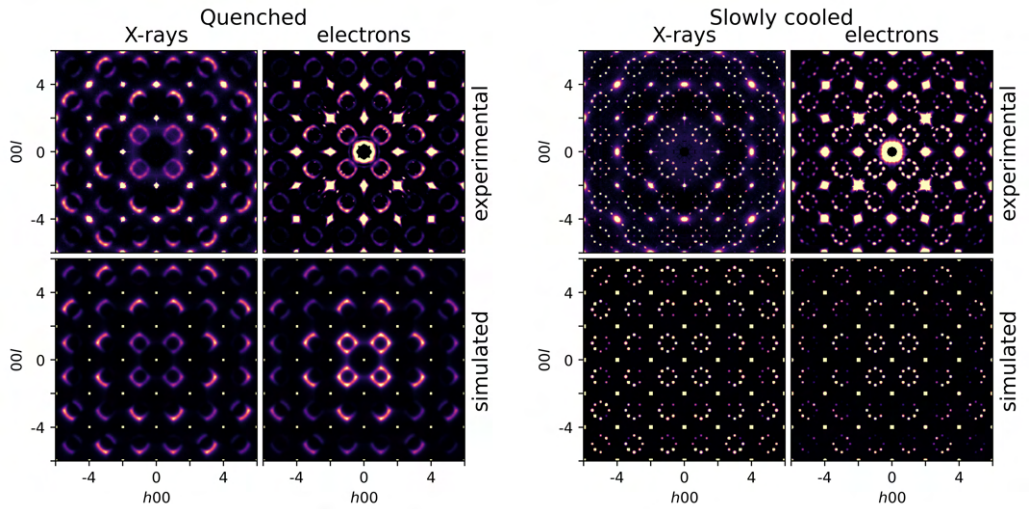


Figure 3.11: Comparison of the  $h0l$  plane from single-crystal X-ray and single-crystal electron diffraction, both for the thermally quenched sample (Q-0.84 #2) and the slowly cooled sample (SC-0.81). The top row shows the experimental diffuse scattering; the bottom row shows the diffuse scattering calculated in *Scatty* from the structure models calculated in *DISCUS*. The experimental single-crystal X-ray diffraction data were previously reported by [156].

for  $-20 \leq h, l \leq 20$  is shown in Figure 3.12. The  $h0.5l$  and  $hhl$  planes are shown in Figure 3.13 and Figure 3.14.

The diffuse scattering intensity at lower scattering angles is higher for electron diffraction than for X-ray diffraction, which can be explained by differences in the atomic form factors for electrons and X-rays. Figure 3.15 shows the X-ray and electron atomic form factors of Co, Nb and Sb as a function of the scattering angle. The X-ray atomic form factor is the Fourier transform of the electron density, whereas the electron atomic form factor is the Fourier transform of the atomic charge density. Because the electrostatic potential is broader than the electron density, the electron atomic form factors decrease faster to zero than the X-ray atomic form factors, which explains the

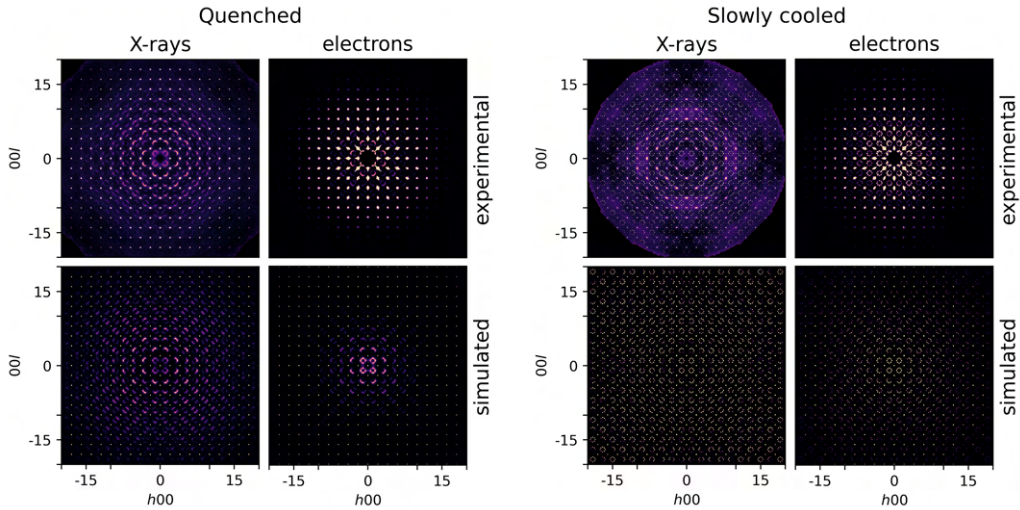


Figure 3.12: Comparison of the  $h0l$  plane from single-crystal X-ray and single-crystal electron diffraction, both for the thermally quenched sample (Q-0.84 #2) and the slowly cooled sample (SC-0.81). The top row shows the experimental diffuse scattering; the bottom row shows the diffuse scattering calculated in *Scatty* from the structure models calculated in *DISCUS*. The experimental single-crystal X-ray diffraction data were previously reported by [156].

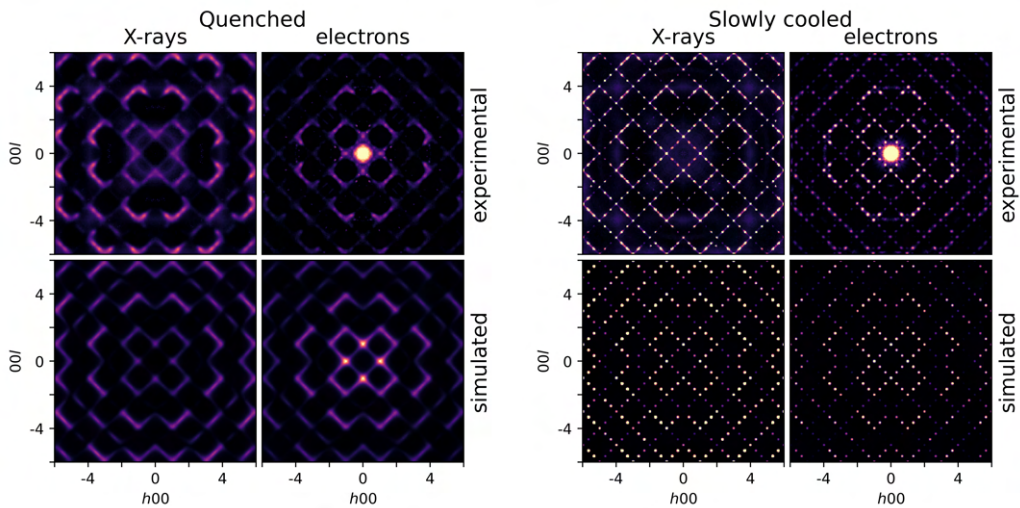


Figure 3.13: Comparison of the  $h0.5l$  plane from single-crystal X-ray and single-crystal electron diffraction, both for the thermally quenched sample (Q-0.84 #2) and the slowly cooled sample (SC-0.81). The top row shows the experimental diffuse scattering; the bottom row shows the diffuse scattering calculated in *Scatty* from the structure models calculated in *DISCUS*.

### 3.5. CALCULATED DIFFUSE SCATTERING

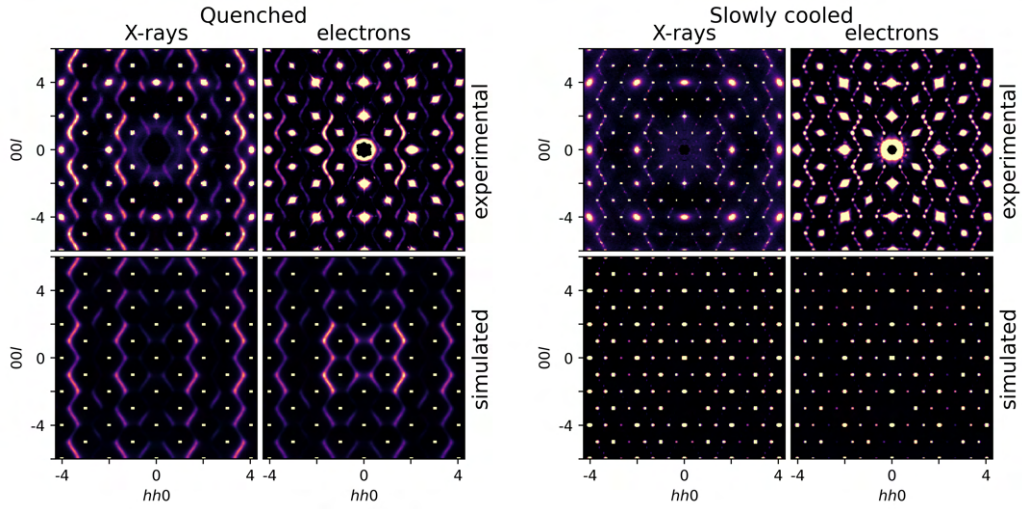


Figure 3.14: Comparison of the  $hhl$  plane from single-crystal X-ray and single-crystal electron diffraction, both for the thermally quenched sample (Q-0.84 #2) and the slowly cooled sample (SC-0.81). The top row shows the experimental diffuse scattering; the bottom row shows the diffuse scattering calculated in *Scatty* from the structure models calculated in *DISCUS*. The experimental single-crystal X-ray diffraction data were previously reported by [156].

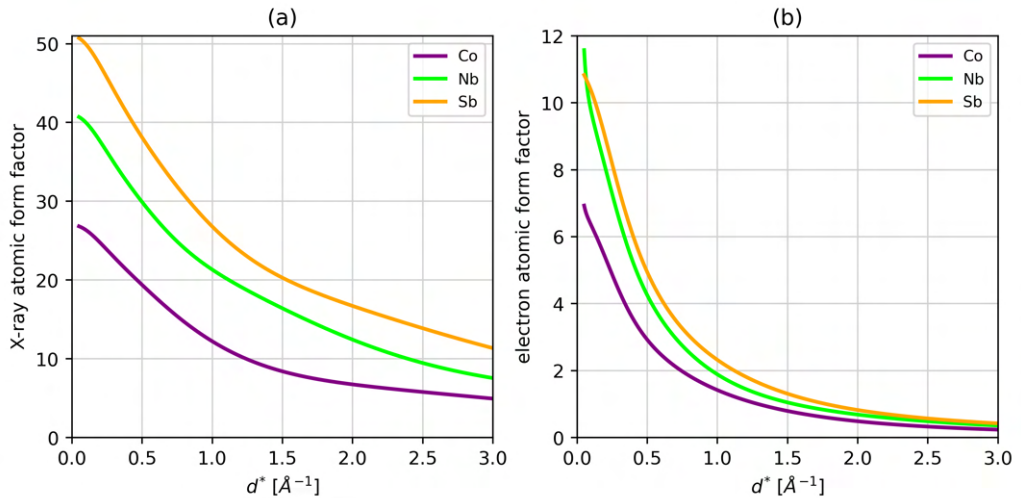


Figure 3.15: (a) X-ray and (b) electron atomic form factors of Co, Nb and Sb as a function of  $d^* = 2 \sin(\theta)/\lambda$ . With  $d$  the distance between the lattice planes,  $\theta$  the scattering angle and  $\lambda$  the wavelength.

difference in the intensity distribution of the diffuse scattering.

The bottom row in Figure 3.11 shows the  $h0l$  plane of the three-dimensional diffuse scattering calculated in *Scatty* from the structure models calculated in *DISCUS*. For the thermally quenched sample (Q-0.84 #2), the diffuse scattering was calculated from the short-range order model with a correlation coefficient for nearest neighbour vacancies of  $c_{(1/2,1/2,0)} = -0.19$  and a correlation coefficient for next-nearest neighbour vacancies of  $c_{(1,0,0)} = -0.012$ . The values for  $c_{(1/2,1/2,0)}$  and  $c_{(1,0,0)}$  were determined based on a series of Monte Carlo simulations and gave the best visual agreement between the observed and calculated diffuse scattering. It should be noted that the values for  $c_{(1/2,1/2,0)}$  and  $c_{(1,0,0)}$  are different from the ones used for the calculation of the diffuse scattering in [156]. The diffuse scattering was calculated for an Sb displacement of 0.141 Å and a Co displacement of 0.130 Å (displacements refined from the Bragg reflections in single-crystal X-ray diffraction data in Table 3.1). For the slowly cooled sample (SC-0.81), the diffuse scattering was calculated from the long-range order model. Symmetry with Laue class  $m\bar{3}m$  was applied to the three-dimensional diffuse scattering calculated in *Scatty* (Figure 3.16).

The short-range order model in *DISCUS* was calculated for  $kT = 0.001$  (Equation 3.4). If  $T = 0$ , only changes that decrease the energy  $E$  of the crystal will be accepted. The higher the temperature  $T$ , the more moves will be accepted that lead to a higher energy  $E$  [92, 4, 37]. Figure 3.17 shows the diffuse scattering in the  $h0l$  plane calculated for different values of  $kT$ . Differences in the sharpness of the diffuse scattering can be explained by differences between the target and the achieved correlation coefficients. The diffuse scattering was calculated for a target correlation between nearest neighbour vacancies of  $c_{(1/2,1/2,0)} = -0.20$  and a target correlation between next-nearest neighbour vacancies of  $c_{(1,0,0)} = -0.10$ . For  $kT = 0.001$ , the achieved correlations are  $c_{(1/2,1/2,0)} = -0.18$  and  $c_{(1,0,0)} = -0.09$ , while for  $kT = 1$ , the achieved correlations are  $c_{(1/2,1/2,0)} = -0.16$  and  $c_{(1,0,0)} = -0.07$ . The achieved correlations are thus lower for higher values of  $kT$ , which explains the differences in the calculated diffuse scattering.

Figure 3.18(a) shows the diffuse scattering calculated for a Nb<sub>0.84</sub>CoSb crystal with only occupational disorder (correlations between nearest and next-nearest neighbour vacancies). The intensity of the diffuse scattering for a crystal with only occupational disorder decreases with increasing scattering angle. Figure 3.18 (b) shows the diffuse scattering calculated for a Nb<sub>0.84</sub>CoSb crystal with only displacive disorder<sup>2</sup> (displacements of Sb and Co atoms around the vacancies). The diffuse scattering for a crystal with only displacive disorder shows asymmetries with respect to the Bragg reflections. The observed diffuse scattering in the  $h0l$  plane in Figure 3.11 is thus due to both occupational and displacive disorder (Figure 3.18 (c)).

---

<sup>2</sup>It should be noted that the diffuse scattering calculated for the crystal with only displacive disorder looks different from the one reported in the Supporting Information of [156], which was calculated using a custom Python script.

### 3.5. CALCULATED DIFFUSE SCATTERING

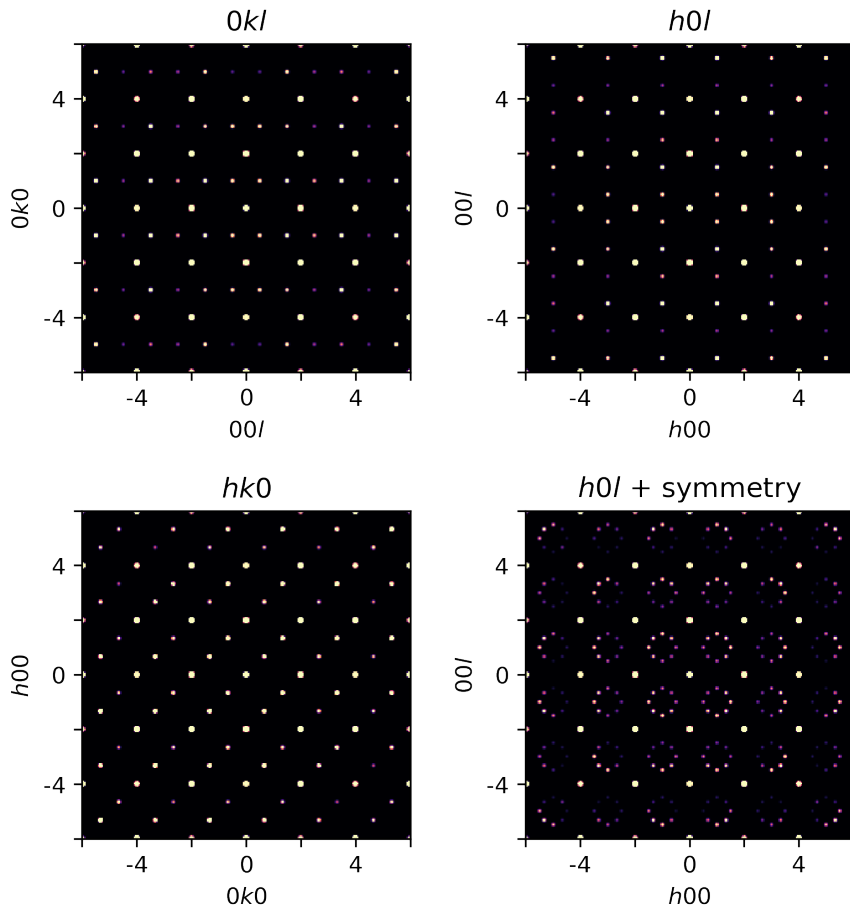


Figure 3.16: Symmetry with Laue class  $m\bar{3}m$  was applied to the three-dimensional diffuse scattering calculated in *Scatty*.

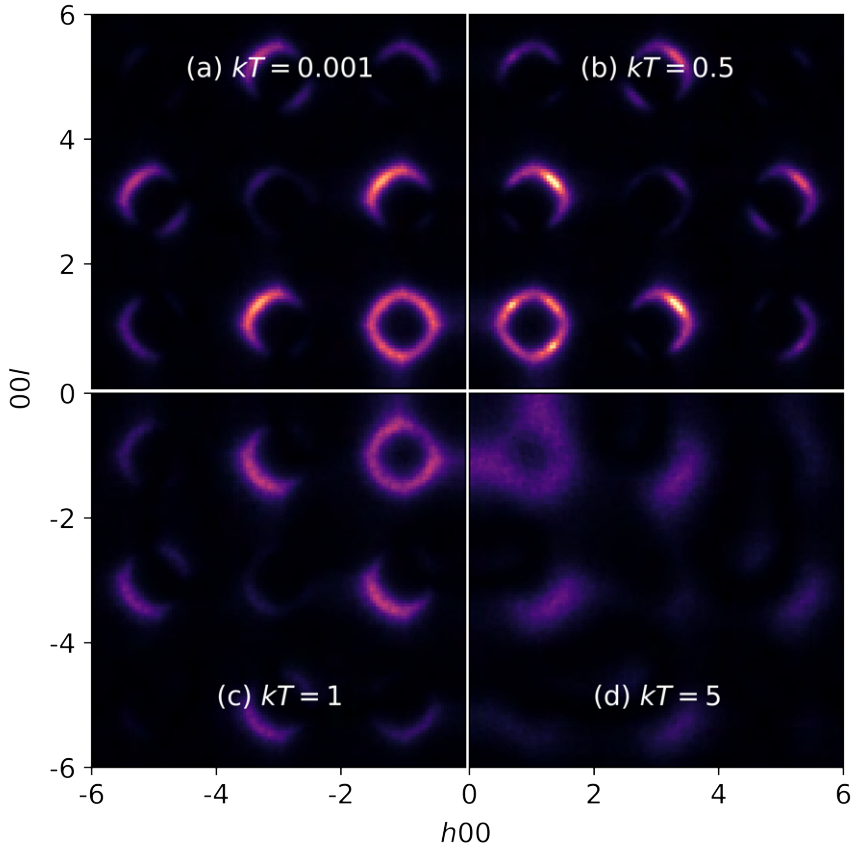


Figure 3.17: Diffuse scattering in the  $h0l$  plane calculated for a)  $kT = 0.001$ , b)  $kT = 0.5$ , c)  $kT = 1$  and d)  $kT = 5$ . The diffuse scattering was averaged over ten crystals with a size of  $25 \times 25 \times 25$  unit cells. For each crystal, the diffuse scattering was also averaged over 50 lots with a size of  $12 \times 12 \times 12$  unit cells. The diffuse scattering was calculated for a target correlation between nearest neighbour vacancies of  $c_{(1/2,1/2,0)} = -0.20$  and a target correlation between next-nearest neighbour vacancies of  $c_{(1,0,0)} = -0.10$ .



### 3.5. CALCULATED DIFFUSE SCATTERING

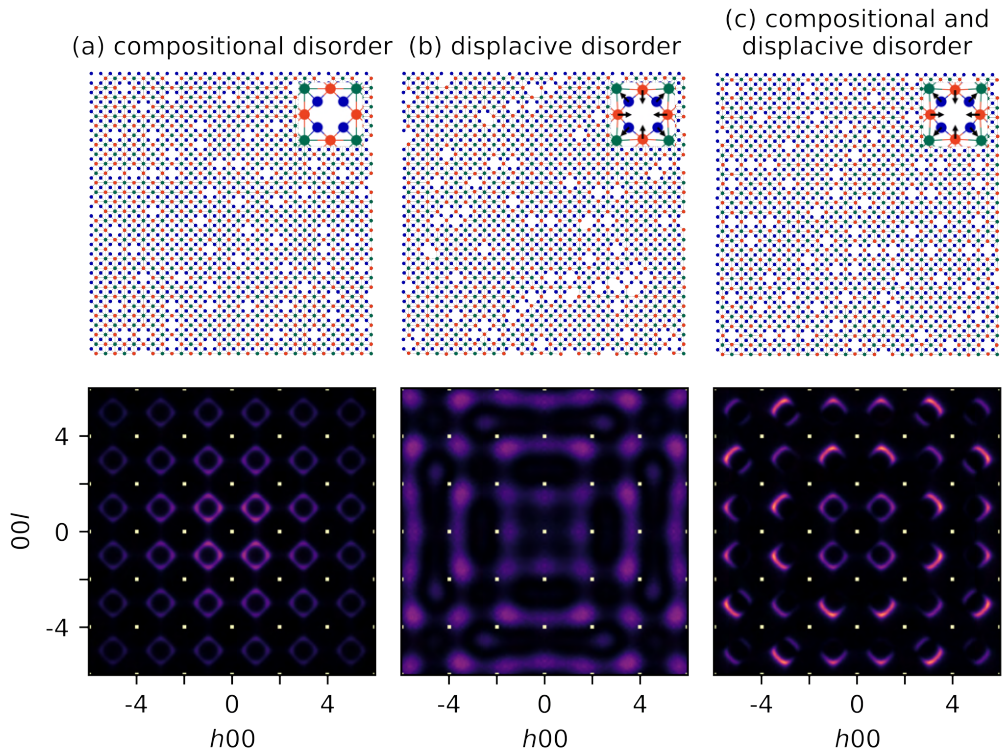


Figure 3.18: Structure models and their corresponding calculated single crystal X-ray diffraction patterns. (a) The calculated  $h0l$  plane for a  $\text{Nb}_{0.84}\text{CoSb}$  crystal with only occupational disorder. Correlations between nearest and next-nearest neighbour vacancies give rise to the observed diffuse scattering. (b) The calculated  $h0l$  plane for a  $\text{Nb}_{0.84}\text{CoSb}$  crystal with only displacive disorder. Displacements of Sb and Co atoms give rise to the observed diffuse scattering. (c) The highly structured diffuse scattering in the  $h0l$  plane is due to both occupational and displacive disorder.

### 3.6 Three-dimensional difference pair distribution function

The 3D- $\Delta$ PDF was calculated in *MANTID* [167]. *MANTID* was installed on a high performance computing (HPC) cluster, and the 3D- $\Delta$ PDF was calculated in parallel on a node with 128 GB RAM. The 3D- $\Delta$ PDF was obtained by removing the Bragg reflections and Fourier transforming the three-dimensional diffuse scattering/satellite reflections (see Figure 3.19).

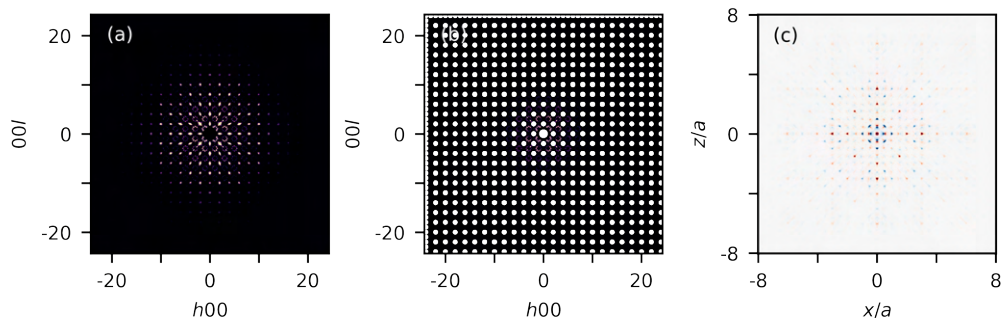


Figure 3.19: (a)  $h0l$  plane reconstructed from 3D ED data acquired on the slowly cooled sample (SC-0.81). (b)  $h0l$  plane after removing the Bragg reflections. (c)  $x0z$  plane of the 3D- $\Delta$ PDF. Positive 3D- $\Delta$ PDF features are red and negative features are blue.

For the simulated 3D- $\Delta$ PDF maps, *Scatty* was used to calculate the three-dimensional diffuse scattering from the *DISCUS* models. *Scatty* uses a fast Fourier transform (FFT) algorithm to calculate the structure factor in Equation 1.11, which accelerates the calculation of the diffuse scattering by a factor  $10^2 - 10^3$  compared to the DFT. Lanczos resampling was used to reduce the high-frequency noise. For the short-range Nb-vacancy order model, the calculation of the three-dimensional diffuse scattering took about eight days. The diffuse scattering was calculated for expansion order 10, expansion maximum error 0.05 and window 2. The meaning of these parameters can be found in [168]. To have an error smaller than 5%, the outer part of the three-dimensional reciprocal lattice (about 18%) was calculated using the DFT. For the long-range Nb-vacancy order model, the calculation of the three-dimensional diffuse scattering took only 35 minutes. The diffuse scattering was calculated for expansion order 1 and window 2.

For the experimental three-dimensional diffuse scattering data, the three-dimensional reciprocal lattice was reconstructed on a grid with  $901 \times 901 \times 901$  voxels for  $-25.2 \leq h, k, l \leq 25.2$ . For the three-dimensional diffuse scattering data calculated in *Scatty*, the three-dimensional reciprocal lattice was reconstructed on a grid with  $401 \times 401 \times 401$  voxels for  $-20 \leq h, k, l \leq 20$ .

Figure 3.20 shows the  $x0z$  plane of the X-ray and electron 3D- $\Delta$ PDF, both for the

### 3.6. THREE-DIMENSIONAL DIFFERENCE PAIR DISTRIBUTION FUNCTION

thermally quenched sample (Q-0.84 #2) and the slowly cooled sample (SC-0.81). The

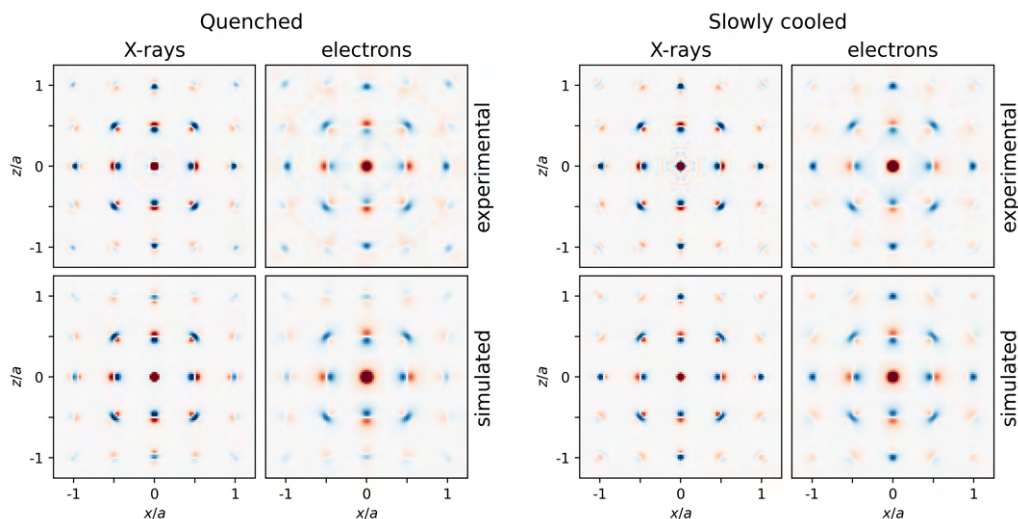


Figure 3.20: Comparison of the  $x0z$  plane of the X-ray and electron 3D- $\Delta$ PDF, both for the thermally quenched sample (Q-0.84 #2) and the slowly cooled sample (SC-0.81). The 3D- $\Delta$ PDF was reconstructed from the three-dimensional diffuse scattering data of which the  $h0l$  plane is shown in Figure 3.11. The top row shows the 3D- $\Delta$ PDF of the experimental diffuse scattering; the bottom row shows the corresponding 3D- $\Delta$ PDF of the calculated diffuse scattering. Positive 3D- $\Delta$ PDF features are red and negative features are blue.

3D- $\Delta$ PDF was reconstructed from the three-dimensional diffuse scattering data of which the  $h0l$  plane is shown in Figure 3.11. The calculated 3D- $\Delta$ PDF maps are in good agreement with the experimental ones. A similar comparison for the  $x0.27z$  plane of the 3D- $\Delta$ PDF is shown in Figure 3.21. Because the Bragg reflections close to the central beam were overexposed due to the limited dynamical range of the CCD, the Bragg reflections in the electron diffraction data could not entirely be subtracted (Figure 3.22). The experimental electron 3D- $\Delta$ PDF is thus affected by blooming artefacts due to saturated Bragg reflections (deformation of the features in the 3D- $\Delta$ PDF and weak additional features).

The 3D- $\Delta$ PDF maps show features that are positive on one side and negative on the other side, which is due to the relaxation of Sb and Co atoms around vacancies. From Figure 3.1 (a), it can be seen that the  $(0.5,0,0)$  interatomic vector corresponds to the distance between a Nb atom/vacancy and an Sb atom. The corresponding feature in the  $x0z$  plane of the 3D- $\Delta$ PDF is negative towards the origin and positive away from the origin, which means that when a Nb atom is present at  $(0,0,0)$ , the Sb atom with coordinates  $(0.5,0,0)$  will move away from the Nb atom. The  $(0.25, 0.25, 0.25)$  interatomic vector corresponds to the distance between a Nb atom/vacancy and a Co atom or the distance between an Sb atom and a Co atom (Figure 3.1 (a)). The

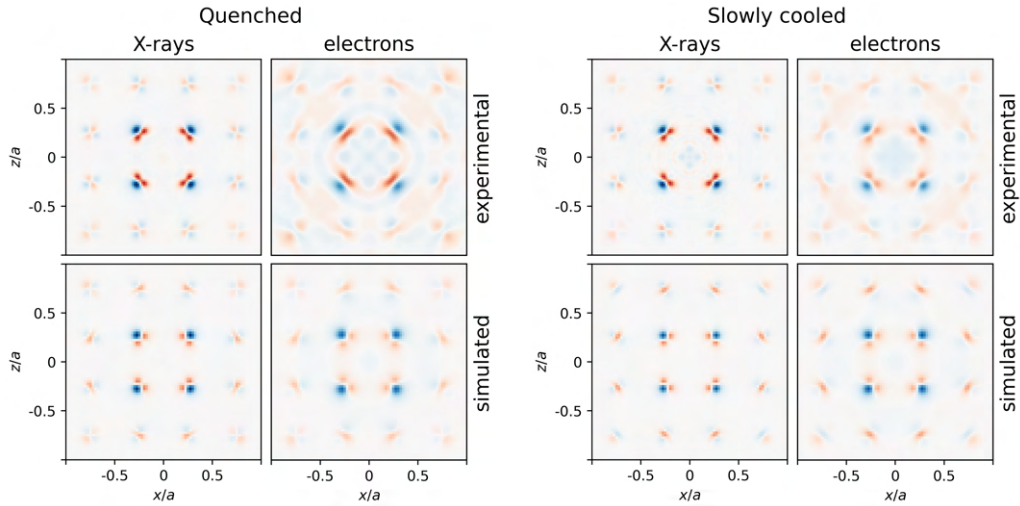


Figure 3.21: Comparison of the  $x0.27z$  plane of the X-ray and electron 3D- $\Delta$ PDF, both for the thermally quenched sample (Q-0.84 #2) and the slowly cooled sample (SC-0.81). The 3D- $\Delta$ PDF was reconstructed from the three-dimensional diffuse scattering data of which the  $h0l$  plane is shown in Figure 3.11. The top row shows the 3D- $\Delta$ PDF of the experimental diffuse scattering; the bottom row shows the corresponding 3D- $\Delta$ PDF of the calculated diffuse scattering. Positive 3D- $\Delta$ PDF features are red and negative features are blue.

corresponding feature in the  $x0.27z$  plane of the 3D- $\Delta$ PDF is positive towards the origin and negative away from the origin, which means that when a Nb atom is present at  $(0,0,0)$ , the Co atom with coordinates  $(0.25, 0.25, 0.25)$  will move towards the Nb atom.

The  $x0z$  plane of the experimental 3D- $\Delta$ PDF in Figure 3.20 is almost identical for the thermally quenched sample (Q-0.84 #2) and the slowly cooled sample (SC-0.81). A positive peak is found at the origin since the distance of an atom to itself is always zero. Strong negative features are visible at interatomic vectors  $(0.5,0,0.5)$  and  $(1,0,0)$ , which correspond to respectively nearest and next-nearest neighbour Nb atoms. The probability of finding two nearest or two next-nearest neighbour Nb atoms is thus lower in the real structure than in the average structure. Consequently, the probability of finding two nearest or two next-nearest neighbour vacancies is also lower in the real structure than in the average structure. Figure 3.23 shows the  $x0z$  plane of the 3D- $\Delta$ PDF for longer interatomic distances. Strong positive features are visible at interatomic vectors  $(1.5,0,1.5)$ ,  $(2,0,0)$  and  $(3,0,0)$ , showing the preferred distances between Nb atoms. Besides, the magnitudes of the 3D- $\Delta$ PDF features decrease more quickly for the thermally quenched sample than for the slowly cooled sample, which means that the correlation length of the local Nb-vacancy order is longer for the slowly cooled sample than for the thermally quenched sample.

### 3.6. THREE-DIMENSIONAL DIFFERENCE PAIR DISTRIBUTION FUNCTION

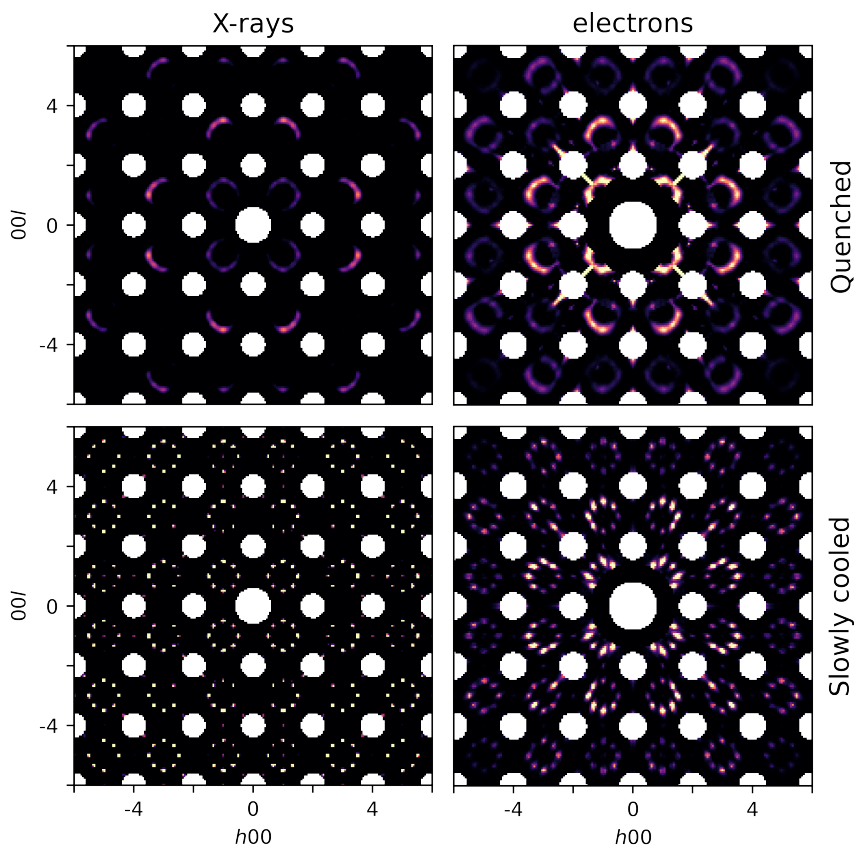


Figure 3.22: Comparison of the  $h0l$  plane reconstructed from single-crystal X-ray diffraction and 3D ED after removing the Bragg reflections, both for the thermally quenched sample (Q-0.84 #2) and the slowly cooled sample (SC-0.81).

The electron 3D- $\Delta$ PDF and the X-ray 3D- $\Delta$ PDF of  $\text{Nb}_{0.84}\text{CoSb}$  contain the same information about correlations between neighbouring atoms, and they can thus both be used to determine the origin of the diffuse scattering. The maximum observable correlation length in the 3D- $\Delta$ PDF (8.93 r.l.u.) is determined by the voxel size in reciprocal space ( $\Delta h, \Delta k, \Delta l \approx 0.056$ ). The intensity of the diffuse scattering goes faster to zero for electrons than for X-rays (Figure 3.11), which results in broader features in the electron 3D- $\Delta$ PDF maps than in the X-ray 3D- $\Delta$ PDF maps (Figure 3.20) but which does not hinder the qualitative interpretation of the 3D- $\Delta$ PDF. Besides, the diffuse scattering is broader for electron diffraction than for X-ray diffraction, which results in a faster decay of the features in the electron 3D- $\Delta$ PDF maps than in the X-ray 3D- $\Delta$ PDF maps, as can be seen in Figure 3.23.

The 3D- $\Delta$ PDF of  $\text{Nb}_{0.84}\text{CoSb}$  is similar to the 3D- $\Delta$ PDF of  $\text{Zr}_{0.82}\text{Y}_{0.18}\text{O}_{1.91}$  [13, 40] and the origin of the diffuse scattering (correlations between neighbouring vacancies

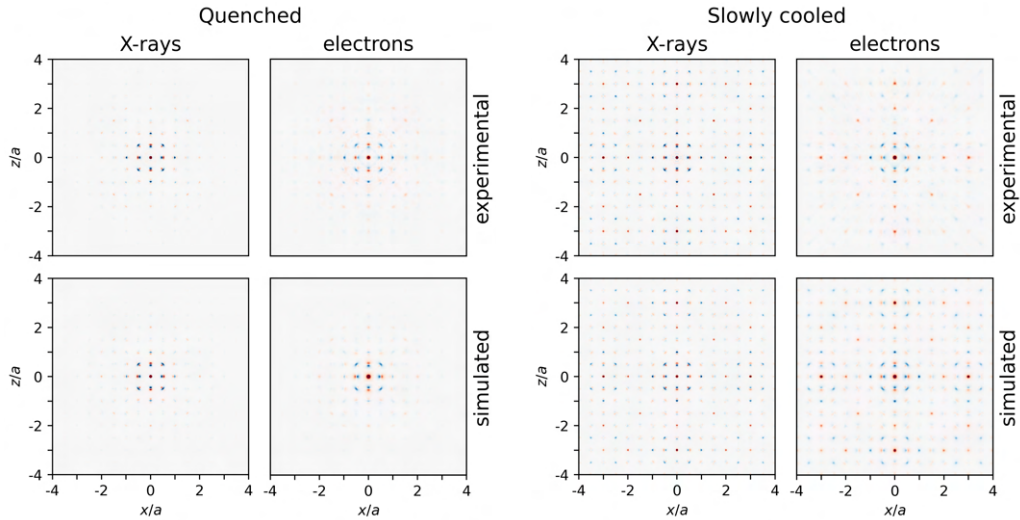


Figure 3.23: Comparison of the  $x0z$  plane of the X-ray and electron 3D- $\Delta$ PDF, both for the thermally quenched sample (Q-0.84 #2) and the slowly cooled sample (SC-0.81). The 3D- $\Delta$ PDF was reconstructed from the three-dimensional diffuse scattering data of which the  $h0l$  plane is shown in Figure 3.11. The top row shows the 3D- $\Delta$ PDF of the experimental diffuse scattering; the bottom row shows the corresponding 3D- $\Delta$ PDF of the calculated diffuse scattering. Positive 3D- $\Delta$ PDF features are red and negative features are blue.

and the relaxation of the Zr-, Y- and O-atoms around these vacancies) is also similar. However, the 3D- $\Delta$ PDF of  $Zr_{0.82}Y_{0.18}O_{1.91}$  was only interpreted in a qualitative way and no refinement of the short-range order parameters was applied to the diffuse scattering. The features in the 3D- $\Delta$ PDF maps of  $Nb_{0.84}CoSb$  in Figure 3.20 are much sharper than the ones in the 3D- $\Delta$ PDF maps of  $Zr_{0.82}Y_{0.18}O_{1.91}$  [13, 40], which can be explained by the different Q-range. The three-dimensional diffuse scattering data of  $Zr_{0.82}Y_{0.18}O_{1.91}$  were acquired for  $-10 \leq h, k, l \leq 10$ , whereas the three-dimensional diffuse scattering data of  $Nb_{0.84}CoSb$  were acquired for  $-20 \leq h, k, l \leq 20$ . Figure 3.24 illustrates that the width of the features in the 3D- $\Delta$ PDF is inversely proportional to the Q-range.

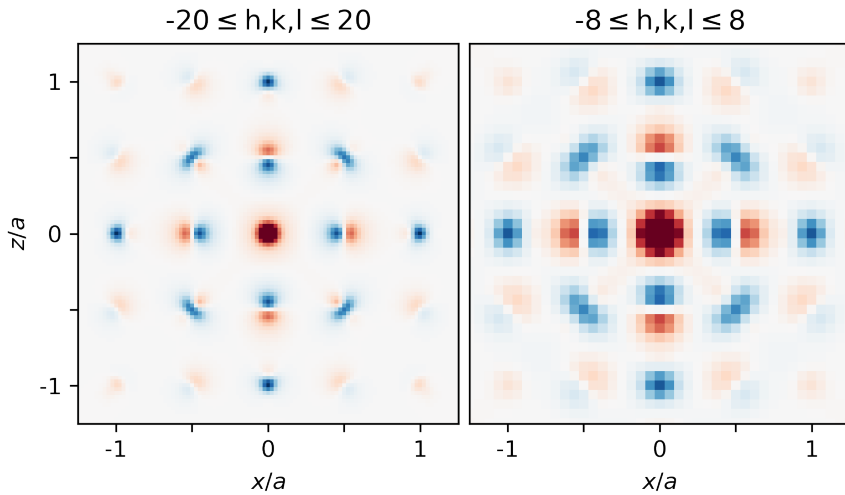


Figure 3.24: Comparison of the  $x0z$  plane of the simulated electron 3D- $\Delta$ PDF for two different Q-ranges ( $-8 \leq h,k,l \leq 8$  and  $-20 \leq h,k,l \leq 20$ ). The 3D- $\Delta$ PDF maps were calculated from the simulated three-dimensional reciprocal lattice of the slowly cooled sample (SC-0.81). Positive 3D- $\Delta$ PDF features are red and negative features are blue.

## 3.7 Refinement of the short-range order

### 3.7.1 Monte Carlo refinement

The model of the short-range Nb-vacancy order (Subsection 3.5.2) was implemented in a differential evolutionary algorithm in *DISCUS*. The Monte Carlo refinement was performed on a model crystal with  $25 \times 25 \times 25$  unit cells. The limited crystal size introduces high-frequency noise in the calculated diffuse scattering. The diffuse scattering was averaged over ten crystals to reduce the high-frequency noise. For each crystal, the diffuse scattering was also averaged over 50 lots with a size of  $12 \times 12 \times 12$  unit cells, randomly distributed within the model crystal. The lot size should be larger than the correlation length of the longest correlations but smaller than or equal to the crystal size divided by two [53]. Increasing the crystal size, the number of crystals, and the number of lots reduces the noise but increases the refinement time. Figure 3.25 and Figure 3.26 show that increasing the crystal size from  $25 \times 25 \times 25$  unit cells to  $30 \times 30 \times 30$  unit cells, increasing the number of crystals from 10 to 20, and increasing the number of lots from 50 to 500 improves the quality of the calculated diffuse scattering only marginally.

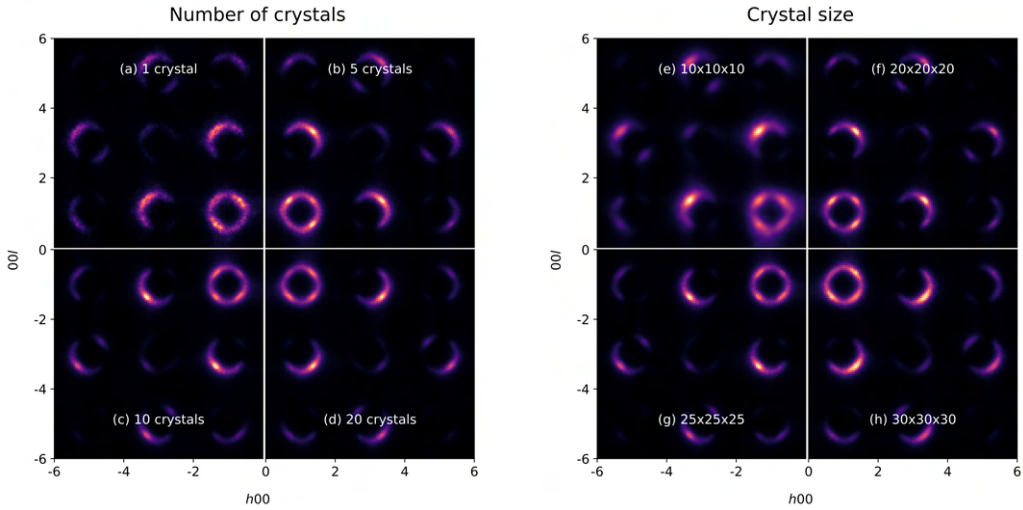


Figure 3.25: Left: Diffuse scattering in the  $h0l$  plane averaged over (a) 1 crystal, (b) 5 crystals, (c) 10 crystals, and (d) 20 crystals. For each crystal, the diffuse scattering was averaged over 50 lots with a size of  $12 \times 12 \times 12$  unit cells. Right: Diffuse scattering in the  $h0l$  plane averaged over ten crystals with (e) a size of  $10 \times 10 \times 10$  unit cells and 50 lots with a size of  $5 \times 5 \times 5$  unit cells, (f) a size of  $20 \times 20 \times 20$  unit cells and 50 lots with a size of  $10 \times 10 \times 10$  unit cells, (g) a size of  $25 \times 25 \times 25$  unit cells and 50 lots with a size of  $12 \times 12 \times 12$  unit cells and (h) a size of  $30 \times 30 \times 30$  unit cells and 50 lots with a size of  $15 \times 15 \times 15$  unit cells. The lot size should be smaller than or equal to the crystal size divided by two to avoid contributions from periodic images of the crystal. The diffuse scattering was calculated for  $c_{(1/2,1/2,0)}/c_{(1,0,0)} = 1$ .

The Monte Carlo refinement was used to refine the correlations between nearest neighbour vacancies  $c_{(1/2,1/2,0)}$  and next-nearest neighbour vacancies  $c_{(1,0,0)}$ . Because nearest and next-nearest neighbour vacancies avoid each other, both  $c_{(1/2,1/2,0)}$  and  $c_{(1,0,0)}$  should be negative. The effect of the ratio  $c_{(1/2,1/2,0)}/c_{(1,0,0)}$  and the displacements of Sb and Co atoms on the intensity distribution of the diffuse scattering is shown in Figure 3.27. Because the intensity distribution of the diffuse scattering depends on the ratio  $c_{(1/2,1/2,0)}/c_{(1,0,0)}$ ,  $c_{(1/2,1/2,0)}$  was fixed to -0.20 (a value close to the actual correlation coefficient, determined based on a series of Monte Carlo simulations) and  $c_{(1,0,0)}$  was refined. In total, three parameters were refined: the correlation between next-nearest neighbour vacancies ( $c_{(1,0,0)}$ ), the distance between a vacancy  $i$  and a neighbouring Sb atom  $k$  ( $\tau_{ik}$ ), and the distance between a vacancy  $i$  and a neighbouring Co atom  $k'$  ( $\tau_{ik'}$ ) (see Equation 3.5). Because next-nearest neighbour vacancies avoid each other, starting values for  $c_{(1,0,0)}$  were chosen in the range  $[-0.60, -0.01]$ . The average distance between a vacancy  $i$  and a neighbouring Sb atom  $k$  is  $\tau_{ik} = 2.801$ . Because Sb atoms move towards neighbouring vacancies, starting values for  $\tau_{ik}$  were chosen in the range  $[2.545, 2.945]$ . The average distance between a vacancy  $i$  and a neighbouring Co atom  $k'$  is  $\tau_{ik'} = 2.680$ . Because Co atoms move away from neighbouring vacancies, starting values for  $\tau_{ik'}$  were



### 3.7. REFINEMENT OF THE SHORT-RANGE ORDER

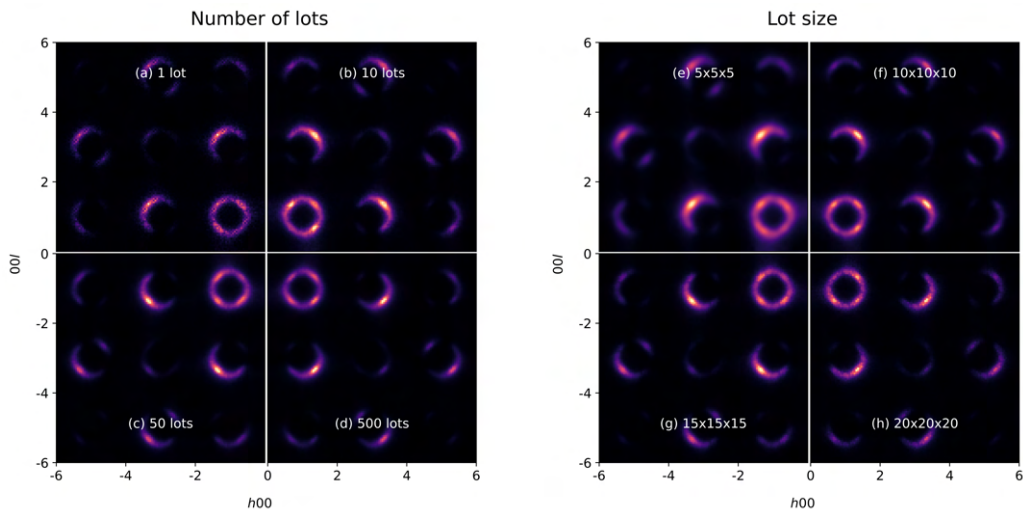


Figure 3.26: Left: Diffuse scattering in the  $h0l$  plane averaged over (a) 1 lot, (b) 10 lots, (c) 50 lots, and (d) 500 lots with a size of  $12 \times 12 \times 12$  unit cells. Right: Diffuse scattering in the  $h0l$  plane averaged over 50 lots with a size of (e)  $5 \times 5 \times 5$  unit cells, (f)  $10 \times 10 \times 10$  unit cells, (g)  $15 \times 15 \times 15$  unit cells, and (h)  $20 \times 20 \times 20$  unit cells. The diffuse scattering was calculated for  $c_{(1/2,1/2,0)}/c_{(1,0,0)} = 1$  and was averaged over ten crystals with a size of  $25 \times 25 \times 25$  unit cells.

chosen in the range  $[2.550, 2.950]$ .

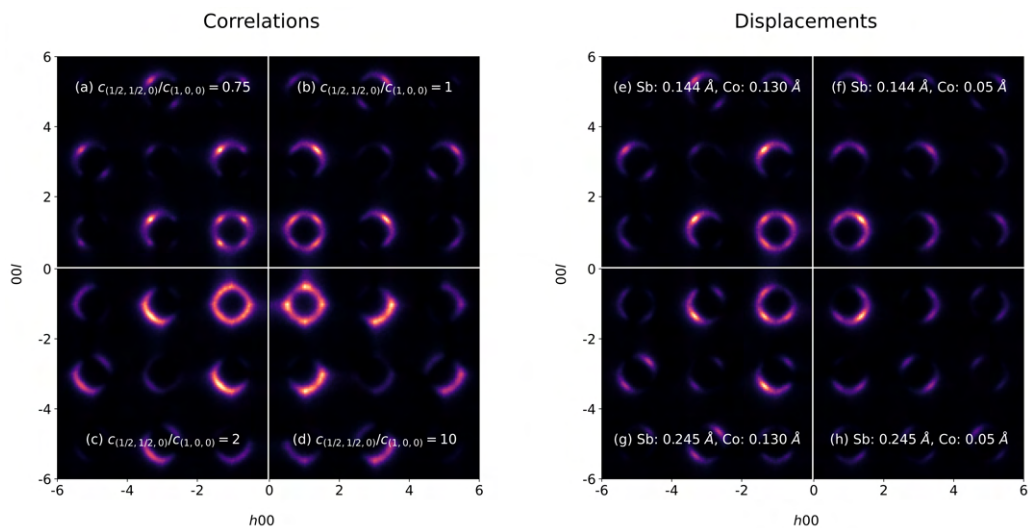


Figure 3.27: Left: Diffuse scattering in the  $h0l$  plane calculated for (a)  $c_{(1/2,1/2,0)}/c_{(1,0,0)} = 0.75$ , (b)  $c_{(1/2,1/2,0)}/c_{(1,0,0)} = 1$ , (c)  $c_{(1/2,1/2,0)}/c_{(1,0,0)} = 2$ , and (d)  $c_{(1/2,1/2,0)}/c_{(1,0,0)} = 10$ . With  $c_{(1/2,1/2,0)}$  the correlation between nearest neighbour vacancies and  $c_{(1,0,0)}$  the correlation between next-nearest neighbour vacancies. Right: Diffuse scattering in the  $h0l$  plane calculated for different displacements of the Sb and Co atoms. The diffuse scattering was calculated for  $c_{(1/2,1/2,0)}/c_{(1,0,0)} = 1$ . The diffuse scattering was averaged over ten crystals with a size of  $25 \times 25 \times 25$  unit cells. For each crystal, the diffuse scattering was also averaged over 50 lots with a size of  $12 \times 12 \times 12$  unit cells.

The Monte Carlo refinement was applied to the diffuse scattering in the  $h0l$  plane from the single-crystal X-ray diffraction data and the 3D ED data of the thermally quenched sample (Q-0.84 #2) in Figure 3.11. The Bragg reflections were subtracted using *MANTID*, and the three-dimensional diffuse scattering data were cropped on a grid with  $215 \times 215$  pixels for  $-6 \leq h, l \leq 6$ . The intensities in the  $h0l$  plane were converted to input for *DISCUS* using a custom Python script (<https://doi.org/10.5281/zenodo.8212162>).

### 3.7. REFINEMENT OF THE SHORT-RANGE ORDER

In Section 3.4, we showed that the spatial resolution of the observed diffuse scattering depends on various effects including the convergence of the beam, the detector point spread function and the crystal mosaicity. To account for resolution effects, the intensity of each pixel in the calculated  $h0l$  plane was convoluted with a Gaussian function (Figure 3.28). The standard deviation of the Gaussian function ( $\sigma = 0.006 \text{ \AA}^{-1}$  for X-ray

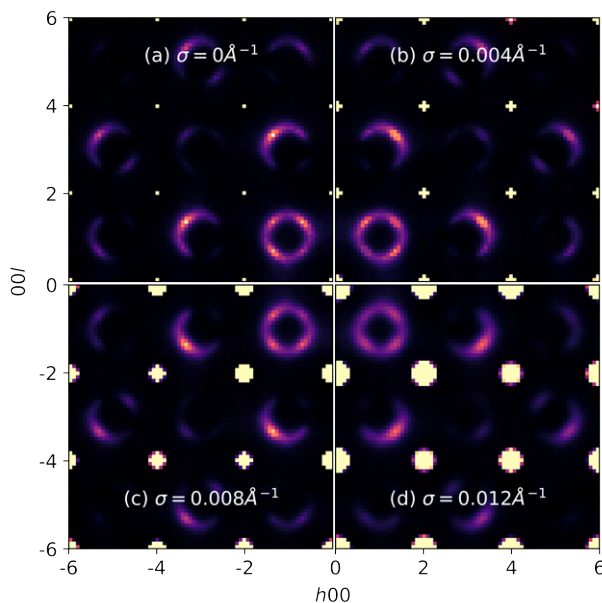


Figure 3.28: Every pixel in the  $h0l$  plane was convoluted with a Gaussian with a standard deviation of (a)  $0 \text{ \AA}^{-1}$ , (b)  $0.004 \text{ \AA}^{-1}$ , (c)  $0.008 \text{ \AA}^{-1}$ , and (d)  $0.012 \text{ \AA}^{-1}$ . The diffuse scattering was calculated for  $c_{(1/2,1/2,0)}/c_{(1,0,0)} = 1$  and was averaged over ten crystals with a size of  $25 \times 25 \times 25$  unit cells. For each crystal, the diffuse scattering was also averaged over 50 lots with a size of  $12 \times 12 \times 12$  unit cells.

diffraction and  $\sigma = 0.008 \text{ \AA}^{-1}$  for electron diffraction) was estimated from the intensity profile of unsaturated Bragg reflections.

The Monte Carlo refinement (<https://doi.org/10.5281/zenodo.8212024>) took about seven days for 19 refinement cycles on a desktop computer using eight cores in parallel. The 24 children were calculated in parallel, whereas the individual crystals and the individual lots were calculated in series. The refined short-range order parameters are listed in Table 3.2. The standard uncertainties of the short-range order parameters are underestimated. Systematic errors could be due to: (i) the limited number of correlations that were included in the model; (ii) non-perfect background subtraction; (iii) inaccurate resolution function correction; (iv) distortions in the reconstructed three-dimensional diffuse scattering (e.g., due to small crystal movements during the acquisition of the data or the instability of the goniometer of the TEM sample stage); and (v) no correction for multiple scattering.

In *DISCUS*, there is a difference between target correlations and displacements (the refined correlations and displacements) and achieved correlations and displacements (the actual correlations and displacements) [37]. The achieved correlations and displacements were calculated from the target correlations and displacements after the refinement. The achieved Co displacements are identical to the target Co displacements, while the achieved Sb displacements are lower than the target Sb displacements. The reason is that an Sb atom with two neighbouring vacancies on opposite sides of the Sb atom will not move away from its average position. A Co atom may also have two neighbouring vacancies, but these two neighbouring vacancies cannot be on opposite sides of the Co atom (Figure 3.1 (b)). Each Co atom with at least one neighbouring vacancy will thus move away from its average position.

Table 3.2: Monte Carlo refinement in *DISCUS* applied to the diffuse scattering in the *h0l* plane from the single-crystal X-ray diffraction data and the 3D ED data acquired on the thermally quenched sample (Q-0.84 #2). Refined short-range order parameters and R-value after 19 refinement cycles. After the refinement, the achieved correlations and displacements were calculated from the target correlations and displacements.  $c_{(1/2,1/2,0)}$  is the correlation between nearest neighbour vacancies and  $c_{(1,0,0)}$  is the correlation between next-nearest neighbour vacancies.

	X-rays		electrons	
	target	achieved	target	achieved
$c_{(1/2,1/2,0)}$	-0.200	-0.188	-0.200	-0.185
$c_{(1,0,0)}$	-0.053(17)	-0.047(17)	-0.082(22)	-0.067(22)
Sb shift (Å)	0.160(11)	0.142(11)	0.158(23)	0.142(23)
Co shift (Å)	0.112(8)	0.112(8)	0.071(21)	0.071(21)
R-value (%)	37.2		63.5	

The R-value in Table 3.2 is much higher for the short-range order parameters refined from the diffuse scattering in the 3D ED data than for the short-range order parameters refined from the diffuse scattering in the single-crystal X-ray diffraction data. The evolution of the R-values and the short-range order parameters during the refinement applied to the diffuse scattering in single-crystal X-ray diffraction and 3D ED data is shown in Figure 3.29 and Figure 3.30, respectively. The diffuse scattering calculated for the refined short-range order parameters is shown in Figure 3.31. At lower scattering angles, the observed diffuse scattering intensities are higher than the calculated diffuse scattering intensities. The satellite reflections are also sharper in the observed diffuse

### 3.7. REFINEMENT OF THE SHORT-RANGE ORDER

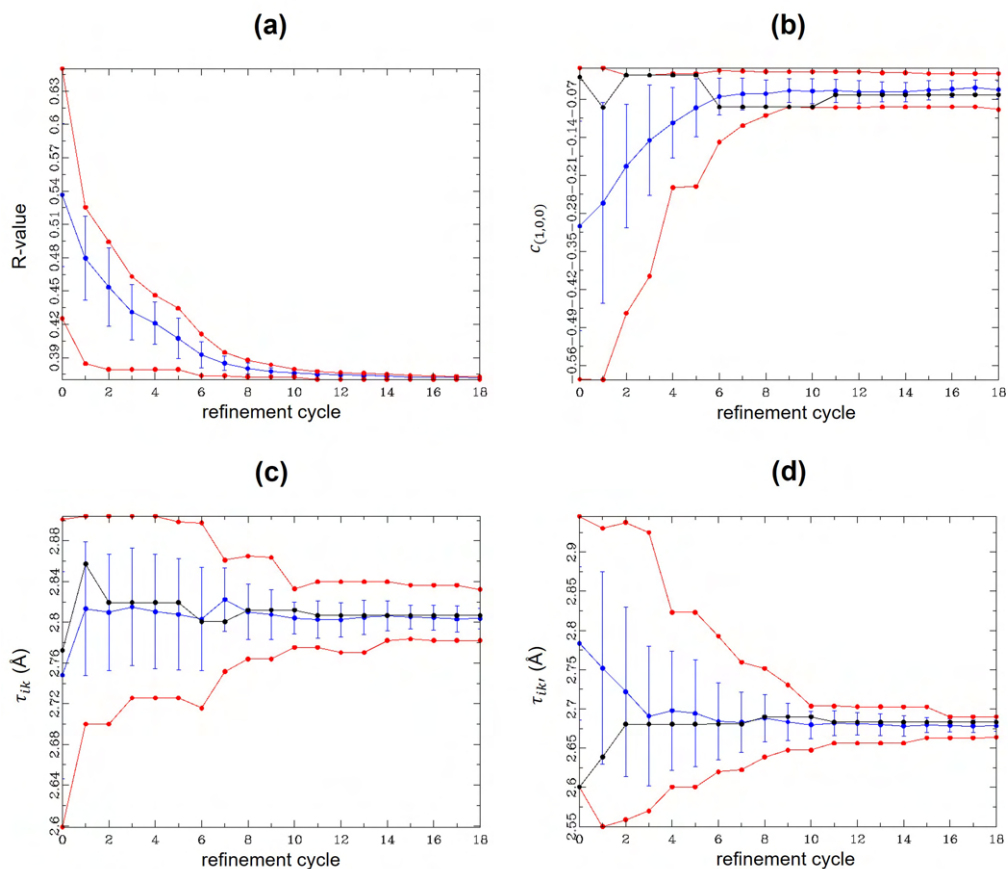


Figure 3.29: Monte Carlo refinement applied to the diffuse scattering in the  $h0l$  plane from single-crystal X-ray diffraction data of the thermally quenched sample (Q-0.84 #2). Evolution of (a) the R-value, (b) the target correlation between next-nearest neighbour vacancies ( $c_{(1,0,0)}$ ), (c) the target distance between a vacancy  $i$  and a neighbouring Sb atom  $k$  ( $\tau_{ik}$ ), and (d) the target distance between a vacancy  $i$  and a neighbouring Co atom  $k'$  ( $\tau_{ik'}$ ). The figure shows the average value (blue) and the smallest and highest value (red) at each refinement cycle. The value with the lowest R-value at each refinement cycle is shown in black.

scattering than in the calculated diffuse scattering, especially for the diffuse scattering in the 3D ED data.

The Monte Carlo refinement in *DISCUS* was done against the diffuse scattering in the  $h0l$  plane ( $-6 \leq h, l \leq 6$ ), whereas the 3D- $\Delta$ PDF refinement in *Yell* in the next section will be done against the three-dimensional diffuse scattering ( $-6 \leq h, k, l \leq 6$ ). To be able to compare the R-value of the Monte Carlo refinement with the R-value of the 3D- $\Delta$ PDF refinement, the R-value of the Monte Carlo refinement was also calculated for the three-dimensional diffuse scattering using a custom Python script

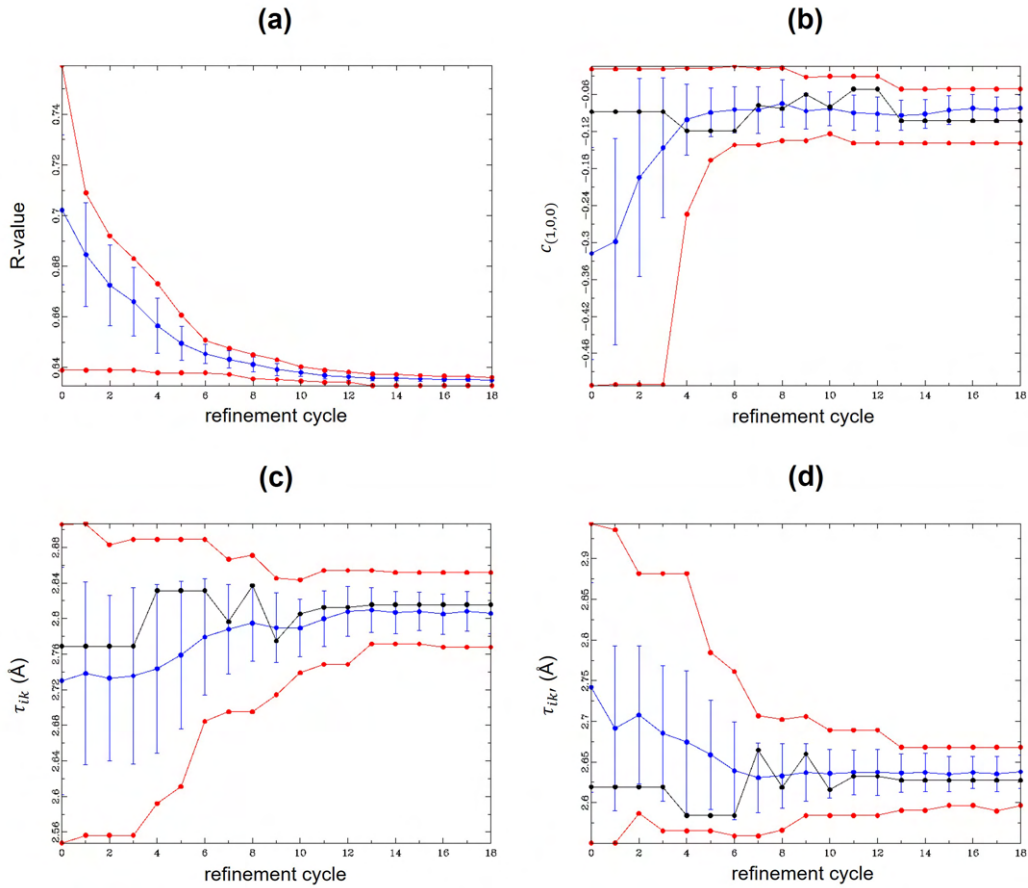


Figure 3.30: Monte Carlo refinement applied to the diffuse scattering in the  $h0l$  plane from 3D ED data of the thermally quenched sample (Q-0.84 #2). Evolution of (a) the R-value, (b) the target correlation between next-nearest neighbour vacancies ( $c_{(1,0,0)}$ ), (c) the target distance between a vacancy  $i$  and a neighbouring Sb atom  $k$  ( $\tau_{ik}$ ), and (d) the target distance between a vacancy  $i$  and a neighbouring Co atom  $k'$  ( $\tau_{ik'}$ ). The figure shows the average value (blue) and the smallest and highest value (red) at each refinement cycle. The value with the lowest R-value at each refinement cycle is shown in black.

(<https://zenodo.org/records/10043149>). The script was first tested on the diffuse scattering in the  $h0l$  plane calculated in *DISCUS* and on the three-dimensional diffuse scattering calculated in *Yell*. Then, a supercell was calculated in *DISCUS* for the short-range order parameters refined from the diffuse scattering in single-crystal X-ray diffraction data (Table 3.2). The R-value was first calculated for the diffuse scattering in the  $h0l$  plane calculated in *Scatty* (38.42%), which is  $\sim 1.38\%$  higher than the R-value for the diffuse scattering in the  $h0l$  plane calculated in *DISCUS* (37.04% for the member with the lowest R-value). The increase in R-value is probably due to small differences between the achieved correlation coefficients and a different method used to reduce the

### 3.7. REFINEMENT OF THE SHORT-RANGE ORDER

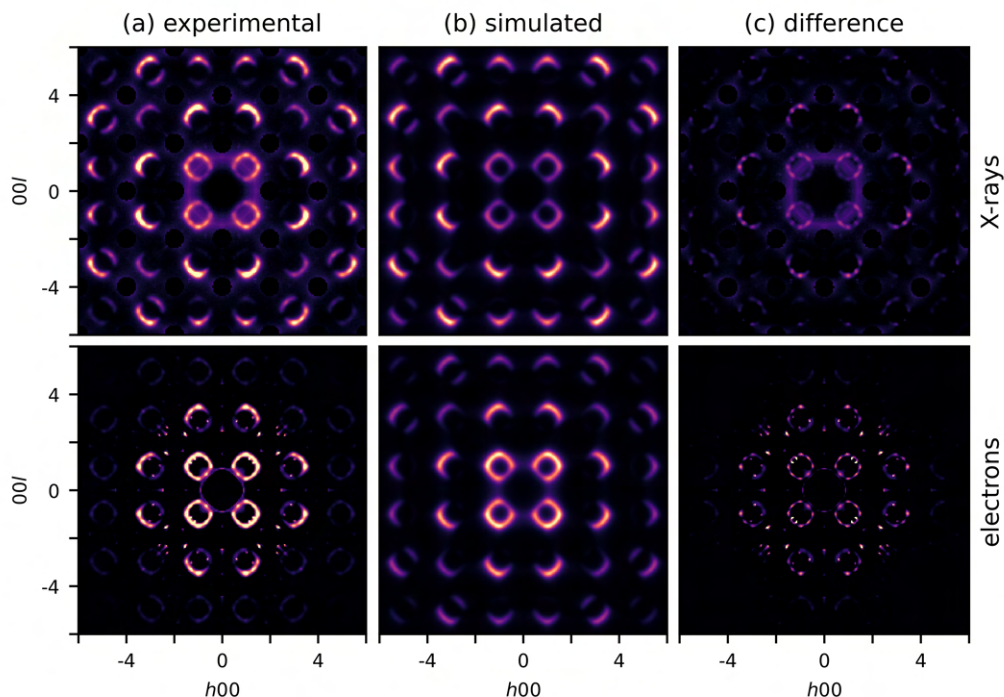


Figure 3.31: Monte Carlo refinement in *DISCUS* applied to the diffuse scattering in the  $h0l$  plane from the single-crystal X-ray diffraction data and the 3D ED data acquired on the thermally quenched sample (Q-0.84 #2). Comparison of (a) the experimental diffuse scattering, (b) the diffuse scattering calculated for the refined short-range order parameters in Table 3.2, and (c) the differences between observed and calculated intensities ( $I_{\text{obs}} - I_{\text{calc}}$ ).

high-frequency noise (lots vs. Lanczos resampling). Next, the R-value was calculated for the three-dimensional diffuse scattering calculated in *Scatty* (38.38%), which is quasi identical to the R-value for the diffuse scattering in the  $h0l$  plane calculated in *Scatty* (38.42%).

The displacements refined from the diffuse scattering in single-crystal X-ray diffraction data are 0.142(11) Å for Sb and 0.112(8) Å for Co. The displacements refined from the diffuse scattering in 3D ED data are 0.142(23) Å for Sb and 0.071(21) Å for Co. The difference between the Sb and Co displacements refined from the diffuse scattering and the Sb and Co displacements refined from the Bragg reflections in single-crystal X-ray diffraction data (0.141(1) Å for Sb, and 0.130(1) Å for Co) is 0.012(7) Å for the refinement on the diffuse scattering in single-crystal X-ray diffraction data, and 0.03(2) Å for the refinement on the diffuse scattering in 3D ED data. The standard uncertainties only considers random errors in the intensities of the Bragg reflections and are thus underestimated. The accuracy of the short-range order parameters refined from 3D ED

is less than the accuracy of the short-range order parameters refined from single-crystal X-ray diffraction. However, the main advantage of 3D ED is that it requires much smaller crystal sizes than X-ray diffraction, which allows to refine short-range order parameters in materials for which no crystals large enough for single-crystal X-ray diffraction are available.

It should be noted that the displacements refined from the diffuse scattering are local displacements, while the displacements refined from the Bragg reflections are average displacements. Sb atoms with two neighbouring vacancies on opposite sides of the Sb atom will not move away from their average positions, and the average Sb displacement is thus slightly smaller than the local Sb displacement.

The Monte Carlo refinement of the short-range order parameters took about seven days for 19 refinement cycles. The refinement time is proportional to the number of pixels/voxels in reciprocal space and the number of refined short-range order parameters. Therefore, the refinement was done against the diffuse scattering in one two-dimensional plane, and only three parameters were refined. Refining short-range order parameters against the three-dimensional diffuse scattering and refining the correlations between further nearest neighbour vacancies could further improve the match between observed and calculated intensities.

### 3.7.2 Three-dimensional difference pair distribution function refinement

The 3D- $\Delta$ PDF refinement in *Yell* was applied to the three-dimensional diffuse scattering in single-crystal X-ray diffraction data acquired on  $Nb_{0.84}CoSb$ . The Bragg reflections were subtracted using *MANTID*, and the three-dimensional diffuse scattering data were cropped on a grid with  $214 \times 214 \times 214$  voxels for  $-6 \leq h, k, l \leq 6$ . A constant background was subtracted. In total, 19 parameters were refined: the correlations between neighbouring vacancies up to the 16<sup>th</sup> nearest neighbour, the displacements of Sb and Co atoms and one scale factor. The 3D- $\Delta$ PDF refinement (<https://doi.org/10.5281/zenodo.8212680>) took about 20 minutes on a desktop computer.

A cubic unit cell with cell parameter  $a = 5.89864(3)$  Å was chosen as a structural building block. The origin of the unit cell was occupied by a Nb atom with a probability of 5/6 and by a vacancy with a probability of 1/6. The Nb atom/vacancy was surrounded by 6 Sb atoms and 4 Co atoms, forming a cluster (Figure 3.32).

The relaxations of Sb and Co atoms around the vacancies were not defined in terms of size-effect parameters (see Equation 1.22) but were included in the fractional coordinates of the Sb and Co atoms in the unit cell. Because the diffuse scattering from atomic displacement correlations is much weaker than the diffuse scattering from substitutional correlations [121], correlations between the atomic displacement



### 3.7. REFINEMENT OF THE SHORT-RANGE ORDER

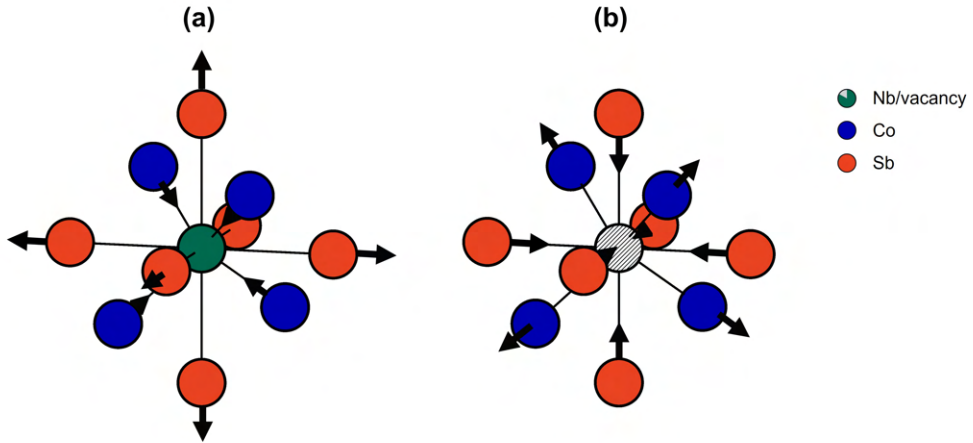


Figure 3.32: (a) A cluster with a Nb atom in the centre surrounded by 6 Sb atoms and 4 Co atoms. (b) A cluster with a vacancy in the centre surrounded by 6 Sb atoms and 4 Co atoms. Displacements of Sb and Co atoms are indicated by arrows. Sb atoms move towards neighbouring vacancies, whereas Co atoms move away from neighbouring vacancies.

parameters of Nb, Sb and Co were ignored. Equation 1.22 could thus be simplified to:

$$I(\mathbf{Q})_{\text{diff}} = \sum_{uvw} \sum_{mn} \left( p_{mn}^{uvw} - c_m c_n \exp[-\mathbf{Q}^T (\boldsymbol{\beta}_m + \boldsymbol{\beta}_n) \mathbf{Q}] \right) \exp[2\pi i \mathbf{Q} \cdot \mathbf{r}_{mn}^{uvw}] f_m^*(\mathbf{Q}) f_n(\mathbf{Q}), \quad (3.6)$$

with  $\mathbf{r}_{mn}^{uvw}$  the vector between the average positions of atoms  $m$  and  $n$  that are  $(u, v, w)$  unit cells apart,  $p_{mn}^{uvw}$  the probability of finding the atoms  $m$  and  $n$  separated by the vector  $\mathbf{r}_{mn}^{uvw}$ ,  $c_m$  and  $c_n$  the average occupancies,  $\boldsymbol{\beta}_m$  and  $\boldsymbol{\beta}_n$  the matrices of the average atomic displacement parameters, and  $f_m(\mathbf{Q})$  and  $f_n(\mathbf{Q})$  the atomic form factors. The intensity of the diffuse scattering was calculated from the 3D- $\Delta$ PDF via an FFT algorithm.

Currently, the 3D- $\Delta$ PDF refinement in *Yell* can only be applied to the diffuse scattering in single-crystal X-ray diffraction data. A 3D- $\Delta$ PDF refinement in *Yell* was applied to the three-dimensional diffuse scattering in the single-crystal X-ray diffraction data of the thermally quenched sample (Q-0.84 #2). The 3D- $\Delta$ PDF refinement was used to refine the correlations between neighbouring vacancies up to the 16<sup>th</sup> nearest neighbour. In total, 19 parameters were refined: the correlations between neighbouring vacancies up to the 16<sup>th</sup> nearest neighbour, the displacements of Sb and Co atoms and one scale factor. Memory limitations did not allow to refine all 19 short-range order parameters simultaneously. The short-range order parameters were therefore refined in groups of 5 parameters.

CHAPTER 3. THREE-DIMENSIONAL DIFFUSE SCATTERING -  
*Nb<sub>0.84</sub>COsB*

The refined short-range order parameters and R-value are listed in Table 3.3.  $c_{(1,1/2,1/2)}$

Table 3.3: Short-range order parameters refined in *Yell*. With  $c_{mn}^{uvw}$  the correlations between vacancies separated by  $(u, v, w)$  unit cells. The correlations refined in *Yell* were divided by  $\text{occ}_{\text{Nb}}/(1 - \text{occ}_{\text{Nb}})$  to compare them to the correlations refined/calculated in *DISCUS*. With  $\text{occ}_{\text{Nb}}$  the Nb occupancy.

parameter	<i>Yell</i>	<i>DISCUS</i>
$c_{(1/2,1/2,0)}$	-0.22021(12)	-0.188
$c_{(1,0,0)}$	-0.08006(13)	-0.047
$c_{(1,1/2,1/2)}$	0.17861(9)	0.134
$c_{(1,1,0)}$	-0.07452(9)	-0.041
$c_{(3/2,1/2,0)}$	-0.07965(7)	-0.013
$c_{(1,1,1)}$	-0.14213(11)	-0.121
$c_{(3/2,1,1/2)}$	-0.04754(5)	-0.023
$c_{(2,0,0)}$	0.03525(12)	0.050
$c_{(2,1/2,1/2)}$	-0.01273(8)	
$c_{(3/2,3/2,0)}$	0.04064(8)	
$c_{(2,1,0)}$	0.033630(6)	0.026
$c_{(2,1,1)}$	0.02773(6)	0.026
$c_{(5/2,1/2,0)}$	-0.01405(6)	-0.015
$c_{(2,2,0)}$	-0.01288(8)	-0.006
$c_{(5/2,3/2,0)}$	-0.00934(8)	-0.021
$c_{(3,0,0)}$	0.017038(12)	-0.002
Sb shift (Å)	0.1442(6)	
Co shift (Å)	0.1299(9)	
R-value (%)	46.76	

is the highest positive correlation coefficient, which indicates the preferred distance between neighbouring vacancies. The R-value in Table 3.3 (46.76%) is higher than the R-value of the three-dimensional diffuse scattering calculated for the refined short-range order parameters in Table 3.2 using a Monte Carlo refinement in *DISCUS* (38.42%). Correlation coefficients  $c_{mn}^{uvw}$  between neighbouring vacancies in *Yell* are defined as [118]:

$$c_{mn}^{uvw} = P_{mn}^{uvw} - (\text{occ}_{\text{Nb}})^2, \quad (3.7)$$

with  $P_{mn}^{uvw}$  the probability that sites  $m$  and  $n$  are occupied by the same atom type,  $uvw$  the interatomic vector and  $\text{occ}_{\text{Nb}}$  the Nb occupancy. The correlations refined in *Yell* were

### 3.7. REFINEMENT OF THE SHORT-RANGE ORDER

divided by  $\text{occ}_{\text{Nb}}/(1 - \text{occ}_{\text{Nb}})$  to compare them to the correlations refined/calculated in *DISCUS*. For the Monte Carlo refinement in *DISCUS*, only two correlations were refined ( $c_{(1/2,1/2,0)}$  and  $c_{(1,0,0)}$ ). To compare the other correlations as well, I wrote a script that calculates the correlations between neighbouring vacancies up to the 16<sup>th</sup> nearest neighbour (<https://zenodo.org/records/10051581>). The correlations were calculated from a supercell calculated for the refined short-range order parameters in Table 3.2. The  $c_{(2,1/2,1/2)}$  and  $c_{(3/2,3/2,0)}$  correlations could not be calculated since they both correspond to a distance of 12.495 Å between neighbouring vacancies. For most correlations, the absolute values refined in *Yell* are higher than the absolute values refined in *DISCUS* (Table 3.3). A possible explanation could be that the correlations refined in *Yell* are not achievable in practice since the refinement in *Yell* does not require the construction of a model crystal.

The displacements of Sb and Co atoms refined from the diffuse scattering in single-crystal X-ray diffraction data using a 3D- $\Delta$ PDF refinement in *Yell* (Table 3.3) can be compared with the displacements refined from the Bragg reflections in single-crystal X-ray diffraction data (Table 3.1). The difference in bond length is 0.0019(9) Å for the 3D- $\Delta$ PDF refinement on the diffuse scattering in single-crystal X-ray diffraction data, which is much lower than the difference in bond length for the Monte Carlo refinement. The refined displacements of Sb and Co atoms are thus in good agreement with the values refined from the Bragg reflections in single-crystal X-ray diffraction data.

Figure 3.33 (b) and Figure 3.34 (b) show the diffuse scattering calculated for the refined short-range order parameters in the  $h0l$  and  $h0.5l$  planes. The main difference is that the satellite reflections are sharper in the observed diffuse scattering than in the calculated diffuse scattering. The diffuse scattering contours calculated in *Yell* are also broader than the ones calculated in *DISCUS* (Figure 3.31).

Figure 3.33 (d-f) shows the  $x0z$  plane of the calculated and the experimental 3D- $\Delta$ PDF, and the 3D- $\Delta^2$ PDF, which is the difference between the calculated and the experimental 3D- $\Delta$ PDF. A similar comparison for the  $x0.27z$  plane of the 3D- $\Delta$ PDF is shown in Figure 3.34 (d-f). The magnitude of the features in the 3D- $\Delta$ PDF agrees with the refined correlation coefficients in Table 3.3. The higher the magnitude of a feature in the 3D- $\Delta$ PDF, the larger the absolute value of the corresponding correlation coefficient. The feature at (0.5,0,0.5) in the  $x0z$  plane of the calculated 3D- $\Delta$ PDF in Figure 3.33 (e) is mostly blue, which means that the corresponding correlation coefficient ( $c_{(1/2,1/2,0)}$ ) should be negative.

The feature at (0.5,0,0) in the  $x0z$  plane of the experimental 3D- $\Delta$ PDF is not well reproduced by the simulated 3D- $\Delta$ PDF (Figure 3.33). The (0.5,0,0) interatomic vector corresponds to the distance between a Nb atom/vacancy and an Sb atom. The discrepancy between the feature at (0.5,0,0) in the experimental and simulated 3D- $\Delta$ PDF could thus suggest a difference between the real and the refined Sb displacement. A similar explanation can be made for the feature at (0.25, 0.25, 0.25) in the  $x0.27z$  plane of the

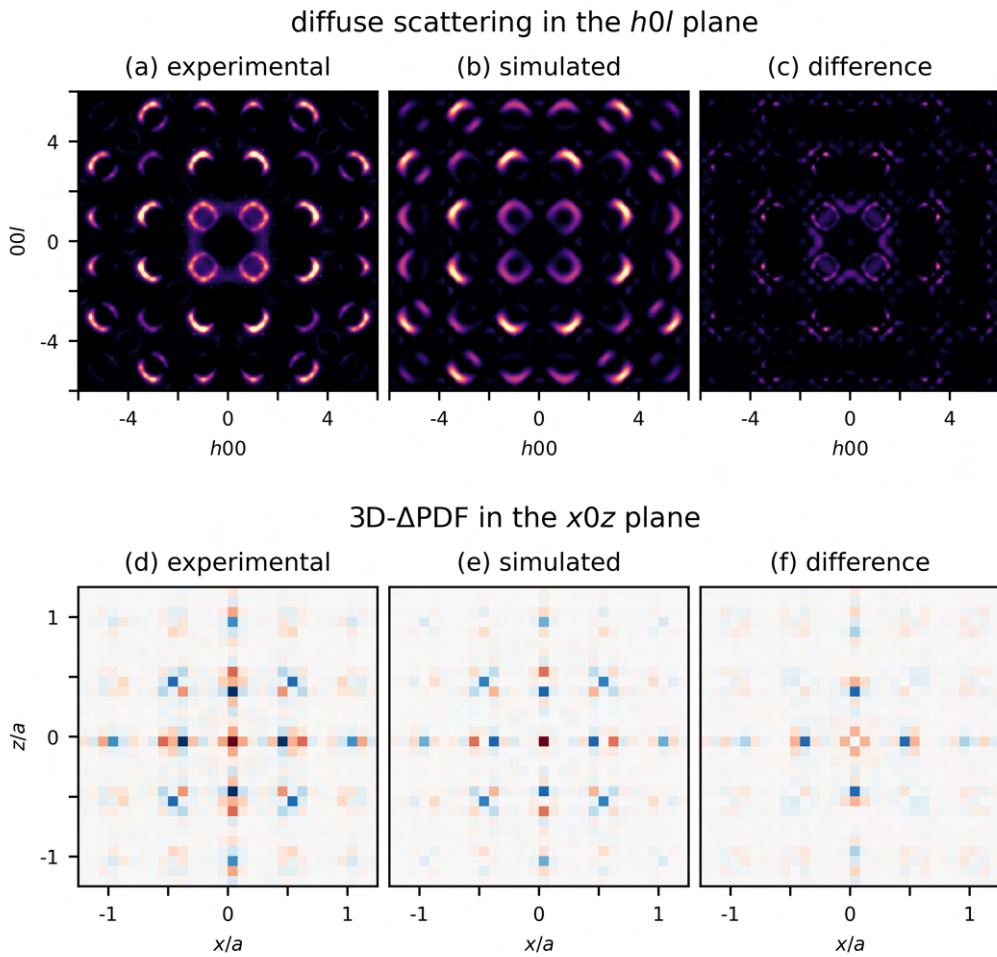


Figure 3.33: 3D- $\Delta$ PDF refinement in *Yell* applied to the three-dimensional diffuse scattering in the single-crystal X-ray diffraction data of the thermally quenched sample (Q-0.84 #2). Comparison of the  $h0l$  plane of (a) the experimental diffuse scattering, (b) the diffuse scattering calculated for the refined short-range order parameters in Table 3.3, and (c) the differences between observed and calculated intensities ( $I_{\text{obs}} - I_{\text{calc}}$ ). Comparison of the  $x0z$  plane of (d) the experimental 3D- $\Delta$ PDF, (e) the 3D- $\Delta$ PDF calculated for the refined short-range order parameters in Table 3.3, and (f) the differences between the experimental and calculated 3D- $\Delta$ PDF (3D- $\Delta^2$ PDF). Positive 3D- $\Delta$ PDF features are red and negative features are blue.

3D- $\Delta$ PDF in Figure 3.34. The (0.25, 0.25, 0.25) interatomic vector corresponds to the distance between a Nb atom/vacancy and a Co atom or the distance between an Sb atom and a Co atom. The discrepancy between the feature at (0.25, 0.25, 0.25) in the experimental and simulated 3D- $\Delta$ PDF could thus suggest a difference between the real and the refined Co displacement.

### 3.7. REFINEMENT OF THE SHORT-RANGE ORDER

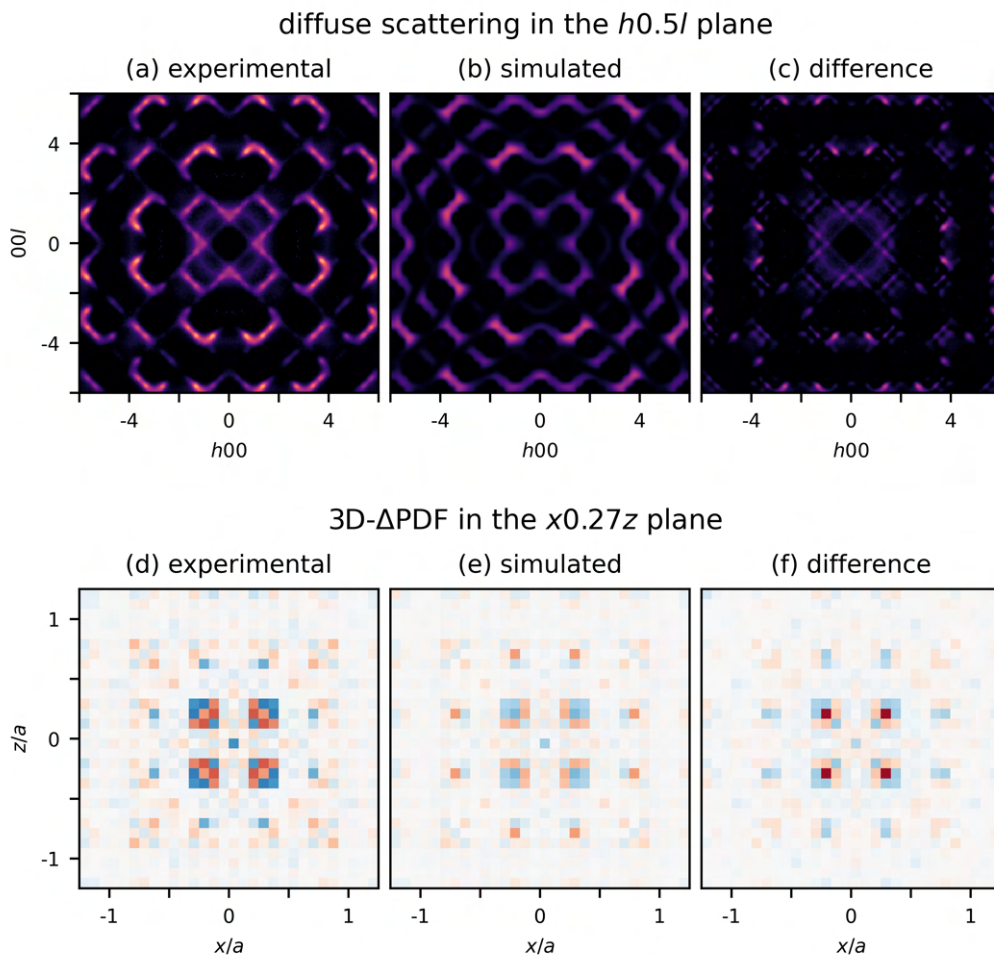


Figure 3.34: 3D- $\Delta$ PDF refinement in *Yell* applied to the three-dimensional diffuse scattering in the single-crystal X-ray diffraction data of the thermally quenched sample (Q-0.84 #2). Comparison of the  $h0.5l$  plane of (a) the experimental diffuse scattering, (b) the diffuse scattering calculated for the refined short-range order parameters in Table 3.3, and (c) the differences between observed and calculated intensities ( $I_{\text{obs}} - I_{\text{calc}}$ ). Comparison of the  $x0.27z$  plane of (d) the experimental 3D- $\Delta$ PDF, (e) the 3D- $\Delta$ PDF calculated for the refined short-range order parameters in Table 3.3, and (f) the differences between the experimental and calculated 3D- $\Delta$ PDF (3D- $\Delta^2$ PDF). Positive 3D- $\Delta$ PDF features are red and negative features are blue.

It should be noted that resolution effects were not considered in the 3D- $\Delta$ PDF refinement. In Section 3.4, we showed that the spatial resolution of the observed diffuse scattering depends on various effects including the convergence of the beam, the detector point spread function and the crystal mosaicity. To account for resolution effects, the

intensity of each voxel in the calculated three-dimensional reciprocal lattice should be convoluted with a Gaussian function. The effect of convoluting each voxel in the calculated  $h0l$  plane with a Gaussian function was previously shown in Figure 3.28. The satellite reflections in the calculated  $h0l$  and  $h0.5l$  planes in Figure 3.33 (b) and Figure 3.34 (b) are thus too sharp, which will affect the refined correlation coefficients.

The standard uncertainties of the short-range order parameters refined in *Yell* do not consider systematic errors in the intensity of the observed diffuse scattering, which could be due to: (i) non-perfect background subtraction; (ii) no resolution function correction; (iv) distortions in the reconstructed three-dimensional diffuse scattering [119].

The 3D- $\Delta$ PDF refinement of the short-range order parameters took about 20 minutes, while the Monte Carlo refinement took about seven days. 3D- $\Delta$ PDF refinements are much faster than Monte Carlo refinements since they do not require the construction of a model crystal. The 3D- $\Delta$ PDF refinement in *Yell* was done against three-dimensional diffuse scattering data, whereas the Monte Carlo refinement in *DISCUS* was done against the diffuse scattering in one two-dimensional plane. In *DISCUS*, we only refined the correlation between next-nearest neighbour vacancy pairs  $c_{(1,0,0)}$ . Because 3D- $\Delta$ PDF refinements are much faster than Monte Carlo refinements, the 3D- $\Delta$ PDF refinement in *Yell* allowed us to refine the correlations between neighbouring vacancies up to the 16<sup>th</sup> nearest neighbour. Defining correlations in *Yell* is also easier than in *DISCUS*. The disadvantage of 3D- $\Delta$ PDF refinements is that they may result in non-physical structure models [118]. Also, in cases where the construction of the whole three-dimensional reciprocal lattice or the subtraction of the Bragg reflections would not be possible, Monte Carlo refinements are still desirable.

## 3.8 Application of the model to $LiNi_{0.5}Sn_{0.3}Co_{0.2}O_2$

### 3.8.1 Introduction

$LiNi_{0.5}Sn_{0.3}Co_{0.2}O_2$  was synthesized as a potential cathode material for lithium-ion batteries and has similar diffuse scattering as  $Nb_{0.84}CoSb$ . The short-range order in defective half-Heusler systems  $X_{1-x}YZ$ , such as  $Nb_{1-x}CoSb$ , belongs to a more general type of short-range order found in many materials with a cubic rock salt structure [169]. Examples of materials with similar diffuse scattering are: transition-metal carbides and nitrides, e.g.  $MC_{1-x}$  and  $MN_{1-x}$  with  $M = Ti, Nb, Ni, V, Zr$  [170, 171, 172]; lithium transition metal oxides, e.g.  $LiFeO_2$  [173, 174, 175],  $LiFe_{0.6}Ni_{0.4}O_2$  [176],  $Li_{1.2}Mn_{0.4}Fe_{0.4}O_2$  [177] and  $Li_2SnO_3-CoO$  [178]; oxyfluorides, e.g.  $K_3MoO_3F_3$ ,  $Rb_2KMoO_3F_3$  and  $Tl_3MoO_3F_3$  [81, 179]; rare earth sulfides, e.g.  $Mg_{1-x}Yb_{2x/3}\square_{x/3}S$  with  $\square$  a vacancy [180, 181] and  $La_{0.7}I_{0.86}Al_{0.14}$  [182].

### 3.8. APPLICATION OF THE MODEL TO $\text{LiNi}_{0.5}\text{Sn}_{0.3}\text{Co}_{0.2}\text{O}_2$

The three-dimensional diffuse scattering in these compounds can be described by the equation  $[\cos(\pi h) + \cos(\pi k) + \cos(\pi l)] - C [\cos(\pi h) \cos(\pi k) \cos(\pi l)] = 0$  [171], with  $C$  a parameter that depends on the nature and composition of the compound. For transition-metal carbides and nitrides,  $C$  varies from 0 to 3 [169], while for lithium oxides,  $C$  varies from 6 to 10 [174].

The diffuse scattering in these compounds is often explained in terms of the cluster model [171, 183, 184] where the stoichiometry of each cluster is as close as possible to the average stoichiometry of the sample. In the average structure of  $\text{LiNi}_{0.5}\text{Sn}_{0.3}\text{Co}_{0.2}\text{O}_2$ , each O atom is surrounded by six Li, Ni, Sn or Co atoms, forming an octahedron. Avoidance of the nearest and next-nearest Li atoms requires each such octahedron to have 3 Li atoms and 3 Ni, Sn or Co atoms.

#### 3.8.2 Scanning transmission electron microscopy

Figure 3.35 (a) shows a high-angle annular dark-field scanning transmission electron microscopy (HAADF-STEM) image acquired on  $\text{LiNi}_{0.5}\text{Sn}_{0.3}\text{Co}_{0.2}\text{O}_2$ . The intensity

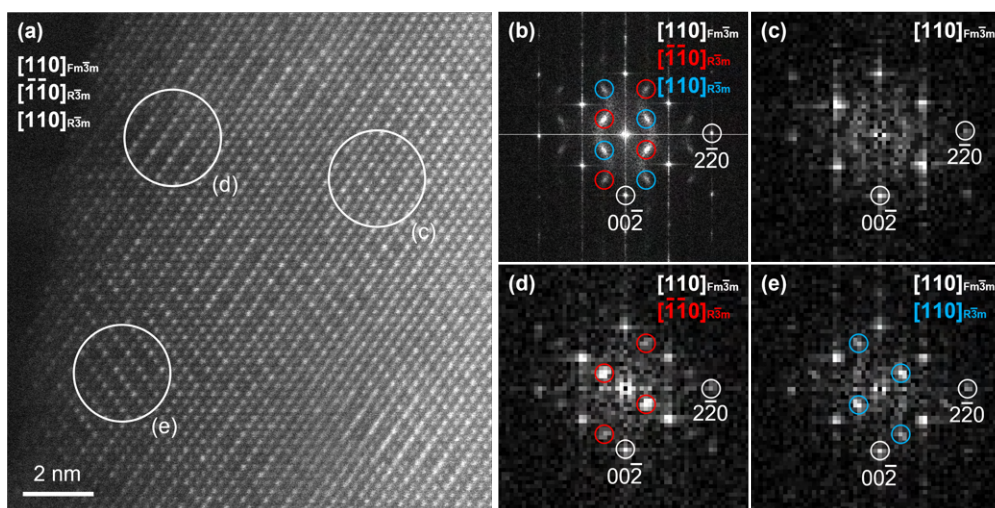


Figure 3.35: (a) HAADF-STEM image of  $\text{LiNi}_{0.5}\text{Sn}_{0.3}\text{Co}_{0.2}\text{O}_2$ . (b) FFT of the whole HAADF-STEM image. (c-e) FFTs of specific regions indicated in the HAADF-STEM image. The FFTs confirm that the structure consists of both nanodomains with a cubic rock salt structure (space group  $Fm\bar{3}m$ ) [region (c)] and nanodomains with a layered structure (space group  $R\bar{3}m$ ) [regions (d) and (e)]. (HAADF-STEM image acquired by Dr. Mylène Hendrickx)

of the atom columns in an HAADF-STEM image is proportional to the atomic number of the element ( $I \sim Z^2$ ). The intensity is thus higher for atomic columns that contain more Ni, Sn and Co atoms. The FFT of the HAADF-STEM image is shown in

CHAPTER 3. THREE-DIMENSIONAL DIFFUSE SCATTERING -  
 $NB_{0.84}CO_{0.2}SB$

Figure 3.35 (b). The satellite reflections indicated by the blue and the red circles are due to the presence of nanodomains with a layered structure (cell parameters  $a=b=2.8 \text{ \AA}$ ,  $c=14.1 \text{ \AA}$ ,  $\alpha=\beta=90^\circ$ ,  $\gamma=120^\circ$  and space group  $R\bar{3}m$ ). The diffuse intensity contours in Figure 3.35 (b) are due to short-range order of Li atoms in the cubic rock salt structure (lattice constant of  $4.23 \text{ \AA}$  and space group  $Fm\bar{3}m$ ). The FFTs of specific regions indicated in the HAADF-STEM image [Figure 3.35 (c-e)] confirm that the structure of  $LiNi_{0.5}Sn_{0.3}Co_{0.2}O_2$  consists of both nanodomains with a cubic rock salt structure [region (c) indicated in Figure 3.35 (a)] and nanodomains with a layered structure [regions (d) and (e) indicated in Figure 3.35 (a)].

Figure 3.36 (a) shows a HAADF-STEM image of a nanodomain at the surface of a  $LiNi_{0.5}Sn_{0.3}Co_{0.2}O_2$  crystal. The FFT of region (b) [Figure 3.36 (b)] reveals that the nanodomain at the crystal surface has a cubic spinel structure (lattice constant of  $8.46 \text{ \AA}$  and space group  $Fd\bar{3}m$ ). The FFT of region (c) [Figure 3.36 (c)] is similar to the FFT shown in Figure 3.35 (c) and confirms that the structure consists of nanodomains with a cubic rock salt structure. The diffuse intensity contours in Figure 3.36 (c) are due to short-range order of Li atoms in the cubic rock salt structure.

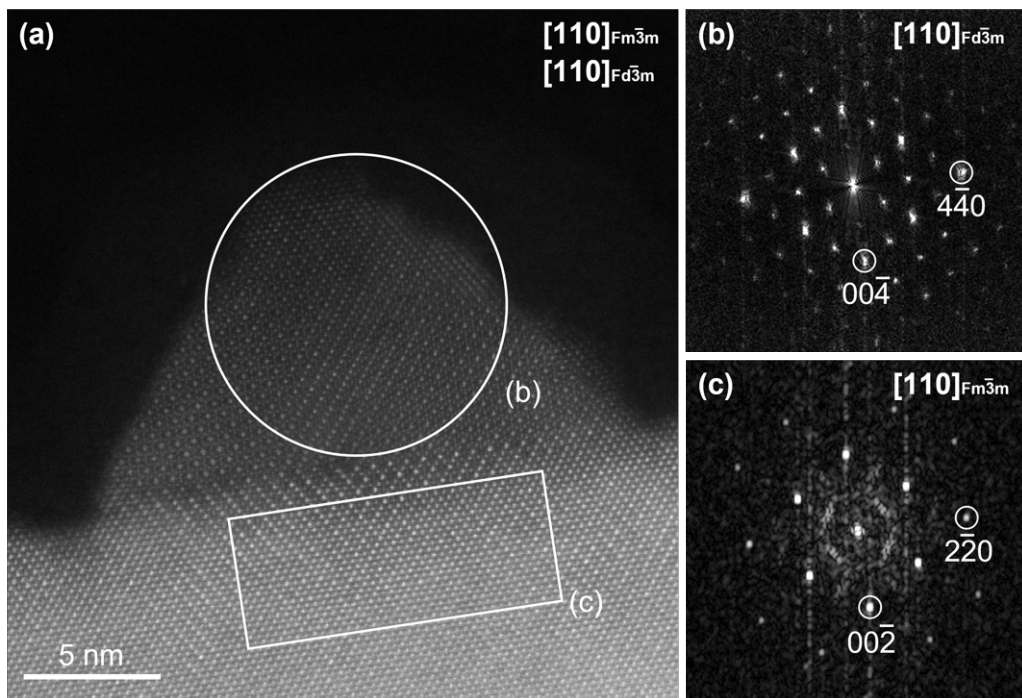


Figure 3.36: (a) HAADF-STEM image of  $LiNi_{0.5}Sn_{0.3}Co_{0.2}O_2$ . (b-c) FFTs of the two regions indicated in (a). (b) The nanodomains at the surface of the particles have a spinel structure (space group  $Fd\bar{3}m$ ). The FFT of region (c) confirms that the structure consists of nanodomains with a cubic rock salt structure (space group  $Fm\bar{3}m$ ). (HAADF-STEM image acquired by Dr. Mylène Hendrickx)



### 3.8. APPLICATION OF THE MODEL TO $\text{LiNi}_{0.5}\text{Sn}_{0.3}\text{Co}_{0.2}\text{O}_2$

Figure 3.37 shows the difference between the rock salt structure, the layered structure and the spinel structure. The layered structure consists of alternating layers of Li atoms and transition metal atoms whereas the rock salt structure has a random distribution of Li atoms and transition metal atoms. The layered structure and the rock salt structure have a common oxygen sublattice, but these are not shown for clarity. The transformation matrix that gives the relationship between the rock salt structure and the layered structure is given by:

$$P_{Fm\bar{3}m \rightarrow R\bar{3}m} = \begin{pmatrix} -2/3 & 4/3 & -2/3 \\ -4/3 & 2/3 & 2/3 \\ 1/6 & 1/6 & 1/6 \end{pmatrix} \quad (3.8)$$

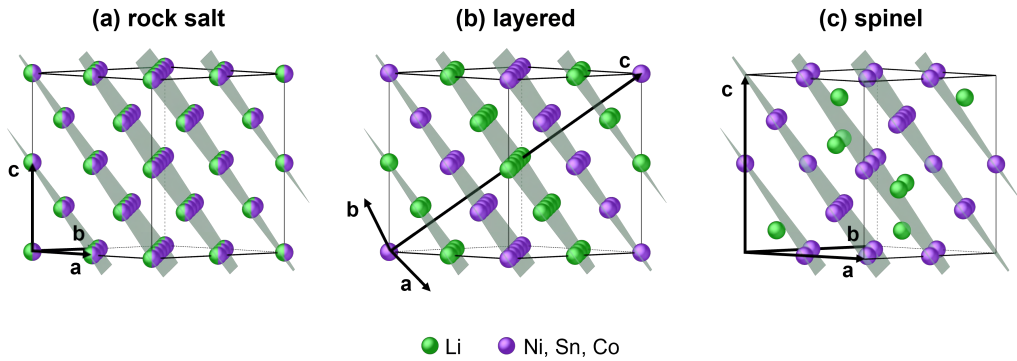


Figure 3.37: Different possible phases in  $\text{LiNi}_{0.5}\text{Sn}_{0.3}\text{Co}_{0.2}\text{O}_2$ . Crystallographic relation between (a) the rock salt phase, (b) the layered phase and (c) the spinel phase. The cell parameters of the unit cells of the different phases are indicated. Green spheres represent Li atoms, purple spheres represent Ni, Sn and Co atoms. O atoms are not shown for clarity.

#### 3.8.3 Powder X-ray diffraction

The powder X-ray diffraction pattern of  $\text{LiNi}_{0.5}\text{Sn}_{0.3}\text{Co}_{0.2}\text{O}_2$  is shown in Figure 3.38. All indexed peaks, except for the one indicated by the red arrow, can be attributed to the rock salt structure. The peak indicated by the red arrow corresponds to both the (100) reflection in the layered structure and the (111) reflection in the spinel structure.

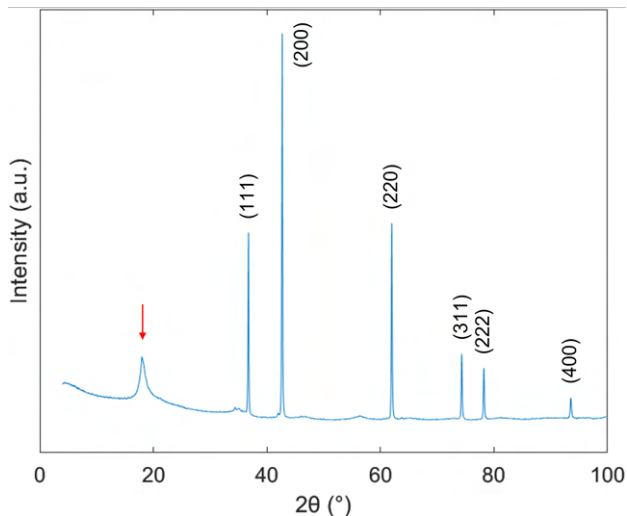


Figure 3.38: Powder X-ray diffraction pattern of  $LiNi_{0.5}Sn_{0.3}Co_{0.2}O_2$ . (powder X-ray diffraction data acquired by Dr. Mylène Hendrickx)

### 3.8.4 Three-dimensional electron diffraction

Figure 3.39 shows a comparison of the  $h0l$ ,  $hhl$ ,  $h2hl$  and  $h3hl$  planes reconstructed from 3D ED data acquired on  $Nb_{0.84}CoSb$  and  $LiNi_{0.5}Sn_{0.3}Co_{0.2}O_2$ . The  $h0l$ ,  $hhl$ ,  $h2hl$  and  $h3hl$  planes of  $LiNi_{0.5}Sn_{0.3}Co_{0.2}O_2$  show additional reflections due to the presence of the spinel phase and the layered phase.

As a first attempt, we created a model of a random distribution of small layered nanodomains with different orientations of the Li layers and the transition metal layers in *DISCUS* (Figure 3.40). However, this model only gave rise to the observed satellite reflections but not to the observed diffuse scattering. As a second attempt, the model of the short-range Nb-vacancy order in  $Nb_{0.84}CoSb$  was adjusted to a model of the short-range Li-transition metal order in  $LiNi_{0.5}Sn_{0.3}Co_{0.2}O_2$ . The vacancies were replaced by Li atoms, the Nb atoms were replaced by Ni, Sn and Co atoms, the Sb atoms were replaced by O atoms and the Co atoms were removed. Only interactions between nearest neighbour Li atoms and next-nearest neighbour Li atoms were considered. Because nearest and next-nearest neighbour vacancies avoid each other, the correlations between nearest neighbour Li atoms  $c_{(1/2,1/2,0)}$  and next-nearest neighbour Li atoms  $c_{(1,0,0)}$  should both be negative. Figure 3.41 shows the effect of the ratio  $c_{(1/2,1/2,0)}/c_{(1,0,0)}$  on the intensity distribution of the diffuse scattering in the  $h0l$  plane. The diffuse circles are more diamond-shaped for larger values of  $c_{(1/2,1/2,0)}/c_{(1,0,0)}$ .

The diffuse scattering in Figure 3.41 was calculated in *Scatty* and not in *DISCUS*. The diffuse scattering in *DISCUS* should be averaged over multiple lots to reduce the high-frequency noise. Because we noticed that the shape of the diffuse scattering

### 3.8. APPLICATION OF THE MODEL TO $\text{LiNi}_{0.5}\text{Sn}_{0.3}\text{Co}_{0.2}\text{O}_2$

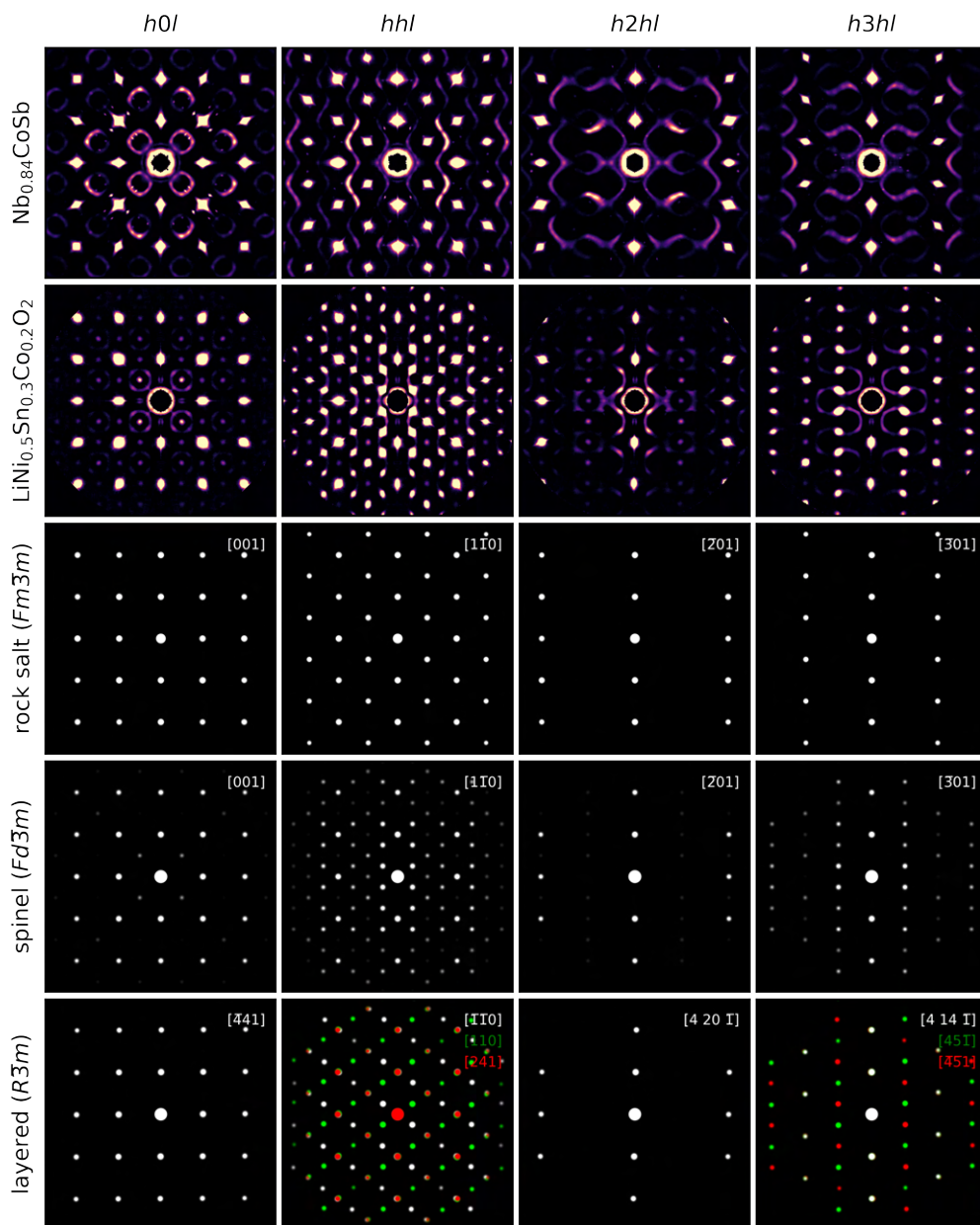


Figure 3.39: Row 1-2: Comparison of the  $h0l$ ,  $hhl$ ,  $h2hl$  and  $h3hl$  planes reconstructed from 3D ED data acquired on  $\text{Nb}_{0.84}\text{CoSb}$  and  $\text{LiNi}_{0.5}\text{Sn}_{0.3}\text{Co}_{0.2}\text{O}_2$ . Row 3-5: Electron diffraction patterns of the rock salt structure, the spinel structure and the layered structure calculated in *SingleCrystal*.

depends on the lots size (Figure 3.42), we calculated the diffuse scattering in *Scatty* from the structure models calculated in *DISCUS*.

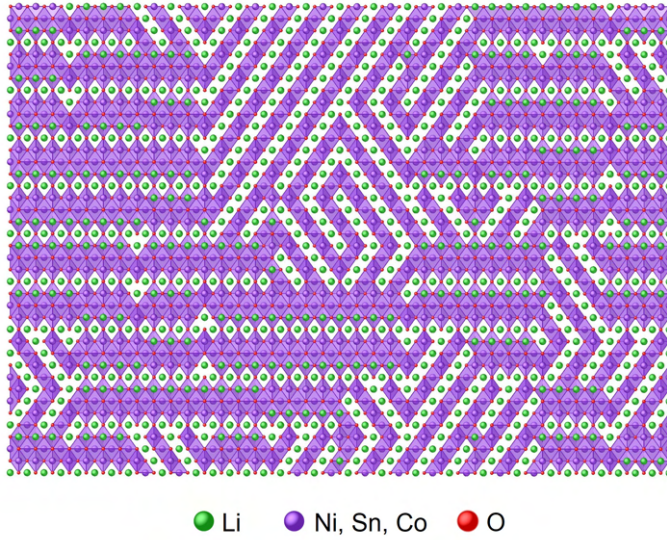


Figure 3.40: A random distribution of small layered nanodomains with different orientations of the Li layers and the transition metal layers created in *DISCUS*. Green spheres represent Li atoms, purple spheres represent Ni, Sn and Co atoms and red spheres represent O atoms.

Figure 3.43 shows a comparison of the experimental and calculated diffuse scattering in the  $h0l$ ,  $hhl$ ,  $h2hl$  and  $h3hl$  planes. The diffuse scattering was calculated for  $c_{(1/2,1/2,0)} = -0.076$  and  $c_{(1,0,0)} = -0.55$  ( $c_{(1/2,1/2,0)}/c_{(1,0,0)} = 0.14$  in Figure 3.41). The weak reflections in the experimental  $h0l$ ,  $hhl$ ,  $h2hl$  and  $h3hl$  planes that are not present in the simulated ones are due to the presence of the spinel phase, which was not considered in our *DISCUS* model. The diffuse scattering contours are sharper in the experimental  $h0l$ ,  $hhl$ ,  $h2hl$  and  $h3hl$  planes than in the simulated ones. A possible explanation is that the diffuse scattering was partially subtracted while removing the background of the individual frames in *PETS2*. Figure 3.44 shows the  $h0l$ ,  $hhl$ ,  $h2hl$  and  $h3hl$  planes reconstructed from 3D ED data acquired on  $LiNi_{0.5}Sn_{0.3}Co_{0.2}O_2$ , before and after background subtraction in *PETS2*. The diffuse scattering contours seem indeed sharper after background subtraction. Because the diffuse scattering is weaker for  $LiNi_{0.5}Sn_{0.3}Co_{0.2}O_2$  than for  $Nb_{0.84}CoSb$ , the effect of non-perfect background subtraction is more pronounced for  $LiNi_{0.5}Sn_{0.3}Co_{0.2}O_2$  (see Figure 3.4 for comparison). An alternative method to subtract the experimental background is to repeat the 3D ED data acquisition under the same conditions but without the crystal illuminated by the electron beam. The thermal diffuse scattering could then be subtracted by acquiring energy-filtered 3D ED data. Because of the non-perfect background subtraction, no Monte Carlo refinement was applied to the diffuse scattering in the 3D ED data acquired on  $LiNi_{0.5}Sn_{0.3}Co_{0.2}O_2$ .

### 3.8. APPLICATION OF THE MODEL TO $\text{LiNi}_{0.5}\text{Sn}_{0.3}\text{CO}_{0.2}\text{O}_2$

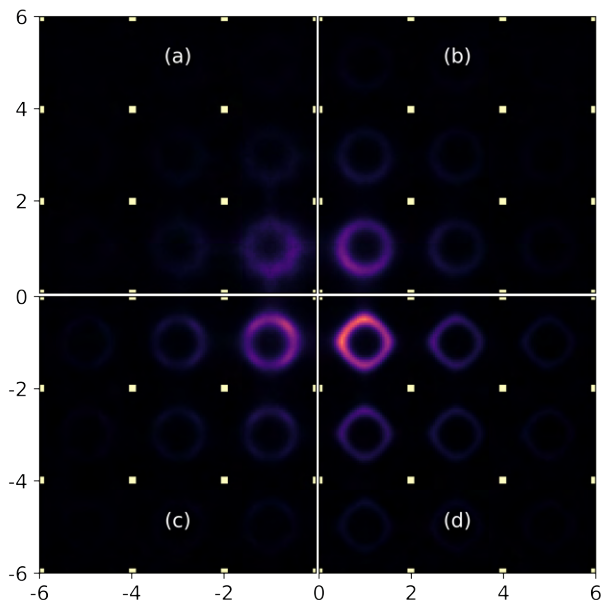


Figure 3.41: Diffuse scattering in the  $h0l$  plane calculated for (a)  $c_{(1/2,1/2,0)}/c_{(1,0,0)} = 0.03$ , (b)  $c_{(1/2,1/2,0)}/c_{(1,0,0)} = 0.14$ , (c)  $c_{(1/2,1/2,0)}/c_{(1,0,0)} = 0.23$  and (d)  $c_{(1/2,1/2,0)}/c_{(1,0,0)} = 0.86$ . With  $c_{(1/2,1/2,0)}$  the achieved correlation between nearest neighbour Li atoms and  $c_{(1,0,0)}$  the achieved correlation between next-nearest neighbour Li atoms. The diffuse scattering was calculated in *Scatty* from the structure models calculated in *DISCUS*. The diffuse scattering was averaged over 10 crystals with a size of  $25 \times 25 \times 25$  unit cells.

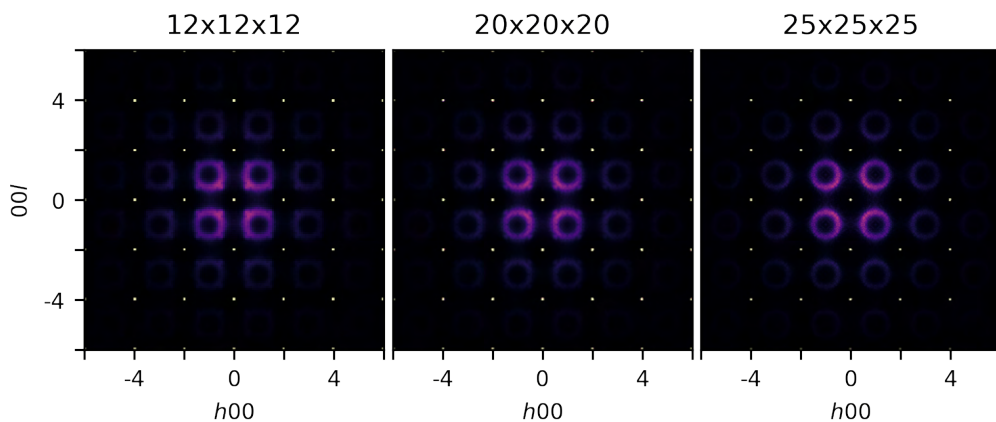


Figure 3.42: Diffuse scattering in the  $h0l$  plane averaged over 50 lots with a size of (a)  $12 \times 12 \times 12$  unit cells, (b)  $20 \times 20 \times 20$  unit cells and (c)  $25 \times 25 \times 25$  unit cells. The diffuse scattering was calculated for  $c_{(1/2,1/2,0)}/c_{(1,0,0)} = 0.14$  and was averaged over 10 crystals with a size of  $25 \times 25 \times 25$  unit cells.

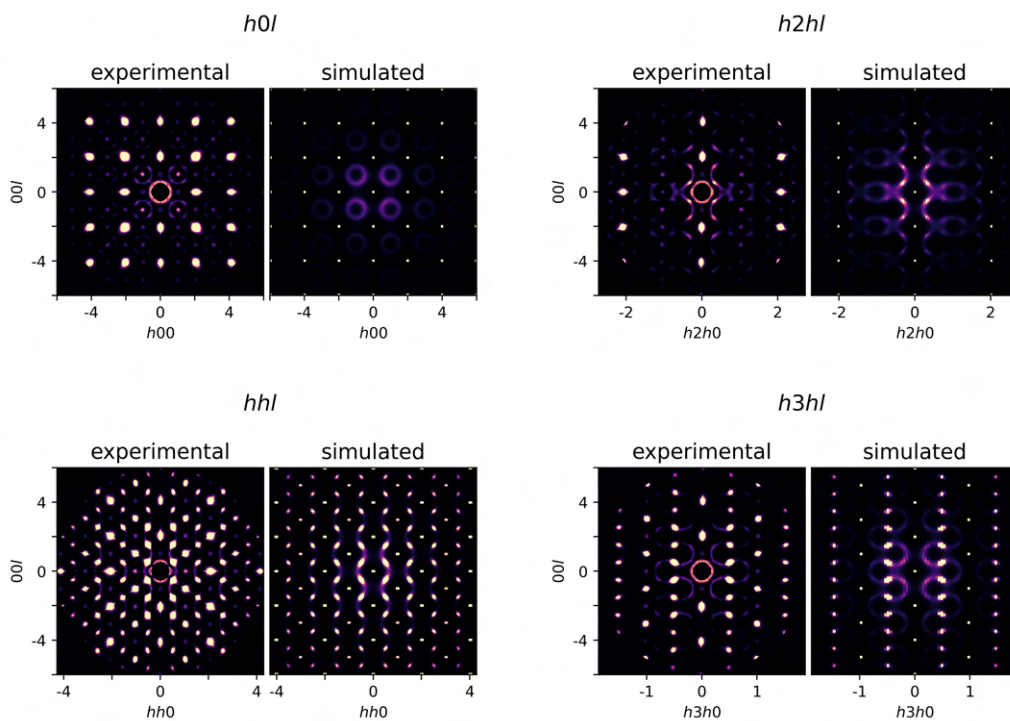


Figure 3.43: Comparison of the experimental and calculated diffuse scattering in the  $h0l$ ,  $hhl$ ,  $h2hl$  and  $h3hl$  planes. The diffuse scattering was calculated in *Scatty* from a structure model with  $c_{(1/2,1/2,0)} = -0.076$  and  $c_{(1,0,0)} = -0.55$  calculated in *DISCUS*. With  $c_{(1/2,1/2,0)}$  the achieved correlation between nearest neighbour Li atoms and  $c_{(1,0,0)}$  the achieved correlation between next-nearest neighbour Li atoms. The diffuse scattering was averaged over 10 crystals with a size of  $25 \times 25 \times 25$  unit cells.

3.8. APPLICATION OF THE MODEL TO  $\text{LiNi}_{0.5}\text{SN}_{0.3}\text{CO}_{0.2}\text{O}_2$

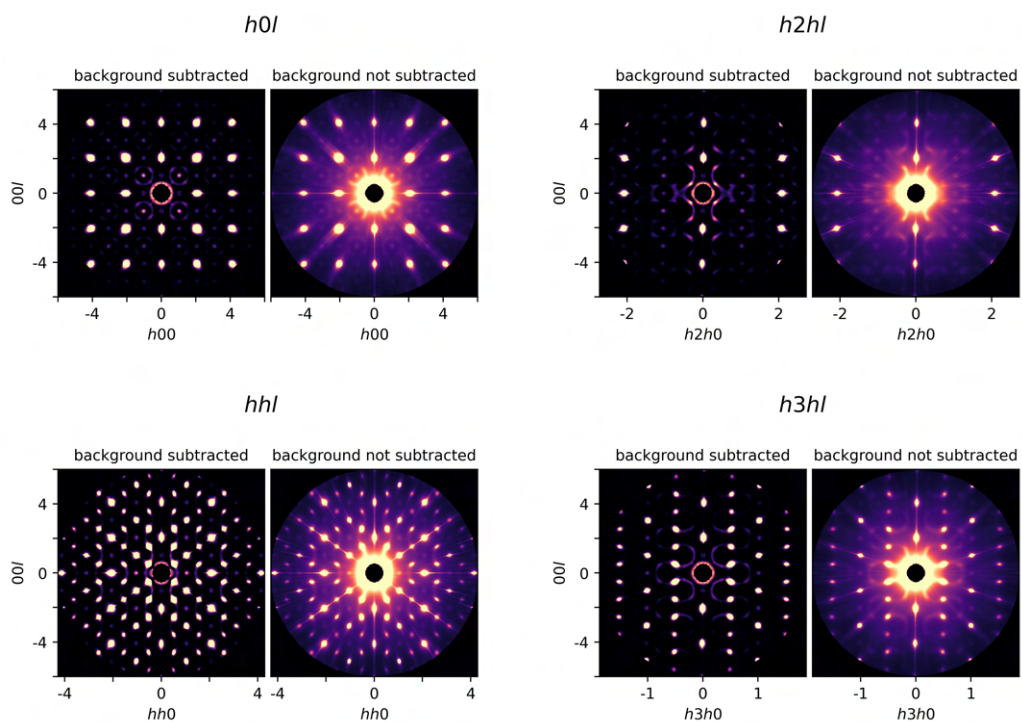


Figure 3.44: Comparison of the  $h0l$ ,  $hhl$ ,  $h2hl$  and  $h3hl$  planes reconstructed from 3D ED data, before and after background subtraction in *PETS2*.

### 3.9 Conclusion

We showed that the three-dimensional diffuse scattering in 3D ED data can be obtained with a quality comparable to that from single-crystal X-ray diffraction. The 3D- $\Delta$ PDF obtained from 3D ED data is also in good agreement with the one obtained from single-crystal X-ray diffraction data. The 3D- $\Delta$ PDF can thus be used to determine the origin of the diffuse scattering in 3D ED data. As electron diffraction requires much smaller crystal sizes than X-ray diffraction, this opens up the possibility to investigate the local structure of materials for which no crystals large enough for single-crystal X-ray diffraction are available.

Short-range order parameters were refined from the three-dimensional diffuse scattering in both 3D ED and single-crystal X-ray diffraction data acquired on Nb<sub>0.84</sub>CoSb. The correlations between neighbouring vacancies and the displacements of Sb and Co atoms were refined from the diffuse scattering using a Monte Carlo refinement in *DISCUS* and using a 3D- $\Delta$ PDF refinement in *Yell*. Because 3D- $\Delta$ PDF refinements are much faster than Monte Carlo refinements, the 3D- $\Delta$ PDF refinement allowed us to refine the correlations between neighbouring vacancies up to the 16<sup>th</sup> nearest neighbour. To determine the accuracy of the refined correlations, the displacements of Sb and Co atoms refined from the diffuse scattering were compared with the displacements refined from the Bragg reflections in single-crystal X-ray diffraction data. The local Sb and Co displacements refined from the diffuse scattering in single-crystal X-ray diffraction data using a 3D- $\Delta$ PDF refinement (0.1442(6) Å and 0.1299(9) Å) are close to the average Sb and Co displacements refined from the Bragg reflections in single-crystal X-ray diffraction data (0.141(1) Å and 0.130(1) Å). The local Sb and Co displacements refined from the diffuse scattering using a Monte Carlo refinement are 0.142(11) Å and 0.112(8) Å for the refinement on single-crystal X-ray diffraction data, and 0.142(23) Å and 0.071(21) Å for the refinement on 3D ED data. The difference with the average Sb and Co displacements is much smaller for the 3D- $\Delta$ PDF refinement than for the Monte Carlo refinement, which indicates that the correlations refined using the 3D- $\Delta$ PDF refinement are also likely to be more accurate.

The spatial resolution of the observed diffuse scattering is lower in 3D ED data than in single-crystal X-ray diffraction data. The spatial resolution of the observed diffuse scattering depends on the convergence of the beam, the detector point spread function and the crystal mosaicity. For high-resolution experiments, 3D ED data should be acquired in SAED mode using a CCD.

The Nb occupancy and the average displacements of Sb and Co atoms were also refined from the Bragg reflections in 3D ED data, and compared with reference values refined from the Bragg reflections in single-crystal X-ray diffraction data. The Nb occupancy refined from the Bragg reflections in 3D ED data differs by only 0.014(11) from the Nb occupancy refined from the Bragg reflections in single-crystal X-ray diffraction



data. The displacements of Sb and Co atoms refined from the Bragg reflections in 3D ED data differ by 0.040(5) Å from the displacements of Sb and Co atoms refined from the Bragg reflections in single-crystal X-ray diffraction data.

Finally, we showed that the model of the short-range Nb-vacancy order in  $\text{Nb}_{0.84}\text{CoSb}$  can also be applied to materials with similar diffuse scattering such as  $\text{LiNi}_{0.5}\text{Sn}_{0.3}\text{Co}_{0.2}\text{O}_2$ .



## Conclusions and outlook

---

In this thesis, we showed that short-range order parameters can be refined from the diffuse scattering in three-dimensional electron diffraction (3D ED) data. As 3D ED requires much smaller crystal sizes than single-crystal X-ray diffraction, this opens up the possibility to refine short-range order parameters in materials for which no crystals large enough for single-crystal X-ray diffraction are available.

In Chapter 2, we refined short-range order parameters from the one-dimensional diffuse scattering in 3D ED data acquired on  $\text{Li}_{1.2}\text{Ni}_{0.13}\text{Mn}_{0.54}\text{Co}_{0.13}\text{O}_2$ . The number of stacking faults and the twin percentages were refined from the diffuse scattering using a Monte Carlo refinement in *DISCUS*. For the diffuse scattering in the  $[\bar{2}10]$  reciprocal space section of the investigated crystal, the best agreement between the observed and calculated intensities was achieved for a stacking fault probability of 29(2) % and twin percentages of  $p_{[100]} = 40(3)$  %,  $p_{[\bar{1}10]} = 34(3)$  % and  $p_{[\bar{1}\bar{1}0]} = 26(6)$  %.

In Chapter 3, we refined short-range order parameters from the three-dimensional diffuse scattering in both 3D ED and single-crystal X-ray diffraction data acquired on  $\text{Nb}_{0.84}\text{CoSb}$ . The correlations between neighbouring vacancies and the displacements of Sb and Co atoms were refined from the diffuse scattering using a Monte Carlo refinement in *DISCUS* and using a three-dimensional difference pair distribution function (3D- $\Delta$ PDF) refinement in *Yell*. To determine the accuracy of the refined correlations, the displacements of Sb and Co atoms refined from the diffuse scattering were compared with the displacements refined from the Bragg reflections in single-crystal X-ray diffraction data. The difference between the Sb and Co displacements refined from the diffuse scattering and the Sb and Co displacements refined from the Bragg reflections in single-crystal X-ray diffraction data is 0.012(7) Å for the Monte Carlo refinement applied to the diffuse scattering in single-crystal X-ray diffraction data, 0.03(2) Å for the Monte Carlo refinement applied to the diffuse scattering in 3D ED data, and 0.0019(9) Å for the 3D- $\Delta$ PDF refinement applied to the diffuse scattering in single-crystal X-ray diffraction data. The difference is much smaller for the 3D- $\Delta$ PDF refinement (0.0019(9) Å) than for the Monte Carlo refinement (0.012(7) Å), which indicates that the correlations refined using the 3D- $\Delta$ PDF refinement are also likely to be more accurate.

We showed that the three-dimensional diffuse scattering in 3D ED data can be obtained with a quality comparable to that from single-crystal X-ray diffraction. The spatial resolution of the observed diffuse scattering depends on the convergence of the

### CHAPTER 3. THREE-DIMENSIONAL DIFFUSE SCATTERING - $Nb_{0.84}CoSb$

beam, the detector point spread function and the crystal mosaicity. For high-resolution experiments, 3D ED data should be acquired in selected area electron diffraction (SAED) mode using a charge-coupled device (CCD). Differences between the observed and calculated intensities in 3D ED data are likely due to multiple scattering. As the probability for multiple scattering to occur increases with increasing sample thickness, it is important to acquire 3D ED data on small crystals. For  $Nb_{0.84}CoSb$ , the effect of multiple scattering seemed less than for  $Li_{1.2}Ni_{0.13}Mn_{0.54}Co_{0.13}O_2$ , probably because the three-dimensional diffuse scattering of  $Nb_{0.84}CoSb$  did not overlap with the Bragg reflections.

The 3D- $\Delta$ PDF is often used to determine the origin of the diffuse scattering in single-crystal diffraction data, and can be obtained by Fourier transforming the three-dimensional diffuse scattering. Full reciprocal space coverage is required for the calculation of the 3D- $\Delta$ PDF. Modern diffractometers, synchrotrons and neutron sources are designed so that full reciprocal space coverage is routinely achieved. Because transmission electron microscopes are designed for imaging experiments, the angular range for 3D ED data collection is limited by the presence of the objective lens pole pieces. For  $Li_{1.2}Ni_{0.13}Mn_{0.54}Co_{0.13}O_2$ , the one-dimensional diffuse scattering had only inversion symmetry, and applying symmetry averaging was not sufficient to achieve full reciprocal space coverage. The electron 3D- $\Delta$ PDF could thus not be reconstructed. A solution could be to increase the data completeness by combining data sets from several crystals, or combining several data sets from the same crystal acquired with a different orientation of the grid in the sample holder. For  $Nb_{0.84}CoSb$ , the three-dimensional diffuse scattering was highly symmetric, and the missing wedge in the three-dimensional reciprocal space could be filled by applying symmetry averaging with Laue class  $m\bar{3}m$ . The electron 3D- $\Delta$ PDF could be reconstructed and could be used to determine the origin of the observed diffuse scattering.

Monte Carlo refinements are computationally very demanding. The Monte Carlo refinement for  $Li_{1.2}Ni_{0.13}Mn_{0.54}Co_{0.13}O_2$  was done on a high performance computing (HPC) cluster and took three days of wall-clock time for 50 refinement cycles, using 28 cores in parallel. Further parallelizing the refinement script so that the individual crystals and lots are also calculated in parallel could further decrease the refinement time. Due to a problem with the installation of *DISCUS* on the HPC cluster, the Monte Carlo refinement for  $Nb_{0.84}CoSb$  was done on a desktop computer and took about seven days for 19 refinement cycles, using eight cores in parallel. In contrast, the 3D- $\Delta$ PDF refinement took about 20 minutes. 3D- $\Delta$ PDF refinements are much faster than Monte Carlo refinements since they do not require the construction of a model crystal. The 3D- $\Delta$ PDF refinement in *Yell* was done against three-dimensional diffuse scattering data, whereas the Monte Carlo refinement in *DISCUS* was done against the diffuse scattering in one two-dimensional plane. In *DISCUS*, we only refined the correlation between next-nearest neighbour vacancy pairs  $c_{(1,0,0)}$ . Because 3D- $\Delta$ PDF refinements are much faster than Monte Carlo refinements, the 3D- $\Delta$ PDF refinement in *Yell* allowed us to refine the correlations between neighbouring vacancies up to the 16<sup>th</sup> nearest neighbour. The

disadvantage of 3D- $\Delta$ PDF refinements is that they may result in non-physical structure models [118]. Also, in cases where the 3D- $\Delta$ PDF cannot be reconstructed (such as for  $\text{Li}_{1.2}\text{Ni}_{0.13}\text{Mn}_{0.54}\text{Co}_{0.13}\text{O}_2$ ), Monte Carlo refinements are still desirable.

Monte Carlo refinements and 3D- $\Delta$ PDF refinements require the construction of a model crystal with short-range order. Information on the type of short-range order can be obtained from the diffuse scattering itself (one-, two- or three-dimensional), the interpretation of the features in the 3D- $\Delta$ PDF, the average structure refinement (refined occupancies, displacements and atomic displacement parameters), high-resolution scanning transmission electron microscopy (HR-STEM) images and other prior knowledge. In practice, identification of a proper real structure model requires significant experience from the user and many cycles of trials-and-errors. The refinement of short-range order parameters from the diffuse scattering takes thus much more time than the refinement of average structure parameters from the Bragg reflections.

In future experiments, we will investigate the effect of temperature and gas environment on the three-dimensional diffuse scattering in 3D ED data. 3D ED data can be acquired in a gas environment using special sample holders [185]. The temperature or pressure of the gas in the sample holder could be adjusted while acquiring several 3D ED data sets on the same crystal. Such experiments allow to investigate the effect of temperature or pressure on the crystal structure. For materials with short-range order, such experiments would allow to follow changes in the intensity distribution of the diffuse scattering with changing temperature/pressure. Refining short-range order parameters from the intensity distribution of the diffuse scattering would then allow to quantify changes in the short-range order parameters.



## Bibliography

---

- [1] International Union of Crystallography. Report of the Executive Committee for 1991. *Acta Crystallogr. Sect. A Found. Crystallogr.*, A48:922–946, 1992. 8
- [2] Walther Friedrich. Röntgenstrahlinterferenzen. *Phys Z.*, 14:1079–1087, 1913. 8
- [3] M V Laue. Röntgenstrahlinterferenz und Mischkristalle. *Ann. Phys.*, 361(15):497–506, 1918. 8
- [4] T. R. Welberry and T. Weber. One hundred years of diffuse scattering. *Crystallogr. Rev.*, 22(1):2–78, 2016. 8, 10, 11, 12, 27, 30, 31, 75, 76, 82, 86
- [5] Joseph A.M. Paddison. Ultrafast calculation of diffuse scattering from atomistic models. *Acta Crystallogr. Sect. A Found. Adv.*, 75(1):14–24, 2019. 8
- [6] Colin R. Groom, Ian J. Bruno, Matthew P. Lightfoot, and Suzanna C. Ward. The Cambridge structural database. *Acta Crystallogr. Sect. B Struct. Sci. Cryst. Eng. Mater.*, 72(2):171–179, 2016. 8, 19
- [7] Ella Mara Schmidt. *Disorder models from reciprocal space analysis in single crystal diffuse scattering*. PhD thesis, Friedrich-Alexander Universität Erlangen-Nürnberg, 2019. 8, 17
- [8] D. Williams and C Carter. *Transmission Electron Microscopy. A Textbook for Materials Science*. 2009. 8, 14, 15, 16, 18, 20, 21
- [9] Ella Mara Schmidt, Sofia Thomas, Johnathan M. Bulled, Arianna Minelli, and Andrew L. Goodwin. Interplay of thermal diffuse scattering and correlated compositional disorder in KCl1-xBrx. *Acta Crystallogr. Sect. B Struct. Sci. Cryst. Eng. Mater.*, 78:385–391, 2022. 9, 10
- [10] P. Tsampas, M. N., Sapountzi, F. M., & Vernoux. Applications of yttria stabilized zirconia (YSZ) in catalysis. *Catal. Sci. Technol.*, 5(11):4884–4900, 2015. 9
- [11] K. Schindler, D. Schmeisser, U. Vohrer, H. D. Wiemhöfer, and W. Göpel. Spectroscopic and electrical studies of yttria-stabilized zirconia for oxygen sensors. *Sensors and Actuators*, 17(3-4):555–568, 1989. 9
- [12] Ai Quoc Pham and Robert S. Glass. Oxygen pumping characteristics of yttria-stabilized-zirconia. *Electrochim. Acta*, 43(18):2699–2708, 1998. 9

## BIBLIOGRAPHY

- [13] Ella Mara Schmidt, Reinhard B. Neder, James D. Martin, Arianna Minelli, Marie-Hélène Lemée, and Andrew L. Goodwin. Direct interpretation of the X-ray and neutron three-dimensional difference pair distribution functions (3D- $\Delta$ PDFs) of yttria-stabilized zirconia. *Acta Crystallogr. Sect. B Struct. Sci. Cryst. Eng. Mater.*, 79(2):138–147, 2023. 9, 10, 78, 93, 94
- [14] Nikolaj Roth and Bo B. Iversen. Solving the disordered structure of  $\beta$ -Cu<sub>2-x</sub>Se using the three-dimensional difference pair distribution function. *Acta Crystallogr. Sect. A Found. Adv.*, 75(3):465–473, 2019. 9, 10
- [15] Nikolaj Roth, Andrew F. May, Feng Ye, Bryan C. Chakoumakos, and Bo Brummerstedt Iversen. Model-free reconstruction of magnetic correlations in frustrated magnets. *IUCrJ*, 5:410–416, 2018. 9, 10, 12
- [16] B. E. Warren, B. L. Averbach, and B. W. Roberts. Atomic size effect in the x-ray scattering by alloys. *J. Appl. Phys.*, 22(12):1493–1496, 1951. 10, 12
- [17] Werner Schweika. *Disordered alloys: diffuse scattering and Monte Carlo simulations*, volume 147. Springer Science & Business Media, 1998. 11
- [18] T. Yamamoto, M. S. Choi, S. Majima, T. Fukuda, and T. Kakeshita. Origin of diffuse scattering appearing in iron-doped Ti-Ni shape memory alloys. *Eur. Phys. J. Spec. Top.*, 158(1):1–5, 2008. 11
- [19] M. Paciak, T. R. Welberry, J. Kulda, M. Kempa, and J. Hlinka. Polar nanoregions and diffuse scattering in the relaxor ferroelectric PbMg<sub>1/3</sub>Nb<sub>2/3</sub>O<sub>3</sub>. *Phys. Rev. B - Condens. Matter Mater. Phys.*, 85(22):1–9, 2012. 11
- [20] M. Izquierdo, S. Megtert, J. P. Albouy, J. Avila, M. A. Valbuena, G. Gu, J. S. Abell, G. Yang, M. C. Asensio, and R. Comes. X-ray diffuse scattering experiments from bismuth-based high-T<sub>c</sub> superconductors. *Phys. Rev. B*, 74(5):054512, 2006. 11
- [21] M. Izquierdo, S. Megtert, D. Colson, V. Honkimäki, A. Forget, H. Raffy, and R. Comès. One dimensional ordering of doping oxygen in HgBa<sub>2</sub>Cu<sub>0.4+ $\delta$</sub>  superconductors evidenced by X-ray diffuse scattering. *J. Phys. Chem. Solids*, 72(5):545–548, 2011. 11
- [22] David A. Keen. Disordering phenomena in superionic conductors. *J. Phys. Condens. Matter*, 14(32), 2002. 11
- [23] T. R. Welberry and M. Paściak. Monte carlo and molecular dynamics simulation of disorder in the Ag + fast ion conductors pearceite and polybasite. *Metall. Mater. Trans. A Phys. Metall. Mater. Sci.*, 42(1):6–13, 2011. 11
- [24] M. Barchuk, V. Holý, B. Miljević, B. Krause, T. Baumbach, J. Hertkorn, and F. Scholz. X-ray diffuse scattering from threading dislocations in epitaxial GaN layers. *J. Appl. Phys.*, 108(4):1–7, 2010. 11



- [25] E. J. Chan, T. R. Welberry, D. J. Goossens, A. P. Heerdegen, A. G. Beasley, and P. J. Chupas. Single-crystal diffuse scattering studies on polymorphs of molecular crystals. I. the room-temperature polymorphs of the drug benzocaine. *Acta Crystallogr. Sect. B Struct. Sci.*, 65(3):382–392, 2009. 11, 27
- [26] E. J. Chan, T. R. Welberry, A. P. Heerdegen, and D. J. Goossens. Diffuse scattering study of aspirin forms (I) and (II). *Acta Crystallogr. Sect. B Struct. Sci.*, 66(6):696–707, 2010. 11
- [27] John Maxwell Cowley. An approximate theory of order in alloys. *Phys. Rev.*, 77(5):669–675, 1950. 11, 12
- [28] T. Janssen and A. Janner. Aperiodic crystals and superspace concepts. *Acta Crystallogr. Sect. B Struct. Sci. Cryst. Eng. Mater.*, 70(4):617–651, 2014. 11
- [29] Olive S. Edwards and H. Lipson. Imperfections in the structure of Cobalt. I. Experimental work and proposed structure. *Proc. R. Soc. London. Ser. A.*, 180:268–277, 1942. 12
- [30] A.J.C. Wilson. Imperfections in the structure of cobalt. II. Mathematical treatment of proposed structure. *Proc. R. Soc. London. Ser. A. Math. Phys. Sci.*, 180(982):277–285, 1942. 12
- [31] Sterling Hendricks and Edward Teller. X-ray interference in partially ordered layer lattices. *J. Chem. Phys.*, 10(3):147–167, 1942. 12
- [32] H. Jagodzinski. Eindimensionale Fehlordnung in Kristallen und ihr Einfluss auf die Röntgeninterferenzen. I. Berechnung des Fehlordnungsgrades aus den Röntgenintensitäten. *Acta Crystallogr.*, 2(4):201–207, 1949. 12
- [33] H. Jagodzinski. Eindimensionale Fehlordnung in Kristallen und ihr Einfluss auf die Röntgeninterferenzen. II. Berechnung der fehlgeordneten dichtesten Kugelpackungen mit Wechselwirkungen der Reichweite 3. *Acta Crystallogr.*, 2(4):208–214, 1949. 12
- [34] H. Jagodzinski. Eindimensionale Fehlordnung in Kristallen und ihr Einfluss auf die Röntgeninterferenzen. III. Vergleich der Berechnungen mit experimentellen Ergebnissen. *Acta Crystallogr.*, 2(5):298–304, 1949. 12
- [35] John Maxwell Cowley. X-ray measurement of order in single crystals of Cu<sub>3</sub>Au. *J. Appl. Phys.*, 21(1):24–30, 1950. 12
- [36] John Maxwell Cowley. *Diffraction physics*. Elsevier Science, Amsterdam, 1995. 12, 21
- [37] Reinhard B. Neder and Thomas Proffen. *Diffuse Scattering and Defect Structure Simulations: A cook book using the program DISCUS*, volume 11. Oxford University Press, 2008. 12, 25, 28, 29, 31, 32, 81, 82, 86, 100

## BIBLIOGRAPHY

- [38] P. Schaub, T. Weber, and W. Steurer. Exploring local disorder in single crystals by means of the three-dimensional pair distribution function. *Philos. Mag.*, 87(18-21):2781–2787, 2007. 12
- [39] Thomas Weber and Arkadiy Simonov. The three-dimensional pair distribution function analysis of disordered single crystals: Basic concepts. *Zeitschrift für Krist.*, 227(5):238–247, 2012. 12, 14, 31, 32
- [40] Ella Mara Schmidt, Paul Benjamin Klar, Yasar Krysiak, Petr Svora, Andrew L. Goodwin, and Lukas Palatinus. Quantitative three-dimensional local order analysis of nanomaterials through electron diffraction. (1):1–8, 2023. 14, 93, 94
- [41] Th Proffen, S. J.L. Billinge, T. Egami, and D. Louca. Structural analysis of complex materials using the atomic pair distribution function - A practical guide. *Zeitschrift für Krist.*, 218(2):132–143, 2003. 14
- [42] Mauro Gemmi, Enrico Mugnaioli, Tatiana E. Gorelik, Ute Kolb, Lukas Palatinus, Philippe Boullay, Sven Hovmöller, and Jan Pieter Abrahams. 3D electron diffraction: The nanocrystallography revolution. *ACS Cent. Sci.*, 5(8):1315–1329, 2019. 14, 21, 22, 24, 74
- [43] Vitalij K. Pecharsky and Peter Y. Zavalij. *Fundamentals of powder diffraction and structural characterization of materials*. Number November 2008. 2005. 15, 16, 17, 18, 19, 20, 21
- [44] Alec Belkly, Mariette Helderma, Vicky Lyman Karen, and Peter Ulkch. New developments in the Inorganic Crystal Structure Database (ICSD): Accessibility in support of materials research and design. *Acta Crystallogr. Sect. B Struct. Sci.*, 58(3 PART 1):364–369, 2002. 19
- [45] Saulius Graulis, Daniel Chateigner, Robert T. Downs, A. F.T. Yokochi, Miguel Quirós, Luca Lutterotti, Elena Manakova, Justas Butkus, Peter Moeck, and Armel Le Bail. Crystallography Open Database - An open-access collection of crystal structures. *J. Appl. Crystallogr.*, 42(4):726–729, 2009. 19
- [46] Stephen K. Burley, Helen M. Berman, Charmi Bhikadiya, Chunxiao Bi, Li Chen, Luigi Di Costanzo, Cole Christie, Ken Dalenberg, Jose M. Duarte, Shuchismita Dutta, Zukang Feng, Sutapa Ghosh, David S. Goodsell, Rachel K. Green, Vladimir Guranović, Dmytro Guzenko, Brian P. Hudson, Tara Kalro, Yuhe Liang, Robert Lowe, Harry Namkoong, Ezra Peisach, Irina Periskova, Andreas Prlić, Chris Randle, Alexander Rose, Peter Rose, Raul Sala, Monica Sekharan, Chenghua Shao, Lihua Tan, Yi Ping Tao, Yana Valasatava, Maria Voigt, John Westbrook, Jesse Woo, Huanwang Yang, Jasmine Young, Marina Zhuravleva, and Christine Zardecki. RCSB Protein Data Bank: Biological macromolecular structures enabling research and education in fundamental biology, biomedicine, biotechnology and energy. *Nucleic Acids Res.*, 47(D1):D464–D474, 2019. 19

- [47] Jessica F. Bruhn, Giovanna Scapin, Anchi Cheng, Brandon Q. Mercado, David G. Waterman, Thejusvi Ganesh, Sargis Dallakyan, Brandon N. Read, Travis Nieuwma, Kyle W. Lucier, Megan L. Mayer, Nicole J. Chiang, Nicole Poweleit, Philip T. McGilvray, Timothy S. Wilson, Michael Mashore, Camille Hennessy, Sean Thomson, Bo Wang, Clinton S. Potter, and Bridget Carragher. Small Molecule Microcrystal Electron Diffraction for the Pharmaceutical Industry—Lessons Learned From Examining Over Fifty Samples. *Front. Mol. Biosci.*, 8(July):1–16, 2021. 19, 22
- [48] Edward Prince. *International Tables for Crystallography . Volume C: Mathematical Physical and Chemical Tables* , volume 49. Springer Science & Business Media, 1993. 19
- [49] Tim Gruene, Julian J. Holstein, Guido H. Clever, and Bernhard Keppler. Establishing electron diffraction in chemical crystallography. *Nat. Rev. Chem.*, 5(9):660–668, 2021. 20, 23
- [50] Max T B Clabbers, Tim Gruene, Van Genderen, and Jan Pieter. Reducing dynamical electron scattering reveals hydrogen atoms research papers. *Acta Crystallogr. A*, pages 82–93, 2019. 21, 52
- [51] Paul B. Klar, Yaşar Krysiak, Hongyi Xu, Gwladys Steciuk, Jung Cho, Xiaodong Zou, and Lukas Palatinus. Accurate structure models and absolute configuration determination using dynamical effects in continuous-rotation 3D electron diffraction data. *Nat. Chem.*, 2023. 21, 22, 23, 24
- [52] *SingleCrystal User's Guide*. CrystalMaker Software Ltd. All, Oxford, 2020. 21
- [53] Joseph A.M. Paddison. Ultrafast calculation of diffuse scattering from atomistic models. *Acta Crystallogr. Sect. A Found. Adv.*, 75(1):14–24, 2019. 21, 24, 25, 95
- [54] R. Vincent and P.a. Midgley. Double conical beam-rocking system for measurement of integrated electron diffraction intensities. *Ultramicroscopy*, 53(3):271–282, mar 1994. 22
- [55] U. Kolb, T. Gorelik, C. Kübel, M. T. Otten, and D. Hubert. Towards automated diffraction tomography: Part I-Data acquisition. *Ultramicroscopy*, 107(6-7):507–513, 2007. 22, 23, 24, 26
- [56] U. Kolb, T. Gorelik, and M. T. Otten. Towards automated diffraction tomography. Part II-Cell parameter determination. *Ultramicroscopy*, 108(8):763–772, 2008. 22, 23, 26
- [57] E. Hand, G. Vogel, K. Garber, J. Kaiser, K. Servick, D. Clery, R. F. Service, and M. Wadman. Breakthrough of the year, Runners-up. *Science (80-. )*, 362(6421):1346–1351, 2018. 22

## BIBLIOGRAPHY

- [58] Paul B Klar, Yaşar Krysiak, Hongyi Xu, Gwladys Steciuk, Jung Cho, Xiaodong Zou, and Lukas Palatinus. Accurate structure models and absolute configuration determination using dynamical effects in continuous-rotation 3D electron diffraction data. 2023. 23
- [59] Bernhard Spingler, Stephan Schnidrig, Tonya Todorova, and Ferdinand Wild. Some thoughts about the single crystal growth of small molecules. *CrystEngComm*, 14(3):751–757, 2012. 22
- [60] Mauro Gemmi and Peter Oleynikov. Scanning reciprocal space for solving unknown structures: Energy filtered diffraction tomography and rotation diffraction tomography methods. *Zeitschrift fur Krist.*, 228(1):51–58, 2013. 23
- [61] Daliang Zhang, Peter Oleynikov, Sven Hovmoller, and Xiaodong Zou. Collecting 3D electron diffraction data by the rotation method. *Zeitschrift fur Krist.*, 225(2-3):94–102, 2010. 23
- [62] Wei Wan, Junliang Sun, Jie Su, Sven Hovmöller, and Xiaodong Zou. Three-dimensional rotation electron diffraction: Software RED for automated data collection and data processing. *J. Appl. Crystallogr.*, 46(6):1863–1873, 2013. 23
- [63] E. Mugnaioli, T. Gorelik, and U. Kolb. "Ab initio" structure solution from electron diffraction data obtained by a combination of automated diffraction tomography and precession technique. *Ultramicroscopy*, 109(6):758–765, 2009. 23
- [64] Philippe Boullay, Lukas Palatinus, and Nicolas Barrier. Precession electron diffraction tomography for solving complex modulated structures: The case of Bi<sub>5</sub>Nb<sub>3</sub>O<sub>15</sub>. *Inorg. Chem.*, 52(10):6127–6135, 2013. 23
- [65] Brent L. Nannenga, Dan Shi, Andrew G.W. Leslie, and Tamir Gonen. High-resolution structure determination by continuous-rotation data collection in MicroEDED. *Nat. Methods*, 11(9):927–930, 2014. 23
- [66] Mauro Gemmi, Maria G.I. La Placa, Athanassios S. Galanis, Edgar F. Rauch, and Stavros Nicolopoulos. Fast electron diffraction tomography. *J. Appl. Crystallogr.*, 48(i):718–727, 2015. 23
- [67] Yunchen Wang, Sofia Takki, Ocean Cheung, Hongyi Xu, Wei Wan, and A Ken Inge. Elucidation of the elusive structure and formula of the active pharmaceutical ingredient bismuth subgallate by continuous rotation electron. *Chem. Commun.*, pages 7018–7021, 2017. 23
- [68] Shuai Yuan, Jun Sheng Qin, Hai Qun Xu, Jie Su, Daniel Rossi, Yuanping Chen, Liangliang Zhang, Christina Lollar, Qi Wang, Hai Long Jiang, Dong Hee Son, Hongyi Xu, Zhehao Huang, Xiaodong Zou, and Hong Cai Zhou. Cluster: An ideal inorganic building unit for photoactive metal-organic frameworks. *ACS Cent. Sci.*, 4(1):105–111, 2018. 23

- [69] L. Palatinus, D. Jacob, P. Cuvillier, M. Klementová, W. Sinkler, and L. D. Marks. Structure refinement from precession electron diffraction data. *Acta Crystallogr. Sect. A Found. Crystallogr.*, 69(2):171–188, 2013. 24
- [70] Lukáš Palatinus, Václav Petříček, and Cinthia Antunes Correâ. Structure refinement using precession electron diffraction tomography and dynamical diffraction: Theory and implementation. *Acta Crystallogr. Sect. A Found. Adv.*, 71:235–244, 2015. 24, 40, 66, 68, 69
- [71] Lukáš Palatinus, Cinthia Antunes Corrêa, Gwladys Steciuk, Damien Jacob, Pascal Roussel, Philippe Boullay, Mariana Klementová, Mauro Gemmi, Jaromír Kopeček, M. Chiara Domeneghetti, Fernando Cámara, and Václav Petříček. Structure refinement using precession electron diffraction tomography and dynamical diffraction: Tests on experimental data. *Acta Crystallogr. Sect. B Struct. Sci. Cryst. Eng. Mater.*, 71:740–751, 2015. 24, 44, 66
- [72] Václav Petříček, Lukáš Palatinus, Jakub Plášil, and Michal Dušek. J ana 2020 - a new version of the crystallographic computing system J ana. *Zeitschrift fur Krist. - Cryst. Mater.*, 238:271–282, 2023. 24
- [73] Lukáš Palatinus, Petr Brázda, Martin Jelínek, Jaromíra Hrdá, Gwladys Steciuk, and Mariana Klementová. Specifics of the data processing of precession electron diffraction tomography data and their implementation in the program PETS2.0. *Acta Crystallogr. Sect. B Struct. Sci. Cryst. Eng. Mater.*, 75(4):512–522, 2019. 24
- [74] James W. Cooley and John W. Tukey. An Algorithm for the Machine Calculation of Complex Fourier Series. *Math. Comput.*, 19(90):297, 1965. 24
- [75] RICHARD C. Singleton. An algorithm for computing the mixed radix fast Fourier transform. *IEEE Trans. audio Electroacoust.*, 17(2):93–103, 1969. 24
- [76] B. D. Butler and T. R. Welberry. Calculation of diffuse scattering from simulated disordered crystals: A comparison with optical transforms. *J. Appl. Crystallogr.*, 25:391–399, 1992. 25
- [77] Th Proffen and R. B. Neder. DISCUS: A program for diffuse scattering and defect-structure simulation. *J. Appl. Crystallogr.*, 30(2):171–175, 1997. 25
- [78] Thomas Weber and Hans Beat Bürgi. Determination and refinement of disordered crystal structures using evolutionary algorithms in combination with Monte Carlo methods. *Acta Crystallogr. Sect. A Found. Crystallogr.*, 58(6):526–540, 2002. 25, 27, 28, 30
- [79] Cornelius Lanczos. *Applied analysis*. Englewood Cliffs, New Jersey: Prentice-Hall, 1956. 25
- [80] Claude E. DUCHON. *Lanczos filtering in one and two dimensions*, volume 18. 1979. 25

## BIBLIOGRAPHY

- [81] R. L. Withers, T. R. Welberry, F. J. Brink, and L. Norén. Oxygen/fluorine ordering, structured diffuse scattering and the local crystal chemistry of  $K_3MoO_3F_3$ . *J. Solid State Chem.*, 170(2):211–220, 2003. 26, 110
- [82] R. L. Withers, T. R. Welberry, A. K. Larsson, Y. Liu, L. Norén, H. Rundlöf, and F. J. Brink. Local crystal chemistry, induced strain and short range order in the cubic pyrochlore  $(Bi_{1.5-\alpha}Zn_{0.5-\beta})(Zn_{0.5-\gamma}Nb_{1.5-\delta})O_{(7-1.5\alpha-\beta-\gamma-2.5\delta)}$  (BZN). *J. Solid State Chem.*, 177(1):231–244, 2004. 26
- [83] Yasuhiro Fujii, Hiroshi Miura, Naoto Suzuki, Takayuki Shoji, and Noriaki Nakayama. Structural and electrochemical properties of  $LiNi_{1/3}Co_{1/3}Mn_{1/3}O_2-LiMg_{1/3}Co_{1/3}Mn_{1/3}O_2$  solid solutions. *Solid State Ionics*, 178(11-12):849–857, 2007. 26
- [84] A. L. Goodwin, R. L. Withers, and H. B. Nguyen. Real-space refinement of single-crystal electron diffuse scattering and its application to  $Bi_2Ru_2O_7-\delta$ . *J. Phys. Condens. Matter*, 19(33):335216, 2007. 26
- [85] Petr Brázda, Lukáš Palatinus, Jan Drahoš, Karel Knížek, and Josef Buršík. Calcium-induced cation ordering and large resistivity decrease in  $Pr_{0.3}CoO_2$ . *J. Phys. Chem. Solids*, 96:10–16, 2016. 26
- [86] Haishuang Zhao, Yaşar Krysiak, Kristin Hoffmann, Bastian Barton, Leopoldo Molina-Luna, Reinhard B. Neder, Hans Joachim Kleebe, Thorsten M. Gesing, Hartmut Schneider, Reinhard X. Fischer, and Ute Kolb. Elucidating structural order and disorder phenomena in mullite-type  $Al_4B_2O_9$  by automated electron diffraction tomography. *J. Solid State Chem.*, 249:114–123, 2017. 26
- [87] Alexandra Neagu and Cheuk Wai Tai. Local disorder in  $Na_{0.5}Bi_{0.5}TiO_3$ -piezoceramic determined by 3D electron diffuse scattering. *Sci. Rep.*, 7(1):1–12, 2017. 26
- [88] Tatiana E. Gorelik, Sándor L. Bekő, Jaroslav Teteruk, Winfried Heyse, and Martin U. Schmidt. Analysis of diffuse scattering in electron diffraction data for the crystal structure determination of Pigment Orange 13,  $C_{32}H_{24}Cl_2N_8O_2$ . *Acta Crystallogr. Sect. B Struct. Sci. Cryst. Eng. Mater.*, 79(2):122–137, 2023. 26
- [89] Yaşar Krysiak, Bastian Barton, Bernd Marler, Reinhard B. Neder, and Ute Kolb. Ab initio structure determination and quantitative disorder analysis on nanoparticles by electron diffraction tomography. *Acta Crystallogr. Sect. A Found. Adv.*, 74(2):93–101, 2018. 26, 57
- [90] Yasar Krysiak, Bernd Marler, Bastian Barton, Sergi Plana-Ruiz, Hermann Gies, Reinhard B. Neder, and Ute Kolba. New zeolite-like RUB-5 and its related hydrous layer silicate RUB-6 structurally characterized by electron microscopy, 2020. 26, 57

- [91] Nicholas Metropolis, Arianna W Rosenbluth, Marshall N Rosenbluth, Augusta H Teller, and Edward Teller. Equation of state calculations by fast computing machines. *J. Chem. Phys.*, 21(6):1087–1092, 1953. 26
- [92] Th Proffen and T. R. Welberry. Analysis of diffuse scattering of single crystals using Monte Carlo methods. *Phase Transitions*, 67(1):373–397, 1998. 27, 30, 31, 82, 86
- [93] S. C. Mayo, T. H. Proffen, M. Bown, and T. R. Welberry. Diffuse scattering and Monte Carlo simulations of cyclohexane-perhydrotriphenylene (PHTP) inclusion compounds, C<sub>6</sub>H<sub>12</sub>/C<sub>18</sub>H<sub>30</sub>. *J. Appl. Crystallogr.*, 32(3):464–471, 1999. 27, 28
- [94] T. R. Welberry. *Diffuse x-ray scattering and models of disorder*. Oxford University Press, USA, 2010. 27
- [95] T. R. Welberry, Th Proffen, and M. Bown. Analysis of Single-Crystal Diffuse X-ray Scattering via Automatic Refinement of a Monte Carlo Model. *Acta Crystallogr. Sect. A Found. Crystallogr.*, 54(5):661–674, 1998. 27, 28
- [96] T. R. Welberry. Diffuse X-ray scattering and disorder in p-methyl-N-(p-chlorobenzylidene)aniline, C<sub>14</sub>H<sub>12</sub>ClN (CIME): Analysis via automatic refinement of a Monte Carlo model. *Acta Crystallogr. Sect. A Found. Crystallogr.*, 56(4):348–358, 2000. 28
- [97] T. R. Welberry, D. J. Goossens, A. J. Edwards, and W. I.F. David. Diffuse X-ray scattering from benzil, C<sub>14</sub>H<sub>10</sub>O<sub>2</sub>: Analysis via automatic refinement of a Monte Carlo model. *Acta Crystallogr. Sect. A Found. Crystallogr.*, 57(1):101–109, 2001. 28
- [98] K. Price, R. M. Storn, and J. A. Lampinen. *Differential evolution: a practical approach to global optimization*. Springer Science and Business Media, 1 edition, 2005. 28
- [99] Reinhard Neder. DIFFEV Users Guide. 2019. 29
- [100] Reinhard B. Neder and Vladimir I. Korsunskiy. Structure of nanoparticles from powder diffraction data using the pair distribution function. *J. Phys. Condens. Matter*, 17:S125–S134, 2005. 29
- [101] H. B. Bürgi, J. Hauser, T. Weber, and R. B. Neder. Supramolecular architecture in a disordered perhydrotriphenylene inclusion compound from diffuse x-ray diffraction data. *Cryst. Growth Des.*, 5(6):2073–2083, 2005. 29
- [102] R. B. Neder, V. I. Korsunskiy, Ch Chory, G. Müller, A. Hofmann, S. Dembski, Ch Graf, and E. Rühl. Structural characterization of II–VI semiconductor nanoparticles. *Phys. Status Solidi Curr. Top. Solid State Phys.*, 4(9):3221–3233, 2007. 29

## BIBLIOGRAPHY

- [103] Katharine Page, Taylor C. Hood, Thomas Proffen, and Reinhard B. Neder. Building and refining complete nanoparticle structures with total scattering data. *J. Appl. Crystallogr.*, 44(2):327–336, 2011. 29
- [104] Wojciech A. Sławiński, David S. Wragg, Duncan Akporiaye, and Helmer Fjellvåg. Intergrowth structure modelling in silicoaluminophosphate SAPO-18/34 family. *Microporous Mesoporous Mater.*, 195:311–318, 2014. 29
- [105] Wojciech A. Sławiński, Anja Olafsen Sjøstad, and Helmer Fjellvåg. Stacking Faults and Polytypes for Layered Double Hydroxides: What Can We Learn from Simulated and Experimental X-ray Powder Diffraction Data? *Inorg. Chem.*, 55(24):12881–12889, 2016. 29
- [106] Wojciech A. Sławiński, Eirini Zacharaki, Helmer Fjellvåg, and Anja Olafsen Sjøstad. Structural Arrangement in Close-Packed Cobalt Polytypes. *Cryst. Growth Des.*, 18(4):2316–2325, 2018. 29
- [107] R. L. McGreevy and L. Pusztai. Reverse Monte Carlo Simulation: A New Technique for the Determination of Disordered Structures. *Mol. Simul.*, 1(6):359–367, 1988. 30
- [108] V. M. Nield, D. A. Keen, and R. L. McGreevy. The interpretation of single-crystal diffuse scattering using reverse Monte Carlo modelling. *Acta Crystallogr. Sect. A*, 51(5):763–771, 1995. 31
- [109] T. H. Proffen and T. R. Welberry. Analysis of Diffuse Scattering via the Reverse Monte Carlo Technique: A Systematic Investigation. *Acta Crystallogr. Sect. A Found. Crystallogr.*, 53(2):202–216, 1997. 31
- [110] T. H. Proffen and T. R. Welberry. An improved method for analysing single crystal diffuse scattering using the Reverse Monte Carlo technique. *Zeitschrift für Krist. - New Cryst. Struct.*, 212(11):764–767, 1997. 31
- [111] Th Proffen and T. R. Welberry. Analysis of Diffuse Scattering from Single Crystals via the Reverse Monte Carlo Technique. II. The Defect Structure of Calcium-Stabilized Zirconia. *J. Appl. Crystallogr.*, 31(3):318–326, 1998. 31
- [112] T. R. Welberry and Th Proffen. Analysis of Diffuse Scattering from Single Crystals via the Reverse Monte Carlo Technique. I. Comparison with Direct Monte Carlo. *J. Appl. Crystallogr.*, 31(3):309–317, 1998. 31
- [113] Matthew G. Tucker, Matthew P. Squires, Martin T. Dove, and David A. Keen. Dynamic structural disorder in cristobalite: neutron total scattering measurement and reverse Monte Carlo modelling. *J. Phys. Condens. Matter*, 13(3):403–423, 2001. 31
- [114] Matthew G. Tucker, Martin T. Dove, and David A. Keen. Application of the reverse Monte Carlo method to crystalline materials. *J. Appl. Crystallogr.*, 34(5):630–638, 2001. 31



- [115] Matthew G. Tucker, David A. Keen, Martin T. Dove, Andrew L. Goodwin, and Qun Hui. RMCProfile: Reverse Monte Carlo for polycrystalline materials. *J. Phys. Condens. Matter*, 19(33):335218, 2007. 31
- [116] Joseph A M Paddison and Andrew L Goodwin. Empirical Magnetic Structure Solution of Frustrated Spin Systems. 017204(January):4–7, 2012. 31
- [117] Zachary J. Morgan, Haidong D. Zhou, Bryan C. Chakoumakos, and Feng Ye. Rmc-discord: reverse Monte Carlo refinement of diffuse scattering and correlated disorder from single crystals. *J. Appl. Crystallogr.*, 54:1867–1885, 2021. 31
- [118] A. Simonov, T. Weber, and W. Steurer. Yell: A computer program for diffuse scattering analysis via three-dimensional delta pair distribution function refinement. *J. Appl. Crystallogr.*, 47(3):1146–1152, 2014. 31, 32, 106, 110, 125
- [119] Arkadiy Simonov. The three-Dimensional Pair Distribution Function Method for Analyzing Single Crystal Diffuse Scattering –Theory, Software Development and Application. *Thesis*, (21974):139, 2014. 32, 110
- [120] Julia Dshemuchadse, Sandro Bigler, Arkadiy Simonov, Thomas Weber, and Walter Steurer. A new complex intermetallic phase in the system Al-Cu-Ta with familiar clusters and packing principles. *Acta Crystallogr. Sect. B Struct. Sci. Cryst. Eng. Mater.*, 69(3):238–248, 2013. 32
- [121] Arkadiy Simonov, Thomas Weber, and Walter Steurer. Experimental uncertainties of three-dimensional pair distribution function investigations exemplified on the diffuse scattering from a tris-tert-butyl-1,3,5-benzene tricarboxamide single crystal. *J. Appl. Crystallogr.*, 47(6):2011–2018, 2014. 32, 104
- [122] Philipp Urban, Arkadiy Simonov, Thomas Weber, and Oliver Oeckler. Real structure of Ge<sub>4</sub>Bi<sub>2</sub>Te<sub>7</sub>: Refinement on diffuse scattering data with the 3D- $\Delta$ PDF method. *J. Appl. Crystallogr.*, 48(1):200–211, 2015. 32
- [123] Boris Sangiorgio, Emil S. Bozin, Christos D. Malliakas, Michael Fechner, Arkadiy Simonov, Mercouri G. Kanatzidis, Simon J.L. Billinge, Nicola A. Spaldin, and Thomas Weber. Correlated local dipoles in PbTe. *Phys. Rev. Mater.*, 2(8), 2018. 32
- [124] Laurent Guérin, Takefumi Yoshida, Edoardo Zatterin, Arkadiy Simonov, Dmitry Chernyshov, Hiroaki Iguchi, Bertrand Toudic, Shinya Takaishi, and Masahiro Yamashita. Elucidating 2D Charge-Density-Wave Atomic Structure in an MX-Chain by the 3D- $\Delta$ Pair Distribution Function Method. *ChemPhysChem*, 23(6), 2022. 32
- [125] A. Simonov, P. Rabiller, C. Mariette, L. Guérin, A. Bosak, A. Popov, and B. Toudic. Short-range order in the quasiliquid phases of alkane substructures within aperiodic urea inclusion crystals. *Phys. Rev. B*, 106(5):1–8, 2022. 32

## BIBLIOGRAPHY

- [126] Yunjian Liu, Qiliang Wang, Zhiqiang Zhang, Aichun Dou, Jun Pan, and Mingru Su. Investigation the electrochemical performance of layered cathode material  $\text{Li}_{1.2}\text{Ni}_{0.2}\text{Mn}_{0.6}\text{O}_2$  coated with  $\text{Li}_4\text{Ti}_5\text{O}_{12}$ . *Adv. Powder Technol.*, 27(4):1481–1487, 2016. 34, 45, 57
- [127] Yanhong Xiang, Zhen Sun, Jian Li, Xianwen Wu, Zhixiong Liu, Lizhi Xiong, Zeqiang He, Bo Long, Chen Yang, and Zhoulan Yin. Improved electrochemical performance of  $\text{Li}_{1.2}\text{Ni}_{0.2}\text{Mn}_{0.6}\text{O}_2$  cathode material for lithium ion batteries synthesized by the polyvinyl alcohol assisted sol-gel method. *Ceram. Int.*, 43(2):2320–2324, 2017. 34, 57
- [128] Vanessa Pimenta, Mariyappan Sathiya, Dmitry Batuk, Artem M. Abakumov, Domitille Giaume, Sophie Cassaignon, Dominique Larcher, and Jean Marie Tarascon. Synthesis of Li-Rich NMC: A Comprehensive Study. *Chem. Mater.*, 29(23):9923–9936, 2017. 34, 57
- [129] Prasant Kumar Nayak, Evan M. Erickson, Florian Schipper, Tirupathi Rao Penki, Nookala Munichandraiah, Philipp Adelhelm, Hadar Sclar, Francis Amalraj, Boris Markovsky, and Doron Aurbach. Review on Challenges and Recent Advances in the Electrochemical Performance of High Capacity Li- and Mn-Rich Cathode Materials for Li-Ion Batteries. *Adv. Energy Mater.*, 8(8):1–16, 2018. 34, 57
- [130] M. Sathiya, G. Rousse, K. Ramesha, C. P. Laisa, H. Vezin, M. T. Sougrati, M. L. Doublet, D. Foix, D. Gonbeau, W. Walker, A. S. Prakash, M. Ben Hassine, L. Dupont, and J. M. Tarascon. Reversible anionic redox chemistry in high-capacity layered-oxide electrodes. *Nat. Mater.*, 12(9):827–835, 2013. 34, 57
- [131] Meng Gu, Ilias Belharouak, Jianming Zheng, Huiming Wu, Jie Xiao, Arda Genc, Khalil Amine, Suntharampillai Thevuthasan, Donald R. Baer, Ji Guang Zhang, Nigel D. Browning, Jun Liu, and Chongmin Wang. Formation of the spinel phase in the layered composite cathode used in Li-Ion batteries. *ACS Nano*, 7(1):760–767, 2013. 34, 57
- [132] Hungru Chen and M. Saiful Islam. Lithium extraction mechanism in Li-rich  $\text{Li}_2\text{MnO}_3$  involving oxygen hole formation and dimerization. *Chem. Mater.*, 28(18):6656–6663, 2016. 34, 57
- [133] Keiji Shimoda, Masatsugu Oishi, Toshiyuki Matsunaga, Miwa Murakami, Keisuke Yamanaka, Hajime Arai, Yoshio Ukyo, Yoshiharu Uchimoto, Toshiaki Ohta, Eiichiro Matsubara, and Zempachi Ogumi. Direct observation of layered-to-spinel phase transformation in  $\text{Li}_2\text{MnO}_3$  and the spinel structure stabilised after the activation process. *J. Mater. Chem. A*, 5(14):6695–6707, 2017. 34, 57
- [134] Karin Kleiner, Benjamin Strehle, Annabelle R. Baker, Sarah J. Day, Chiu C. Tang, Irmgard Buchberger, Frederick Francois Chesneau, Hubert A. Gasteiger, and Michele Piana. Origin of High Capacity and Poor Cycling Stability of Li-Rich Layered Oxides: A Long-Duration in Situ Synchrotron Powder Diffraction Study. *Chem. Mater.*, 30(11):3656–3667, 2018. 34, 57, 60, 62

- [135] Jon Serrano-Sevillano, Marine Reynaud, Amaia Saracibar, Thomas Altantzis, Sara Bals, Gustaaf Van Tendeloo, and Montse Casas-Cabanas. Enhanced electrochemical performance of Li-rich cathode materials through microstructural control. *Phys. Chem. Chem. Phys.*, 20(35):23112–23122, 2018. 34
- [136] M. Casas-Cabanas, J. Rodríguez-Carvajal, and M. R. Palacín. FAULTS, a new program for refinement of powder diffraction patterns from layered structures. *Zeitschrift für Krist. Suppl.*, 1(23):243–248, 2006. 34
- [137] Olesia M. Karakulina, Arnaud Demortière, Walid Dachraoui, Artem M. Abakumov, and Joke Hadermann. In Situ Electron Diffraction Tomography Using a Liquid-Electrochemical Transmission Electron Microscopy Cell for Crystal Structure Determination of Cathode Materials for Li-Ion batteries. *Nano Lett.*, 18(10):6286–6291, 2018. 34
- [138] Andreas Paulus, Mylène Hendrickx, Marnik Bercx, Olesia M. Karakulina, Maria A. Kirsanova, Dirk Lamoen, Joke Hadermann, Artem M. Abakumov, Marlies K. Van Bael, and An Hardy. An in-depth study of Sn substitution in Li-rich/Mn-rich NMC as a cathode material for Li-ion batteries. *Dalt. Trans.*, 49(30):10486–10497, 2020. 34, 35, 36, 57
- [139] K. A. Jarvis, Z. Q. Deng, L. F. Allard, A. Manthiram, and P. J. Ferreira. Understanding Structural Defects in Lithium-rich Layered Oxide Cathodes by Aberration-Corrected STEM. *Microsc. Microanal.*, 18(Suppl 2):1414–1415, 2012. 35
- [140] Hideyuki Koga, Laurence Croguennec, and Philippe Manneziej. Li<sub>1.20</sub>Mn<sub>0.54</sub>Co<sub>0.13</sub>Ni<sub>0.13</sub>O<sub>2</sub> with different particle sizes as attractive positive electrode materials for lithium-ion batteries: insights into their structure. *J. Phys. Chem., C* 116:13497–13506, 2012. 35
- [141] Alpesh Khushalchand Shukla, Quentin M. Ramasse, Colin Ophus, Hugues Duncan, Fredrik Hage, and Guoying Chen. Unravelling structural ambiguities in lithium- and manganese-rich transition metal oxides. *Nat. Commun.*, 6(1):1–9, 2015. 35
- [142] Julien Bréger, Meng Jiang, Nicolas Dupré, Ying S. Meng, Yang Shao-Horn, Gerbrand Ceder, and Clare P. Grey. High-resolution X-ray diffraction, DIFFaX, NMR and first principles study of disorder in the Li<sub>2</sub>MnO<sub>3</sub>-Li[Ni<sub>1/2</sub>Mn<sub>1/2</sub>]O<sub>2</sub> solid solution. *J. Solid State Chem.*, 178(9):2575–2585, 2005. 35
- [143] C. H. Lei, J. G. Wen, M. Sardela, J. Bareño, I. Petrov, S. H. Kang, and D. P. Abraham. Structural study of Li<sub>2</sub>MnO<sub>3</sub> by electron microscopy. *J. Mater. Sci.*, 44(20):5579–5587, 2009. 35
- [144] Karalee A. Jarvis, Zengqiang Deng, Lawrence F. Allard, Arumugam Manthiram, and Paulo J. Ferreira. Atomic structure of a lithium-rich layered oxide material for

## BIBLIOGRAPHY

- lithium-ion batteries: Evidence of a solid solution. *Chem. Mater.*, 23(16):3614–3621, 2011. 35
- [145] Lars Riekehr, Jinlong Liu, Björn Schwarz, Florian Sigel, Ingo Kerkamm, Yongyao Xia, and Helmut Ehrenberg. Fatigue in 0.5Li<sub>2</sub>MnO<sub>3</sub>:0.5Li(Ni<sub>1/3</sub>Co<sub>1/3</sub>Mn<sub>1/3</sub>)O<sub>2</sub> positive electrodes for lithium ion batteries. *J. Power Sources*, 325:391–403, 2016. 37, 45
- [146] Matthias Quintelier, Tyché Perkisas, Romy Poppe, Maria Batuk, Mylene Hendrickx, and Joke Hadermann. Determination of spinel content in cycled Li<sub>1.2</sub>Ni<sub>0.13</sub>Mn<sub>0.54</sub>Co<sub>0.13</sub>O<sub>2</sub> using three-dimensional electron diffraction and precession electron diffraction. *Symmetry (Basel)*, 13(11):1–17, 2021. 45
- [147] Karalee A. Jarvis, Chih Chieh Wang, Arumugam Manthiram, and Paulo J. Ferreira. The role of composition in the atomic structure, oxygen loss, and capacity of layered Li-Mn-Ni oxide cathodes. *J. Mater. Chem. A*, 2(5):1353–1362, 2014. 45
- [148] Artem M. Abakumov, Chen Li, Anton Boev, Dmitry A. Aksyonov, Aleksandra A. Savina, Tatiana A. Abakumova, Gustaaf Van Tendeloo, and Sara Bals. Grain Boundaries as a Diffusion-Limiting Factor in Lithium-Rich NMC Cathodes for High-Energy Lithium-Ion Batteries. *ACS Appl. Energy Mater.*, 4(7):6777–6786, 2021. 48
- [149] Wei Yin, Alexis Grimaud, Gwenaëlle Rousse, Artem M. Abakumov, Anatoliy Senyshyn, Leitong Zhang, Sigita Trabesinger, Antonella Iadecola, Dominique Foix, Domitille Giaume, and Jean Marie Tarascon. Structural evolution at the oxidative and reductive limits in the first electrochemical cycle of Li<sub>1.2</sub>Ni<sub>0.13</sub>Mn<sub>0.54</sub>Co<sub>0.13</sub>O<sub>2</sub>. *Nat. Commun.*, 11(1):1–11, 2020. 48
- [150] Daphne Vandemeulebroucke. *Kwantificatie van de stapelfouten in het gelaagd Li-rijk Mn-rijk NMC kathodemateriaal voor lithium-ionbatterijen op basis van diffuse verstrooiing uit elektronendiffractie*. PhD thesis, University of Antwerp, 2020. 49
- [151] Debasish Mohanty, E Andrew Payzant, Athena S Sefat, Jianlin Li, Daniel P Abraham, David L Wood, and Claus Daniel. Article pubs.acs.org/cm Neutron Diffraction and Magnetic Susceptibility Studies on a High-Voltage Li<sub>1.2</sub>Mn<sub>0.55</sub>Ni<sub>0.15</sub>Co<sub>0.10</sub>O<sub>2</sub> Lithium Ion Battery Cathode: Insight into the Crystal Structure. *Chem. Mater.*, 25(20):4064–4070, 2013. 52, 53, 56, 57, 59
- [152] A. Mosbah, A. Verbaere, and M. Tournoux. Phases Li<sub>x</sub>MnO<sub>2</sub> rattachees au type spinelle. *Mater. Res. Bull.*, 18(11):1375–1381, 1983. 57, 59
- [153] Ping Lu, Pengfei Yan, Eric Romero, Erik David Spoerke, Ji Guang Zhang, and Chong Min Wang. Observation of electron-beam-induced phase evolution mimicking the effect of the charge-discharge cycle in Li-rich layered cathode materials used for Li ion batteries. *Chem. Mater.*, 27(4):1375–1380, 2015. 58

- [154] Feng Lin, Isaac M. Markus, Dennis Nordlund, Tsu Chien Weng, Mark D. Asta, Huolin L. Xin, and Marca M. Doeff. Surface reconstruction and chemical evolution of stoichiometric layered cathode materials for lithium-ion batteries. *Nat. Commun.*, 5:3529, 2014. 58
- [155] F. Lin, I.M. Markus, M.M. Doeff, and H.L. Xin. Chemical and structural stability of lithium-ion battery electrode materials under electron beam. *Sci. Rep.*, 4(5694), 2014. 58
- [156] Nikolaj Roth, Jonas Beyer, Karl F. F. Fischer, Kaiyang Xia, Tiejun Zhu, and Bo B. Iversen. Tuneable local order in thermoelectric crystals. *IUCrJ*, 8(4):695–702, 2021. 64, 65, 66, 67, 68, 80, 83, 84, 85, 86
- [157] Nikolaj Roth, Tiejun Zhu, and Bo B. Iversen. A simple model for vacancy order and disorder in defective half-Heusler systems. *IUCrJ*, 7:673–680, 2020. 64, 80, 81
- [158] Junjie Yu, Chenguang Fu, Yintu Liu, Kaiyang Xia, Umut Aydemir, Thomas C. Chasapis, G. Jeffrey Snyder, Xinbing Zhao, and Tiejun Zhu. Unique Role of Refractory Ta Alloying in Enhancing the Figure of Merit of NbFeSb Thermoelectric Materials. *Adv. Energy Mater.*, 8(1):1–8, 2018. 64
- [159] Wolfgang G. Zeier, Shashwat Anand, Lihong Huang, Ran He, Hao Zhang, Zhifeng Ren, Chris Wolverton, and G. Jeffrey Snyder. Using the 18-Electron Rule To Understand the Nominal 19-Electron Half-Heusler NbCoSb with Nb Vacancies. *Chem. Mater.*, 29(3):1210–1217, 2017. 65, 80, 81
- [160] Lukáš Palatinus. PETS2. 68
- [161] Kaiyang Xia, Pengfei Nan, Shihua Tan, Yumei Wang, Binghui Ge, Wenqing Zhang, Shashwat Anand, Xinbing Zhao, G. Jeffrey Snyder, and Tiejun Zhu. Short-range order in defective half-Heusler thermoelectric crystals. *Energy Environ. Sci.*, 12(5):1568–1574, 2019. 73
- [162] P. Kraft, A. Bergamaschi, Ch Broennimann, R. Dinapoli, E. F. Eikenberry, B. Henrich, I. Johnson, A. Mozzanica, C. M. Schlepütz, P. R. Willmott, and B. Schmitt. Performance of single-photon-counting PILATUS detector modules. *J. Synchrotron Radiat.*, 16(3):368–375, 2009. 75
- [163] Patrick Pangaud, Stephanie Basolo, Nathalie Boudet, Jean François Berar, Benoît Chantepie, Jean Claude Clemens, Pierre Delpierre, Bernard Dinkespiler, Kadda Medjoubi, Stephanie Hustache, Mohsine Menouni, and Christian Morel. XPAD3-S: A fast hybrid pixel readout chip for X-ray synchrotron facilities. *Nucl. Instruments Methods Phys. Res. Sect. A Accel. Spectrometers, Detect. Assoc. Equip.*, 591(1):159–162, 2008. 75

## BIBLIOGRAPHY

- [164] Eva N. Gimenez, Rafael Ballabriga, Michael Campbell, Ian Horswell, Xavier Llopart, Julien Marchal, Kawal J.S. Sawhney, Nicola Tartoni, and Daniel Turecek. Characterization of Medipix3 with synchrotron radiation. *IEEE Trans. Nucl. Sci.*, 58(1 PART 2):323–332, 2011. 75
- [165] J. Jakůbek. Semiconductor Pixel detectors and their applications in life sciences. *J. Instrum.*, 4(3), 2009. 76
- [166] T. R. Welberry. Diffuse x-ray scattering and models of disorder. *Reports Prog. Phys.*, 48(11):1543–1593, 1985. 81
- [167] O. Arnold, J. C. Bilheux, J. M. Borreguero, A. Buts, S. I. Campbell, L. Chapon, M. Doucet, N. Draper, R. Ferraz Leal, M. A. Gigg, V. E. Lynch, A. Markvardsen, D. J. Mikkelson, R. L. Mikkelson, R. Miller, K. Palmén, P. Parker, G. Passos, T. G. Perring, P. F. Peterson, S. Ren, M. A. Reuter, A. T. Savici, J. W. Taylor, R. J. Taylor, R. Tolchenov, W. Zhou, and J. Zikovsky. Mantid - Data analysis and visualization package for neutron scattering and  $\mu$  SR experiments. *Nucl. Instruments Methods Phys. Res. Sect. A Accel. Spectrometers, Detect. Assoc. Equip.*, 764:156–166, 2014. 90
- [168] Joe Paddison. Scatty : Quick-start guide Input files. pages 1–5, 2018. 90
- [169] Aleksandr I. Gusev. Short-range order and diffuse scattering in nonstoichiometric compounds. *Uspekhi Fiz. Nauk*, 176(7):717, 2006. 110, 111
- [170] J. Billingham, P. S. Bell, and M. H. Lewis. Vacancy short-range order in substoichiometric transition metal carbides and nitrides with the NaCl structure. I. Electron diffraction studies of short-range ordered compounds. *Acta Crystallogr. Sect. A*, 28(6):602–606, 1972. 110
- [171] M. Sauvage and E. Parthé. Vacancy short-range order in substoichiometric transition metal carbides and nitrides with the NaCl structure. II. Numerical calculation of vacancy arrangement. *Acta Crystallogr. Sect. A*, 28(6):607–616, 1972. 110, 111
- [172] P. Li and J. M. Howe. Short-range ordering and  $\{1,1/2,0\}$  diffuse intensity maxima in  $ZrN_x$ . *Acta Mater.*, 51(5):1261–1270, 2003. 110
- [173] M. Brunel, F. De Bergevin, and M. Gondrand. Determination theorique et domaines d’existence des differentes surstructures dans les composes  $A_3+B_1+X_{22}$ -de type NaCl. *J. Phys. Chem. Solids*, 33(10):1927–1941, 1972. 110
- [174] R. De Ridder, D. Van Dyck, G. Van Tendeloo, and S. Amelinckx. A Cluster Model for the Transition State and Its Study by Means of Electron Diffraction. *Phys. Status Solidi*, 40(2):669–683, 1977. 110, 111
- [175] Masanori Mitome, Shigemi Kohiki, Yusuke Murakawa, Kyoko Hori, Keiji Kurashima, and Yoshio Bando. Transmission electron microscopy and electron diffraction study of the short-range ordering structure of  $\alpha$ -LiFeO<sub>2</sub>. *Acta Crystallogr. Sect. B Struct. Sci.*, 60(6):698–704, 2004. 110

- [176] D G Kellerman, E V Shalaeva, and A I Gusev. Cluster Formation in  $\text{LiNi}_{0.4}\text{Fe}_{0.6}\text{O}_2$ . *Phys. Solid State*, 46(9):1686–1692, 2004. 110
- [177] J. Kikkawa, T. Akita, M. Tabuchi, M. Shikano, K. Tatsumi, and M. Kohyama. Real-space observation of Li extraction/insertion in  $\text{Li}_{1.2}\text{Mn}_{0.4}\text{Fe}_{0.4}\text{O}_2$  positive electrode material for Li-ion batteries. *Electrochem. Solid-State Lett.*, 11(11):183–186, 2008. 110
- [178] M. A. Castellanos Román, A. M. De León Guevara, J. Guzmán-Mendoza, L. Baños, J. L. Heiras-Aguirre, and A. Huanosta-Tera. Diffuse electron scattering of a region in the system  $\text{Li}_2\text{SnO}_3\text{-CoO}$ . *Acta Mater.*, 51(8):2125–2130, 2003. 110
- [179] F. J. Brink, L. Norén, and R. L. Withers. Synthesis, electron diffraction, XRD and DSC study of the new elpasolite-related oxyfluoride,  $\text{Ti}_3\text{MoO}_3\text{F}_3$ . *J. Solid State Chem.*, 174(1):44–51, 2003. 110
- [180] Esteban Urones-Garrote, Adrián Gómez-Herrero, Ángel R. Landa-Cánovas, Ray L. Withers, and L. Carlos Otero-Díaz. Order and disorder in rocksalt and spinel structures in the  $\text{MgS-Yb}_2\text{S}_3$  system. *Chem. Mater.*, 17(13):3524–3531, 2005. 110
- [181] R. L. Withers, E. Urones-Garrote, and L. C. Otero-Díaz. Structured diffuse scattering, local crystal chemistry and metal ion ordering in the  $(1-x)\text{MgS}_x/3 \text{ Yb}_2\text{S}_3$ ,  $0 < x < 0.45$ , 'defect' NaCl system. *Philos. Mag.*, 87(18-21):2807–2813, 2007. 110
- [182] Oliver Oeckler, Thomas Weber, Lorenz Kienle, Hansjürgen Mattausch, and Arndt Simon. Cluster disorder and ordering principles in Al-stabilized "LaI". *Angew. Chemie - Int. Ed.*, 44(25):3917–3921, 2005. 110
- [183] M. Sauvage and E. Parthé. Based on  $\text{ZnS}$ ,  $\text{NaCl}$ ,  $\text{CsCl}$  and Other Structures. *Acta Crystallogr. Sect. A Cryst. Physics, Diffraction, Theor. Gen. Crystallogr.*, 30(2):239–246, 1974. 111
- [184] R. De Ridder, G. Van Tendeloo, and S. Amelinckx. A Cluster Model for the Transition State and Its Study by Means of Electron Diffraction. II. Application to Some Particular Systems. *Acta Crystallogr. A*, 32(2):216–224, 1976. 111
- [185] Maria Batuk, Daphne Vandemeulebroucke, Monica Ceretti, Werner Paulus, and Joke Hadermann. Topotactic redox cycling in  $\text{SrFeO}_{2.5+\delta}$  explored by 3D electron diffraction in different gas atmospheres. *J. Mater. Chem. A*, 11(1):213–220, 2022. 125

*BIBLIOGRAPHY*





## Curriculum vitae

---

NAME: Romy Poppe  
BORN: 5/12/1996, Sint-Niklaas, Belgium  
CONTACT: Campus Groenenborger (G.U.419)  
Groenenborgerlaan 171  
2020 Antwerpen, Belgium  
E-MAIL: Romy.Poppe@uantwerpen.be,  
Romy.Poppe@hotmail.com

### Education

2019-present PhD Researcher, University of Antwerp  
2017-2019 Master Sc. Physics, University of Antwerp, with great distinction  
2015-2017 Bachelor Sc. Physics, University of Antwerp, with great distinction  
2015-2017 Honours program, University of Antwerp

### Teaching

2021-present General Physics III : Electromagnetism, Bachelor of Physics  
2019-2021 Experimental Physics II, Bachelor of Physics

### Research stays

Research stay in the group of Prof. Dr. Andrew Goodwin at the University of Oxford (September 2023).

## Additional Activities

- 2019-present Secretary of the Antwerp Young Minds (part of the European Physical Society Young Minds)
- 2019-present Ombudsperson of the Bachelor of Physics; Member of the Educational Commission Physics, Exam Commission Physics, Fraud Committee Physics and Academic Progress Committee Physics

## Computer skills

Operating systems: Linux, Windows  
Programming languages: Python, Fortran, MATLAB

## Languages

Dutch (native), English (fluent), French (fluent)

## Publications

### Peer-reviewed

Poppe, R., Vandemeulebroucke, D., Neder, R. B., & Hadermann, J. (2022). Quantitative analysis of diffuse electron scattering in the lithium-ion battery cathode material  $\text{Li}_{1.2}\text{Ni}_{0.13}\text{Mn}_{0.54}\text{Co}_{0.13}\text{O}_2$ . *IUCrJ*, 9(5), 695-704.

Quintelier, M., Perkisas, T., Poppe, R., Batuk, M., Hendrickx, M., & Hadermann, J. (2021). Determination of Spinel Content in Cycled  $\text{Li}_{1.2}\text{Ni}_{0.13}\text{Mn}_{0.54}\text{Co}_{0.13}\text{O}_2$  Using Three-Dimensional Electron Diffraction and Precession Electron Diffraction. *Symmetry*, 13(11), 1989.

### Preprints

Poppe, R., & Hadermann, J., Diffuse electron scattering data acquisition for quantitative analysis.

Poppe, R., Roth, N., Neder, R. B., Palatinus, L., Iversen, B. B., & Hadermann,

J., Refinement of the short-range order parameters from the diffuse scattering in single-crystal electron diffraction data.

## Conference presentations

Quantitative analysis of diffuse electron scattering in the lithium-ion battery cathode material  $\text{Li}_{1.2}\text{Ni}_{0.13}\text{Mn}_{0.54}\text{Co}_{0.13}\text{O}_2$ , Oral presentation, Twenty-Fifth Congress and General Assembly of the International Union of Crystallography, Prague (Czech Republic), August 14-22, 2021.

Quantitative analysis of diffuse electron scattering in the lithium-ion battery cathode material  $\text{Li}_{1.2}\text{Ni}_{0.13}\text{Mn}_{0.54}\text{Co}_{0.13}\text{O}_2$ , Poster presentation, Twenty-Fifth Congress and General Assembly of the International Union of Crystallography, Prague (Czech Republic), August 11-13, 2021.

Quantitative analysis of diffuse electron scattering in the lithium-ion battery cathode material  $\text{Li}_{1.2}\text{Ni}_{0.13}\text{Mn}_{0.54}\text{Co}_{0.13}\text{O}_2$ , Poster presentation, 33rd European Crystallographic Meeting, Versailles (France), August 23-27, 2022.

Quantitative analysis of diffuse electron scattering in the lithium-ion battery cathode material  $\text{Li}_{1.2}\text{Ni}_{0.13}\text{Mn}_{0.54}\text{Co}_{0.13}\text{O}_2$ , Oral presentation, School and Conference on Analysis of Diffraction Data in Real Space, Grenoble (France), October 16-21, 2022.

Quantitative analysis of diffuse electron scattering, Oral presentation, invited talk at the University of Oxford, Oxford (United Kingdom), March 8, 2023.

Quantitative analysis of diffuse electron scattering, Oral presentation, Workshop on Electron Crystallography, Antwerp (Belgium), May 30-31, 2023.

Quantitative comparison between the diffuse scattering from single-crystal X-ray and single-crystal electron diffraction, Oral presentation, Twenty-Sixth Congress and General Assembly of the International Union of Crystallography, Melbourne (Australia), August 22-29, 2023.

*APPENDIX A. CURRICULUM VITAE*

## Acknowledgments

---

First of all, I would like to thank Prof. Dr. **Joke Hadermann** for her constant support and guidance over the years and for giving me the opportunity to do a PhD. I am very grateful for the freedom she provided in deciding the direction of this research.

My very special thanks go to Dr. **Nikolaj Roth** for the fruitful collaboration and discussions. I want to express my gratitude to Prof. Dr. **Arkadiy Simonov** for his help with the 3D- $\Delta$ PDF refinement in *Yell* and Prof. Dr. **Reinhard Neder** for his help with the Monte Carlo refinement in *DISCUS*. I am very grateful for extending the functionality of *DISCUS* to the wishes I developed within my PhD thesis. My gratitude also goes to Dr. **Lukáš Palatinus** for answering all my questions regarding the dynamical refinement in *Jana2020*, Dr. **Joseph Paddison** for including the electron atomic form factors in *Scatty*, Prof. Dr. **Bo Brummerstedt Iversen** for sending us the  $\text{Nb}_{0.84}\text{CoSb}$  samples and Dr. **Andreas Paulus** for the synthesis of the  $\text{LiNi}_{0.5}\text{Sn}_{0.3}\text{Co}_{0.2}\text{O}_2$  powder. I would also like to thank Prof. Dr. **Andrew Goodwin** for the research stay at the University of Oxford.

Many thanks to Dr. **Armand B  ch  ** for the microscopy training and Dr. **Myl  ne Hendrickx** who taught me how to acquire HAADF-STEM images.

I want to thank all my EMAT colleagues for all the pleasant moments during working days. Especially **Daphne Vandemeulebroucke** and **Ine Arts** for being friends and office mates. You made the time at EMAT much more enjoyable. Also thanks to Dr. **Maria Batuk**, **Saleh Gholam**, **Sepideh Rahimi**, **Amirhossein Hajizadeh** and **Matthias Quintelier** for the nice conversations during group meetings and lunch breaks.

Finally, I want to thank my family and friends for always supporting me. Especially my father, who passed away this year, but who was always there for me.

This work was supported by the Research Foundation - Flanders (FWO) (Grant numbers G035619N and G040116N). The computational resources and services used in this work were provided by the HPC core facility CalcUA of the Universiteit Antwerpen,

## *APPENDIX B. ACKNOWLEDGMENTS*

and VSC (Flemish Supercomputer Center), funded by the Research Foundation - Flanders (FWO) and the Flemish Government.



